A SOLUTION-LIQUID-SOLID APPROACH TO COLLOIDAL INDIUM NITRIDE NANOPARTICLES FROM SIMPLE ALKYLAMIDE PRECURSORS AND INVESTIGATION OF ITS MECHANISM

By

Yang Chen

A THESIS

Submitted to
Michigan State University
in partial fulfillment of the requirements
for the degree of

Chemistry-Master of Science

2017

ABSTRACT

A SOLUTION-LIQUID-SOLID APPROACH TO COLLOIDAL INDIUM NITRIDE NANOPARTICLES FROM SIMPLE ALKYLAMIDE PRECURSORS AND INVESTIGATION OF ITS MECHANISM

By

Yang Chen

This thesis reports a solution-based method to synthesize colloidal InN nanomaterials where $InBr_3$ and oleylamide were employed as indium and nitrogen precursors, respectively, and its possible mechanism. Characterizations by X-ray diffraction, Raman spectroscopy, Transmission electron microscopy, X-ray photoelectron spectroscopy and Near infrared-visible absorption support this method as a convincing advancement toward high quality zinc-blende InN nanoparticles. Nuclear magnetic resonance and Gas chromatography were used to qualify the by-products of this approach. A possible reaction mechanism is also proposed here: (1) NH_2^- intermediate is produced as a result of the formation of the secondary imine. (2) NH_2^- intermediate reacts with In^{3+} to form a complex which easily decomposes to produce $(InN)_n$ clusters. (3) $In^{(0)}$ nanoparticles produced by reduction of In^{3+} by H^- catalyzed the formation of zinc-blende InN with high crystallinity.

This thesis is dedicated to Grandma, Mom and Dad.
Thank you for always supporting me.

ACKNOWLEDGMENTS

Firstly, I would like to thank the Department of Chemistry at Michigan State University for giving me a chance to study here and my advisor Dr. Rémi Beaulac for his guidance. In these past two and half years, his patience, visible insights and enthusiasm make me capable to finish my research project. Every time, when I met problems during my research, his useful advice always inspired me and gave me new ideas to solve these problems. His help will always continue to be much appreciated. I am truly grateful to Dr. Richard Staples for teaching me how to use XRD instruments. Thank Dr. Per Askeland for being extremely helpful in XPS analysis. Thank Professor Daniel Jones for spending time discussing with me for LC-MS measurements. Thank Dr. Xudong Fan for TEM measurements. A big thank to Dr. Dan Holmes and Dr. Xie Li for NMR help. I would also like to thank Daniel Little for GC measurements.

Secondly, I would like to thank my committee members: Professor Aaron Odom, Professor Thomas Hamann and Professor Mitch Smith for their support, guidance and suggestion which have always motivated me to move forward.

I would also like to thank my group members for creating such comfortable atmosphere in lab. Thank Poulami Dutta and Chenjia Mi for helping me deal with problems in my research project. Thank Mersedeh Saniepay for making our lab so organized. Thank Zhihui Liu for NIR-Vis absorption measurements. And also thank Geoffrey Bourdon for your support, you are my best friend.

Last but not least, I want to thank my mom, my dad and my grandma. No matter what decision I made, you always stand by me and never lose faith in me. Thank you for this support, making me confident and strong to overcome many of life's challenges.

This two and half year journey would certainly be a valuable memory for me. Thank all of you who accompanied me in this period.

TABLE OF CONTENTS

LIST OF TABLES

LIST OF FIGURES

LIST OF SCHEMES

KEY TO ABBREVIATIONS

ACS: American Chemical Society

COSY: Correlated spectroscopy

Da: Dalton

EDS: Energy dispersive x-ray spectroscopy

GC: Gas chromatography

HMDS: Hexamethyldisilazane

HRTEM: High resolution transmission electron microscopy

HSQC: Heteronuclear single quantum coherence spectroscopy

HVPE: Hydride vapour phase epitaxy

LED: Light-emitting diode

LC-MS: Liquid chromatography-mass spectrometry

MBE: Molecular beam epitaxy

MOCVD: Metalorganic vapour phase epitaxy

NIR-Vis: Near infrared-visible

NMR: Nuclear Magnetic Resonance

NCs: Nanocrystals

NPs: Nanoparticles

NRs: Nanorods

n-BuLi: *n*-Butyl lithium, Butyllithium

OLA：Oleylamine

ODE: 1-Octadecene, Octadec-1-ene

QDs: Quantum dots

QTOF: Quadrupole time-of-flight

SLS: Solution-liquid-solid

TEM: Transmission electron microscopy

TMEDA: Tetramethylethylenediamine, N,N,N',N'-tetramethylethane-1,2-diamine

TMS: Tetramethylsilane, Tetramethylsilane

TCE: Trichloroethylene, 1,1,2-trichloroethene

UV-vis-NIR: Ultraviolet-visible-near infrared

VLS: Vapor-liquid-solid

XRD: X-ray diffraction

XPS: X-ray photoelectron spectroscopy

Chapter 1

INTRODUCTION

1.1: Group III-Nitride Semiconductors

The group III-nitride semiconductors consist of AlN, GaN, InN and their alloys, and span a wide range of bandgap energies depending on composition. In recent decades, they have been investigated as promising materials for a variety of electronic and optoelectronic applications due to their attractive physical, optical, and electronic properties. [1-3]

The group-III nitrides share three common crystal structures: wurtzite, zincblende, and rocksalt structures. [4] Rocksalt structure is very rare and it can be induced in AlN, GaN, and InN at very high pressures. [4] At ambient conditions, wurtzite structure is the thermodynamically stable structure for bulk AlN, GaN, and InN. [5] While topological compatibility can make zinc-blende structure more favored since the cubic structure for GaN and InN has been stabilized by epitaxial growth of thin films on the [011] crystal planes of cubic substrates such as Si, MgO, and GaAs. [4]

As shown in Figure 1.1, wurtzite AlN, GaN and InN have direct bandgaps of 6.1±0.1 eV, [4, 5] 3.5±0.1 eV, [4, 5] and 0.7±0.05 eV [5, 6, 7, 8] at room temperature, respectively, where the low bandgap value of InN is still undergoing revisions. [6] In zinc-blende form, GaN and InN have direct bandgap while AlN has an indirect energy bandgap. [9] Once GaN has been alloyed with AlN and InN, these materials can span a wide and continuous range of direct bandgap (Figure 1.2), from 0.7 eV to 6.2 eV, which covers all the visible spectrum, going well into the ultraviolet wavelengths. This making nitride systems attraction for a wide range of optoelectronic applications. One of the important applications is for light emitting diodes (LEDs). LEDs are electronic devices where light is generated in semiconductor materials (such as GaN or AlInGaP)

by injecting electrons into the conduction band of the material and providing electronic vacancies ("holes") in the valence band that lead to radiative recombination. The color of the light generated in the LEDs corresponds to the bandgap of the semiconductor materials. In 2014, Nobel laureates, Isamu Akasaki, Hiroshi Amano and Shuji Nakamura, are rewarded for having invented a new energy-efficient and environment-friendly light source-the blue LEDs by using group-III nitride semiconductors. InGaN LEDs are now the devices of choice for green traffic signals worldwide and offer significant environmental benefits in the process. [10] More important, white-light sources based on reliable and energy-efficient LEDs have been made possible by using group-III nitride semiconductors. [11] If all conventional white-light sources in the world were converted to LEDs, energy consumption could be reduced by around 1,000 TWh/year. [12]

Another important application from water splitting is InGaN based photoelectrochemical cells for hydrogen generation. InGaN meets the requirements for hydrogen generation, for example, InGaN has been shown to be resistant against wet etchants and stable in aqueous solutions. [13] In addition, the highly tunable bandgap (0.7 to 3.4 eV) matches the sun's spectrum, which may be optimized for solar radiation for improved efficiency and photocurrent.

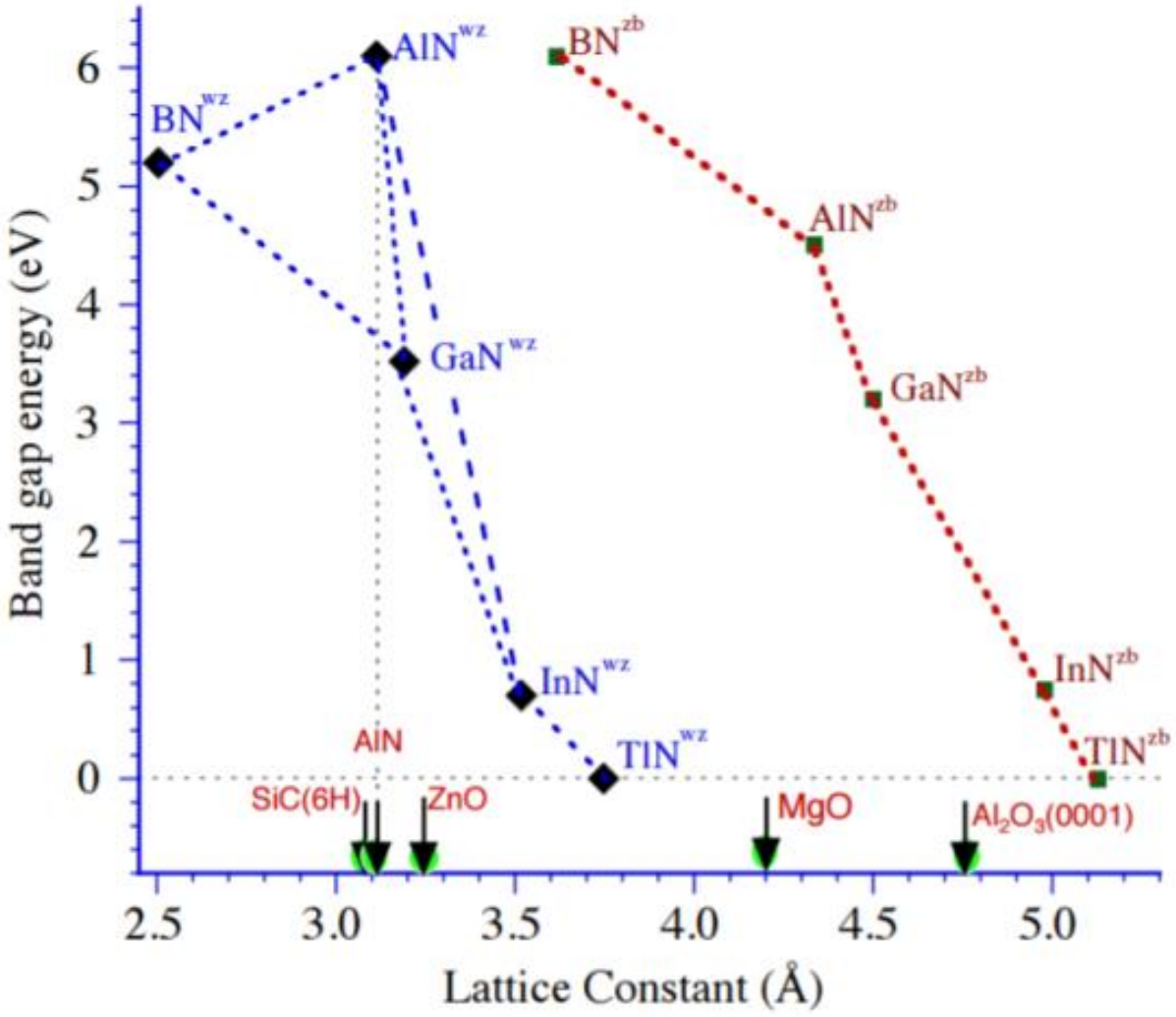

Figure 1.1: Lattice constants and bandgap energies for wurtzite (wz) and zinc-blende (zb) group-III nitride compound semiconductors, together with utilized substrates used in the epitaxial growth (Ref. 5).

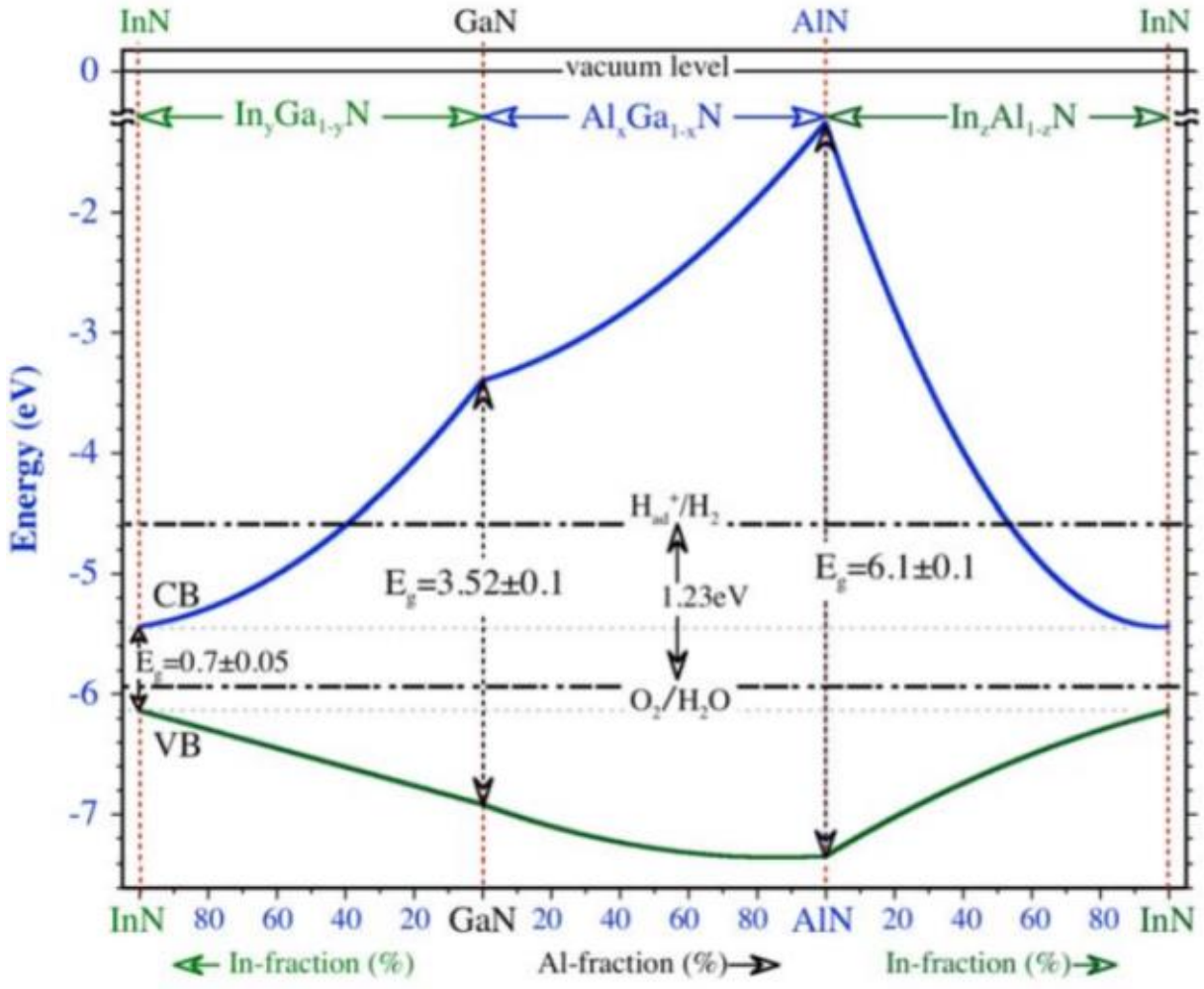

Figure 1.2: Valence band position and offsets for group III-nitrides alloys. Also marked are the hydrogen redox (H_{ad}^+/H_2 located at about 4.6 eV) and oxygen redox (O_2/H_2O located at about 1.23 eV below) potentials for water dissociation (Ref. 5).

1.2: Properties of Indium Nitride

Indium nitride is an important group-III nitride semiconductor with many potential applications. For example, the InN ternary alloy, InGaN, has been fabricated into a variety of heterostructure based optoelectronic devices, such as LEDs, which is possible to extend the emission from ultraviolet to near infrared region. [1-3] But the study and applications of InN is impeded by some challenges. One challenge is the lack of a suitable substrate material for epitaxial growth films causing a high concentration of extended defects in the film. For example, sapphire substrates that are often used to grow InN growth have lattice mismatch as large as 25%. [10] Another challenge is the growth temperature. InN undergoes a rapid dissociation at temperatures above 500 ^{o}C, leaving liquid indium metal (melting point is 156.6 ^{o}C) and N_2. [14, 15] This property of InN requires higher nitrogen overpressures in the system to prevent decomposition, which hinders the film growth, and low growth temperatures, which reduces the efficiency of forming reactive nitrogen from ammonia. Besides, due to the large difference between the heat of formation of InN (34 kcal/mol) and In_2O_3 (221 kcal/mol), oxidation of indium often occurs in preference to nitridation. [16] The surface oxidation of InN has been studied by Foley and Lyngdal. The first stage is oxygen bonds onto nitrogen to form an In-NO complex. In a second stage, In-NO complex is further oxidized to form an In-NO_2 complex. And the final oxidation state was dependent on the sample preparation conditions. [16]

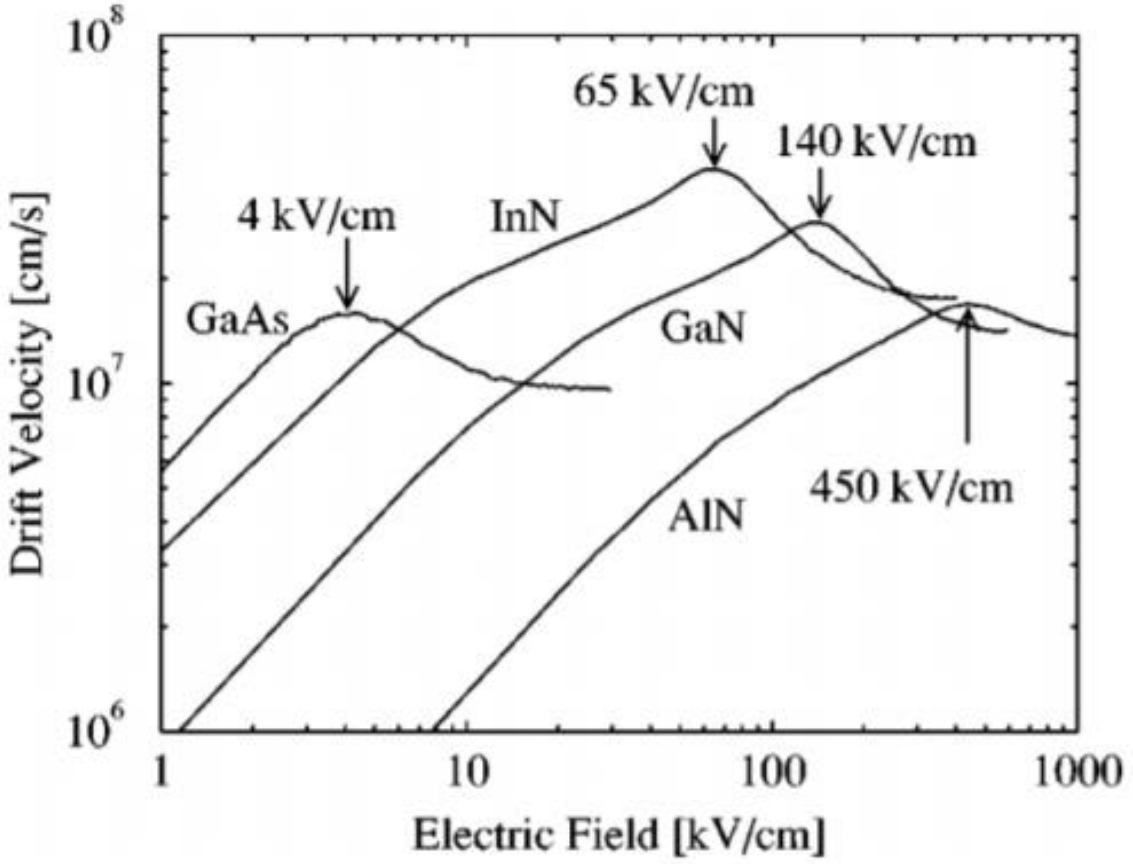

Figure 1.3: The velocity-field characteristic associated with wurtzite GaN, InN, AlN, and zinc-blende GaAs. In all cases, the temperature was set to 300 K and the doping concentration was set to 10^{17} cm^{-3}. The critical field at which the peak drift velocity was achieved for each velocity-field characteristic is marked; 140 kV/cm for GaN, 65 kV/cm for InN, 450 kV/cm for AlN, and 4kV/cm for GaAs (Ref. 20).

Because of these factors, it is difficult to obtain InN of good quality and the InN electron mobility varies depending on the growth techniques. [10] Despite predicted values as high as 3,000 $cm^2V^{-1}S^{-1}$ at room temperature for InN, most of electron mobility reported in the literatures are much smaller than this number, which may be caused by large background electron concentrations as a result of nitrogen vacancies. [10, 17] The theoretical maximum mobility calculated in InN at 300 K is about 4,400 $cm^2V^{-1}S^{-1}$, while the limit is beyond 30,000 $cm^2V^{-1}S^{-1}$ at 77K due to the lowest effective electron mass in all the group-III nitride semiconductors. [18, 19] The electron transport in wurtzite InN was studied by using an ensemble Monte Carlo method.

As shown in Figure 1.3, InN has the highest steady-state peak drift velocity: 4.2×10^7 cm/s. Besides, Bellotti *et al*. concluded that the transport characteristics of InN are superior to those of GaN and GaAs, over a wide range of temperatures from 150 to 500 K and with a doping concentration up to 10^{19} cm^{-3}, and the transport characteristics were shown to be relatively insensitive to variations in temperature and doping concentration. [20]

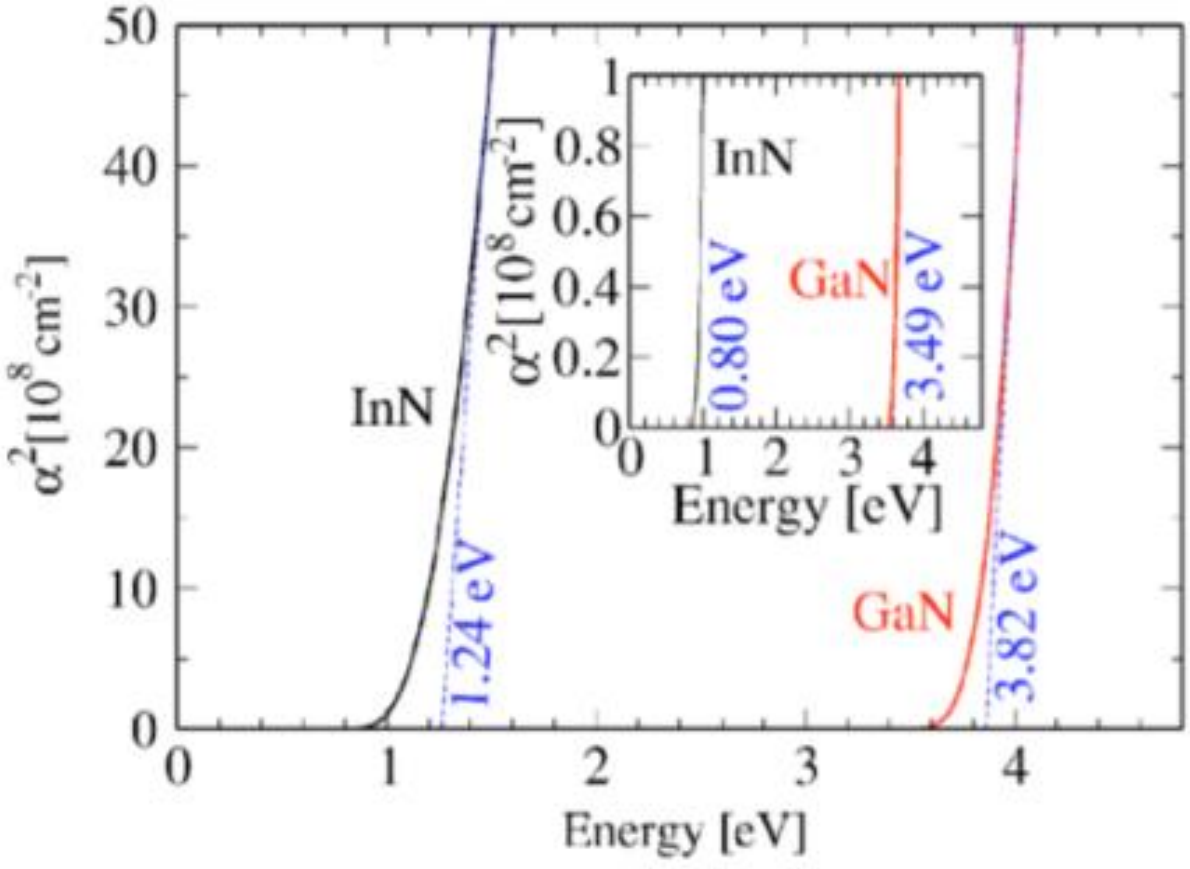

Figure 1.4: Calculated absorption coefficient of InN and GaN. (Ref. 30)

In 1986, Tansley and Foley reported the band gap energy of InN is 1.89 eV, [21] which was the commonly accepted value until the early 2000s when several groups showed by photoluminescence measurements that the band gap energy of InN is between 0.65 and 0.90 eV. [22-29] The principal result of recent studies shows that the wurtzite InN crystal is a narrow-gap semiconductor with a band gap of 0.7±0.05 eV [5, 6, 7, 8] at room temperature. In 2005, Carrier and

Wei gave a possible explanation for the origin of the measured large band gap. [30] First, they found that the conduction band of InN is strongly nonparabolic suggesting the absorption coefficient squared does not have a linear relationship with the absorption energy. Hence, as shown in Figure 1.4, the bandgap determined by the linear extrapolation technique depends on where the straight line is drawn. Second, the measured absorption edge can be shifted by the Moss-Burstein effect. [31, 32] Figure 1.5 shows the absorption edge increases with the carrier density from 0.8 eV for intrinsic InN to ~ 2.5 eV for the sample with electron concentration of ~ 10^{21} cm^3. Besides, as Molten [33] *et al* reported that the large values of InN bandgap may be related to oxygen incorporation into growth InN because polycrystalline film can contain a high density of oxygen atoms at their grain boundaries.

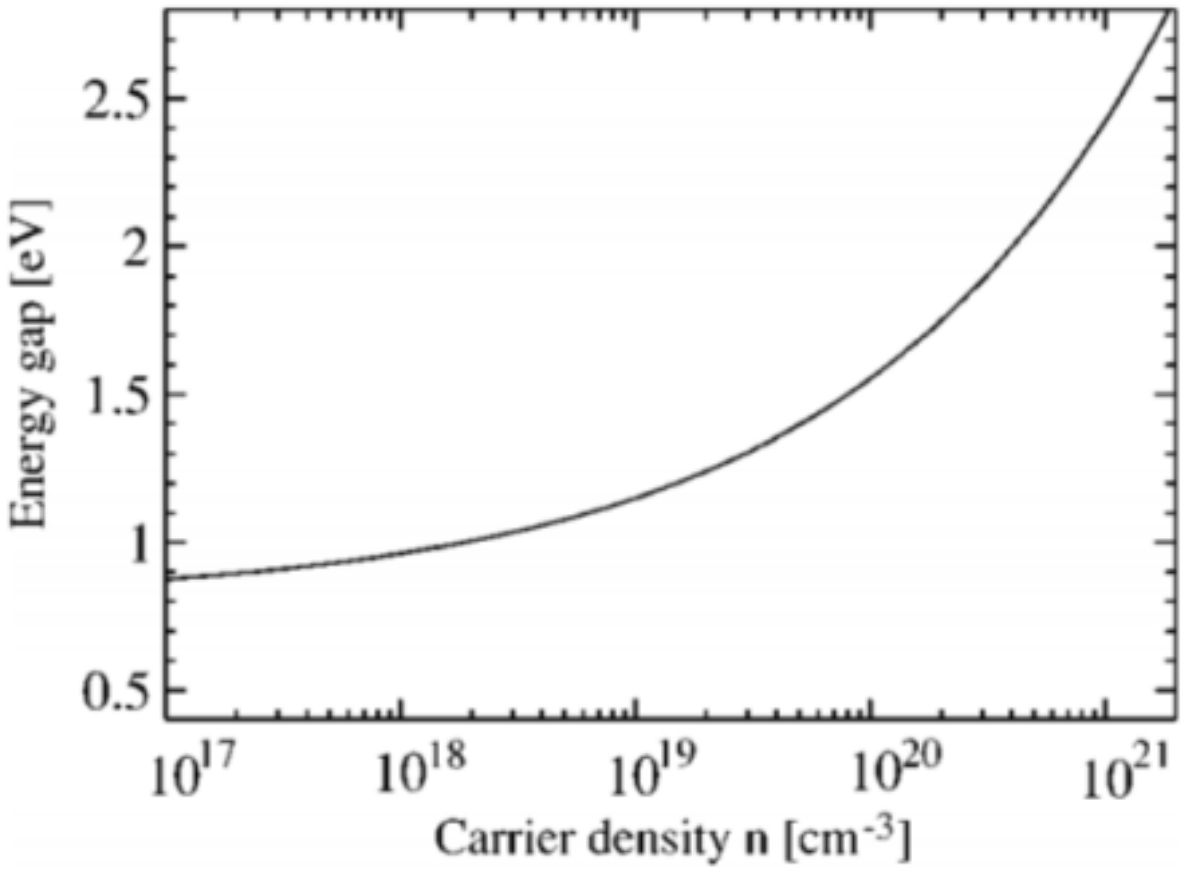

Figure 1.5: Calculated Moss-Burstein shift of the absorption edge energy as a function of the carrier density. (Ref. 30)

1.3: Semiconductor Nanocrystals

Semiconductor nanocrystals (NCs) are crystalline particles with dimensions in the order of 1-100 nm that exhibit size-dependent optical and electronic properties. [34, 35] These NCs typically contain 100 to 10,000 atoms. NCs with all three dimensions in nanometer range are referred to quantum dots (QDs) due to the emergency of quantum confinement effects. [34] These NCs exhibit markedly different chemical and physical properties as compared to the bulk crystalline solids. For example, altering the size of bulk materials has no effect on their optical and electronic properties. However, as the size of the colloidal semiconductor nanocrystals decreases, their bandgap would increase. [34]

Besides the size dependence of the bandgap for semiconductor nanocrystals, the surface atoms also influence the optical properties of semiconductor nanocrystals. The atoms on the surface are often incompletely bonded due to the absent neighbors, leaving one or more "dangling orbital". These unpassivated orbitals may form a band structure similar to that of the nanocrystal itself, [36, 37] or just lead to localized states. If the energy level of these unpassivated orbitals is within the bandgap of semiconductor nanocrystals, they can trap the charge carriers at the surface, reducing the recombination between electrons and holes and increasing the probability of nonradiative recombination. [38] These "dangling orbitals" can be passivated by organic ligands minimizing intraband gap surface states and reducing surface atomic reconstruction. At the same time, solubility of semiconductor nanocrystals can also be tuned by using different type of organic ligands.

Recently, semiconductor nanocrystals have been widely used. The tunability of bandgap make semiconductor nanocrystals become promising materials in solar cells. For example, in 2016, Lan *et al*. reported colloidal PdS nanocrystals based solar cells can achieve a certified solar cell

power conversion efficiency of 10.6%. [39] Chiral imprinted colloidal CdSe nanocrystals can act as spin filters for charge transport which can be used in spintronics devices. [40] Besides, colloidal nanocrystals can also be used for producing images of cancer tumors. [41] All of these motivate us to focus on the colloidal nanocrystal system of group-III nitrides.

1.4: Brief Review of Colloidal Nanocrystal Synthesis

In 2005, Yin gave colloidal nanocrystals a definition, "Colloidal nanocrystals are solution-grown, nanometer-sized, inorganic particles that are stabilized by a layer of surfactants attached to their surface. The inorganic cores possess useful properties that are control by their composition, size and shape, and the surfactant coating ensures that these structures are easy to fabricate and process further into more complex structures." [42]

Three basic components, precursor, organic surfactants and solvents, are required in a typical synthesis system for colloidal nanocrystals. In some cases, surfactants can also be used as solvent. The precursors can be converted into active atomic or molecular species which can be defined as monomers due to sufficiently high temperature; then these monomers can form colloidal nanocrystals. There are two important processes in the formation of nanocrystals, the nucleation followed by the growth of the nanocrystals.

La Mer made a huge contribution to the study of nucleation and growth. [43] La Mer's mechanism is depicted by Figure 1.6, which was reported in the early 1950's on the basis of the crystallization study of the solution-phase synthesis of monodisperse sulfur colloids in ethanol. At the beginning, decomposition of precursors by heating can increase the concentration of monomers steadily. Once the concentration of monomers arrives to supersaturation levels, these monomers start to aggregate into nuclei via self-nucleation. Then these nuclei grow rapidly by consuming the remaining monomers, resulting in the gradual decrease of the monomer

concentration. When the monomer concentration is kept below the critical level, nucleation is hindered. A continuous supply of monomers via ongoing precursor decomposition can convert the nuclei to nanocrystals of increasingly larger size until an equilibrium state is reached between the monomers on the surface and the monomers in the solution. [44]

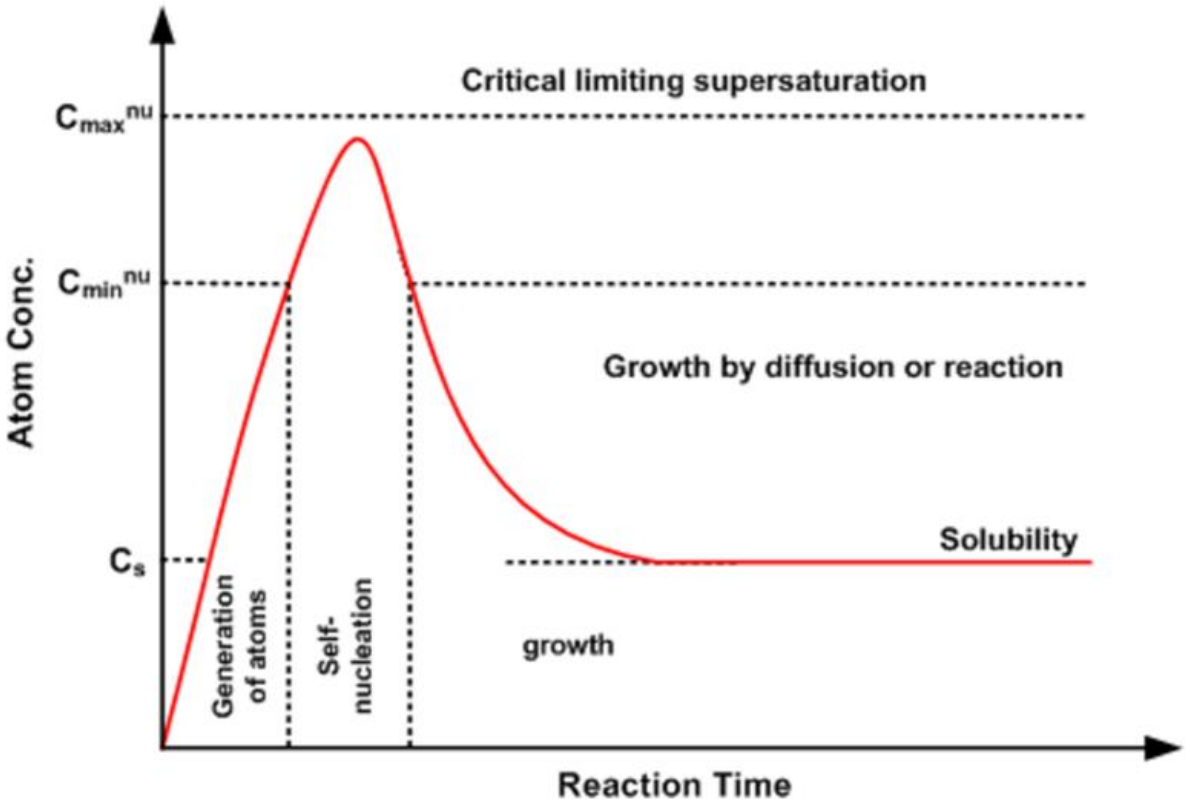

Figure 1.6: La Mer model for the generation of monomers, nucleation, and subsequent growth of colloids. (Ref. 43)

The search suitable precursors is an important step in the generation of colloidal inorganic nanocrystal. The precursors are required to decompose rapidly at the required growth temperature, in order to supply enough concentration of monomers, which then induce nanocrystal nucleation and growth. [45, 46]

Chemists have great interests in colloidal syntheses which can yield nanocrystals with relatively narrow size distributions. Figure 1.7 describes the dependence of growth rate on

nanocrystal radius. Growth rate is zero at the critical size. At this point, nanocrystals neither grow nor shrink. Below critical size, crystals are too small and have a larger fraction of active surface atoms, resulting in the negative growth rate. When the size of crystals becomes larger than critical size, stability increases due to the smaller surface-to-volume ratio and they start growing. Figure 1.7 also demonstrates why slow growth rates yield very broad size-distributions. The critical size depends on the monomer concentration: low monomer concentrations favor larger critical sizes. [42] Slow growth rates are associated with low monomer concentration. In this case, critical size has a high chance to fall within the distribution of nanocrystal sizes. Then the resultant Ostwald ripening leads to a broad, skewed size distribution by growing the larger crystals at the expense of smaller ones. There are two general approaches to obtain narrow size distributions. The first one is size selective precipitation. Stepwise addition of a non-solvent to a stable solution of nanocrystals is employed to gradually reduce the colloidal stability and lead for aggregation. [47, 48] Due to greater attractive Van der Waals or dipolar forces, larger nanoparticles crash out first. This approach is time-consuming, tedious and yields small quantities of materials of desired size. And it only works well with spherical crystals due to the attractive forces between anisotropic nanocrystals depending on multiple parameters. [49] The second approach uses the concept of size-distribution focusing based on the theory of Reiss that small crystals will grow more rapidly than larger ones if monomer concentrations are sufficiently high. [50] In the slow growth conditions, the monomer concentration is abruptly increased by a secondary injection of precursor, resulting in the critical size shift to a smaller value. Because the distribution of nanocrystal sizes present does not change, the entire distribution of sizes will move to the falling side of the growth versus radius curve. As a result, the distribution will

spontaneously narrow. [42] In general, in order to obtain relatively monodisperse samples, the nucleation stage should be separated in time from the growth stage as much as possible.

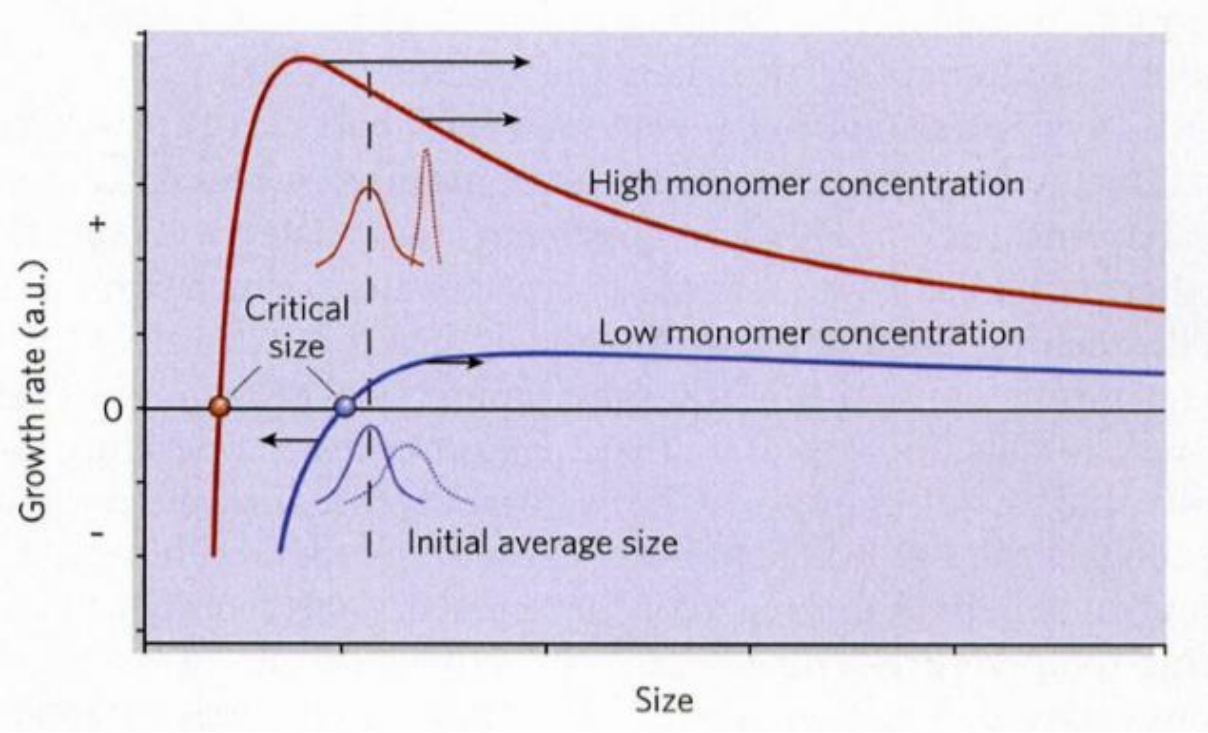

Figure 1.7: Size-distribution focusing. The growth process of nanocrystals can occur in two different modes, 'focusing' and 'defocusing', depending upon the concentration of the monomer present. A critical size exists at any given monomer concentration. At a high monomer concentrations, the critical size is small so that all the particles grow. In this situation, smaller particles grow faster than the larger ones, and as a result, the size distribution can be focused down to one that is nearly mondisperse. If the monomer concentration is below a critical threshold, small nanocrystals are depleted as larger ones grow and the size distribution broadens, or defocuses. The preparation of nearly monodisperse spherical particles can be achieved by arresting the reaction while it is still in the focusing regime, with a larger concentration of monomer still present. a.u., arbitrary units. (Ref. 42)

The foundation of colloidal nanocrystal synthesis dates back 150 years, with the pioneering work of Faraday, in which he added a strong reducing agent (phosphorus) into an aqueous solution of gold chloride to yield a colored solution of nanosized gold colloid. [51] This was the first example of "hot injection" method in which the formation of colloidal nanocrystals is induced by the rapid combination of two or more critical reagents. This method was popularized by Murray, Norris and Bawendi with their synthesis of CdE (E= S, Se, Te) nanocrystal quantum

dots over 20 years ago. [52] Although many methods have been discovered which also produce colloidal nanocrystals in solvent, including laser illumination, and ultrasonic or microwave irradiation, [53, 54] the hot injection method is still the most widely used approach to produce homogeneous nanocrystals with narrow distributions. But it does have some drawbacks: (i) Reagent mixing time: In order to have a control nucleation event, the rapid and homogeneous mixing of reagents at high temperature is required. And the mixing time becomes slower and less predictable as the volume of the batch and the consequent injection volume increases. (ii) Reaction cooling time: In most cases, in order to limit nucleation to a short burst-like event and to slow subsequent nanocrystal growth, the reaction temperature is required to drop. But the rate of cooling is not so easy to control, leading to a scale-dependent cooling time, which perturbs the reaction outcome. (iii) Practicality: Typical injection volumes are on the order of 25-50% of the volume of the mother solution, it becomes impractical and less viable to inject large volumes. (iv) Reproducibility: The time taken to inject a reagent often varies between users and from batch-to-batch, which leads to small differences in the initial reaction kinetics, hindering the reproducibility. [55] These factors make the syntheses of high-quality nanocrystals performed in smaller batches very difficult to reproduce on large scales.

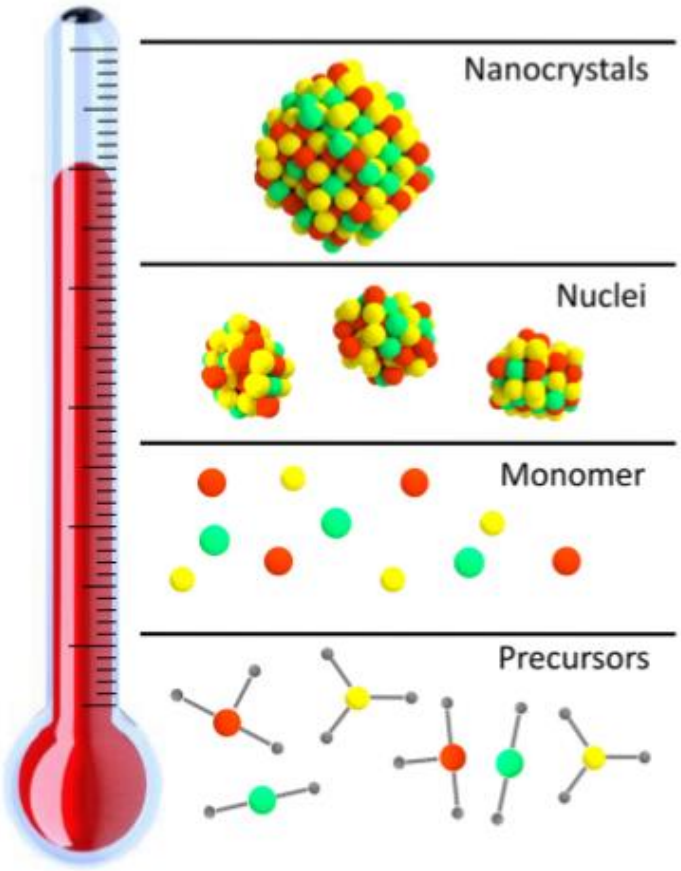

Figure 1.8: Typical heat-up syntheses require a large reservoir of precursor that is stable at room temperature. As the temperature is increased upon heating the reaction vessel, the precursors must react to form monomer that then nucleate to form small nuclei, which eventually grow into mature NCs. (Ref. 51)

Heat-up synthesis can be a promising alternative approach to the synthesis of colloidal nanocrystals. In reactions employing this method, all reagents are mixed into a reaction vessel and heated controllably to induce the nucleation and growth of colloidal nanocrystals. The essential stages of colloidal nanocrystals formation in a typical heat-up synthesis have been depicted by Figure 1.8. At low temperature, reaction mixture is comprised of precursor. These precursors may be the initial reagents used or secondary complexes that form upon reaction of these initial reagents with the ligands in solution. They experience an increased thermodynamic driving force to form monomers as the temperature rises. The heating process eventually triggers

the nucleation of nascent crystallites, with continued heating required to grow these nuclei into mature colloidal nanocrystals. [55]

Nowadays, chemists keep achieving ever more exquisite control over the composition, size, shape, crystal structure and surface properties of colloidal nanocrystals, thus setting the stage for fully exploiting the potential of these remarkable materials.

1.5: Introduction to Solution-Liquid-Solid Synthesis

Since the solution-liquid-solid (SLS) synthesis has been reported in 1995 by Buhro *et al.*, the SLS mechanism and its close variants have provided a general strategy for the growth of pseudo-one-dimensional nanocrystals. [56] Figure 1.9 gives a very straightforward description of the SLS mechanism. In a typical SLS growth, a solution phase is usually organic solvent and low-melting metallic nanoparticles play a role as liquid phase due to its molten liquid form under the reaction conditions (typically at temperature 200-350 ^{o}C). Decomposition of metallo-organic precursors at the solution-liquid interface offers semiconductor components which can readily dissolve in the liquid phase. Supersaturation is very easy to be achieved due to the limited solubility of semiconductor component in the liquid metallic catalyst droplet, resulting in crystallization of the semiconductor phase from the catalyst droplet. And crystalline growth occurs only at the liquid droplet-solid crystal interface. Hence, the growing semiconductor phase usually has a pseudo-one-dimensional morphology. Once the concentration of semiconductor component is below the supersaturation level, SLS growth stops. [57, 58]

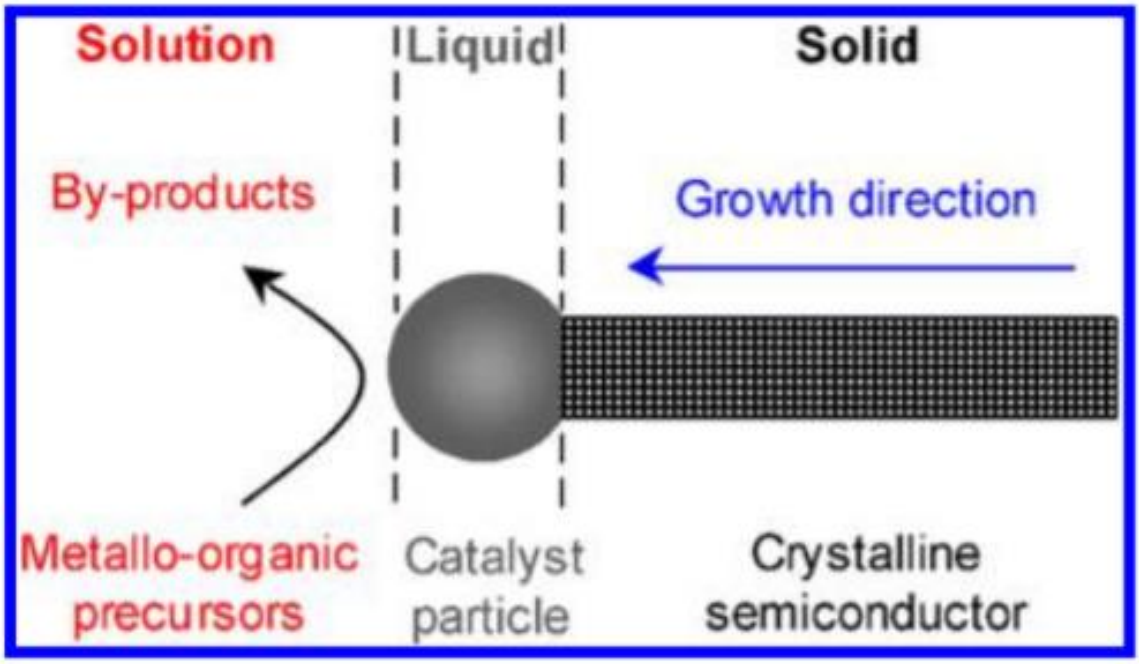

Figure 1.9: Schematic depiction of the SLS-growth mechanism for pseudo-one-dimensional crystalline rods and wires (Ref. 58).

Figure 1.9 also indicates that the sizes of the metallic-catalyst nanoparticles determine the diameters of nanorods or nanowires. Hence, we can tune the diameters of the nanorods or nanowires with narrow size distributions by controlling the sizes of the metallic-catalyst nanoparticles. Other factors such as temperature, the stability of the catalyst nanoparticles against agglomeration, the types, concentrations, and ratios of precursors, and the ligands or stabilizers employed can also limit the diameters and diameter distributions of the resulting nanorods and nanowires. [59]

III-V semiconductors have high covalent character and high symmetry of the zinc-blende crystal structure, making the synthesis of III-V nanorods and nanowires challenging. The growth of III-V nanowires has been dominated by the VLS mechanism introducing a catalytic liquid alloy phase which can rapidly adsorb a vapor to supersaturation levels, and from which crystal growth can subsequently occur from nucleated seeds at the liquid-solid interface. [60, 61] In 1995,

Buhro *et al.* reported the SLS mechanism for nanowire synthesis, in which polycrystalline InP nanofibers were produced by reaction between In(*t*-Bu)$_3$ and PH_3 in the presence of a protic reagent (i.e., MeOH or Thiophenol) at 111-203 ^oC. [62] But due to side reactions and the absence of stabilizers or surfactants in the reaction mixtures, these reactions often lead to poor diameter control. In 2003, shortly after lower-melting, near monodisperse metallic nanoparticles became available, the diameter-controlled SLS growth of III-V quantum wires or rods appeared. [63] In 2011, Yang and co-workers reported a surfactant-free, self-seeded SLS growth of GaP nanowires on a large scale appropriate for use as photocathodes for artificial photosynthesis. [63]

Over the past decade, SLS or SLS-related methods have provided high-quality nanorods and nanowires with well-controlled sizes, size distributions, compositions, and structures. These have opened a new window for the applications of colloidal semiconductor nanorods and nanowires.

1.6: Organization of Thesis

Chapter 2 of this thesis begins by presenting the strategy for developing a new SLS synthesis of colloidal InN nanoparticles from simple alkylamide precursors. The resulting InN nanoparticles are characterized by a variety of methods, including electron microscopy, X-ray diffraction, Raman spectroscopy, energy dispersive spectroscopy, X-ray-photoelectron spectroscopy and optical absorption.

Chapter 3 presents work that investigates the mechanism of this SLS by using nuclear magnetic resonance, liquid chromatography-mass spectrometry and gas chromatography.

Chapter 4 closes the thesis with an outlook at the future directions of this research. Since the quality of the InN nanoparticles is good, and the mechanism of this reaction has been well

explained, we will try to build up $In_xGa_{1-x}N$ system. Furthermore, due to lack of understanding on zinc-blende InN, we will keep working on the investigation of the properties.

LITERATURE CITED

LITERATURE CITED

[1] Chattopadhyay, S.; Ganguly, A.; Chen, K.; Chen, L. *Crit. Rev. Solid State Mater. Sci.* **2009**, *34*, 224.

[2] Wu, J. *J. Appl. Phys.* **2009**, *106*, 011101.

[3] Moses, P. G.; Miao, M.; Yan, Q.; Van de Walle, C. G. *J. Chem. Phys.* **2011**, *134*, 084703.

[4] Hadis, M. (2008). *Handbook of Nitride Semiconductors and Devices*. Richmond, VA: Wiley-VCH.

[5] Lewerenz, H. J., & Laurie, P. (2013). *Photoelectrochemical Water Splitting : Materials, Processes and Architectures.* London, UK: Royal Society of Chemistry.

[6] Davydov, V. Y.; Klochikhin A. A. *Semiconductors* **2004**, *38*, 861.

[7] Yu, K. M.; Weber, Z. L.; Walukiewicz, W.; Shan, W.; Ager, J. W.; Li, S. X.; Jones, R. E.; Haller, E. E.; Lu, H,; Schaff, W. J. *Appl. Phys. Lett.* **2005**, *86*. 071910.

[8] Belabbes, A.; Furthmüller, J.; Bechstedt, F. *Phys. Rev. B.* **2011**, *84*, 205304.

[9] Lin, M. E.; Strite, S.; Morkoc, H. *The Encyclopedia of Advanced Materials* **1994**, 79.

[10] Kasap, S., & Capper, P. (2007). *Springer Handbook of Electronic and Photonic Materials*. Newyork, NY: Springer Science+Business Media, Inc.

[11] Siddha, P.; James, S. S.; Steven, P. D.; Shuji, N. *Nature Photonics* **2009**, *3*, 180.

[12] Krames, M. R. et al. *J. Disp. Technol*. **2007**, *3*, 160.

[13] Vartuli, C. B.; Pearton, S. J.; Abernathy, C. R.; MacKenzie, J. D.; Ren, F.; Zolper, J. C.; Shul, R. J. *Solid-State Elect.* **1997**, *41*, 1947.

[14] Foutz. B. E.; O'Leary, S. K.; Shur, M. S.; Eastman, L. F. *J. Appl. Phys.* **1999**, *85*, 7727.

[15] Guo, Q. X.; Kato, O.; Yoshida, A. *J. Appl. Phys.* **1993**, *73*, 7969.

[16] Foley, C. P.; Lyngdal, J. *J. Vac. Sci. Technol. A* **1987**, *5*, 1708.

[17] T. L. Tansley, C. P. Foley, J. S. Blakemore (Ed.): Proc. 3rd Int. Conf. on Semiinsulating III–V Materials, Warm Springs, OR 1984 (Shiva, London 1985).

[18] Mohammad, S. N.; Morkoc, H. *Progress in Quantum Electronics* **1996**, *20*, 361.

[19] Chin, V. W. L.; Tansley, T. L.; Osotchan. T. *J. Appl. Phys*. **1994**, *75*, 7365.

[20] Bellotti, E.; Doshi, B. K.; Brennan, K. F.; Albrecht, J. D.; Ruden, P. P. *J. Appl. Phys*. **1999**, 85, 916.

[21] Tansley, T. L.; Foley, C. P. *J. Appl. Phys*. **1986**, *59*, 3241.

[22] Davydov, V. Y.; Klochikhin, A. A.; Seisyan, R. P.; Emtsev, V. V.; Ivanov, S. V.; Bechstedt, F.; Furthmuller, J.; Harima, H.; Mudryi, A. V.; Aderhold, J.; Semchinova, O.; Graul, J. *Phys. Stat. Sol. (B)* **2002**, *229*, R1.

[23] Davydov, V. Y.; Klochikhin, A. A.; Emtsev, V. V.; Ivanov, S. V.; Vekshin, V. V.; Bechstedt, F.; Furthmuller, J.; Harima, H.; Mudryi, A. V.; Hashimoto, A.; Yamamoto, A.; Aderhold, J.; Graul, J.; Haller, E. E. *Phys. Stat. Sol. (B)* **2002**, *230*, R4.

[24] Wu, J.; Walukiewicz, W.; Yu, K. M.; Ager III, J. W.; Haller, E.E.; Lu H.; Schaff, W. J.; Saito, Y.; Nanishi, Y. *Appl. Phys. Lett*. **2002**, *80*, 3967.

[25] Matsuoka, T.; Okamoto, H.; Nakao, M.; Harima, H.; Kurimoto, E. *Appl. Phys. Lett*. **2002**, *81*, 1246.

[26] Hori, M.; Kano, K.; Yamaguchi, T.; Saito, Y.; Araki, T.; Nanishi, Y.; Teraguchi, N.; Suzuki, A. *Phys. Stat. Sol. (B)* **2002**, *234*, 750.

[27] Davydov, V. Y.; Smirnov, A. N.; Goncharuk, I. N.; Kyutt, R. N.; Scheglov, M. P.; Baidakova, M. V.; Lundin, W. V.; Zavarin, E. E.; Smirnov, M. B.; Karpov, S. V.; Harima, H. *Phys. Stat. Sol. (B)* **2002**, *234*, 975.

[28] Saito, Y.; Harima, H.; Kurimoto, E.; Yamaguchi, T.; Teraguchi, N.; Suzuki, A.; Araki, T. *Phys. Stat. Sol. (B)* **2002**, *234*, 796.

[29] Miyajima. T.; Kudo, Y.; Liu, K. L.; Urguga, T.; Honma, T.; Saito, Y.; Hori, M.; Nanishi, Y.; Kobayashi, T.; Hirata, S. et al., *Phys. Stat. Sol. (B)* **2002**, *234*, 801.

[30] Carrier, P.; Wei, S. H. *J. Appl. Phys*. **2005**, *97*, 033707.

[31] Moss, T. S. *Proc. Phys. Soc. London, Sect. B* **1954**, *67*, 775.

[32] Burstein, E. *Phys. Rev.* **1954**, *93*, 632.

[33] Motlan; Goldys, E. M.; Tansley, T. L. *J. Cryst. Growth* **2002**, *241*, 165.

[34] Alivisatos, A.P. *Science* **1996**, *271*, 933.

[35] Norris, D. J.; Bawendi, M.G. *Phys. Rev. B* **1996**, *53*, 16338.

[36] Pokrant, S.; Whaley, K. B. *Eur. Phys. J. D.* **1999**, *6*, 255.

[37] Underwood, D. F.; Kippeny, T.; Rosenthal, S. J. *J. Phys. Chem. B* **2001**, *105*, 436.

[38] Smith, A. M.; Nie, S. M. *Acc. Chem. Res.* **2010**, *43*, 190.

[39] Lan, X. Z.; V, O.; Arquer, F. P. G.; Liu, M. X.; Xu, J. X.; Proppe, A. H.; Walters, G.; Fan, F. J.; Tan, H. R.; L, M.; Yang, Z. Y.; Hoogland, S. *Nano. Lett*. **2016**, *16*, 4630.

[40] Bloom, B. P.; Kiran, V.; V, V.; Naaman, R.; Waldeck, D. H. *Nano. Lett.* **2016**, *16*, 4583.

[41] Chitambar, C. R. *Curr. Opin. Oncol.* **2004**, *16*, 547.

[42] Yin, Y.; Alivisatos, P. A. *Nature* **2005**, *437*, 664.

[43] LaMer, V. K.; Dinegar, R. H. *J. Am. Chem. Soc*. **1950**, *72*, 4847.

[44] Xia, Y. N.; Xiong, Y. J.; Lim, B.; Skrabalak, S. E. *Angew. Chem. Int. Ed. Engl*. **2009**, *48*, 60.

[45] Stuczynski, S. M.; Brennan, J. G.; Steigerwald, M. L. *Inorg. Chem.* **1989**, *28*, 4431.

[46] Steigerwald, M. L. *Polyhedron* **1994**, *13*, 1245.

[47] Murray, C. B.; Norris, D. J.; Bawendi, M. G. *J. Am. Chem. Soc*. **1993**, *115*, 8706.

[48] Vossmeyer, T.; Katsikas, L.; Giersig. M.; Popovic, I. G.; Diesner, K.; Chemseddine, A.; Eychmueller, A.; Weller, H. *J. Phys. Chem.* **1994**, *98*, 7665.

[49] Murray, C. B.; Sun, S.; Doyle, H.; Betley, T. *Mater. Res. Soc. Bull.* **2001**, *26*, 985.

[50] Reiss, H. *J. Chem. Phys.* **1951**, *19*, 482.

[51] Faraday, M. *Philos. Trans. R. Soc. London* 1857, 147, 145.

[52] Murray, C. B.; Norris, D. J.; Bawendi, M. G. *J. Am. Chem. Soc.* **1993**, *115*, 8706.

[53] Suslick, K. S.; Fang, M.; Hyeon, T. *J. Am. Chem. Soc.* **1996**, *118*, 11960.

[54] Gerbec, J. A.; Magana, D.; Washington, A.; Strouse, F. G. *J. Am. Chem. Soc.* **2005**, *127*, 15791.

[55] Embden, J. Van.; Chesman, A. S. R.; Jasieniak, J. J. *Chem. Mater.* **2015**, *27*, 2246.

[56] Trentler, T. J.; Hickman, K. M.; Goel, S. C.; Viano, A. M.; Gibbons, P. C.; Buhro, W. E. *Science* **1995**, *270*, 1791.

[57] Trentler, T. J.; Goel, S. C.; Hickman, K. M.; Viano, A. M.; Chiang, M. Y.; Beatty, A. M.; Gibbons, P. C.; Buhro, W. E. *J. Am. Chem. Soc.* **1997**, *119*, 2172.
[58] Wang, F.; Dong, A.; Sun, J.; Tang, R.; Yu, H.; Buhro, W. E. *Inorg. Chem.* **2006**, *45*, 7511.

[59] Wang, F.; Dong, A.; Buhro. W. E. *Chem. Rev.* **2016**, *116*, 10888.

[60] Huang, M. H.; Mao, S.; Feick, H.; Yan, H.; Wu, Y.; Kind, H.; Weber, E.; Russo, R.; Yang, P. *Science* **2001**, *292*, 1897.

[61] Cui, Y.; Wei, Q.; Park, H.; Lieber, C. M. *Science* **2001**, *293*, 1289.

[62] Trentler, T. J.; Hickman, K. M.; Goel, S. C.; Viano, A. M.; Gibbons, P. C.; Buhro, W. E. *Science* **1995**, *270*, 1791.

[63] Yu, H.; Gibbons, P. C.; Kelton, K. F.; Buhro, W. E. *Chem. Rev.* **2016**, *116*, 10888.

Chapter 2

A SOLUTION-LIQUID-SOLID APPROACH TO COLLOIDAL INDIUM NITRIDE NANOPARTICLES

2.1: Introduction

2.1.1: Motivation for a New InN Nanoparticle Synthesis

Group-III nitrides are promising materials for electronics and optoelectronics applications due to their optical and electronic properties, such as a wide range of direct bandgap and high electron mobility, for example, electron mobility of bulk indium nitride is 4,400 cm^2/Vs. [1] Among group-III nitride semiconductors, InN has been the least studied, but recent studies have shown promising properties for a variety of applications, such as small effective mass, [2] large intervalley energy separation, [3] direct bandgap [4] and possibility for alloying with other group-III nitride materials.[5]

Investigating the intrinsic properties of InN provides the basis for much of motivation for finding a method to prepare high quality InN. The past debate about the bandgap of InN has proven how important the method to obtain high quality InN is. Amended from the previously accepted 1.9 eV, there is evidence that the bandgap is as low as 0.7 eV. [6] This controversy comes, in part, from the difficulty in making high quality films of InN due to poor thermal stability, tendency of InN to incorporate defects and without suitable lattice-matched substrates for epitaxial growth. Traditional MOCVD is not a good way to make InN because of a very low dissociation temperature (500 ^oC) of InN and high equilibrium nitrogen vapor pressure. [7] Furthermore, sapphire substrates will grow epitaxial films with ~ 25% lattice mismatch, which contributes to the formation of high densities of dislocations and limits the film thickness. [8] Though Trybus and his co-workers reported InN films grown by MBE on germanium substrates may be used in vertical conduction devices, it still had some structural defects. [9]

Colloidal synthesis can give us the opportunity to obtain highly crystalline InN by eliminating the use of a substrate and synthesizing InN as free-standing nanoparticles. More important, colloidal synthesis can offer a relatively low temperature conditions (< 250 ^{o}C) which can mitigate InN decomposition. Furthermore, the formation of nanocrystalline InN makes it possible to alloy InN with other materials. [10]

2.1.2: Literature Review of InN Nanoparticle Syntheses

Up to date, a variety of methods have been used to synthesize InN nanoparticles. These methods can be generally classified into at least three types, solid-state metathesis, ammonolysis, and solvothermal synthesis, depending on the reaction conditions used. Most of these methods employed commercially available indium(III) salts (such as $InBr_3$, In_2O_3 and In_2S_3) as indium precursors. [11-19] While, in 2000, Dingman used azido precursor (tBu$_2$InN$_3$) to prepare indium nitride fibers through a solution-liquid-solid growth mechanism. [20] In these methods, most of results were typically large agglomeration of nanocrystalline InN with no reports of quantum confinement. Some methods do afford colloidal InN nanoparticles, but challenges still exist. [11-14, 21] First, these methods are time-consuming due to heterogeneous reaction. [11-19] Second, the quality of InN obtained in these methods is generally low and In metal always formed alone, for example InN nanoparticles obtained by Xiao's approach does not have good uniform shape. [11] Third, some methods use unstable and dangerous precursors, such as azido precursors, which impede their practicability in industry. [20]

A typical solid-state metathesis method to prepare InN nanoparticles was reported by Cumberland in 2001. [15] InI_3 and Li_3N were used as starting materials, and the speed of the reaction was mediated by adding different proportions of $LiNH_2$ and NH_4Cl. [15] These four

chemicals were mixed together and put into a bomb calorimeter-type reaction vessel which was ignited through resistive heating. These explosive methods can produce nanocrystalline InN and indium metal with no carbon contamination. But neither grain size nor any optical characteristics for this nano-InN were reported.

In 2002, Murali et al. reported an ammonolysis method to prepare InN nanocrystals. [16] The indium source is held in a ceramic boat which is located in a tube furnace, and ammonia gas is passed over it at high temperature. When the temperature is above 1000 ºC, ammonia cracks into a highly reactive nitrogen species converting oxides to nitrides. Indium oxide nanopowders are typically used as starting materials in this method. [16] In 2004, Schwenzer et al. showed that reaction temperature influenced on the morphology of InN obtained by the ammonolysis method. [17] Lower temperature reactions (600 ºC) produced wurtzite InN nanoparticles with unreacted indium oxide, while higher temperature reactions (730 ºC) afforded aggregated microplates and nanowires. [17] Besides, no luminescence was observed in wurtzite InN nanoparticles obtained by this method.

Solvothermal syntheses use soluble, indium-based salts in a closed, high-pressure environment at low temperature, which can minimize the decomposition of the nitride after formation. Sardar et al. refluxed an $InCl_3$-urea complex in trioctylamine to obtain wurtzite InN, but only little structural or chemical evidence was presented. [18] In 2002, Bai *at al.* also used this method to prepare InN nanocrystals by using $InCl_3$ and xylene, but it was proven that the result was a mixture of indium metal and indium oxide. [19]

The first nano-sized colloidal InN was obtained by Xiao *et al.* in 2003. [11] In their approach, indium (III) salt and sodium amide were employed, and benzene based thermal decomposition would take place at 180 – 200 ºC to afford InN with low quality. In 2010, Belcher et al. showed

that the quality of the materials can be improved by carrying out the reaction at 250 ^{o}C using a high boiling point solvent (hexadecane). [12] Though the quality was improved, no transition was observed in the band gap region, which they tentatively explained by a Moss-Burnstein shift due to high concentration of dopants. Recently, Neale *et al*. proposed this phenomenon is caused by the conduction band of InN nanoparticles with free electrons, as evidenced by the presence of strong plasmonic peak in the near infrared (NIR) region. [13] Interestingly, these extra electrons could be removed from the conduction band by using chemical oxidants. [13] InN nanoparticles prepared by Belcher et al. and Neale et al. have wurtzite crystal structure, presumably because it is more stable than zinc-blende structure. In 2012, Chen et al. first reported a solution- and vapour-phase combined synthetic method to make zinc-blende structure InN nanocrystals. [14] In this method, silica coated In_2O_3 are nitridated using ammonia gas Though this method affords nearly monodisperse InN, monodisperse In_2O_3 is required, making this method very cumbersome. Besides, hydrofluoric acid is employed to remove silica shell which may cause safety problems when the reaction is scaled up.

In general, the road to nanosized InN is difficult and to this day there are no reported quantum confined InN nanocrystals, even though decades have passed.

2.2: New Colloidal InN Nanoparticle Synthesis Method

2.2.1: Highlights of this New Approach

Oleylamine is a commercially available reagent widely used in the synthesis of various nanoparticle systems where it can act as a surfactant, solvent and reducing agent. [22] In most cases, oleylamine is used to solubilize the salt of the corresponding precursor as surfactant in nonpolar solvent due to its long aliphatic carbon chain. While, in our approach, oleylamine is not only used as surfactant to solubilize $InBr_3$, which is our indium precursor, but also used as a

source of nitrogen precursor. Treatment of oleylamine with *n*-butyl lithium can produce real nitrogen precursor oleylamide which has the close reactivity to $LiNH_2$ and $NaNH_2$, but much better solubility in nonpolar solvent. This choice of nitrogen precursor help us solve the heterogeneous problem always existing in traditional methods.

2.2.2: Experimental Section

Chemical used: All solvents were purchased from Aldrich or Fischer, ACS grade or better unless otherwise noted. Reactions were performed in a nitrogen-filled glovebox or on a Schlenk line under positive nitrogen pressure. $InBr_3$ (Alfa Aesar, 99.99%), hexadecane (Sigma Aldrich, 99%), 1-octadecene (ODE, Acros, 90%), oleylamine (OLA, Sigma-Aldrich, ≥ 98%), *n*-butyllithium solution, 2.5 M in hexane (n-BuLi, Sigma Aldrich), N,N,N′,N′-tetramethylethylenediamine (TMEDA, Sigma Aldrich, 99%), hexamethyldisilazane (HMDS, referred to as "bis(trimethylsilyl)amine" in the text, Alfa Aesar, 99+%), trichloroethylene (TCE, Sigma-Aldrich, >99.5%), ethanol (EtOH, Macron), nitric acid (HNO_3, EMD), chloroform ($CHCl_3$, Macron), and toluene (Macron). All compounds were used as received unless otherwise noted. The solvents (1-octadecene and hexadecane) were degassed and dehydrated overnight at 80 °C under dynamic vacuum (< 10 mTorr) before being transferred to and stored in the glovebox.

Synthesis of colloidal indium nitride nanoparticles: In a three-neck round-bottom flask equipped with a water-cooled-condenser and kept under air-free conditions (N_2 Schlenk line), 180 mg $InBr_3$ (0.5 mmol) are solubilized in 2 mL of oleylamine (6.08 mmol) and 5 mL of a high-boiling point aliphatic solvent hexadecane (octadecene also works, with no observed difference). A complete dissolution of the salt is achieved by heating the solution to 220 ^oC under constant vigorous stirring for 5 min. An alkylamide precursor solution is separately prepared under air-

free conditions (N_2 glove box) by reacting 0.50 mL of OLA (1.5 mmol) with a mixture of 0.60 mL of a n-BuLi solution (2.5 M hexane solution, 1.5 mmol n-BuLi) and 0.45 ml TMEDA (3 mmol). This alkylamide solution is then injected promptly with a 6 mL syringe into the indium-OLA mixture to initiate the reaction. After injection, the temperature of the indium solution drops to 175 ± 2 ^{o}C and quickly (< 1 min) rises back to 210 ^{o}C, where it is maintained until the reaction is stopped. The solution changes from colorless to brownish-black over the course of the first 3 min, indicative of the formation of InN nanocrystals. The reaction is stopped after 10 min by removing the heat source and letting the solution cool down to room temperature. The resulting solution is divided into two parts and each part is then sonicated in ethanol (15 mL) for two minutes, followed by a 5 min centrifugation at 4,000 rpm to crash out the solids; this sonication/centrifugation cycle is then repeated a second time, after which the sample is combined and dissolved in 20 mL of nonpolar solvent, toluene or chloroform for routine storage or measurements, or tetrachloroethylene for NIR spectroscopy. The sample is either analyzed directly ("as-prepared"), further functionalized with oleylamine as described below ("as-prepared, functionalized"), or further purified to eliminate $In^{(0)}$ from the sample. For the latter, the as-prepared sample is sonicated in nitric acid (15 mL, 3% vol) for two min then centrifuged at 4,000 rpm for 5 min. The resulting sample ("acid-treated") is then washed following the same protocol described above. The sample can be directly converted into a stable colloidal suspension by heating the solid in 3 mL OLA at 80 ^{o}C for 3 h. The resulting mixture is then washed by sequential ethanol/toluene treatments to yield a toluene (or another non-polar solvent) suspension of InN nanoparticles that remains stable for days without signs of solids crashing out of the solvent. Samples synthesized using other amide precursors were made following the same approach, but substituting a different amine in the deprotonation step above, such as HMDS. For

measurements of the evolution of the reaction, small aliquots (0.6 mL) are taken out at precise times after injection; these aliquots are immediately injected in 6 mL trichloroethylene (TCE) at room temperature to stop the reaction.

2.2.3: Characterization of InN Nanoparticles

Characterization of the nanoparticles fell under three broad categories: structural characterization, chemical characterization, and optical characterization.

Powder X-ray diffraction (pXRD) patterns were recorded on a Bruker D8 DaVinci diffractometer equipped with Cu X-ray radiation (Kα line, $\lambda = 0.154$ nm) operating at 40 kV and 40 mA. Peak intensities were obtained by counting with the Lynxeye detector every 0.02° at sweep rates of 0.5° 2θ /min. Samples were placed in a PVMA sample holder with zero-background silica plates by drop-casting concentrated nanocrystal solutions. The holder was rotated at 5^{o} per minute; no background correction was applied to raw data.

Raman spectroscopy was done on a Renishaw inVia Reflex spectrometer, equipped with a confocal microscope connected to a CW diode-pumped solid-state laser with a fundamental emission at 532 nm. The sample was positioned under the laser light using a motorized stage. The stage position was controlled and the spectral data were acquired with the commercial WiREInterface software. This software allows for control over the laser power, exposure time, spectral range covered, and stage positioning for mapping of a sample. The parameters used were a laser power of 1 mW at the sample and an integration time of 3 s. Each spectrum was generated from an average of five hundred spectral acquisitions.

Transmission electron microscopy (TEM) images and energy dispersive x-ray spectroscopy (EDS) were recorded on a JEOL2200FS microscope operating at 200 keV. Formvar-coated copper grids (Ted Pella, 01800-F) were used as nanocrystal supports for TEM. Thoroughly

cleaned chloroform suspensions were drop-casted on the TEM grid prior to the measurements. Length, width and d-spacing of the particles in the images were analyzed using ImageJ. [23] Quantitative analyses are further processed.

X-ray photoelectron spectroscopy was done on a Perkin Elmer Phi 5600 ESCA system, with a Mg Kα X-ray source at a take off angle of 45^{o}, under ultrahigh vacuum conditions (< 107 torr). Spectra were acquired with a pass energy of 187 eV for survey scans or 29.35 eV for zoomed-in scans, and a step size of 0.8 eV for survey scans or 0.1 eV for zoomed-in scans; the energy scale was calibrated with adventitious carbon at 284.6 eV. Samples for XPS were first precipitated out of solution and dried under nitrogen. Films were then prepared by spreading the nanocrystals powder on a 1 cm^2 copper tape (Ted Pella) attached to a stainless steel holder.

UV-vis-NIR absorption spectra were measured on a Olis 17 spectrometer from 2,500 nm to 500 nm at a rate of 103 nm/min, and three reads per datum, 2,000 increments. 1 cm infrasil cuvettes in both reference (filled with pure solvent only) and sample beam paths were used. All data were acquired with constant signal-to-noise ratio across the whole spectral range by letting the instrument vary the slits width during the acquisition to maintain a constant detector voltage; the bandwidth varied from 0.5 nm to 1.0 nm across the spectral range.

2.3: Characterization Results and Discussions

2.3.1: Structural Characterization

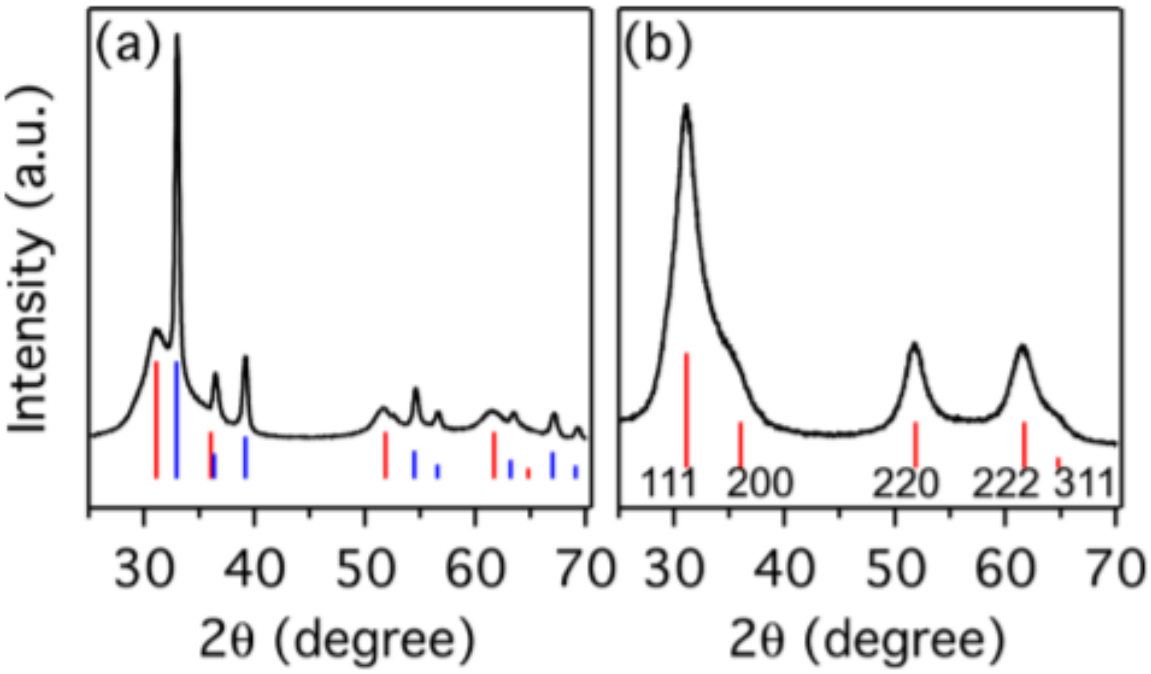

Figure 2.1: XRD pattern for the (a) as-prepared sample and (b) acid-treated sample. The vertical lines show the XRD patterns of bulk zinc-blende InN (red) and tetragonal $In^{(0)}$ (blue).

XRD was used to determine the crystal structure of the final product. Figure 2.1 depicts the X-ray diffraction pattern of the as-prepared sample and acid-treated samples. After diluted nitric acid treatment, the XRD pattern of the acid-treated sample has fewer peaks denoted by blue lines, compared with that of as-prepared sample.

After diluted nitric acid treatment, some peaks in the as-prepared sample disappear and these disappearing peaks match well with the XRD pattern of tetragonal $In^{(0)}$, suggesting the as-prepared sample is a mixture of at least two different crystalline phases. Combined with the fact that diluted nitric acid easily oxidizes $In^{(0)}$ to In^{3+} which can be removed in the following ethanol wash step, we assign this disappearing crystalline phase to tetragonal $In^{(0)}$. [24] The other peaks in acid-treated sample match well with that of zinc-blende indium nitride, [21] indicating the

formation of crystalline zinc-blende InN in our approach. Although wurtzite InN is more thermally stable than zinc-blende InN, [25] the later phase is instead observed here. For this result, we think the wurtzite structure is overcome by kinetically-favored growth of the zinc-blende structure, perhaps due to the growth mechanism proposed later. The width of the $In^{(0)}$ peaks is significantly smaller than that of InN peaks, suggesting the average size of $In^{(0)}$ domains is much larger than those of the InN, consistent with the microscopy data presented below. A straightforward Scherrer analysis of this XRD data (Equation 2.1) puts the average InN crystallites around 5 nm, consistent with the average InN nanocrystal width obtained from the microscopy data presented below.

$$\tau = \frac{K\lambda}{\beta cos\theta} \qquad \text{Eq. (2.1)}$$

$$= \frac{0.9 \times 0.154 \text{ nm}}{0.02864 \times \cos(31.024^{\circ})}$$

$$\approx 5.2 \text{ nm}$$

where:

- τ is the mean size of the crystalline domains, which may be smaller or equal to the grain size;
- K is a dimensionless shape factor, with a value close to unity. The shape factor has a typical value of about 0.9, but varies with the actual shape of the crystallite; here, we use 0.9.
- λ is the X-ray wavelength; here, λ = 0.154 nm.
- β is the line broadening at half the maximum intensity (FWHM), after subtracting the instrumental line broadening, in radians; here, the calculate β based on the XRD result of after-treated sample is 0.02864.
- θ is the Bragg angle (in degrees); here, θ = 31.024°.

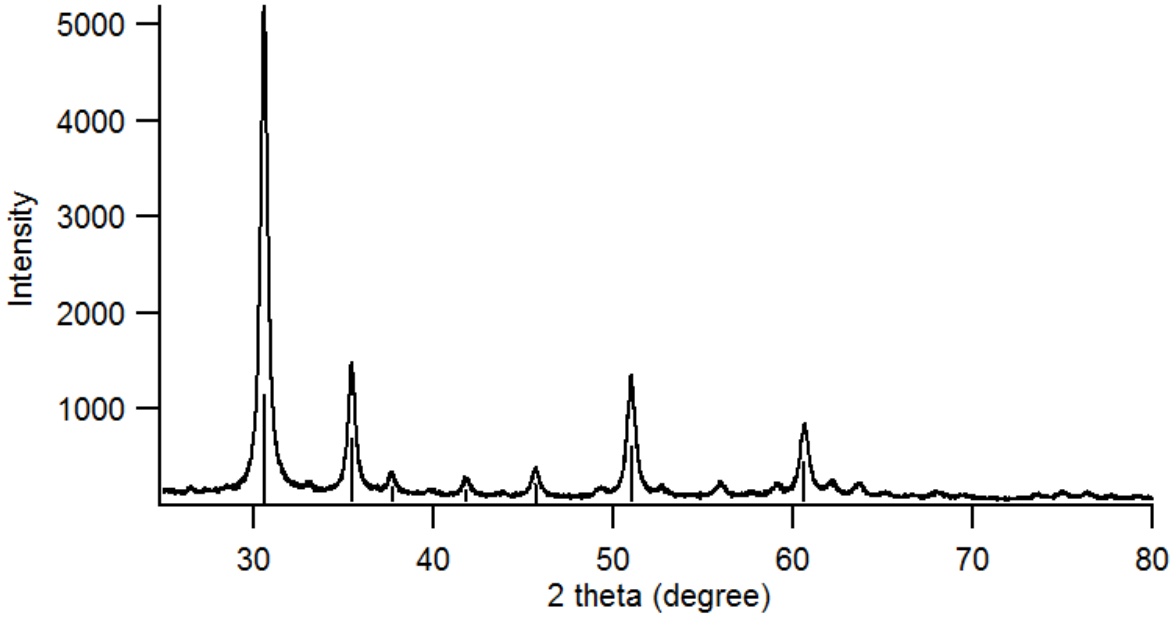

Figure 2.2: XRD pattern of the acid-treated sample after heating at 500 ºC for 5 h. The vertical lines show the XRD pattern of bulk cubic-In_2O_3.

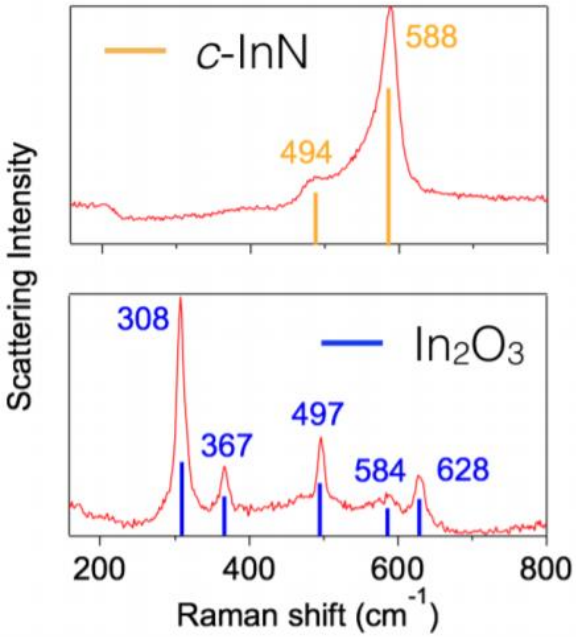

Figure 2.3: Raman spectra of the acid-treated sample before (top) and after (bottom) heating at 500 ºC overnight, which converts the nitride into an oxide; the numbers listed correspond to the phonon energies of the bulk materials, respectively. Excitation wavelength is 532 nm.

Due to the small size of InN nanoparticles obtained by our method, the peaks in InN XRD pattern are very broad, overlapping the In_2O_3 XRD pattern. Raman spectroscopy was used to

further confirm that acid-treated InN sample we obtained is zinc-blende InN, and not cubic In_2O_3. The acid-treated sample was heated to 500 ^oC under air for 5 hours. During this heating process, the black acid-treated sample became yellow powder (In_2O_3 is yellow). XRD pattern of the acid-treated sample after heating shown in Figure 2.2 confirms that is cubic In_2O_3. Raman spectra of the acid-treated sample before and after heating were both measured, as shown in Figure 2.3. Acid-treated sample has two modes located at 494 and 588 cm^{-1}. Acid-treated sample after heating have completely same Raman spectrum pattern of cubic In_2O_3. [26]

Compared with the TO and LO modes of InN reported by previous literatures, these two modes of acid-treated sample located at 494 and 588 cm^{-1} shift to higher energy by 22 cm^{-1} and 2 cm^{-1}, respectively. [27] These shifts may be caused by sample quality, because samples used in previous reports are InN thin films grown under MBE instead of colloidal InN nanoparticles. XRD and Raman results of the sample confirm the formation of cubic In_2O_3 after heating at 500 ^oC. This change caused by the heating process clearly suggests the conversion from zinc-blende InN to cubic In_2O_3 as shown in Figure 2.4. Hence, the acid-treated sample is zinc-blende InN.

$$InN \xrightarrow[500\ ^oC,\ 5\ hours]{O_2} In_2O_3$$

Figure 2.4: Conversion from InN to In_2O_3.

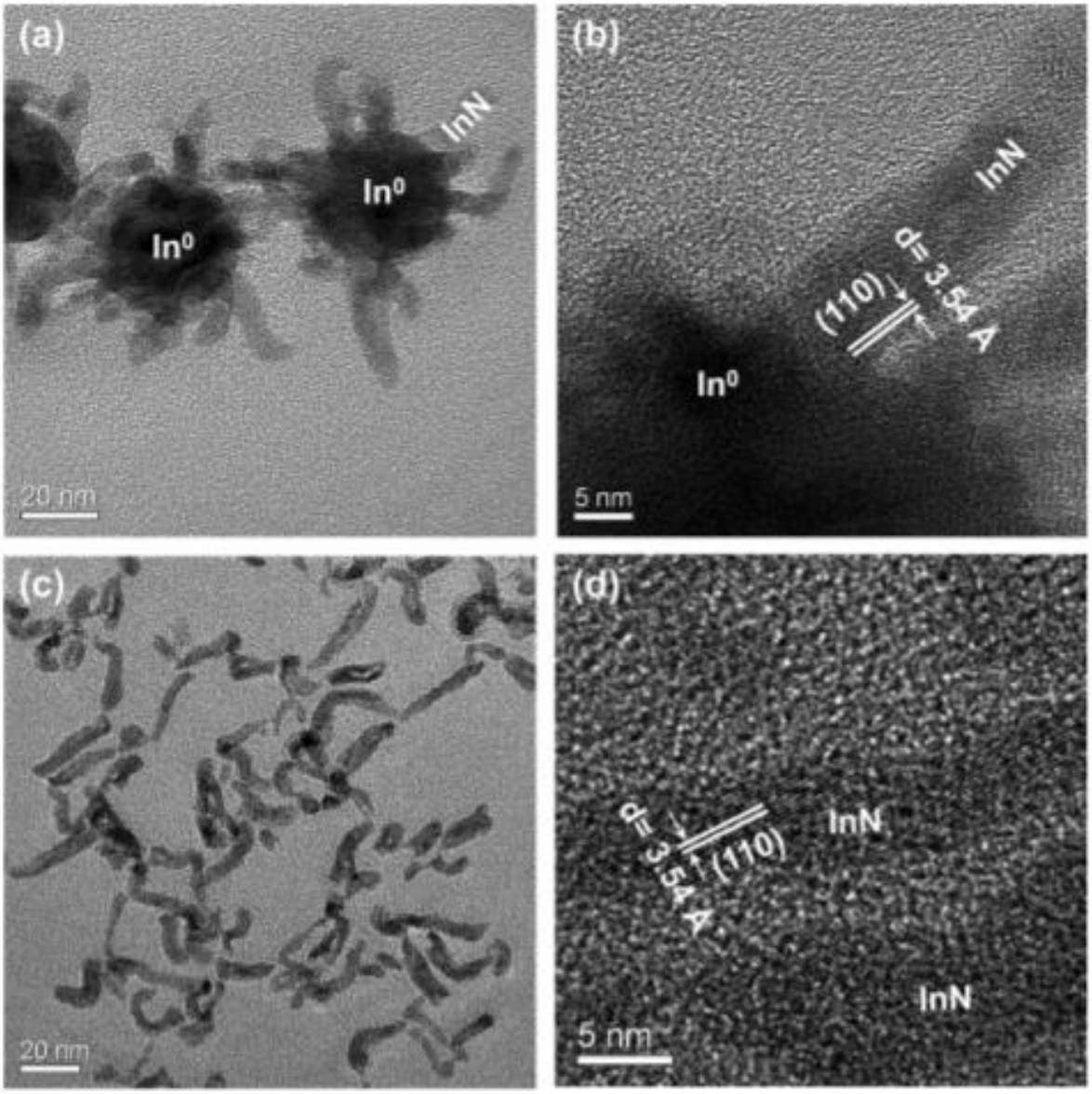

Figure 2.5: TEM images of the nanoparticles. (a) Overview of the as-prepared sample, showing the InN nanorods stemming out of large $In^{(0)}$ nanoparticles. (b) HRTEM image of one the InN branches in (a) at the surface of the $In^{(0)}$ nanoparticle. (c) Overview of the acid-treated sample. (d) HRTEM of one of the InN nanorods in (c).

Transmission electron microscopy (TEM) images of the as-prepared and acid-treated samples are presented in Figure 2.5. The TEM image of the as-prepared sample gives clear evidence that there are two types of nanoparticles: large spherical nanoparticles and more or less straight nanorods, consistent with two different phases observed in the XRD (Figure 2.1a). After

removing $In^{(0)}$ using the diluted nitric acid treatment, the large spherical nanoparticles disappear, while the straight nanorods remain, suggesting the metallic indium structures appear as larger spheres of approximately 30 nm in diameter, whereas the straight nanorods are InN growing from the surface of the $In^{(0)}$ nanoparticles. The crystallinity of the nitride lattice is directly apparent in the high-resolution TEM data presented in Figures 2.4 (b, d), confirming these InN are single crystals. According to the lattice fringes of the InN nanocrystals, the lattice spacing between two planes is ~0.354 nm, corresponding to the distance between [110] planes of zinc-blende indium nitride. [21]

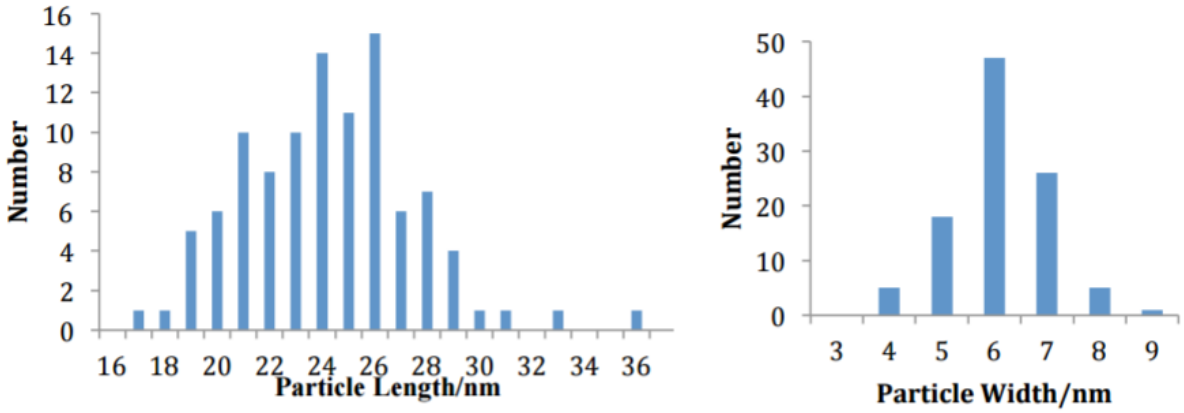

Figure 2.6: Size-distribution of as-prepared sample.

Table 2.1: Statistical analysis of the size-distribution of as-prepared sample shown in Figure 2.5 (*N*=102 particles)

	Length (nm)	Width (nm)	Aspect Ratio
Average	23.8	5.6	4.3
Standard deviation	3.3	0.9	0.8
Median	23.8	5.6	4.3

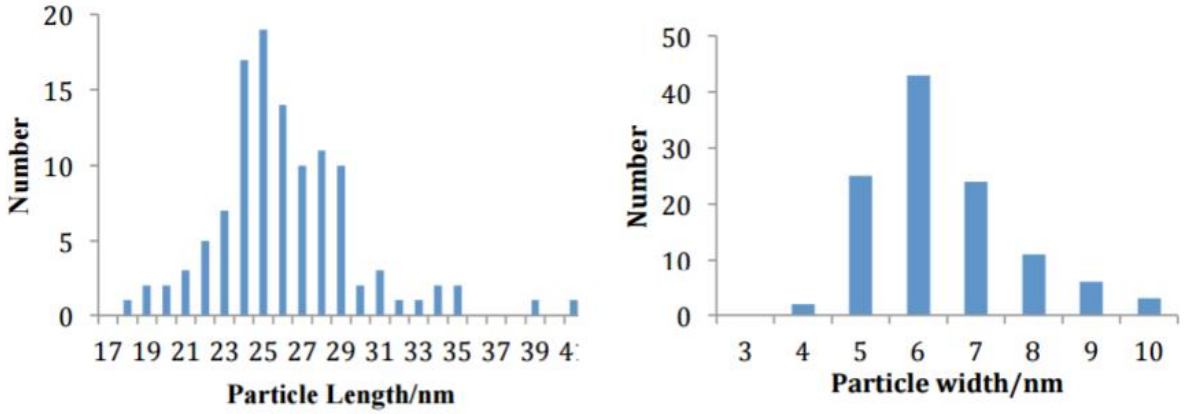

Figure 2.7: Size-distribution of acid-treated sample.

Table 2.2: Statistical analysis of the size-distribution of acid-treated sample shown in Figure 2.6 (*N*=114 particles)

	Length (nm)	**Width (nm)**	**Aspect Ratio**
Average	25.7	5.9	4.5
Standard deviation	3.6	1.2	0.9
Median	25.4	5.7	4.5

Figure 2.6, Figure 2.7, Table 2.1 and Table 2.2 present the quantitative analyses of these TEM images showing that the average length (L) of the InN nanorods is relatively unperturbed by the acid treatment, changing from L = 23.8 ± 3.3 nm to L = 25.7 ± 3.6 nm. Considering the difficulty in determining the exactly location of the InN edge at the $In^{(0)}$/InN interface, the aspect ratio of the InN nanorods, about 4.5, is also unchanged before and after the nitric acid treatment, underlying the fact that the average diameter remains also constant, which is around 6 nm.

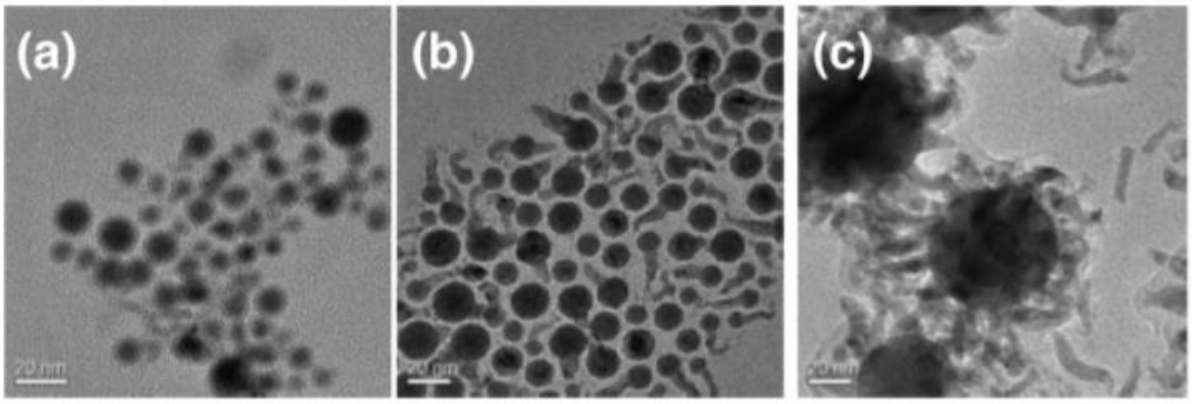

Figure 2.8: TEM images showing the progression of the reaction (a) 30 s, (b) 60 s, and (c) 180 s after the injection of the alkylamide precursor. Identical scale bars in all three panel, 20 nm.

A Solution-Liquid-Solid (SLS) growth mechanism for the formation of the InN nanorods is clearly demonstrated in Figure 2.8, where the $In^{(0)}$ nanoparticles formed first after the addition of the alkylamide solution into the indium(III) solution, then it catalyzed the growth of InN nanorods. In 2000, Dingman *et al.* reported a SLS approach to prepare InN fibers. [20] In their approach, very reactive azido-indium organometallic precursors were formed, and then reacted *in situ* with metallic indium. Compared with their approach, we use much less reactive and safer precursors that are directly synthesized from commercially available materials. Besides, our method yields zinc-blende InN nanorods with very small aspect ratios, while their approach affords micrometer-long wurtzite InN nanofibers. This lattice difference is not quite understood for the moment. In Figure 2.5 a, multiple InN nanorods are connected to single $In^{(0)}$ droplets, while TEM images taken at different reaction times show that this is not the case. About 30 seconds after the injection of the alkylamide precursor (Figure 2.8 a), the reaction mixture is composed almost exclusively of small $In^{(0)}$ droplets, with no visible trace of InN. In Figure 2.8 b, InN nanorods appear around 1 min after injection, and the InN nanorods ensemble at 1 min after injection is practically indistinguishable from that taken after 10 min, which indicates the

completion of the semiconductor growth reaction. After that, the $In^{(0)}$ droplets rapidly increase in size, as shown in Figure 2.8 c, which can be attributed either to an efficient Oswald ripening mechanism of the $In^{(0)}$ phase (which would explain the presence of $In^{(0)}$-free InN nanorods at later stages) or to the coalescence of multiple $In^{(0)}$ liquid droplets (which would explain the presence of multiple InN nanorods per $In^{(0)}$ droplet at later stages).

2.3.2: Chemical Characterization Results and Discussions

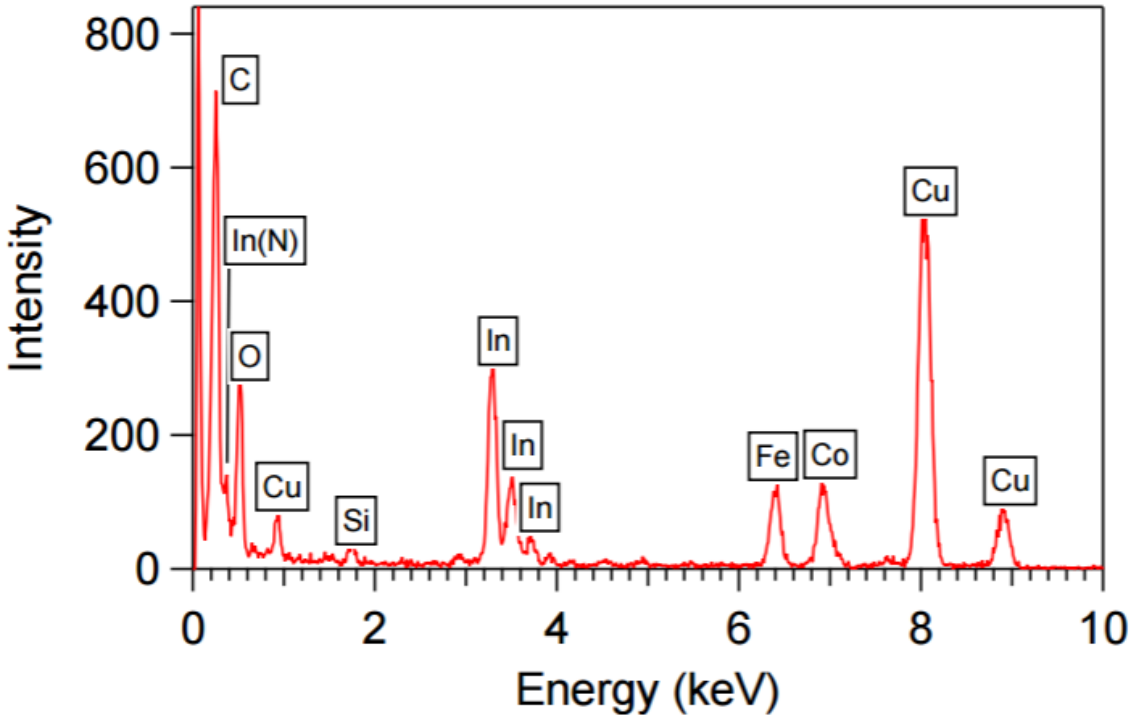

Figure 2.9: Energy-Dispersive X-Ray Spectroscopy of the as-prepared InN/$In^{(0)}$ sample.

Energy dispersive X-ray spectroscopy is an ideal tool to qualitatively determine the chemical composition of a sample. Figure 2.9 clearly shows the existence of indium in the as-prepared InN/$In^{(0)}$ sample. Bromine was not detected, suggesting that most bromide species were efficiently removed from the sample following the washing procedure. Signals of carbon, oxygen, copper, silicon, iron and cobalt were consistently detected across the TEM grid over areas with

and without nanoparticles. Sources of carbon include the grid itself, adventitiously adsorption, and oleylamine surfactants. Oxygen contaminants arise from ambient gas adsorption. Signals of copper, silicon, iron and cobalt arise from the TEM grid. [12]

Unfortunately, the presence (or absence) of nitrogen cannot be assessed by EDS, as the nitrogen peak (around 390 eV) overlaps directly with the indium M-series X-ray (around 450 eV); given the resolution of about 150 eV, one cannot distinguish the two species directly by EDS. Besides, the X-ray signal of nitrogen has very weak intensity, which is hard to detect even in the absence of overlapping bands due to efficient Auger processes that reduce the efficiency of the X-ray emission. [12]

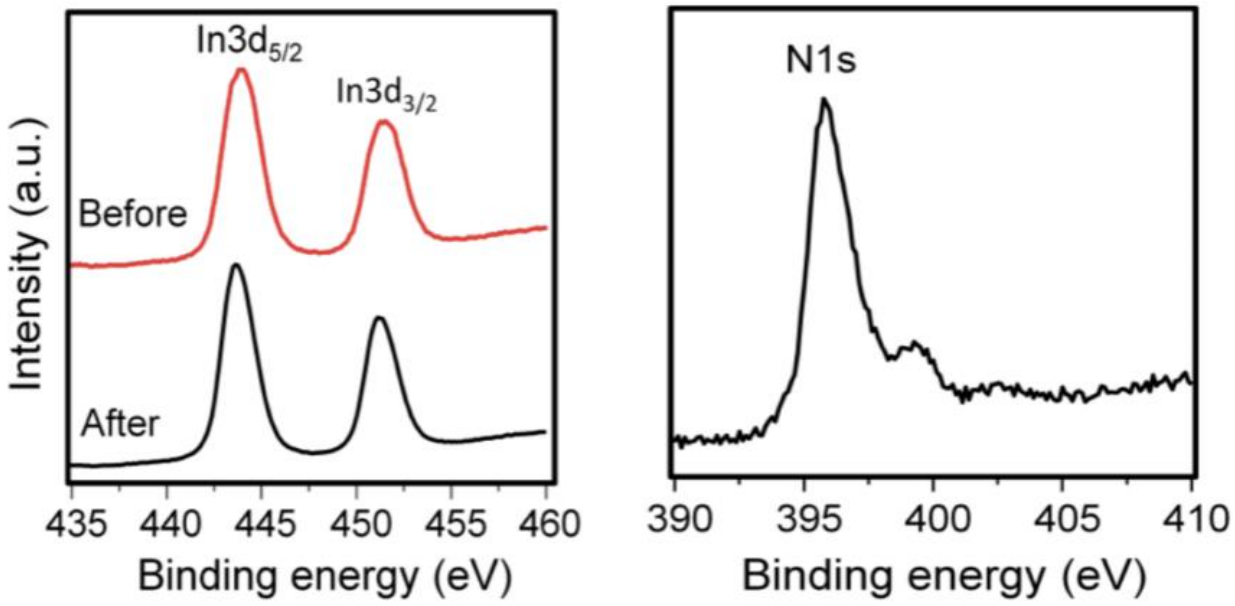

Figure 2.10: XPS data of the as-prepared sample (before) and acid-treated (after) sample.

The oxidation states of the different elements can be determined by X-ray photoelectron spectroscopy. Two atomic species – nitrogen and indium – were measured, as shown in Figure 2.10.

The N 1s XPS peak after nitric acid treatment shows two distinct features. The intense peak located at 396.6 eV corresponds well to In-N bonds. The smaller peak at 399.4 eV has been attributed to N-H bonds. [28]

The indium species of the as-prepared and the acid-treated samples were examined. For the acid-treated sample, the In $3d_{5/2}$ peak is located at 444.8 eV and the In $3d_{3/2}$ peak is located at 452.2 eV, these correspond to the nitride species.

An asymmetric broadening of the N 1s peak is observed in the as-prepared sample. Considering that surface oxidation easily takes place in InN nanoparticles, this broadening peak can be attributed to the In-NO bonds. Compared with acid-treated sample, the as-prepared sample has broader In $3d_{5/2}$ and In $3d_{3/2}$ peaks, consistent with the fact that the as-prepared sample is a mixture of $In^{(0)}$ and InN, whereas the acid-treated sample is mostly InN.

2.3.3: Optical Characterization Results and Discussions

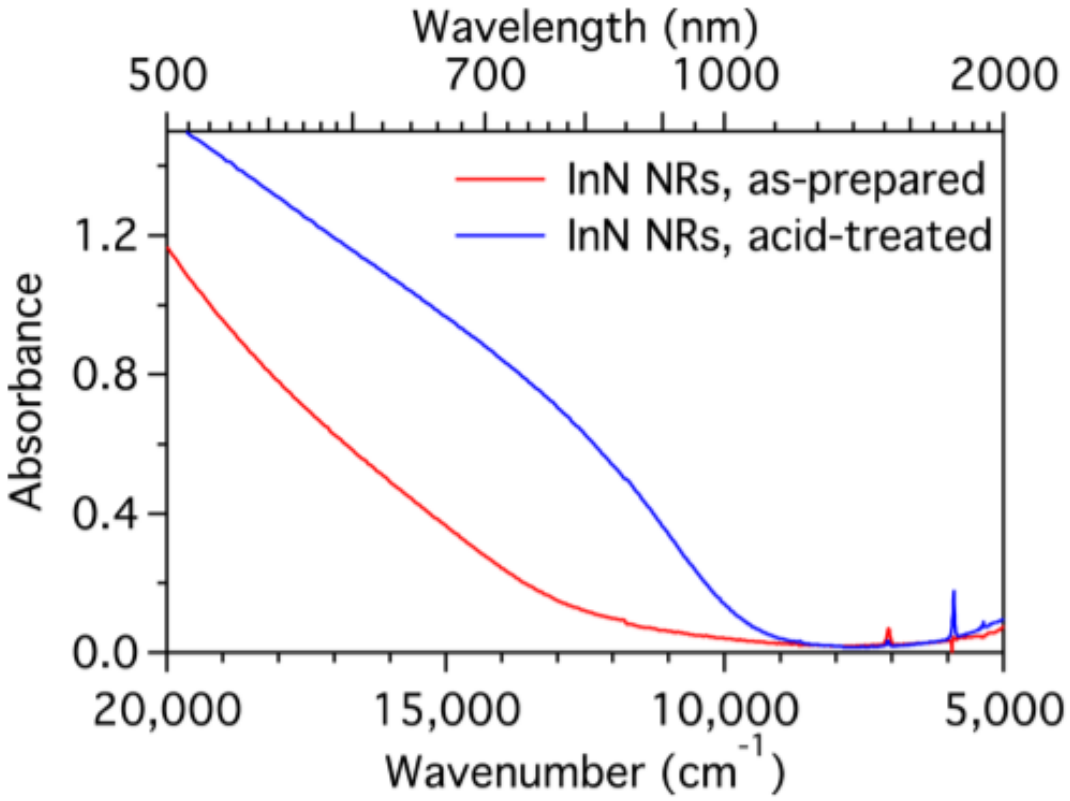

Figure 2.11: NIR-Vis absorption spectra (in Trichloroethylene) of SLS-grown InN NRs shown in Figure 2.1 and 2.5. Red: as-prepared, OLA-functionalized. Blue: acid-treated. The sharp peaks in the NIR are C-H and N-H vibrational overtones from OLA.

Near-infrared-visible (NIR-Vis) spectra of as-prepared and acid-treated InN nanorods were both measured. Figure 2.11 clearly shows the as-prepared sample presents a spectroscopic signature that closely resembles that of colloidal InN nanoparticles reported previously. [13] Besides, redshift of interband transition by ~5,000 cm^{-1} was observed after acid treatment, bringing the onset of the interband transition to around 9,500 cm^{-1}.

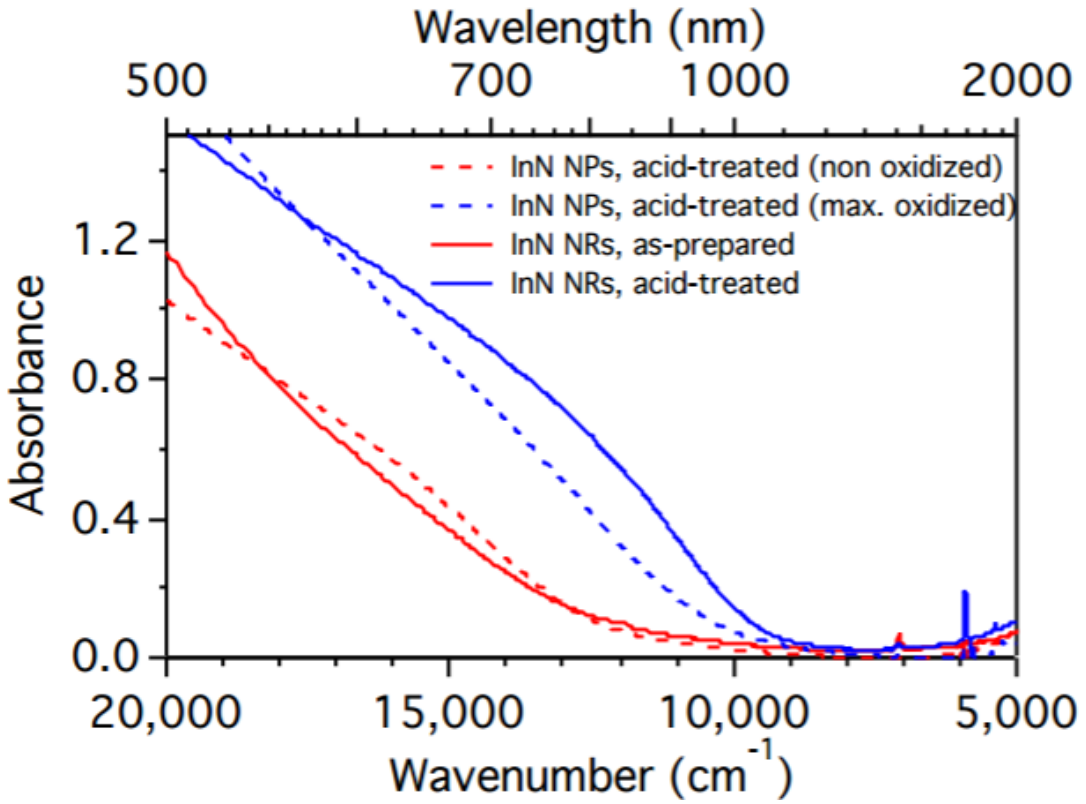

Figure 2.12: Absorption spectra comparing InN nanorods (NRs) as synthesized here, before and after treatment, with 6 nm InN (BF_4^--capped) nanoparticles (NPs) synthesized using the conventional $NaNH_2$ approach [13]. The oxidation is performed exactly as described by Palomaki *et al*., [13] using $NOBF_4$ as the oxidant on BF_4^--capped NPs.

For reference, the electronic structure of colloidal InN nanostructures is generally characterized by two size-independent features (the cubic lattice is expected to be similar to the wurtzite lattice): a Burstein-Moss shifted interband transition around 14,500 cm^{-1} (1.8 eV) and another NIR band at lower energy (typically around 3,300 cm^{-1}/0.4 eV) assigned to localized surface plasmon resonances (LSPR). [30, 31] These two combined size-independent features indicate that colloidal InN nanostructures are degenerately doped, with estimated n-type carrier concentrations around 10^{20} cm^{-3}. [29] Due to the similar spectroscopic signatures between the as-prepared sample and colloidal InN nanoparticles reported previously, the as-prepared InN samples (in which InN is connected to $In^{(0)}$) are also degenerately doped to the same level as colloidal InN nanoparticles prepared from $NaNH_2$. [13] Whereas, $In^{(0)}$ is also formed in $NaNH_2$-

based syntheses [30, 31], these materials are quite different with our case. First, $In^{(0)}$ appears there as a side product [30, 31], while $In^{(0)}$ is very important for the formation of InN in our method (which will be discussed in chapter 3). Second, the removal of $In^{(0)}$ does not affect the InN nanoparticle vis-NIR spectrum [13], whereas significant changes happen following the removal of $In^{(0)}$ in our alkylamide approach, as shown in Figure 2.12. This change may be caused by the intimate relationship between the $In^{(0)}$ phase and InN phase. Although it is possible that nitric acid treatment of the as-prepared sample could slightly oxidize the InN nanorods, the exact same treatment, when applied to traditionally-prepared InN nanoparticles does not cause any observable oxidation; [30, 31] it is thus unlikely that the observed shift reported in Figure 2.12 arises here from the direct action of HNO_3 on the InN nanorods. The overall spectrum of the acid-treated InN nanorods is similar to that of chemically oxidized InN nanoparticles (using $NOBF_4$), suggesting that eliminating $In^{(0)}$ from InN effectively decreases the doping concentration. Under this hypothesis, the origin of at least a large portion of the carriers in the as-prepared samples would be $In^{(0)}$, whereas $In^{(0)}$ is not the doping source in traditionally prepared InN nanoparticles. [30, 31] Due to the very large electron affinity of bulk In (~6 eV) [30] and low work function of $In^{(0)}$ (4.09 eV), [31] it is reasonable to assume that electrically-coupled $In^{(0)}$-InN junctions can lead to the transfer of electrons into the conduction band of InN. Removal of the $In^{(0)}$ presumably would then lower the doping level, concomitant with the smaller Burstein-Moss shift observed in Figure 2.12.

2.4: Summaries

In summary, we have designed a successful approach to prepare colloidal zinc-blende InN nanorods with an average length of 25.7 ± 3.6 nm and width of 5.9 ± 1.2 nm. This method

utilizes commercially available $InBr_3$ and easily prepared olyelamide as precursors to solve heterogenous problem, making our approach much faster. Characterization by XRD, Raman spectrum, TEM, XPS and NIR-Vis absorption support this method as a convincing advancement toward high quality zinc-blende InN nanoparticles. A SLS-type mechanism is proposed for the formation of these InN nanorods, based on TEM data, where the $In^{(0)}$ spherical nanoparticles formed first which then catalyzed the formation of the InN nanorods.

APPENDIX

TEM images for size-distribution analyses

a) As-prepared sample

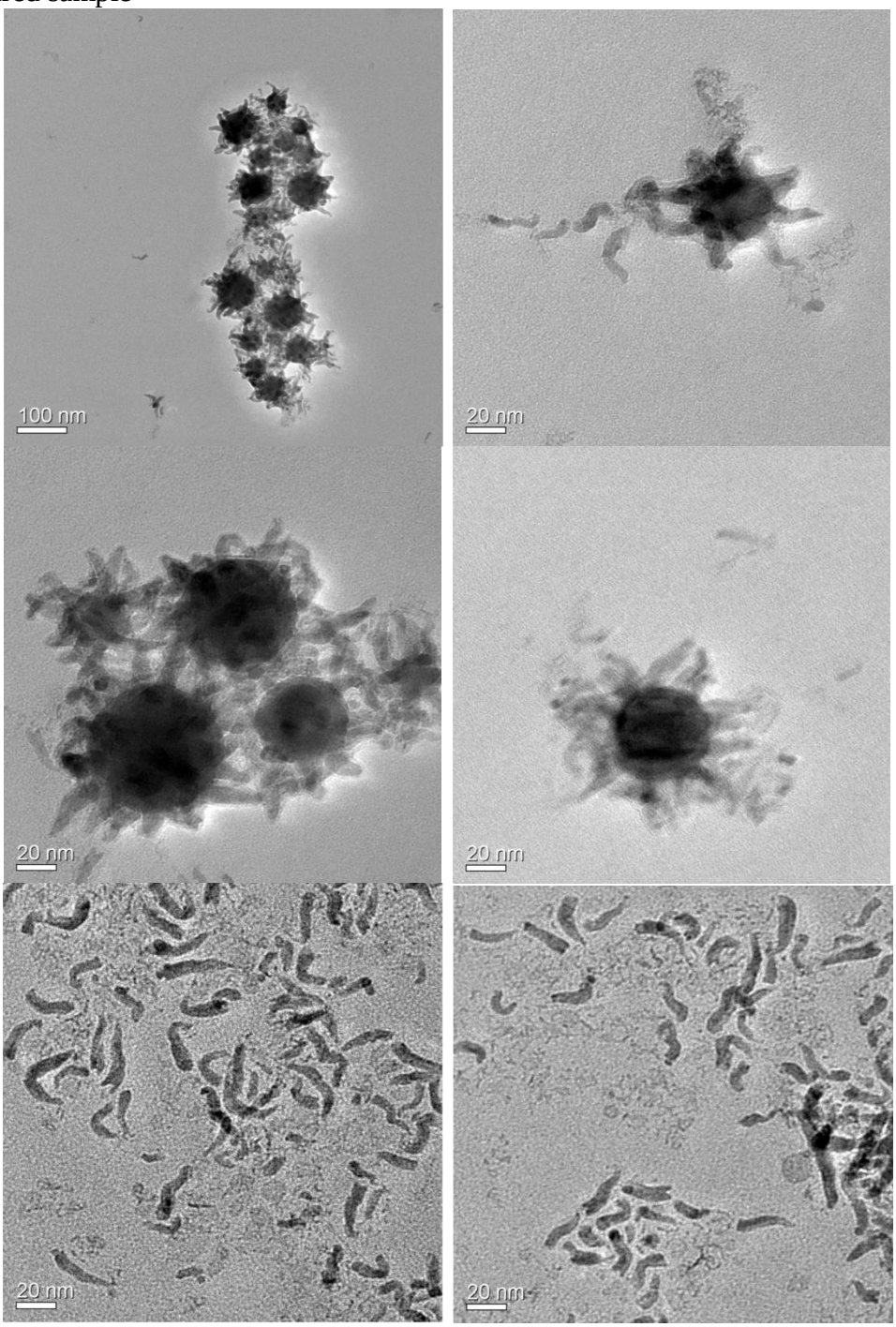

Figure A.1: TEM images of as-prepared sample.

Figure A.1 (cont'd)

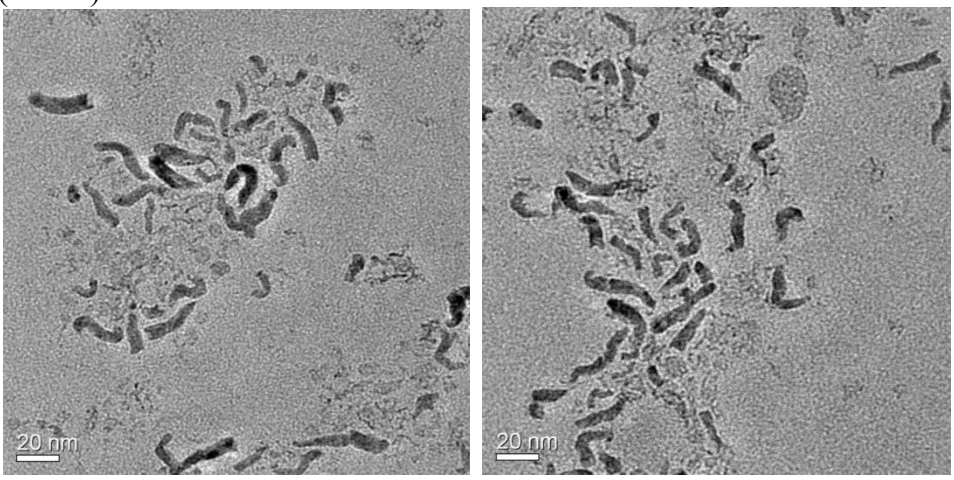

a) Acid treated sample

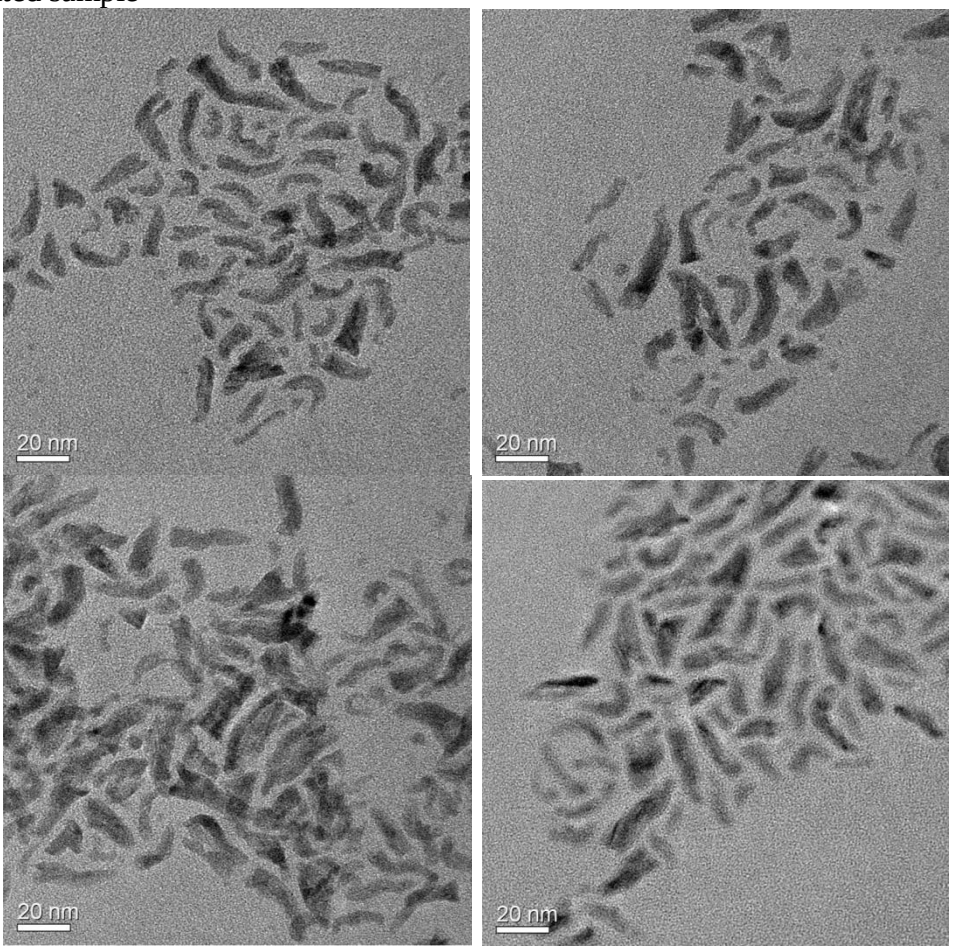

Figure A.2: TEM images of acid-treated sample.

Figure A.2 (cont'd)

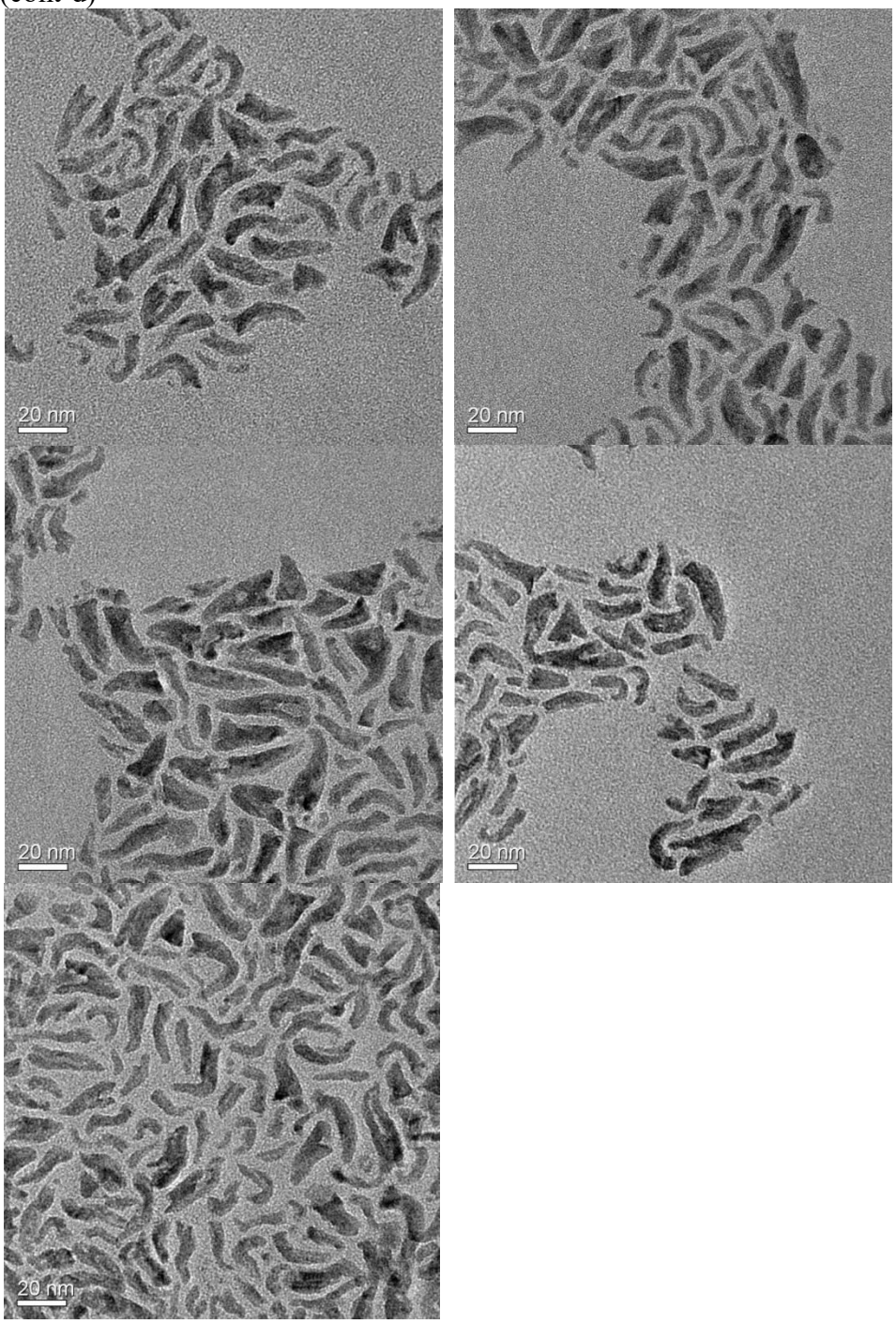

LITERATURE CITED

LITERATURE CITED

[1] Monemar, B. *J. Mater. Sci-Mater. El.* **1999**, *10*, 227.

[2] Goiran, M.; Millot, M.; Poumirol, J. M.; Gherasoiu, I.; Walukiewicz, W.; Leotin, *J. Appl. Phys. Lett*. **2010**, *96*, 052117.

[3] O'Leary, S. K.; Foutz. B. E.; Shur, M. S.; Bhapkar, U. V.; Eastman, L. F. *J. Appl. Phys. Lett*. **1998**, *83*, 826.

[4] Tansley, T. L.; Foley, C. P. *J. Appl. Phys. Lett*. **1986**, *59*, 3241.

[5] Walukiewicz, W.; Ager, J. W.; Yu, K. M.; Liliental-Weber, Z.; Wu, J.; Li, S. X.; Jones, R. E.; Denlinger, *J. D. J. Phys. D Appl. Phys*. **2006**, *39*, R83.

[6] Matsuoka, T.; Okamoto, H.; Nakao, M.; Harima, H.; Kurimoto, E. *Appl. Phys. Lett.* **2002**, *81*, 1246.

[7] Yamamoto, A.; Tanaka, T.; Koide.; Hashimoto, A. *Phys. Stat. Sol. (b)* **2002**, *194*, 510.

[8] Trybus, E.; Namkoong, G.; Henderson, W.; Doolittle, W. A.; Liu, R.; Mei, J.; Ponce, F.; Cheung, M.; Chen, F.; Furis, M.; Cartwright, A. *J. Crys. Growth* **2005**, *279*, 311.

[9] Trybus, E.; Namkoong, G.; Henderson, W.; Burnham, S.; Doolittle, W. A.; Cheung, M.; Cartwright, A. *J. Crys. Growth* **2006**, *288*, 218.

[10] Michalet, X.; Pinaud, E. F.; Bentolila, L. A.; Tsay, J. M.; Doose, S.; Li, J. J.; Sundaresan, G.; Wu, A. M.; Gambhir, S. S.; Weiss, S. *Science* **2005**, *307*, 538.

[11] Xiao, J. P.; Xie, Y.; Tang, R.; Luo, W. *Inorg. Chem.* **2003**, *42*, 107.

[12] Hsieh, J. C.; Yun, D. S.; Hu, E,; Belcher A. M. *J. Mater. Chem*. **2010**, *20*, 1435.

[13] Palomaki, P. K. B.; Miller, E. M.; Neale, N. R. *J. Am. Chem. Soc*. **2013**, *135*, 14142.

[14] Chen, Z.; Li, Y. N.; Cao, C. B.; Zhao, S. R.; Fathololoumi, S.; Mi, Z. T.; Xu, X. Y. *J. Am. Chem. Soc*. **2012**, *134*, 780.

[15] Cumberland, R. W.; Wu, A. M.; Gambhir, S. S.; Weiss, S. *J. Phys. Chem. B* **2001**, *105*, 11922.

[16] Murali, A. K.; Barve, A. D.; Risbud, S. H. *Mat. Sci. Eng.* **2002**, *B96*, 111.

[17] Schwenzer, B.; Loeffler, L.; Seshadri, R.; Keller, S.; Lange, F. F.; DenBaars, S. P.; Mishra, U. K. *J. Mater. Chem.* **2004**, *14*, 637.

[18] Sardar, K.; Dan, M.; Schwenzer, B.; Rao, C. N. R. *J. Mater. Chem.* **2005**, *15*, 2175.

[19] Bai, Y. J.; Liu, Z. G.; Xu, X. G.; Cui, D. L.; Hao, X. P.; Feng, X.; Wang, Q. L. *J. Crys. Growth* **2002**, *241*, 189.

[20] Dingman, S. D.; Rath, N. P.; Markowitz, P. D.; Gibbons, P. C.; Buhro, W. E. *Angew. Chem*. **2000**, *39*, 1470.

[21] Strite, S.; Chandrasekhar, D.; Smith, D. J.; Sariel, J.; Chen, H.; Teraguchi, N.; Morkoc, H. *J. Cryst. Growth* **1993**, *127*, 204.

[22] Mourdikoudis, S.; Liz-Marzan, L. M. *Chem. Mater*. **2013**, *25*, 1465.

[23] Rasband, W. S., ImageJ, National Institutes of Health, Bethesda, Maryland, USA, http:// imagej.nih.gov/ij/, 1997-2016.

[24] Swanson, H. E.; Fuyat, R. K.; Ugrinic, G. M. Standard X-ray Diffraction Powder Patterns; U.S. Dept. of Commerce, National Bureau of Standards: Washington, DC, 1954; Vol. 3.

[25] Paszkowicz, W. *Powder Diffr*. **1999**, *14*, 258.

[26] Berengue, O. M.; Rodrigues, A. D.; Dalmaschio, C. J.; Lanfredi, A. J. C.; Leite, E. R.; Chiquito, C. J. *J. Phys. D: Appl. Phys*. **2010**, *43*, 045401.

[27] Kaczmarczyk, G.; Kaschner, A.; Reich, S.; Hoffmann, A.; Thomsen, C.; As, D. J.; Lima, A. P.; Schikora, D.; Lischka, K.; Averbeck R.; Riechert, H. *Appl. Phys. Lett*. **2000**, *76*, 2122.

[28] Butcher, K. S. A.; Fernandes, A. J.; Chen, P. P. T.; Wintrebert-Fouquet, M.; Timmers, H.; Shrestha, S. K.; Hirshy, H.; Perks, R. M.; Usher, B. F. *J. Appl. Phys.* **2007**, *101*, 123702.

[29] Palomaki, P. K. B.; Miller, E. M.; Neale, N. R. *J. Am. Chem. Soc*. **2013**, *135*, 14142.

[30] Ager, J. W.; Miller, N. R. *Phys. Stat. Sol. (a)* **2012**, *209*, 83.

[31] *CRC Handbook of Chemistry and Physics*, 94th ed.; CRC Press: Boca Raton, FL, 2013−2014.

Chapter 3

INVESTIGATION OF THE REACTION MECHANISM

3.1: Solution-Liquid-Solid Growth of Indium Phosphide Nanofibers: Parallels with Indium Nitride

As discussed in the introduction, InN has attracted much attention for its potential applications in optoelectronic devices. Therefore, more and more efforts are made to prepare InN nanomaterials of high quality. Although various methods have been developed to synthesize InN nanomaterial, most of them require critical reaction conditions, and do not easily lead to large-scale application. Furthermore, the mechanisms underlying the synthesis of InN are unknown. In order to efficiently and scientifically guide future development of synthetic routes to InN nanomaterials, a better understanding of the mechanism of the approach presented in chapter 2 is required. We begin by discussing in detail, a well-studied case, indium phosphide nanofibers grown by SLS; which will provide the basis for the mechanism we will present for InN.

In 1997, Buhro *et al.* reported a solution-liquid-solid approach to grow indium phosphide nanofibers, as shown in Scheme 3.1, in which the methanolysis at 111-203 °C of $\{t\text{-Bu}_2\text{In}[\mu\text{-P(SiMe}_3)_2]\}_2$ in aromatic solvents yields polycrystalline InP nanofibers. [1] Their approach has some similarities with our approach: (1) In both cases, organometallic precursors were chosen; (2) $\text{In}^{(0)}$ droplets form and play a critical role to yield nanocrystals in both of our reactions; (3) Protic species exist in both systems.

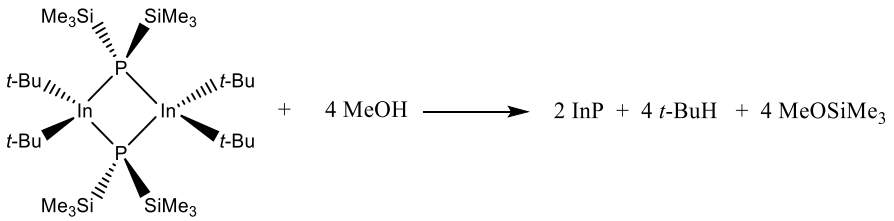

Scheme 3.1: Reaction equation of indium phosphide growth.

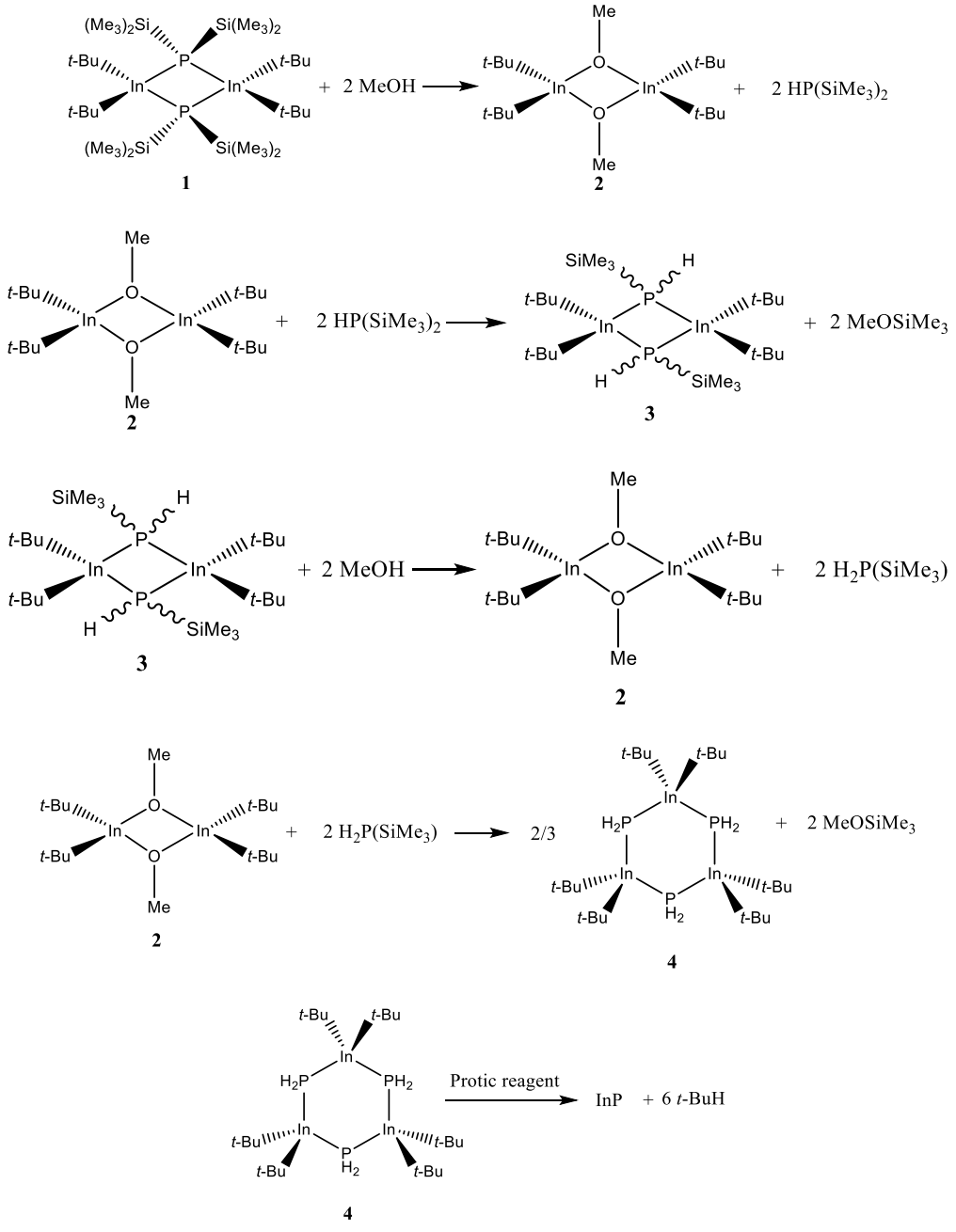

Scheme 3.2: Suggested mechanism for the SLS growth of InP nanofibers (Ref. 1).

In Buhro's approach, the conversion of the precursors $\{t\text{-}Bu_2In[\mu\text{-}P(SiMe_3)_2]\}_2$ to polycrystalline InP fibers involved the molecular and nonmolecular components, which were well demonstrated. [1]

Molecular component of the pathway: Scheme 3.2 clearly illustrates the suggested mechanism of this molecular component. [1] The reaction of methanol with the precursors $\{t\text{-}Bu_2In[\mu\text{-}P(SiMe_3)_2]\}_2$ (**1**) generates indium-alkoxide species (**2**), followed by methanolysis of P-Si bonds to generate new phosphidoindium species (**3**) containing P-H bonds. These phosphidoindium species (**3**) readily react with two the molar equivalents of methanol to reform a indium-alkoxide (**2**) again and $H_2P(SiMe_3)$. The reaction between the indium-alkoxide (**2**) and $H_2P(SiMe_3)$ affords the trimer $[t\text{-}Bu_2In(\mu\text{-}PH_2)]_3$ (**4**). Solution thermolysis, an elimination-condensation process, of **4** at 203 ^oC results in the formation of InP with comparable purity and crystallinity. In this process, *tert*-Butyl hydride elimination is coupled with In-P bond formation followed by the oligomerization (condensation) of molecular intermediates. Since the six-membered metallacycle **4** is the last-detected molecular intermediate, *t*-BuH elimination may proceed by direct intermolecular condensation of **4** (Scheme 3.3) to form chairlike In_3P_3 rings that can produce zinc-blende fragments by condensation. [1] These reactions are presented in Scheme 3.2, and constitute the molecular component of the InP growth mechanism.

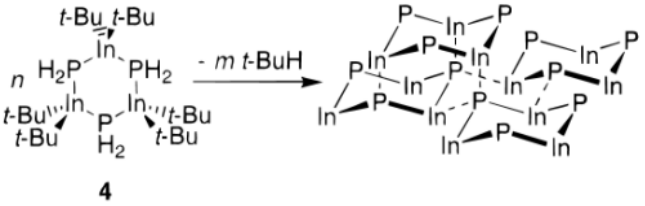

Scheme 3.3: Direct Intermolecular Elimination-Condensation of $[t\text{-}Bu_2In(\mu\text{-}PH_2)]_3$ (**4**) to a Zinc-Blende Cluster Fragment. (Peripheral t-Bu and H cluster substituents are omitted for clarity. The dotted lines are bonds pre-existing in **4**. (Ref. 1))

Nonmolecular component of the pathway: The molecular component provided the sufficient species for the crystal-growth process, which happened in the nonmolecular component of the growth of InP pathway. In their approach, $In^{(0)}$ always formed and they thought it was a side product likely coming from the thermal decomposition of **4** or other tertiary-alkyl-containing intermediates. [1] Meanwhile, a series of control experiments established a critical role for $In^{(0)}$ in InP crystallization. Once the $(InP)_n$ clusters dissolve into the $In^{(0)}$ droplet, nonmolecular component of the growth of InN assembles them to form the polycrystalline fibers.

In the mechanism of indium phosphide fibers growth proposed by Buhro *et al.*, [1] PH_2 is an important species to form a six-membered metallacycle **4** that can readily decompose to afford $(InP)_n$ clusters. Buhro *et al.* also mention that these six-membered metallacycle **4** can also be generated directly from the reaction between *t*-Bu_3In and PH_3, as shown in Scheme 3.4. [1]

Besides, Purdy reported an approach to prepare InN through thermolysis of $In(NH_2)_3$. [2] Although our approach does not involve any NH_3 or NH_2^- species as starting materials, a situation like that described by Buhro *et al.*, in which PH_2 is formed during the course of the reaction, might occur here. That is, an intermediate containing In-NH_2 bond, which has a similar structure with six-membered metallacycle **4**, may form during the reaction, then decompose to offer $(InN)_n$ clusters.

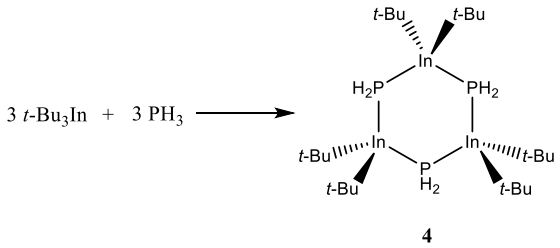

4

Scheme 3.4: Reaction between t-Bu_3In and PH_3 (Ref. 1).

3.2: Analyses of the Reaction Products

3.2.1: Organic Products

3.2.1.1: Experimental Details

Two approaches, labelled A and B, were designed to help identify the nature of the mechanism. Both approaches are identical except for the nature of the alkylamide used: octadecylamine in A and oleylamine in B. The only structural difference between these two different primary amides is the presence of double bond for OLA. In reaction A, we use deprotonated-hexamethyldisilane as amide instead of octadecylamide due to the insolubility of octadecylamide in hexane and hexadecane. Before we conduct reaction A and reaction B, we study the role of deprotonated-HMDS first by designing experiments described below.

The experimental setup is described in Figure 3.1. Control experiment: 2 ml of OLA and 5 ml of hexadecane were mixed in a three-neck round-bottom flask equipped with a water-cooled-condenser and kept under air-free conditions (N_2 Schlenk line) and heated to 210 ^oC. An alkylamide precursor solution is separately prepared under air-free conditions (N_2 glove box) by reacting 0.32 ml of HMDS (1.5 mmol) with a mixture of 0.60 ml of a n-BuLi solution (2.5 M hexane solution, 1.5 mmol n-BuLi) and 0.45 ml TMEDA (3 mmol). This alkylamide solution is then injected promptly with a 6 ml syringe into the flask. Two bubblers were used to trap low boiling point compound (such as HMDS and TMEDA). Each bubbler contains 6 ml of toluene and 1.5 mmol Hexadecane. Hexadecane or dodecylamine were used as reference to quantify the amount of recovered HMDS and TMEDA. After one hour, the trap solution were combined for NMR measurements (*d*-$CHCl_3$).

Experimental tests: In a three-neck round-bottom flask equipped with a water-cooled-condenser and kept under air-free conditions (N_2 Schlenk line), 180 mg $InBr_3$ (0.5 mmol) are

solubilized in 2 ml of oleylamine (6.08 mmol) and 5 ml of hexadecane. A complete dissolution of the salt is achieved by heating the solution to 210 ^{o}C under constant vigorous stirring. An alkylamide precursor solution is separately prepared under air-free conditions (N_2 glove box) by reacting 0.32 ml of HMDS (1.5 mmol) with a mixture of 0.60 ml of a n-BuLi solution (2.5 M hexane solution, 1.5 mmol n-BuLi) and 0.45 ml TMEDA (3 mmol). This alkylamide solution is then injected promptly with a 6 ml syringe into the indium-OLA mixture to initiate the reaction. Two bubbles were used to trap low boiling point compound (such as HMDS and TMEDA). Each bubbler contains 6 ml of toluene and 1.5 mmol Hexadecane (or 1.5 mmol dodecylamine). Hexadecane or dodecylamine were used as reference to quantify the amount of recovered HMDS and TMEDA. After 1 hour, combining trap solution for NMR measurements (d-$CHCl_3$).

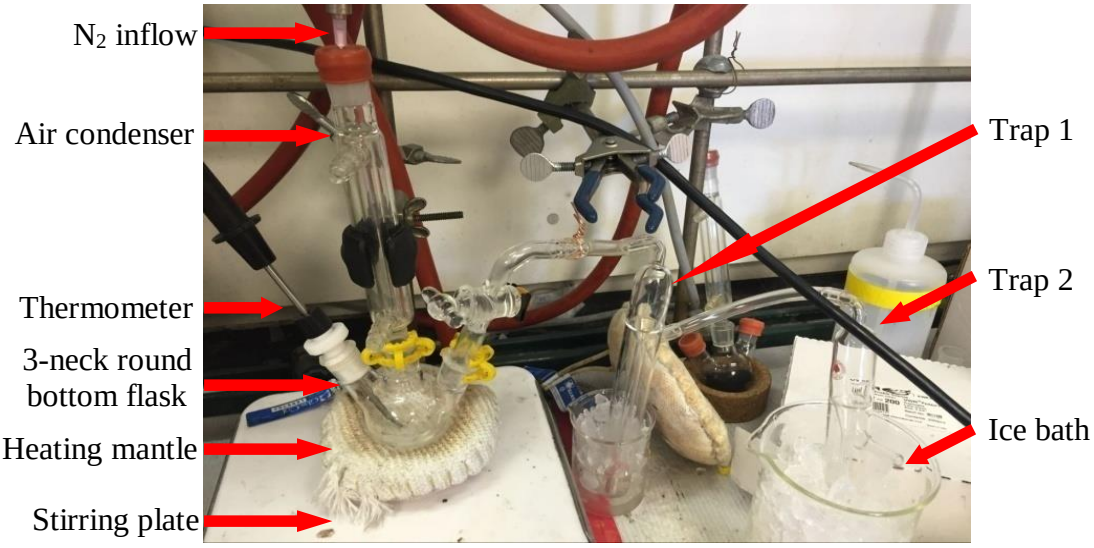

Figure 3.1: Set-up for influence of deprotonated-HMDS on conventional reaction experiment.

Identification of Organic Side-Products is described below:

Reaction A. In a three-neck round-bottom flask equipped with a water-cooled-condenser and kept under air-free conditions (N_2 Schlenk line), 180 mg $InBr_3$ (0.5 mmol) are solubilized in 402 mg octadecylamine (1.5 mmol) and 5 mL hexadecane. This mixture was degassed under vacuum for 30 min both at room temperature and at 80 ^{o}C. A complete dissolution of the salt is achieved

by heating the solution to 210 ºC under constant vigorous stirring within 1 min. An alkylamide precursor solution is prepared separately under air-free conditions (N_2 glove box) by reacting 0.32 mL of HMDS (1.5 mmol) with a mixture of 0.60 mL of a n-BuLi solution (2.5 M hexane solution, 1.5 mmol n-BuLi) and 0.45 mL TMEDA (3 mmol). The alkylamide solution is then injected promptly with a 6 mL syringe into the indium-octadecylamine mixture to initiate the reaction. The reaction is stopped after 10 min by removing the heating mantle and the reaction mixture cool down to room temperature by 20 min. This final reaction mixture is directly used for nuclear magnetic resonance (NMR) measurements. For liquid chromatography-mass spectrometry (LC-MS) measurements, the final reaction mixture is centrifuged to separate the solid parts from the liquid phase; the liquid phase was then dissolved in chloroform for the LC-MS measurements.

Reaction B. In a three-neck round-bottom flask equipped with a water-cooled-condenser and kept under air-free conditions (N_2 Schlenk line), 180 mg $InBr_3$ (0.5 mmol) are solubilized in 2 mL OLA (6.08 mmol) and 5 mL hexadecane. This mixture was degassed under vacuum for 30 min both at room temperature and at 80 ºC. A complete dissolution of the salt is achieved by heating the solution to 210 ºC under constant vigorous stirring within 1 min. An alkylamide precursor solution is prepared separately under air-free conditions (N_2 glove box) by reacting 0.50 mL OLA (1.5 mmol) with a mixture of 0.60 mL of a n-BuLi solution (2.5 M hexane solution, 1.5 mmol n-BuLi) and 0.45 mL TMEDA (3 mmol). This alkylamide solution is then injected promptly with a 6 mL syringe into the indium-OLA mixture to initiate the reaction. The reaction is stopped after 10 min by removing the heating mantle and the reaction mixture cool down to room temperature by 20 min. This final reaction mixture is directly used for nuclear magnetic resonance (NMR) measurements. For liquid chromatography-mass spectrometry (LC-

MS) measurements, the final reaction mixture is centrifuged to separate the solid parts from the liquid phase; the liquid phase was then dissolved in chloroform for the LC-MS measurements.

Nuclear magnetic resonance (NMR) were recorded (at 295 K) on a Varian Inova 500 MHz spectrometer; the chemical shifts are relative to residual solvent peaks with TMS ($\delta = 0$ ppm for ^{1}H and ^{13}C. Deuterated-chloroform was used as solvent).

Liquid chromatography-mass spectrometry (LC-MS) was performed on a Waters Xevo GZ-XS quadrupole time of flight (QTOF) mass spectrometer coupled to a Waters acquity liquid chromatography system. Chloroform was used as eluent.

3.2.1.2: Experimental Results and Discussion

Table 3.1, Figure 3.2 and Figure 3.3 summarized the recovered amount of TMEDA and HMDS in control experiment and experimental group. Though we did not completely recover HMDS, we found the ratio of recovered HMDS to recovered TMEDA in experimental groups and the ratio of that in control experiment are all around 2, which is same with the ratio of HMDS and TMEDA we added in the beginning. In addition, we did ^{29}Si NMR both for final reaction mixture and trapped solution of experimental groups. As shown in Figure 3.3, we see no species containing silicon in final reaction mixture, and only one compound containing silicon, which is HMDS in trapped solution. Hence, HMDS does not decompose in this approach, suggesting that deprotonated-HMDS is not the nitrogen precursor to InN in reaction A.

Table 3.1: Calculated amount of recovered TMEDA and HMDS

	Hexadecane/Dodecane (mmol)	TMEDA (mmol)	HMDS (mmol)	Ratio (TMEDA/HMDS)	Recovered Yield
Expected	3.0	3.0	1.5	2.0	100%
Control experiment	3.0	1.72	0.83	2.07	58%
Experimental test 1	3.0	1.80	0.83	2.17	58%
Experimental test 2	3.0	1.41	0.66	2.14	46%

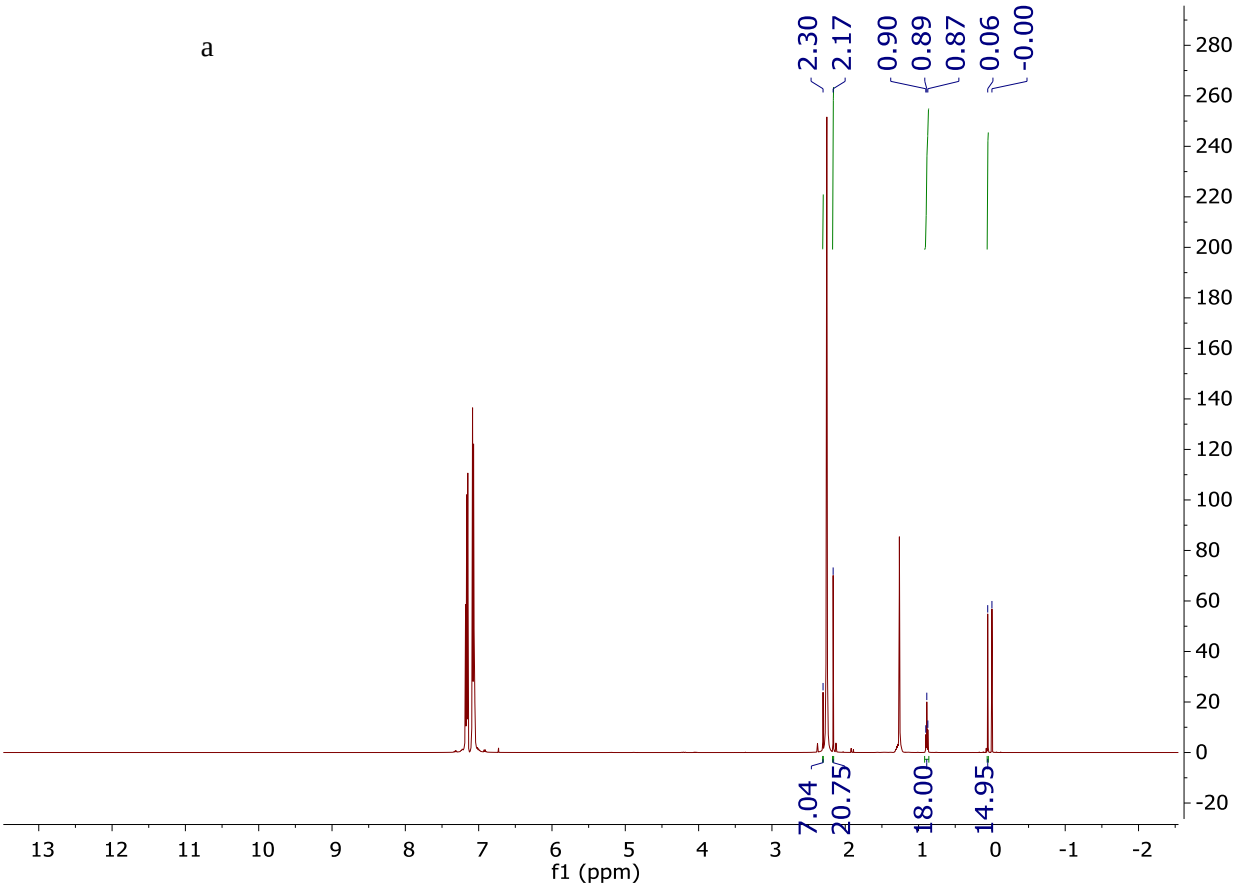

Figure 3.2: a) ^{1}H NMR of trap solution in control experiment. b) ^{1}H NMR of trap solution in experimental group 1. c) ^{1}H NMR of trapped solution in experimental group 2.

Figure 3.2 (cont'd)

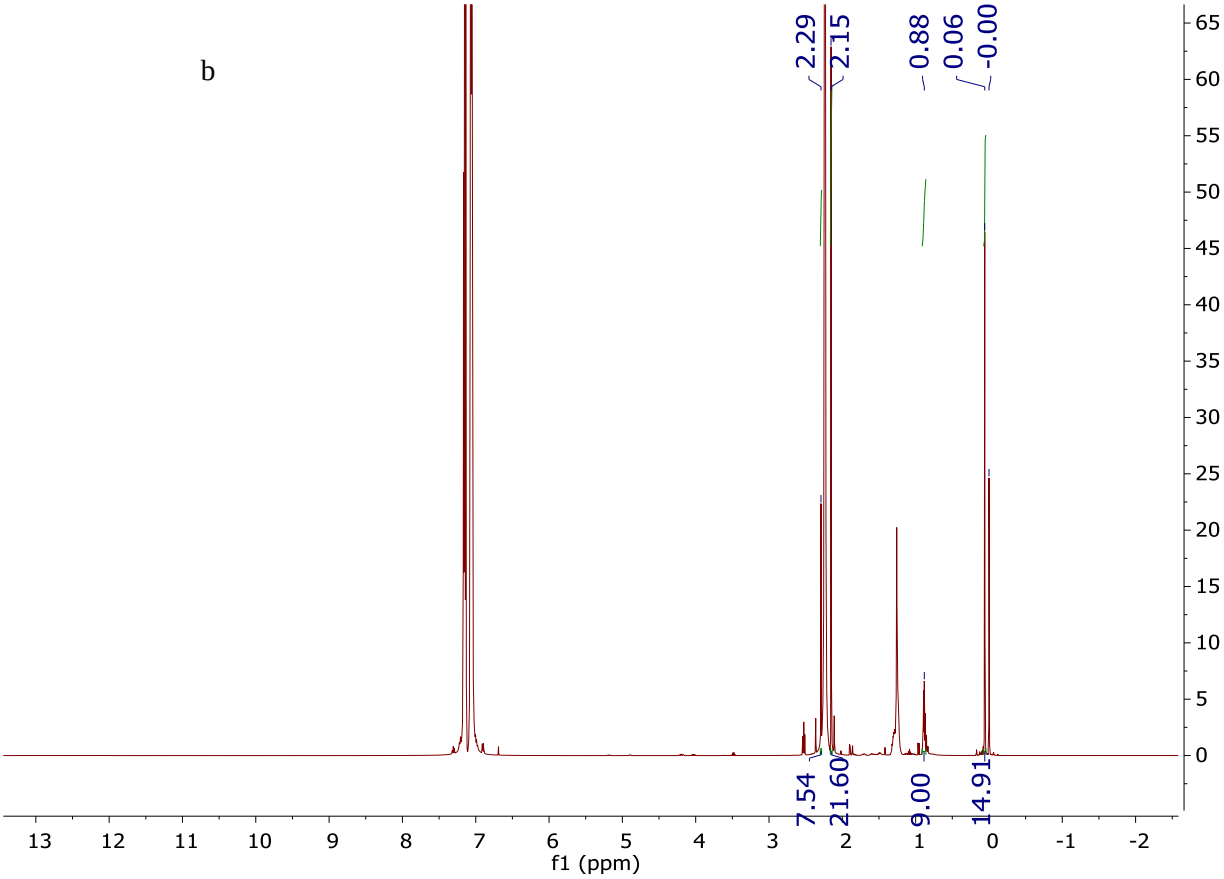

Figure 3.2 (cont'd)

c

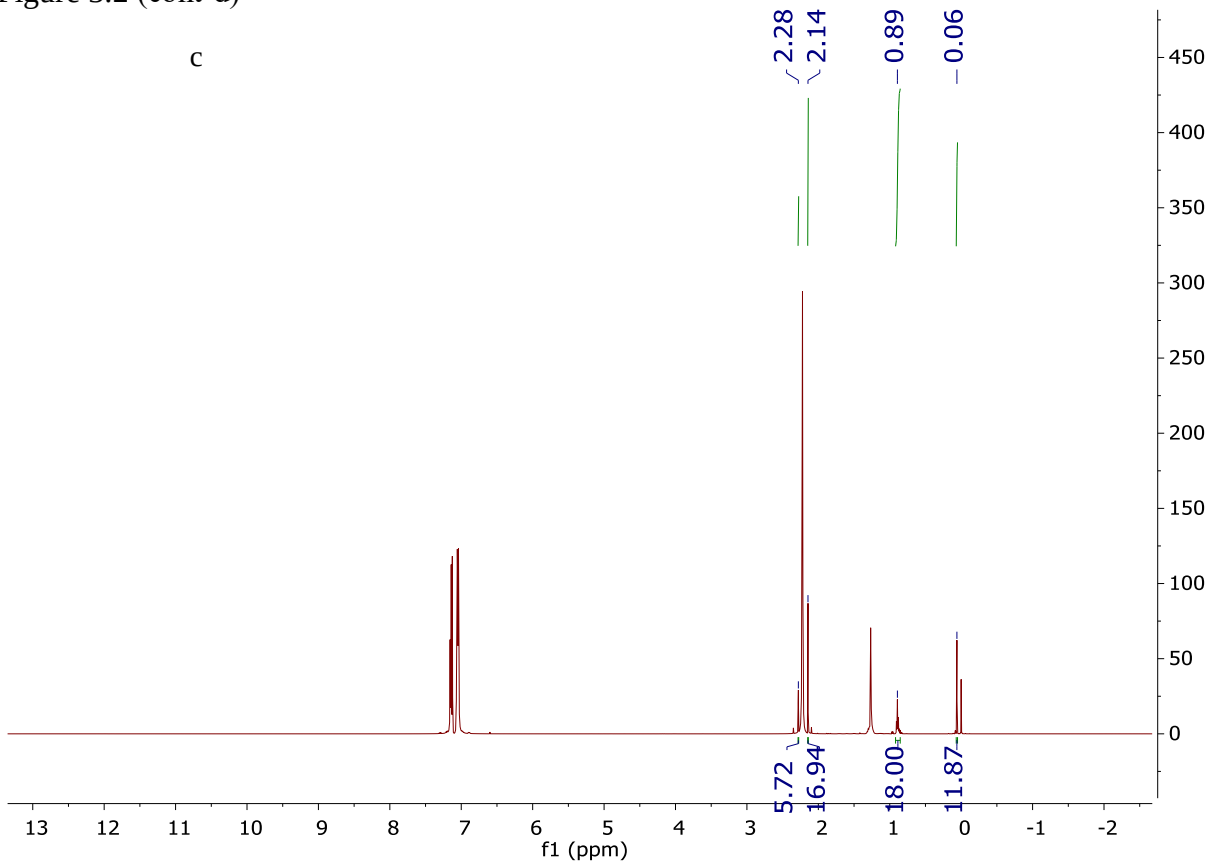

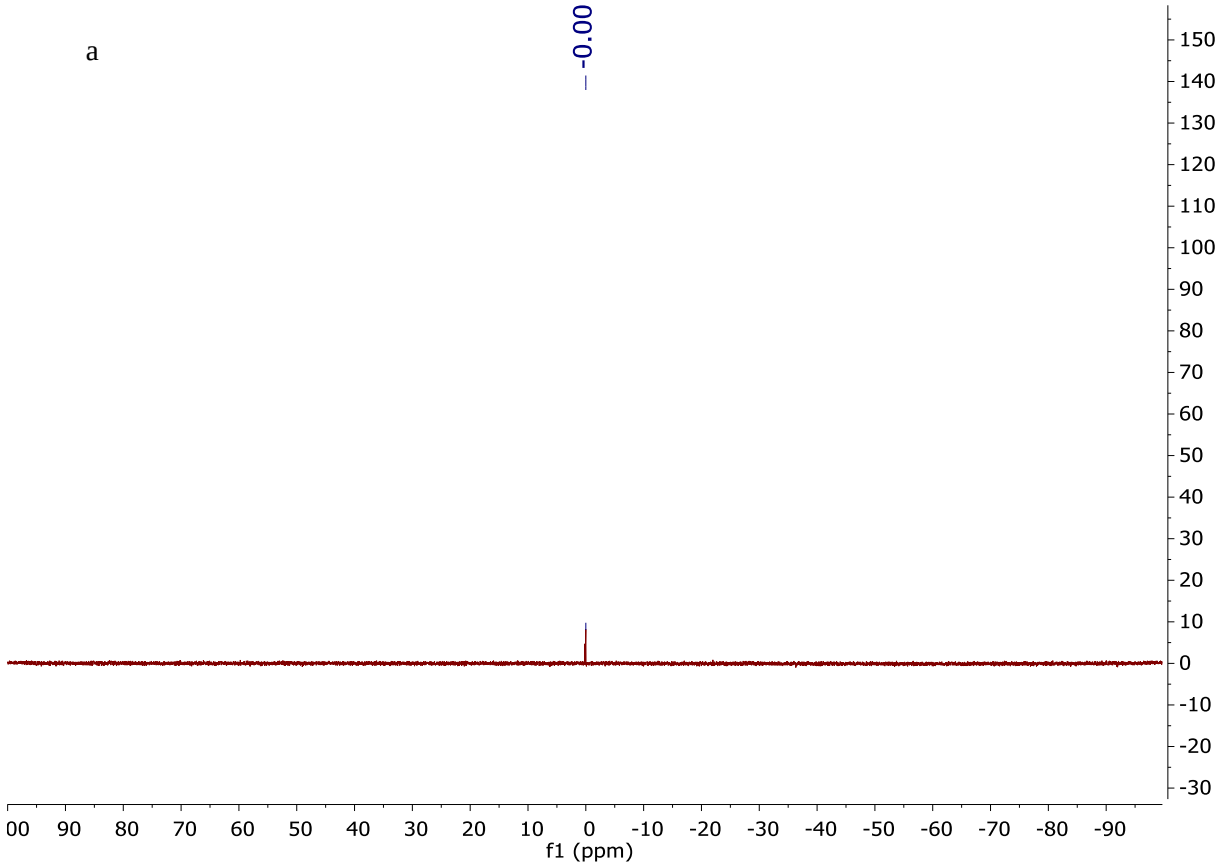

Figure 3.3: a) ^{29}Si NMR of final reaction mixture in control experiment. b) ^{29}Si NMR of trap solution in control experiment. c) ^{29}Si NMR of final reaction mixture in experimental group 1. d) ^{29}Si NMR of trap solution in experimental group 1.

Figure 3.3 (cont'd)

b

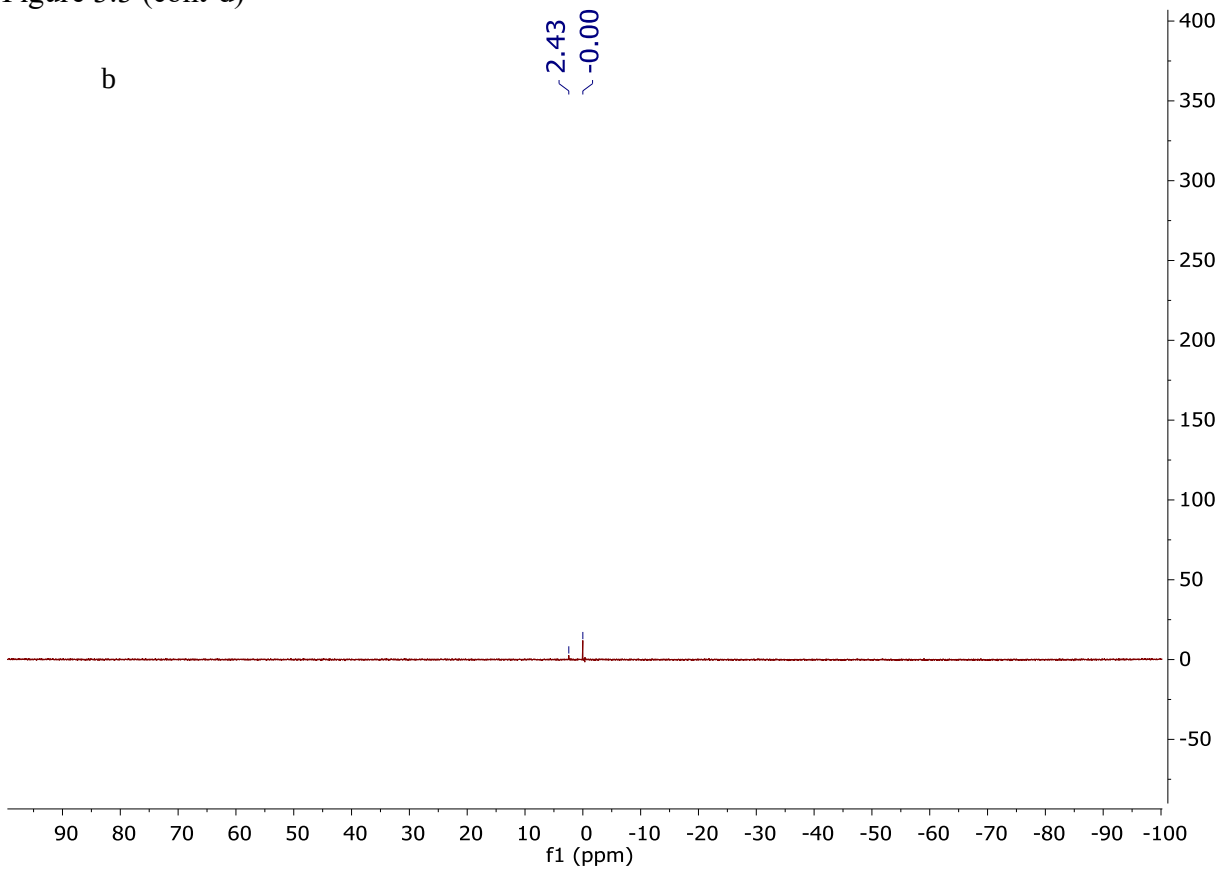

Figure 3.3 (cont'd)

c

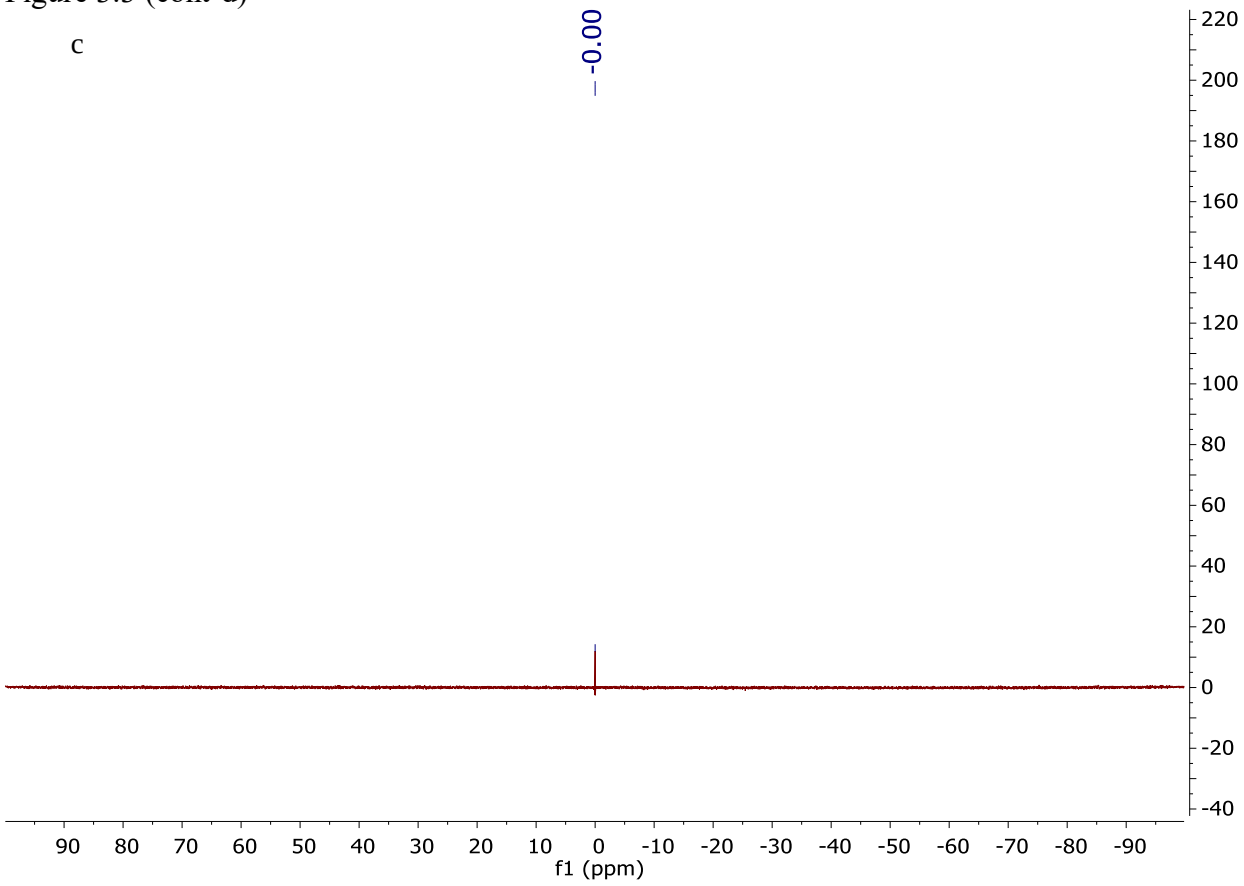

Figure 3.3 (cont'd)

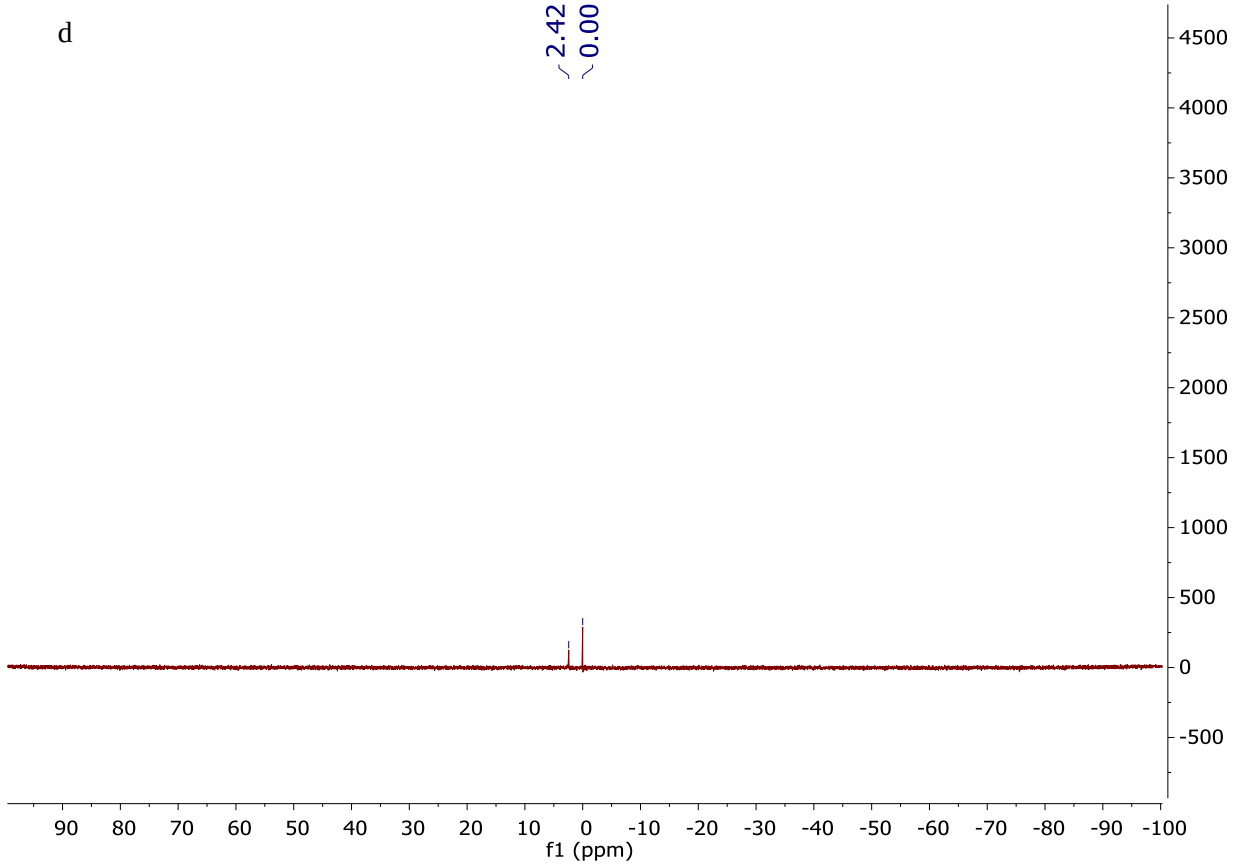

The final reaction mixtures were directly characterized by ^{1}H, and ^{13}C NMR. In ^{1}H NMR (Figure 3.4.a and Figure 3.5.a), peaks located at the range of 0 ppm to 2 ppm, which belong to hexadecane and octadecylamine (or oleylamine), have very high intensities, suggesting the reaction mixture consists of mostly hexadecane, octadecylamine (or oleylamine); the same occurs in ^{13}C NMR. When the spectra are magnified (Figure 3.4.c, d and Figure 3.5.c, d), the final mixtures for both reaction (A&B) show a new triplet peak ~ 7.6 ppm in ^{1}H NMR spectrum (Figure 3.4.c and Figure 3.5.c) and a peak ~164 ppm in ^{13}C NMR spectrum (Figure 3.4.d and Figure 3.5.d). This peak is clearly absent in the starting mixture, suggesting the formation of a new organic product. The ^{1}H and ^{13}C chemical shift of these two new species produced by reaction A and reaction B, respectively, are extremely close to each other, suggesting two

possible scenarios: i) If these two new species produced by reaction A and reaction B are identical, this new compound should not contain the long carbon chain which can only come from octadecylamine or oleylamine. ii) If these two new species are different, but still similar enough that NMR cannot distinguish them. Considering that most imines have proton peak located in the range of 7 to 8 ppm and carbon peak located in the range of 160 to 170 ppm, we suspect these new species are imines.

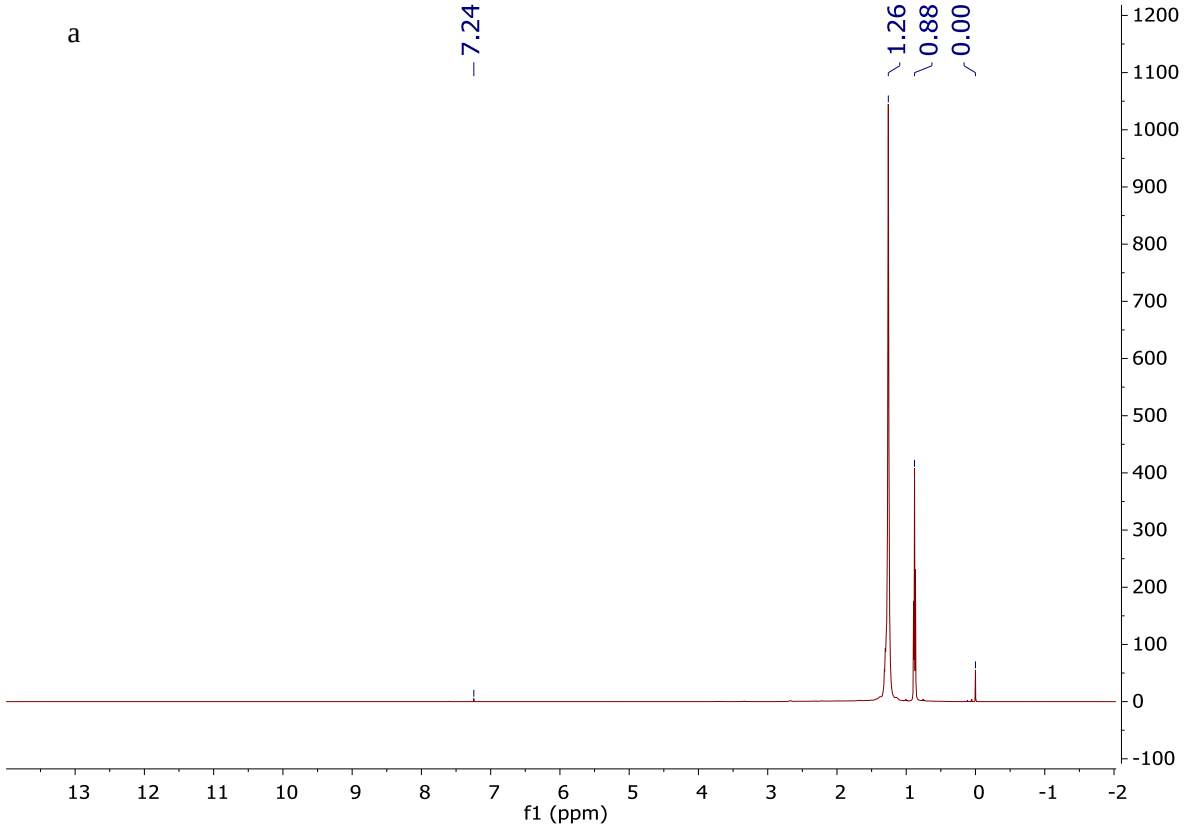

Figure 3.4: a) ^{1}H NMR spectrum of reaction A final mixture. b) ^{13}C NMR spectrum of reaction A final mixture. c) magnified ^{1}H NMR spectrum of reaction A final mixture. d) magnified ^{13}C NMR spectrum of reaction A final mixture.

Figure 3.4 (cont'd)

b

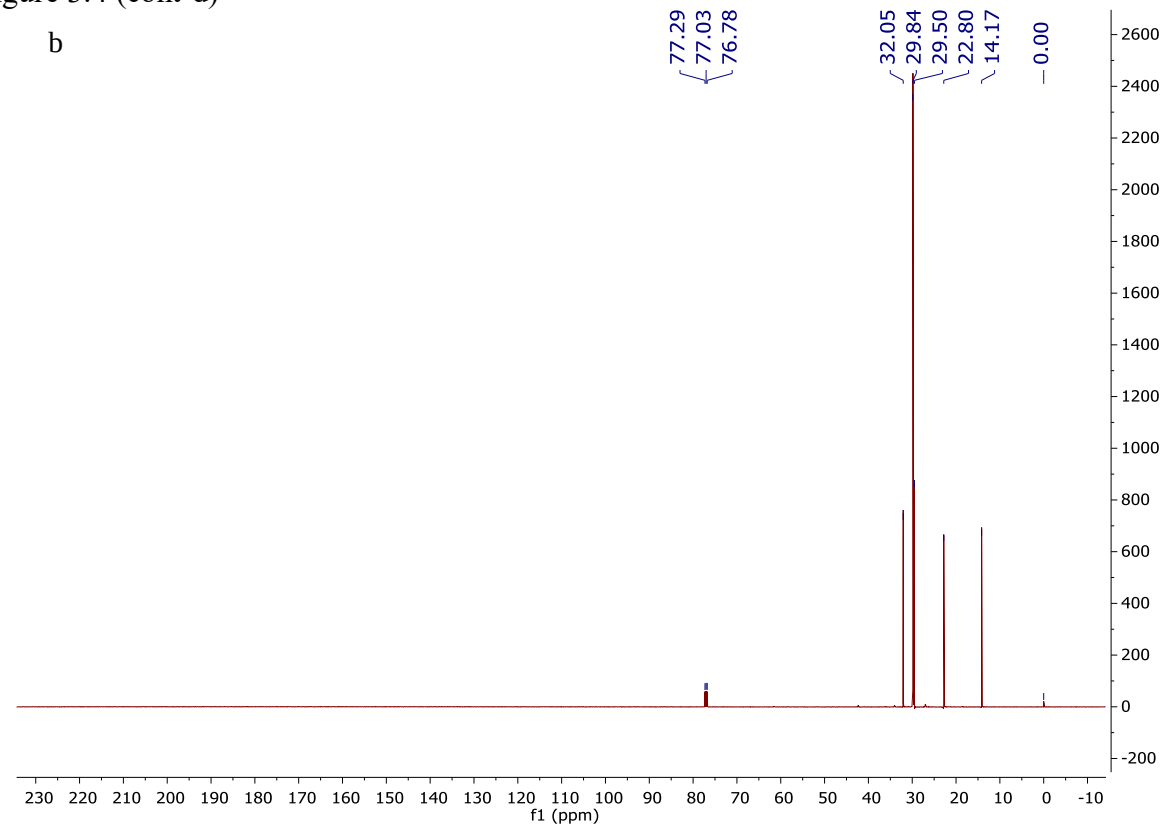

Figure 3.4 (cont'd)

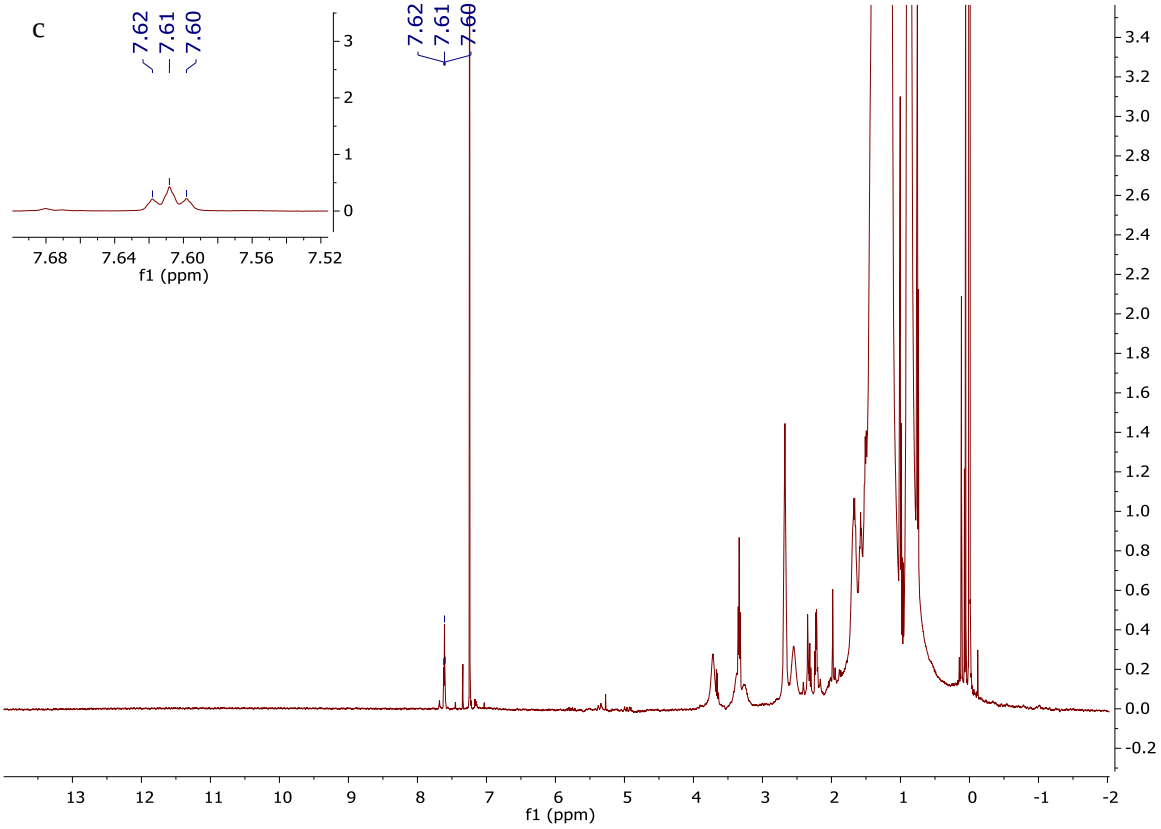

Figure 3.4 (cont'd)

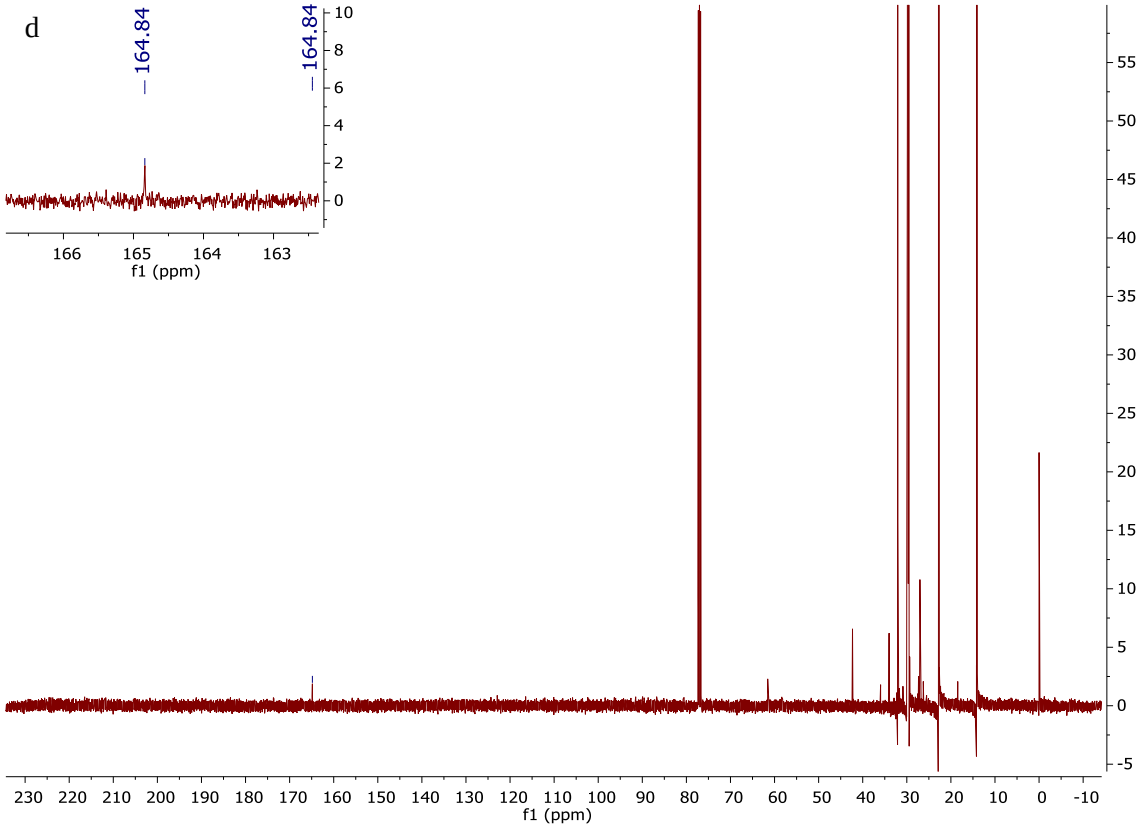

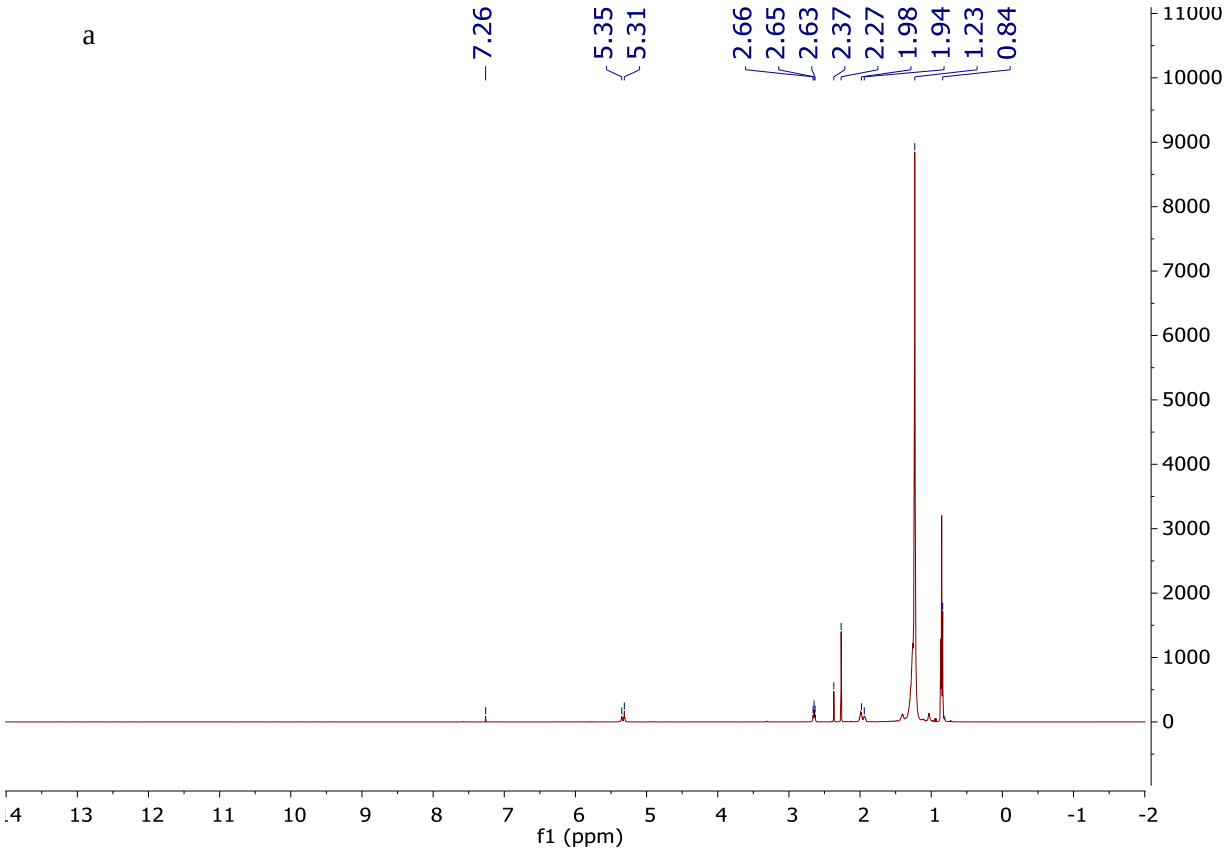

Figure 3.5: a) ^{1}H NMR spectrum of reaction B final mixture. b) ^{13}C NMR spectrum of reaction B final mixture. c) magnified ^{1}H NMR spectrum of reaction B final mixture. d) magnified ^{13}C NMR spectrum of reaction B final mixture.

Figure 3.5 (cont'd)

b

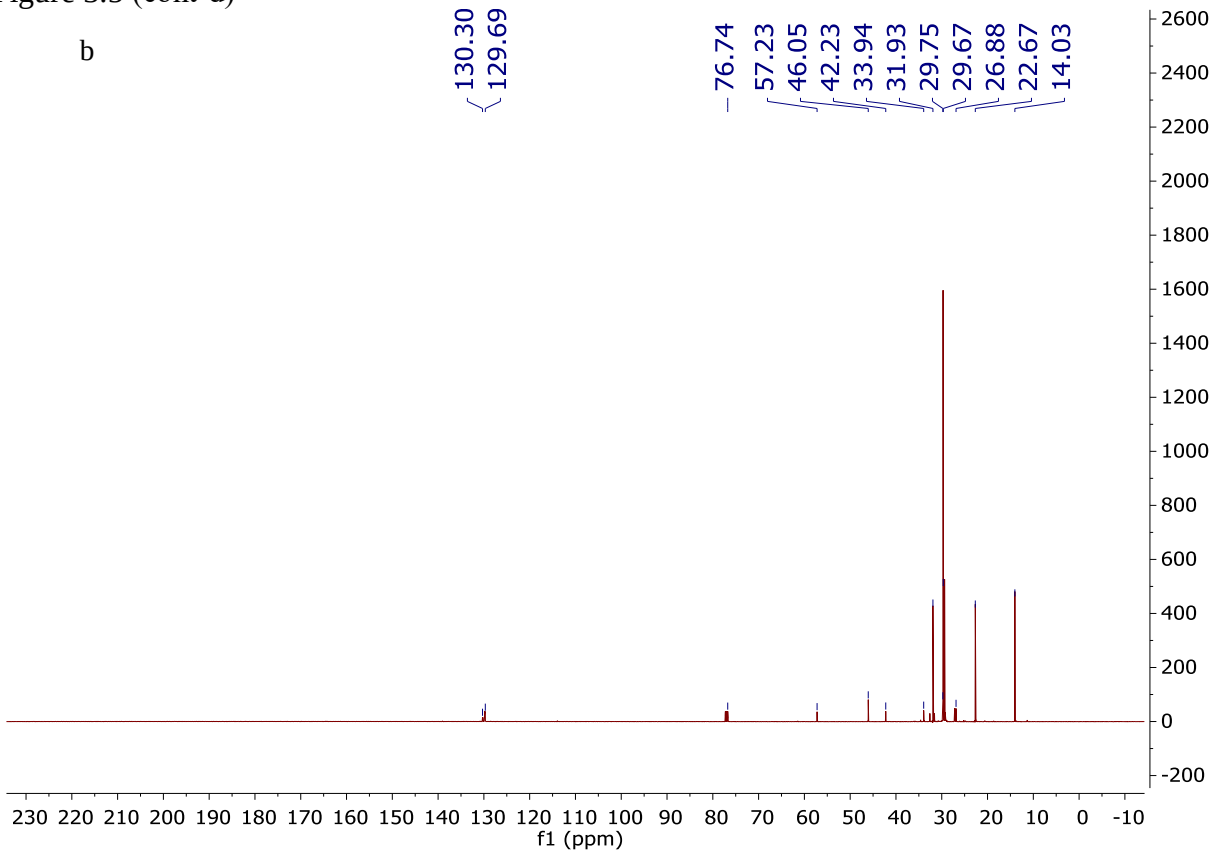

Figure 3.5 (cont'd)

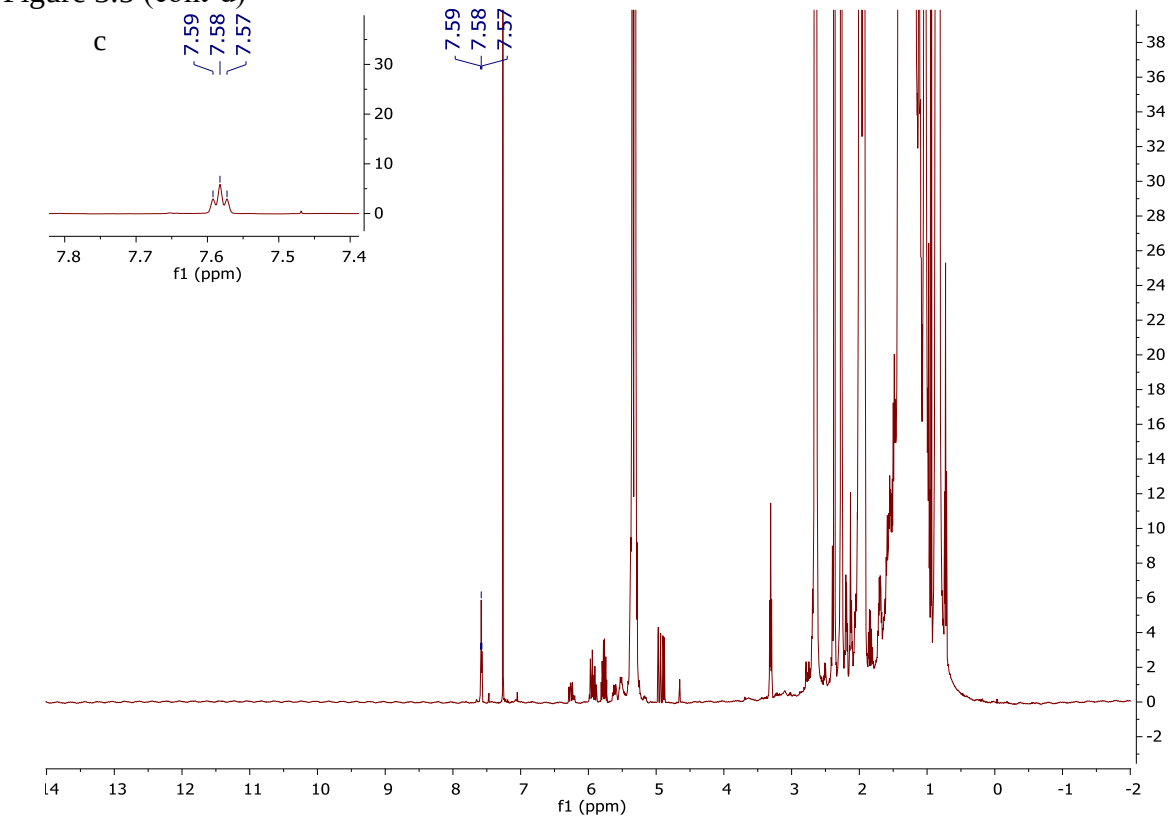

Figure 3.5 (cont'd)

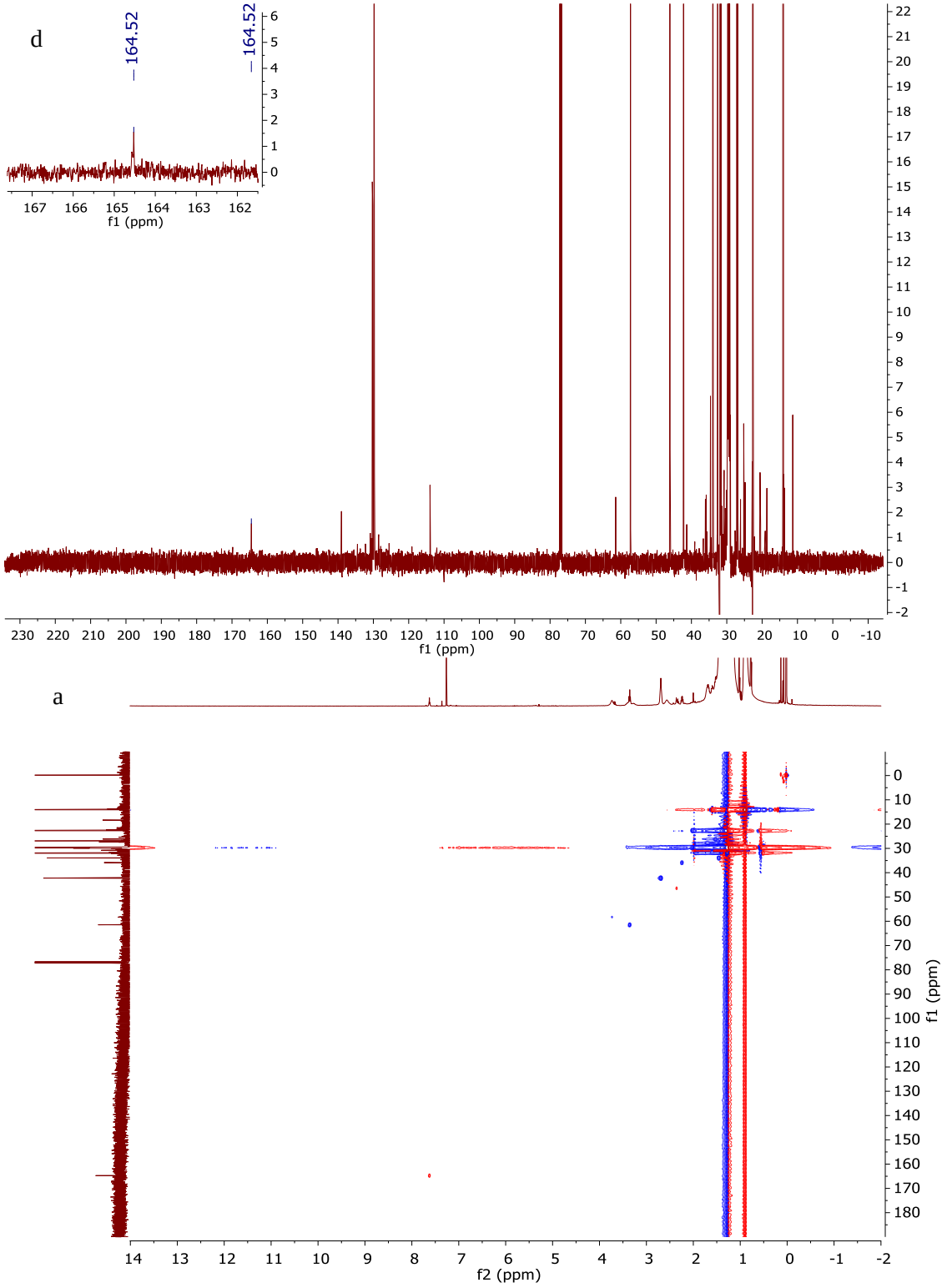

Figure 3.6: a) ^{1}H-^{13}C HSQC of reaction A final mixture. b) ^{1}H-^{13}C HSQC of reaction B final mixture.

Figure 3.6 (cont'd)

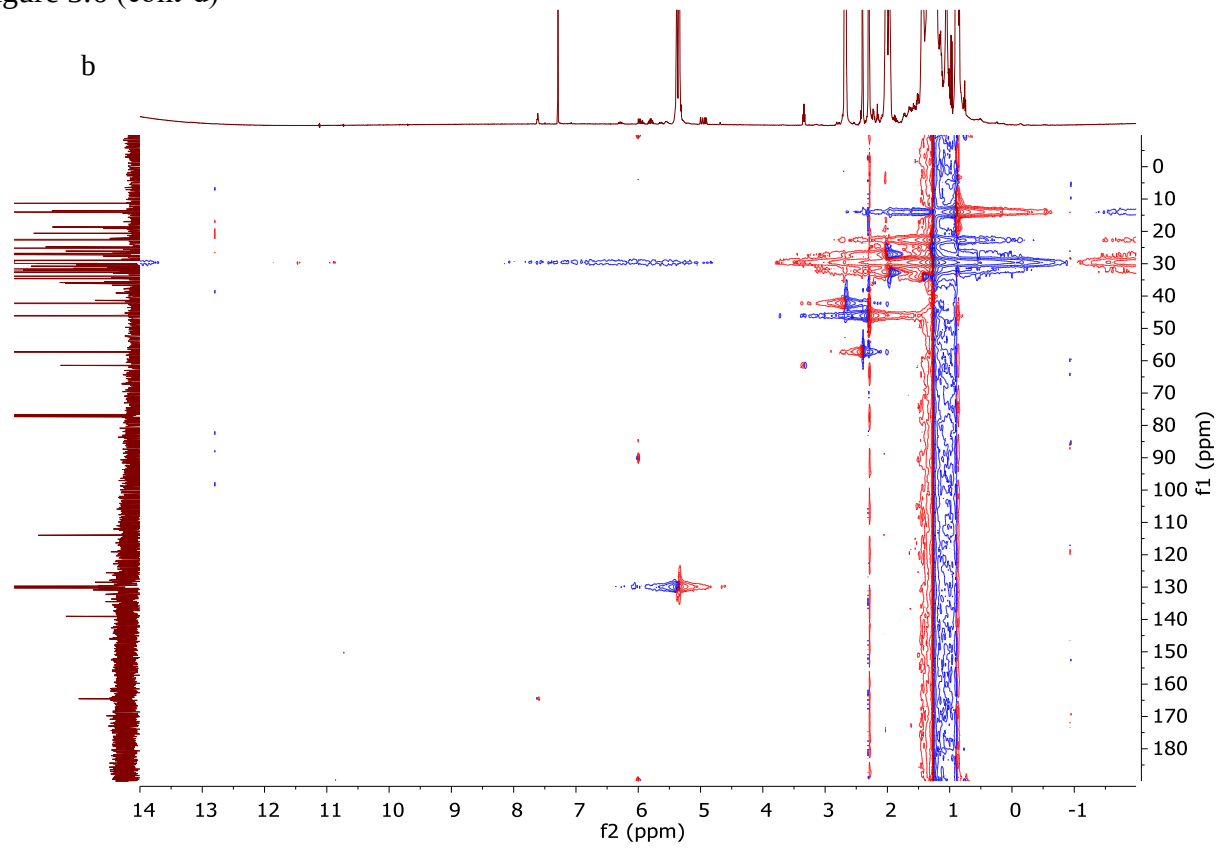

^{1}H-^{13}C Heteronuclear Single Quantum Coherence spectroscopy (^{1}H-^{13}C HSQC) was further used (Figure 3.6), giving clear evidence that the proton with the ~ 7.6 ppm resonance is bound to the carbon with the ~ 164 ppm resonance. Furthermore, the sign of the magnetization of this carbon with ~ 164 ppm resonance is opposite to those with an even number of aliphatic carbon, suggesting this carbon is attached with 3 aliphatic carbon or 1 aliphatic carbon, as shown in Figure 3.6. These results are all consistent with the hypothesis that an imine is formed as a product of the reaction.

^{1}H-^{1}H COSY spectroscopy was employed to clarify whether this side product is primary imine or secondary imine. As shown in Figure 3.7, the proton signal at ~ 7.6 ppm is coupled to two different types of protons, one type of proton is located at around 2.3 ppm and another one type

of proton which has triplet peak in ^{1}H NMR is located at around 3.4 ppm. Because the proton attached to nitrogen atom in methylimine has a chemical shift of 10.5 ppm [3] (as shown in Figure 3.8.a), if this new species is primary imine, which means, the chemical shift of the proton attached to nitrogen atom in this new species should be around 10.5 ppm. In this case, the proton (~ 7.6 ppm) of this primary imine should be coupled with two types of proton, one type of proton is located around 10.5 ppm and one type of proton is located in the range of 0 to 4 ppm, which is in conflict with our ^{1}H-^{1}H COSY spectroscopy result. Hence, this imine is a secondary imine instead of a primary imine. Because we did not see the formation of C=C bond in reaction A (Figure 3.4), and did not see significant disappearance of C=C bond in reaction B (Figure 3.5), we think our approach does not have any influence on the C=C bond of oleylamine. Thus, we strongly think the side organic product is a secondary imine with a structure shown in Figure 3.8.c.

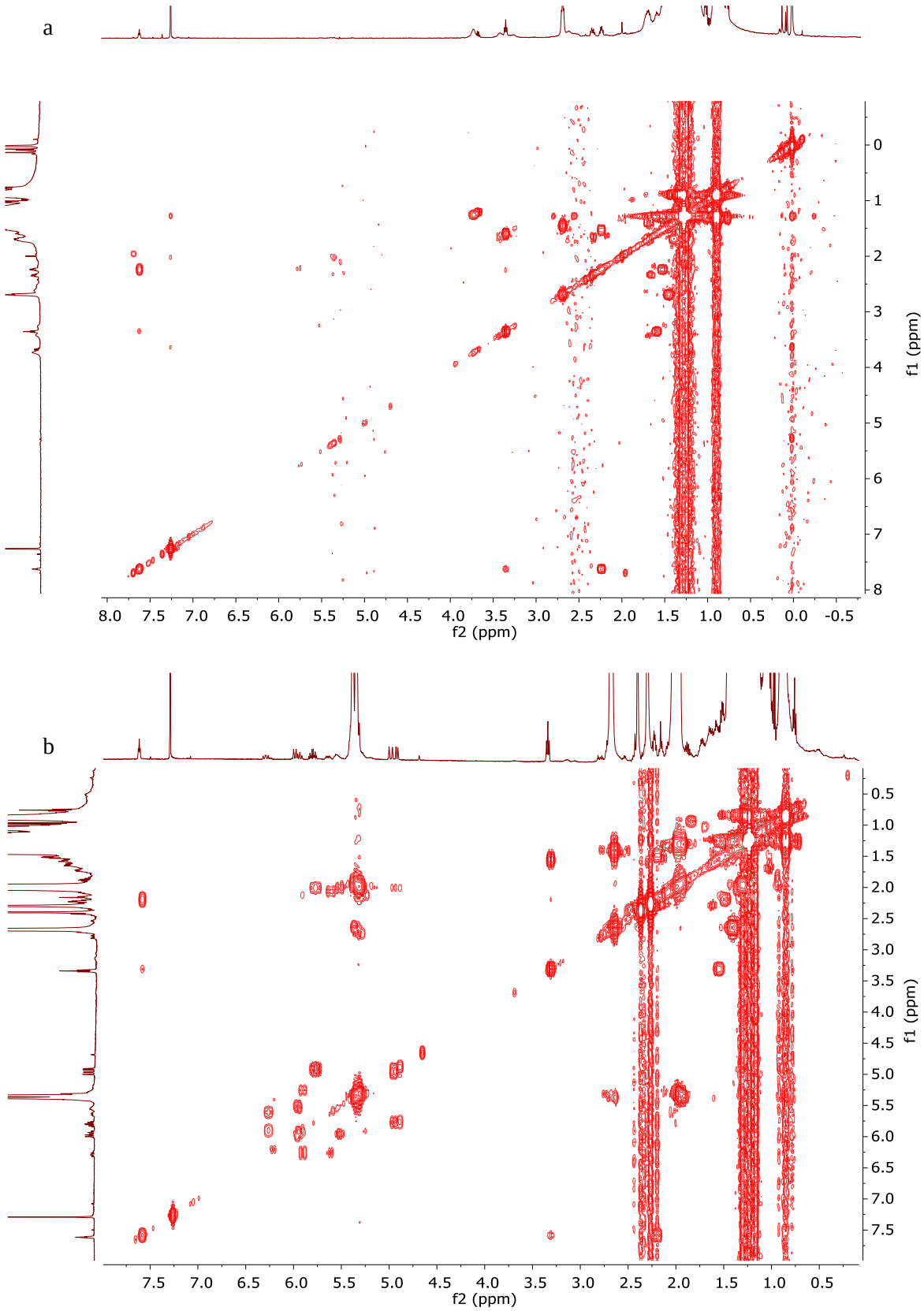

Figure 3.7: a) ^{1}H-^{1}H Cosy Spectroscopy of reaction A final mixture. b) ^{1}H-^{1}H Cosy Spectroscopy of reaction B final mixture.

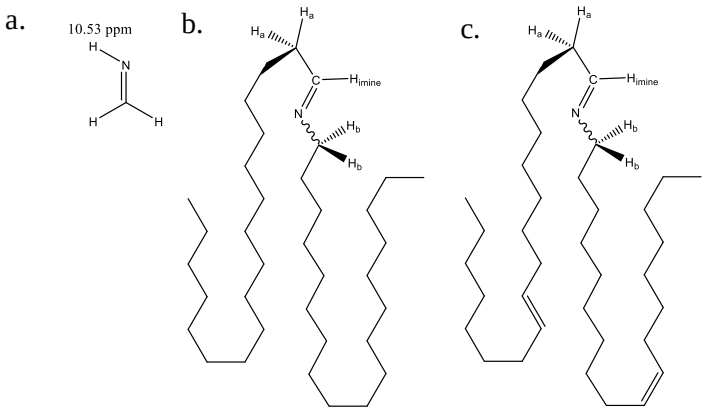

Figure 3.8: a) Methylimine. b) Hypothesized structure of imine produced by reaction A. c) Hypothesized structure of imine produced by reaction B. (H_{imine}= ~7.6 ppm, H_a= ~2.3 ppm, H_b= ~3.4 ppm)

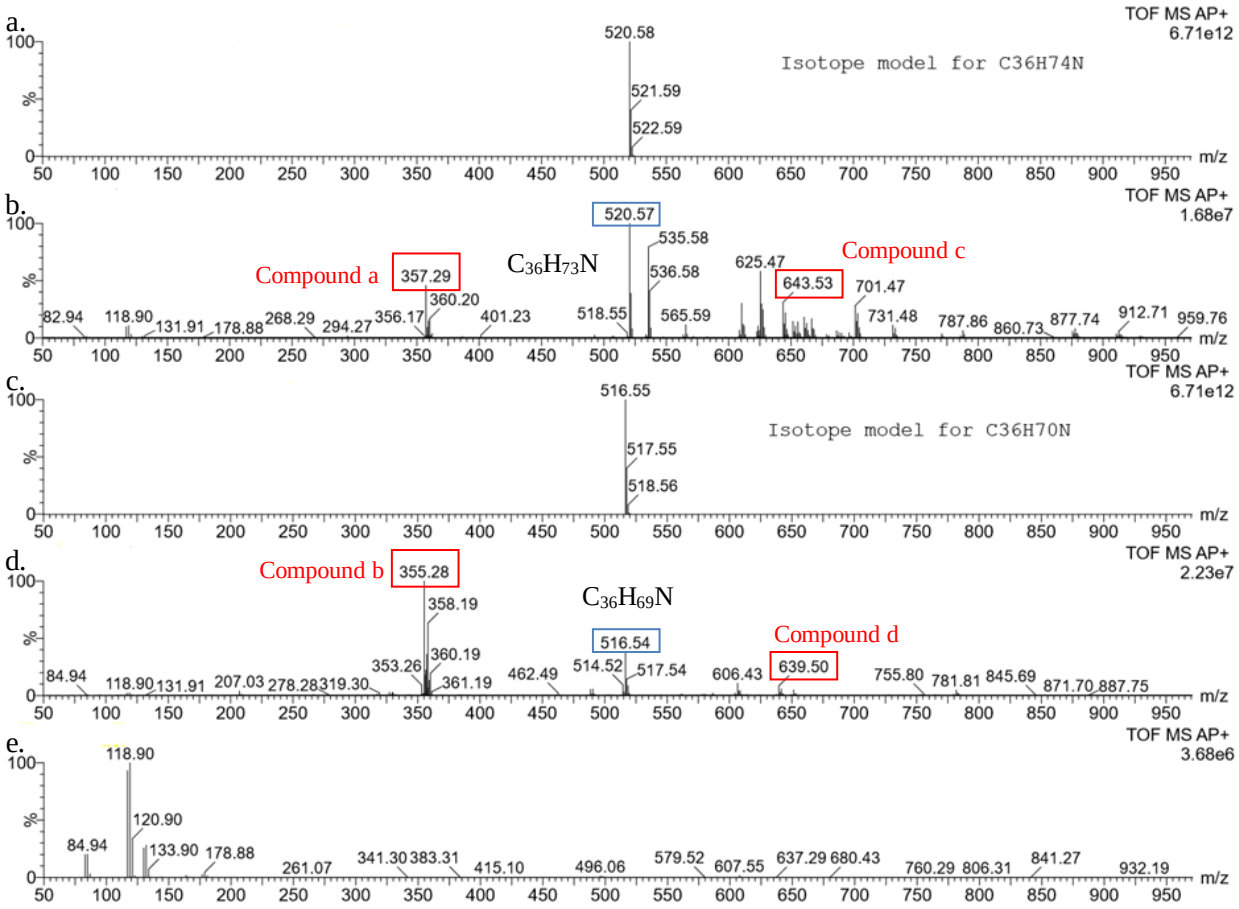

Figure 3.9: a) Simulated mass spectra of R-CH_2-CH_2-N=CH-CH_2-R (R= $C_{16}H_{33}$). b) Mass spectra of reaction A final mixture. c) Simulated mass spectra of R-CH_2-CH_2-N=CH-CH_2-R (R= $C_{16}H_{31}$). d) Mass spectra of reaction B final mixture. e) Mass spectra of chloroform (blank).

In order to confirm the proposed secondary hypothesis, LC-MS was used to measure the molecular mass of the imine. As shown in Figure 3.9, we do find compounds circled in blue that have the same molecular mass then the imines we proposed. Comparing the LC-MS data of reaction A and reaction B, we find four interesting compounds that are circled in red in Figure 3.9. We notice that the difference in molecular mass between compound **a** and compound **b** is 2 Da, whereas the difference in molecular mass between compound **c** and compound **d** is 4 Da. Considering that the difference of the molecular mass between octadecylamine (used in reaction A) and oleylamine (used in reaction B) is 2 Da, we suggested that these four compounds contain the long carbon chain of the starting alkylamides and have similar structure with each other. Unfortunately, we are unable to figure out the real structures of these four compounds at this point. Further studies are required to identify them.

3.2.2: Identification of the Gaseous Side-Products

3.2.2.1: Experimental Details

The experimental set-up is shown in Figure 3.10. In a three-neck round-bottom flask equipped with a water-cooled-condenser and kept under air-free conditions (N_2 balloon), 180 mg $InBr_3$ (0.5 mmol) are solubilized in 2 mL OLA (6.08 mmol) and 5 mL hexadecane. This mixture was degassed under vacuum for 30 min both at room temperature and at 80 ^oC. A complete dissolution of the salt is achieved by heating the solution to 210 ^oC under constant vigorous stirring within 1 min. An alkylamide precursor solution is prepared separately under air-free conditions (N_2 glove box) by reacting 0.50 mL OLA (1.5 mmol) with a mixture of 0.60 mL n-BuLi solution (2.5 M hexane solution, 1.5 mmol n-BuLi) and 0.45 mL TMEDA (3 mmol). This alkylamide solution is then injected promptly with a 6 mL syringe into the indium-OLA mixture

to initiate the reaction. 100 uL of reaction gas is extracted by syringe from reaction flask after 10 min. Gas chromatography was used to analyze the composition of the flask atmosphere.

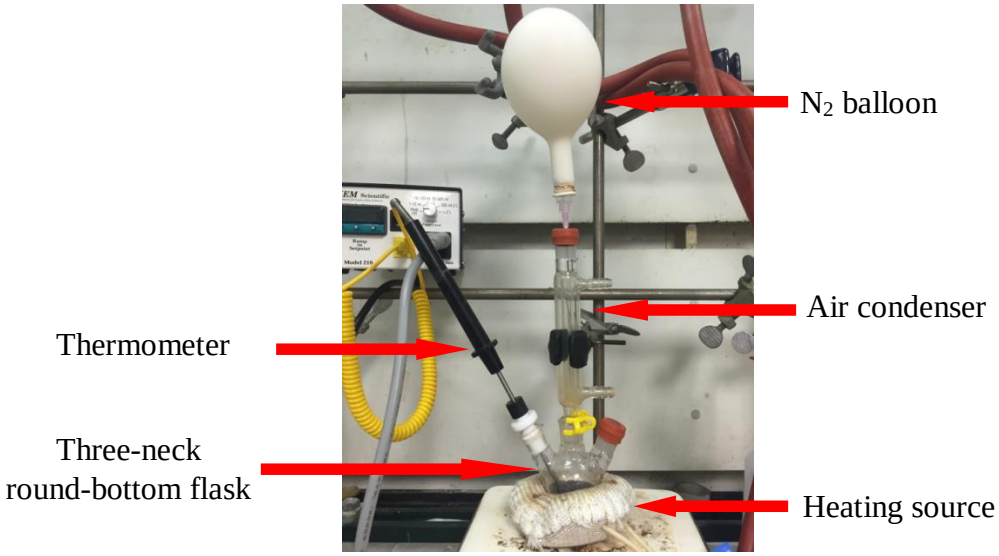

Figure 3.10: Experimental setup for the identification of the gaseous side-products.

Gas chromatography measurements were recorded on an Agilent 7820A gas chromatography. Two columns were used in series: the first one is Plot-U (Agilent) and the second one is Molsieve (Agilent). Thermal conductivity detector was employed and argon was used as the carrier gas. The method we're using starts with both columns in series (Plot-U followed by Molsieve). We flow for 10 minutes, until all of the light, "air" components are onto the Molsieve column (He, H2, N2, O2, Ar, etc.). We then fire a bypass valve that connects the Plot-U column directly to the detector. (Now all of the light things are stuck on the second column). This results in a large spike of signal at the detector due to the sudden change in pressure. We then elute all of the heavier, stickier gasses over the next several minutes. At 14.5 minutes, we fire the valve again, reconnecting both columns in series. Again, a large spike in the signal due to the pressure change. Now all of the light gasses elute. Technically there is also a simple temperature program. The temperature is kept cool (50 ^{o}C) for the first several minutes to ensure sufficient separation between the "air" and everything else. Then we ramp the temperature to the maximum (150

°C) as quickly as possible to encourage the light gasses to elute faster. Otherwise an experiment can take upwards of 45 minutes.

3.2.2.2: Experimental Results and Discussions

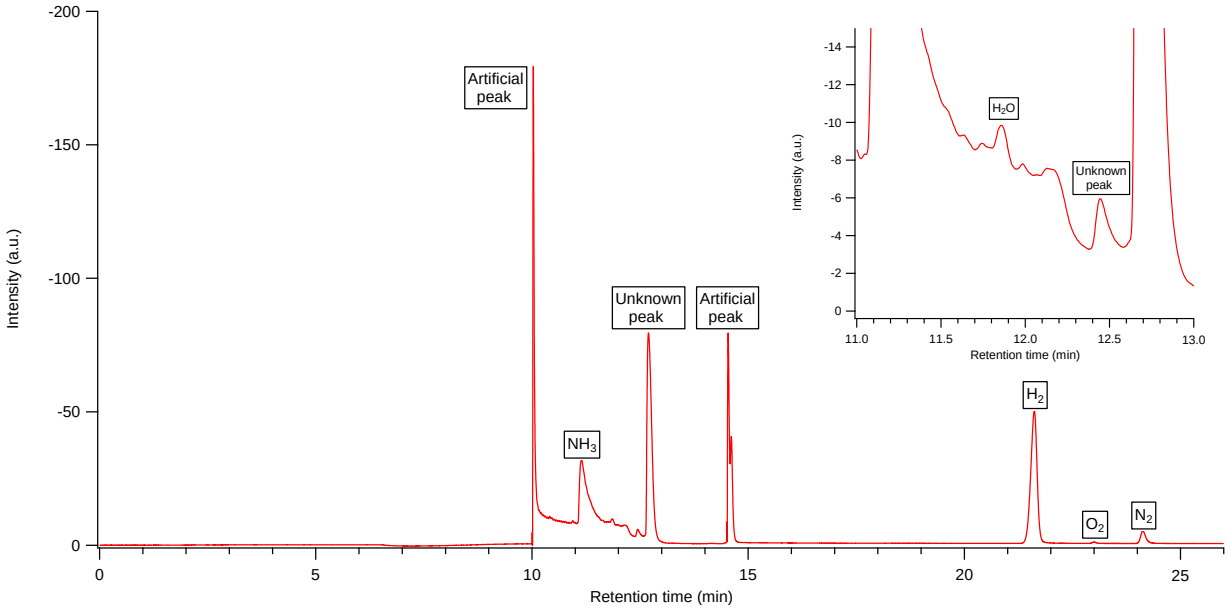

Figure 3.11: GC spectrum of the gas extracted from the headspace after the reaction ran for 10 minutes. Artificial peaks come from instrument. Inset: magnified GC spectra in the 11 to 13 minutes.

The GC spectrum of the gas extracted from the headspace after the reaction ran for 10 minutes is shown in Figure 3.11. The GC result clearly shows the formation of NH_3 and H_2, while O_2, N_2 and H_2O also appear. The amount of each gas component cannot be quantified directly by comparing their peak areas in GC spectrum, because of the different impacts of each gas on thermal conductivity as they elute off the column. For example, since H_2 has a very different thermal conductivity then the carrier gas argon, even slight amounts of H_2 can give rise to large signals in the GC spectrum. Table 3.2 lists the thermal conductivities of gases as a function of temperature. In the GC spectrum, the O_2 and H_2O peaks are very small, compared with the NH_3 peak. Considering that NH_3, O_2 and H_2O have similar thermal conductivities, the existence of O_2 and water may be caused by the leakage of our reaction system, or leakage of the syringe used to

transfer gas to GC instrument. And for N_2, because we use N_2 as the protective gas in our reaction, so it is reasonable to see N_2 peak. We also noticed two peaks labeled as unknown peak. Further studies are required to identify them. But, at least we can conclude our approach can produce NH_3 and H_2, and O_2, N_2 and H_2O are not side products.

Table 3.2: Thermal conductivity of gases as a function of temperature. (Unless otherwise noted, the values refer to a pressure of 100 kPa (1 bar) or to the saturation vapor pressure if that is less than 100 kPa) [4, 5]

Units: mW/m K (milliwatts per meter kelvin)

Name	100K	200K	300K	400K	500K
Air	9.4	18.4	26.2	33.3	39.7
Argon	6.2	12.4	17.9	22.6	26.8
Ammonia	-	-	24.4	37.4	51.6
Oxygen	9.3	18.4	26.3	33.7	41.0
Hydrogen	68.6	131.7	186.9	230.4	-
Nitrogen	9.8	18.7	26.0	32.3	38.3
Water	-	-	18.7	27.1	35.7

3.3: Hypothesized Reaction Mechanism

Before we reported this SLS approach, people usually prepared colloidal InN by treatment of indium salt (such as $InBr_3$, In_2S_3) with sodium amide ($NaNH_2$). [6, 7] In 1994, Purdy synthesized $In(NH_2)_3$ from a reaction between InI_3 and 3 equiv of KNH_2 in anhydrous liquid ammonia at 25 ^oC, then thermolysis of $In(NH_2)_3$ can afford indium nitride. [2] These methods suggest NH_2^- may react with In^{3+} first to form intermediate containing In-NH_2 bond, then decompose to form InN. In Buhro's approach to prepare indium phosphide, though neither PH_3 nor PH_2^- were used as starting materials, In-PH_2 bond formed during reaction. [1] Considering our approach can produce NH_3 as side product, we think In-NH_2 bond also forms during the reaction, then decompose, resulting in the formation of InN and ammonia. If this is the case, three possible scenarios

(Figure 3.12) are responsible for the formation of InN and ammonia, due to two types of amide (NH_2^- and oleylamide) existing in our reaction condition.

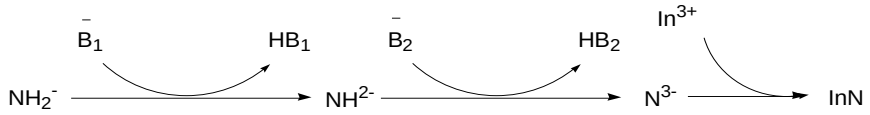

Scenario 1: B_1=B_2=NH_2^-

Scenario 2: B_1=NH_2^-, B_2=R-CH_2-NH^-

Scenario 3: B_1=B_2=R-CH_2-NH^-

Figure 3.12: Three possible scenarios of InN formation.

Because TMEDA is not a necessary reagent in our approach, oleylamide or oleylamine is the nitrogen precursor of both InN and the secondary imine (R-CH=N-CH_2-R, R=$CH_3(CH_2)_7CH=(CH_2)_8$). Comparison between the structure of this secondary imine (R-CH=N-CH_2-R, R=$CH_3(CH_2)_7CH=(CH_2)_8$) with that of its precursor, oleylamide or oleyamine, indicates the formation of the secondary imine is the result of the breakage of C-N bond and the loss of NH_2^-. For reference, the secondary imine can be prepared through the reaction between a primary amine and an unstable intermediate primary aldimine, which may be the pathway to form the important NH_2^- species. [8-11] This transformation is demonstrated in Figure 3.13.

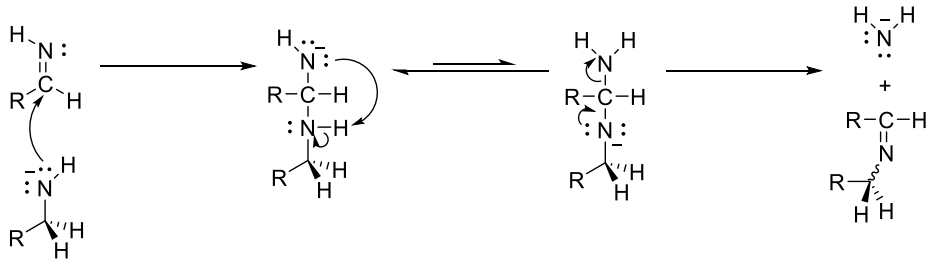

R=$CH_3(CH_2)_7CH=(CH_2)_8$

Figure 3.13: Transformation from primary aldimine to secondary imine.

Due to the extremely instablity of aldimine, this transformation is extremely fast, making it difficult to prove the existence of aldimine. For the NH_2^- species, though we cannot give solid evidence right now, we do see some special things which may indicate its existence. When we

heated the mixture of oleylamine and oleylamide to 210 ^{o}C for 4 hours, we saw only 10% oleylamide were converted to the secondary imine (Figure 3.14, experimental details are in Appendix B). Meanwhile, a single peak located at 8.05 ppm appears which we never see in previous final reaction mixture of our approach, as shown in the inset of Figure 3.14. A heat-up synthesis experiments were further conducted (experimental details are in Appendix B). In this heat-up synthesis experiments, oleylamide solution was injected to In(III)-OLA solution at room temperature, then this mixture was heated to 60 ^{o}C and 175 ^{o}C, respectively. When the reaction mixture stayed at 60 ^{o}C for 40 minutes, we saw a single peak which is downfield shifted to 8.52 ppm, compared with the single peak of the mixture of only oleylamine and oleylamide. This shift may be attributed to the presence of In^{3+}, which has a stronger deshielding effect than Li^{+} due to its stronger electron affinity. Besides, neither $In^{(0)}$ nor InN formed in this condition(Figure 3.15.a). While when the reaction mixture stayed at 175 ^{o}C for 20 minutes, we did not see this single peak, but both $In^{(0)}$ and InN formed(Figure 3.15.b). As mention previously, NH_2^- is responsible for the formation of InN. Hence, we suspect this single peak belongs to NH_2^- whose chemical shift would be changed by the atom combined with it, so the disappearance of this single peak at 175 ^{o}C condition is attributed to the consumption of NH_2^-. When the reaction temperature is low (60 ^{o}C), formation of InN by consuming NH_2^- is so hard that we can see the single peak. Further study will be undertaken to confirm it.

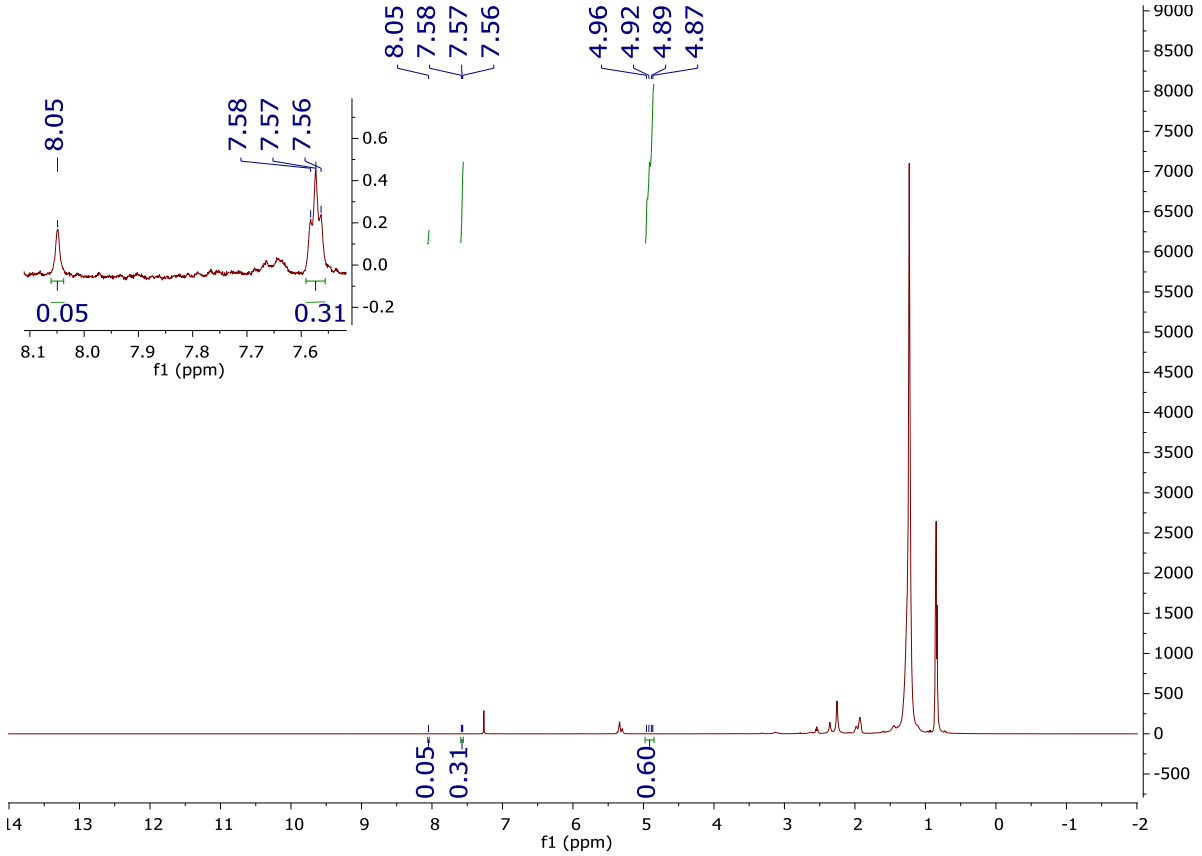

Figure 3.14: ^{1}H NMR of the final liquid obtained from the reaction between oleylamine and oleylamide. Inset is the magnified ^{1}HNMR spectrum at the range of 7.5-8.1 ppm.

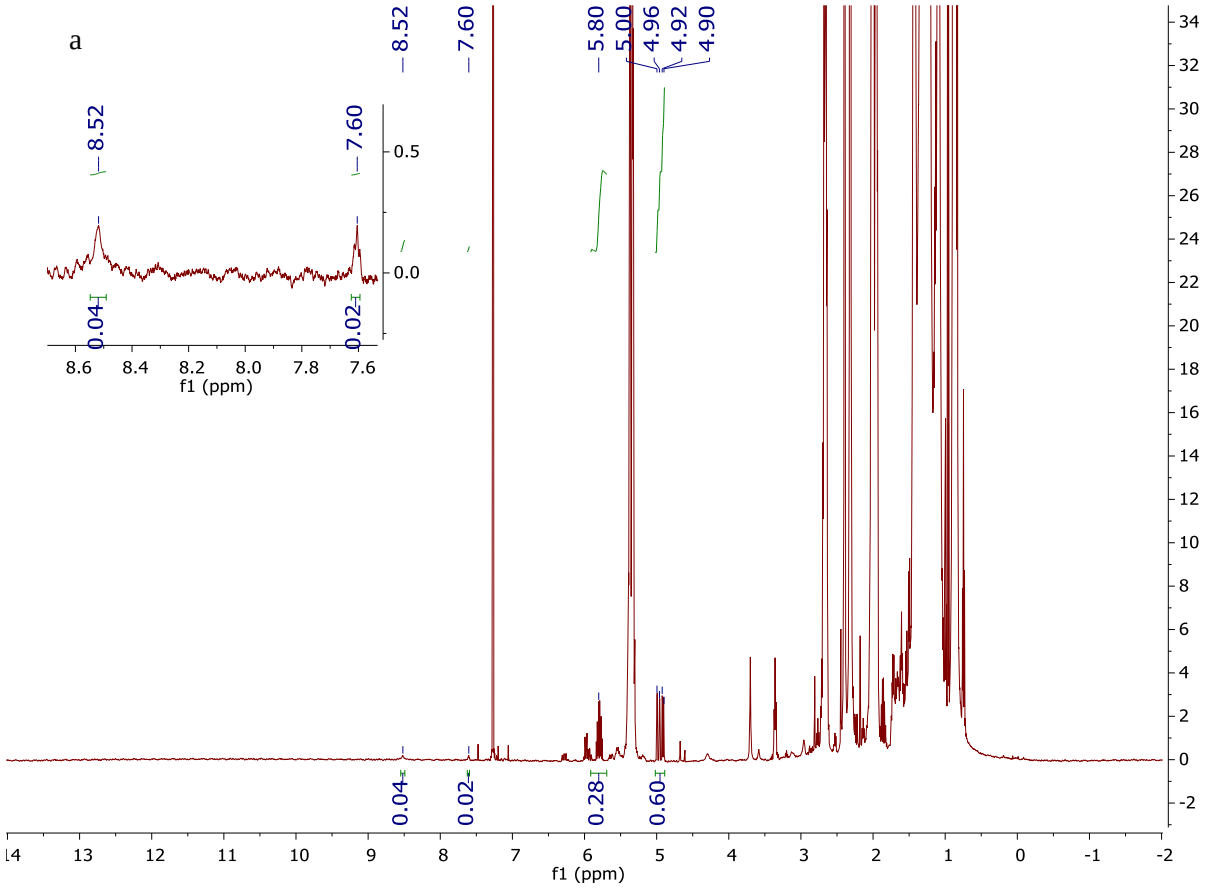

Figure 3.15: (a) ^{1}H NMR of the final liquid obtained from the heat-up synthesis reaction conducted at 60^{o}C. Inset is the magnified ^{1}H NMR spectrum at the range of 7.5-8.7 ppm. (b) ^{1}H NMR of the final liquid obtained from the heat-up synthesis reaction conducted at 175^{o}C. Inset is the magnified ^{1}HNMR spectrum at the range of 7.5-8.7 ppm.

Figure 3.15 (cont'd)

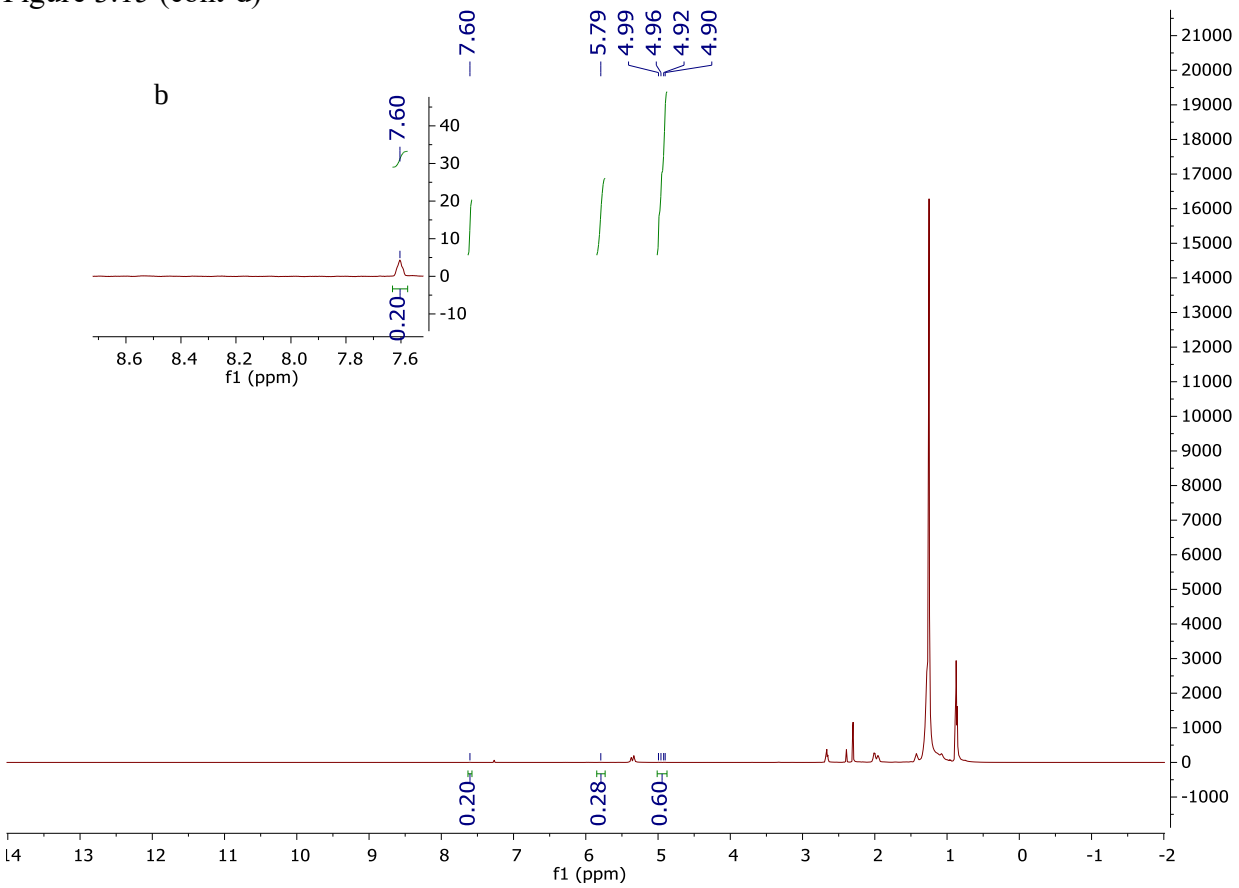

The formation rate of the secondary imine is very slow in the reaction between oleylamine and oleylamide. But the addition of $InBr_3$-OLA mixture to this oleylamine-oleylamide mixture at 210 ^oC can readily initiate the formation of the secondary imine ($In^{(0)}$ and InN also form, experimental details are in Appendix B). For this acceleration, we think In^{3+}, as a lewis acid, has a good ability to store hydride which can push this conversion forward as depicted in Figure 3.16. [12, 13] This stored hydride undergoes two possible pathways to produce H_2 (Figure 3.17). One possible pathway can reduce In^{3+} to form H_2. The other possible pathway is to react with proton to form H_2.

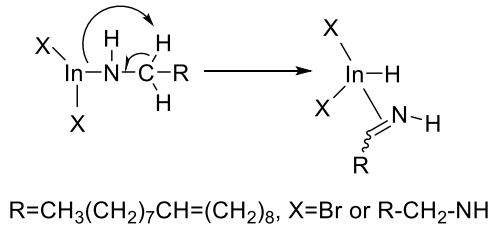

Figure 3.16: Possible mechanism to form primary aldimine.

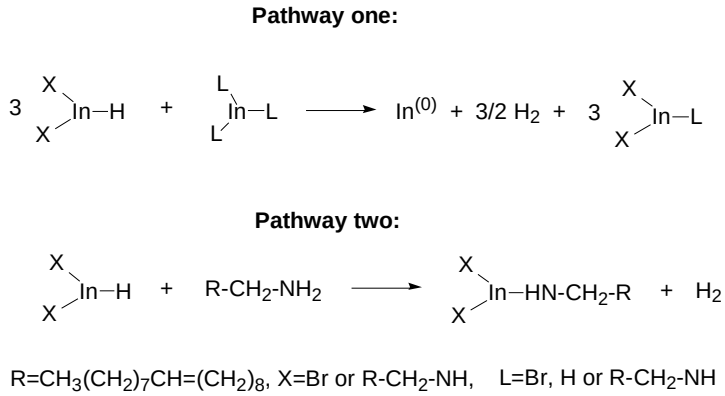

Figure 3.17: Possible pathways to form H_2 and $In^{(0)}$.

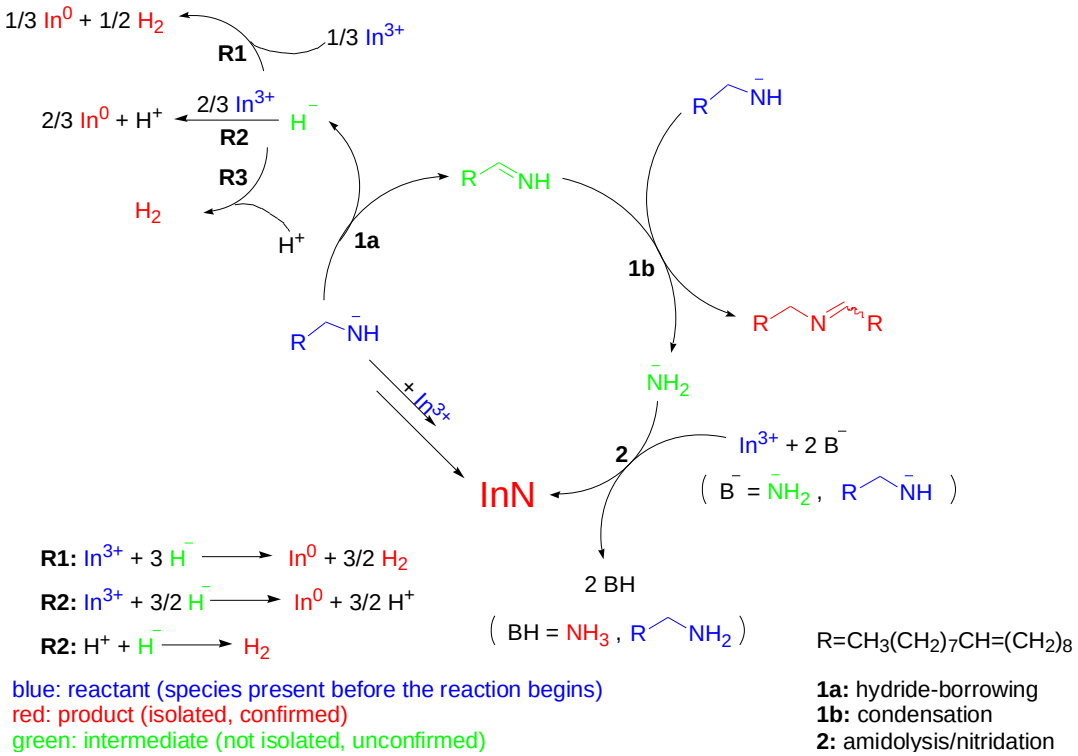

Figure 3.18: Mechanistic overview of InN formation from alkylamides.

Figure 3.18 demonstrates the mechanistic overview of InN formation from alkylamide. Injection of alkylamide at 210 ºC would initiate the conversion from oleylamide to primary aldimine, resulting in the formation of hydride, which would reduce In^{3+} to $In^{(0)}$ and form H_2 eventually. At the same time, primary aldimine would react with olelyamide immediately to produce NH_2^- species, which would further react with In^{3+} to form a complex. This complex can easily decompose in this condition to form InN and NH_3.

3.4: Conclusion

In this chapter, the side products of our approach have been investigated. We have confirmed three side products besides $In^{(0)}$, which are NH_3, H_2 and secondary imine (R-CH=N-CH_2-R, R=$CH_3(CH_2)_7CH=(CH_2)_8$). We also proposed a possible mechanism to elucidate this approach.

APPENDIX

Quantification of the Amount of Imine Formed.

A typical quantification procedure is described as following: In a three-neck round-bottom flask equipped with a water-cooled-condenser and kept under air-free conditions (N_2 Schlenk line), 180 mg $InBr_3$ (0.5 mmol) are solubilized in 2 ml of oleylamine (6.08 mmol), 96 ul of octadecene (0.3 mmol) and 5 ml of hexadecane. A complete dissolution of the salt is achieved by heating the solution to 210 ^oC under constant vigorous stirring. An alkylamide precursor solution is separately prepared under air-free conditions (N_2 glove box) by reacting 0.50 ml of OLA (1.5 mmol) with a mixture of 0.60 ml of a n-BuLi solution (2.5 M hexane solution, 1.5 mmol n-BuLi) and 0.45 ml TMEDA (3 mmol). This alkylamide solution is then injected promptly with a 6 ml syringe into the indium-OLA mixture to initiate the reaction. The reaction is stopped after 30 minutes by removing the heat source and letting the solution cool down to room temperature. A small amount of resulting solution is directly dissolved in deuterated chloroform for NMR measurements.

Results: 0.52 mmol imine was formed (Figure B.1).

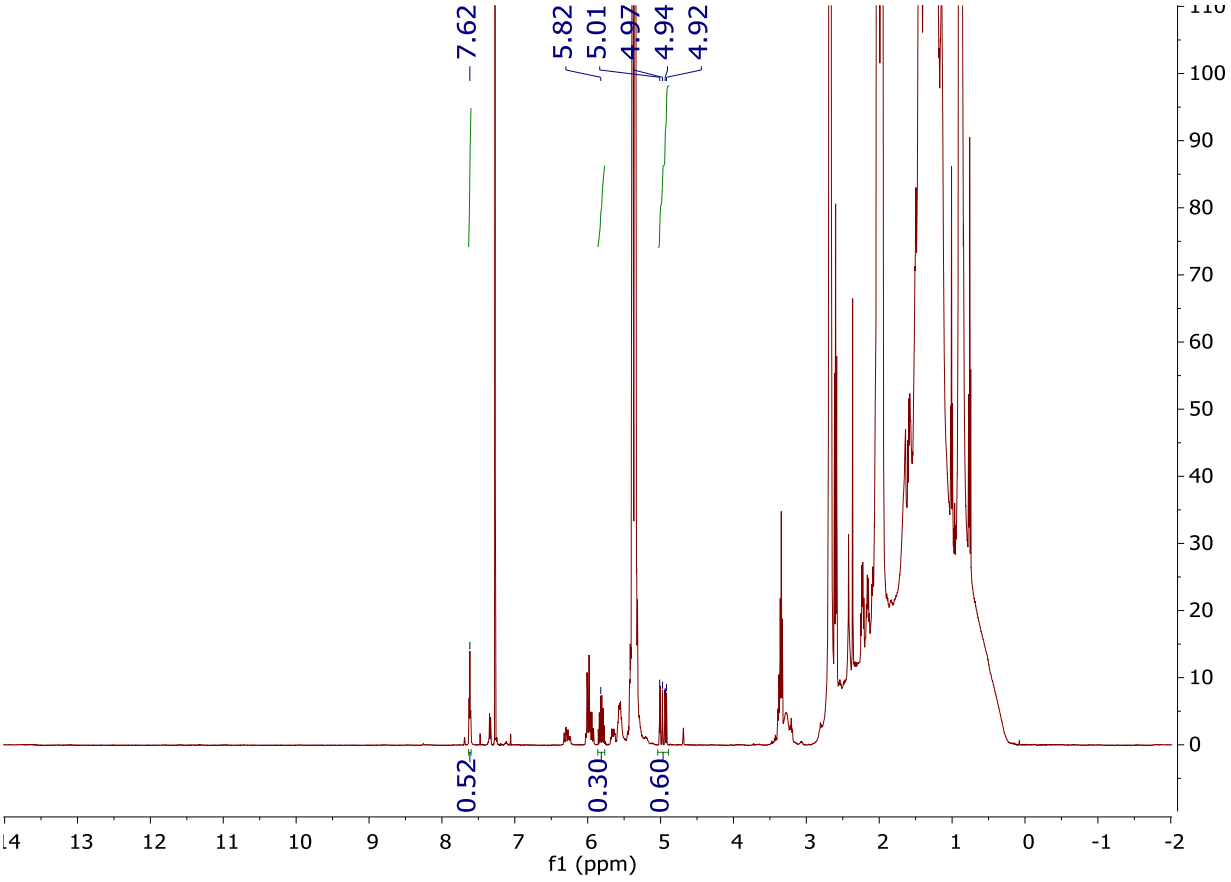

Figure B.1: ^{1}H NMR of final liquid.

Heat-up synthesis.

In a three-neck round-bottom flask equipped with a water-cooled-condenser and kept under air-free conditions (N_2 Schlenk line), 180 mg $InBr_3$ (0.5 mmol) are solubilized in 2 ml of oleylamine (6.08 mmol), 96 ul of octadecene and 5 ml of hexadecane. A complete dissolution of the salt is achieved by heating the solution to 210 ºC under constant vigorous stirring, then cool back to room temperature. An alkylamide precursor solution is separately prepared under air-free conditions (N_2 glove box) by reacting 0.50 ml of OLA (1.5 mmol) with a mixture of 0.60 ml of a n-BuLi solution (2.5 M hexane solution, 1.5 mmol n-BuLi) and 0.45 ml TMEDA (3 mmol). This alkylamide solution is then injected promptly with a 6 ml syringe into the indium-OLA mixture at room temperature. Then the reaction mixture is heat to certain temperature.

Results: Heat-up synthesis experiment is conducted at different temperature: (1) room temperature for 40 minutes. (3) 60 ºC for 90 minutes. (2) 120 ºC for 40 minutes. (3) 175 ºC for 20 minutes.

Room temperature for 90 minutes. Injection of amide into In(III)-OLA mixture at room temperature can increase temperature. The reaction mixture is light yellow gel and very viscous. We do see an extremely low intensity imine peak (the amount is smaller than 0.02 mmol, as shown in Figure B.2.1), which can be thought negligible. And when this reaction mixture is heated to 60 ºC, it can be converted to clear transparent liquid, indicating neither $In^{(0)}$ nor InN were formed.

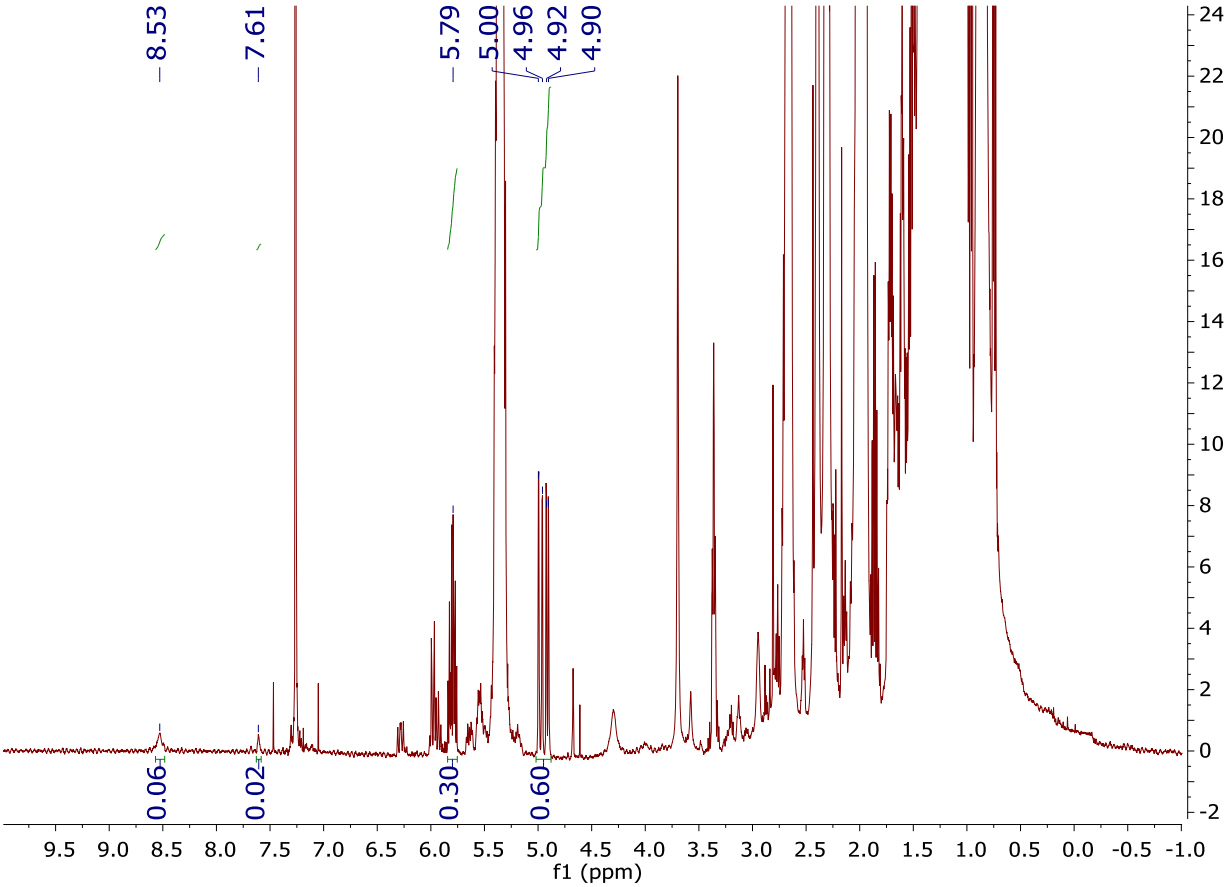

Figure B.2.1: ^{1}H NMR of reaction mixture.

60 °C for 40 minutes. The reaction mixture is clear transparent liquid. An extremely low intensity imine peak (the amount is smaller than 0.02 mmol, as shown in Figure B.2.2), which can be thought negligible, appear. $In^{(0)}$ and InN were not formed.

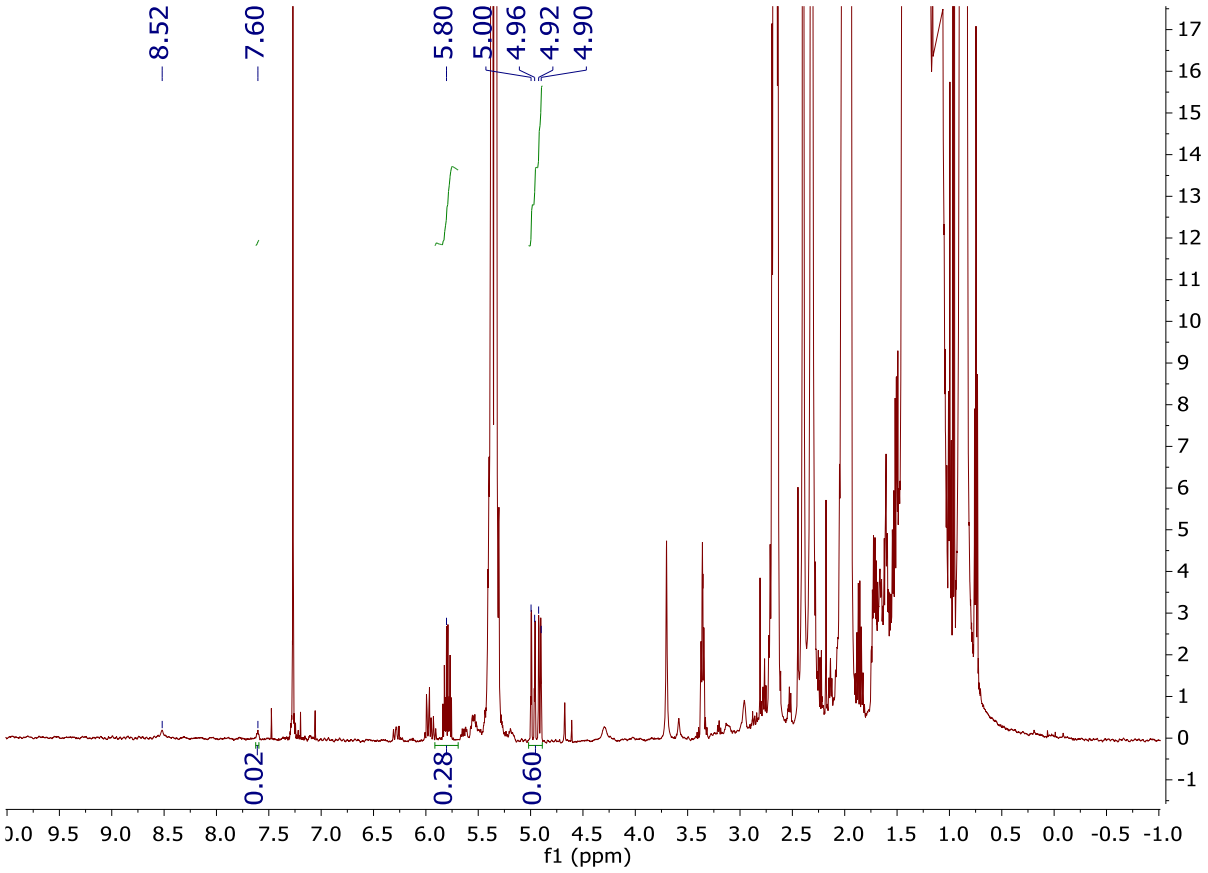

Figure B.2.2: ^{1}H NMR of reaction mixture.

140 °C for 40 minutes. The reaction mixture is black. 0.09 mmol of imine was produced (Figure B.2.3). XRD shows In(0) was formed, but it is hard to tell whether InN was formed (Figure B.2.4).

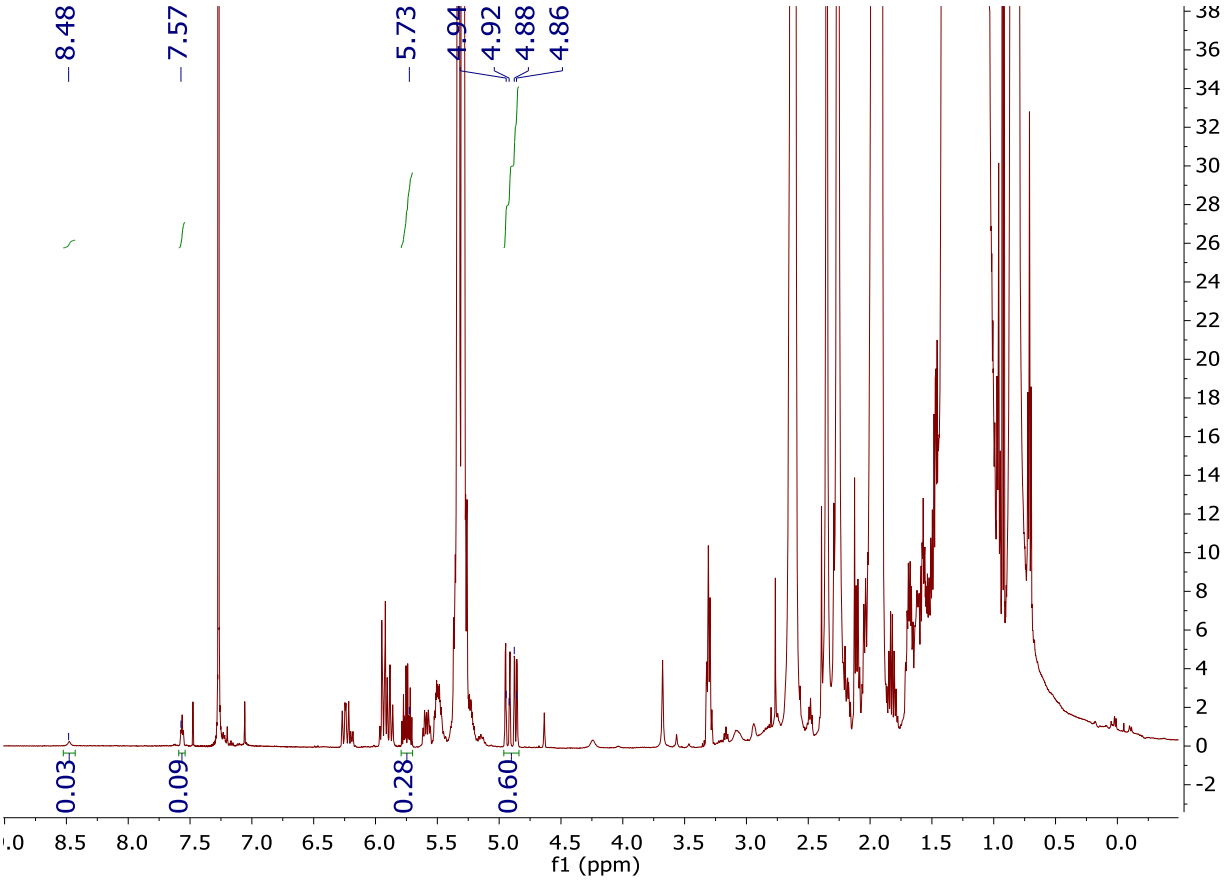

Figure B.2.3: ^{1}H NMR of reaction mixture.

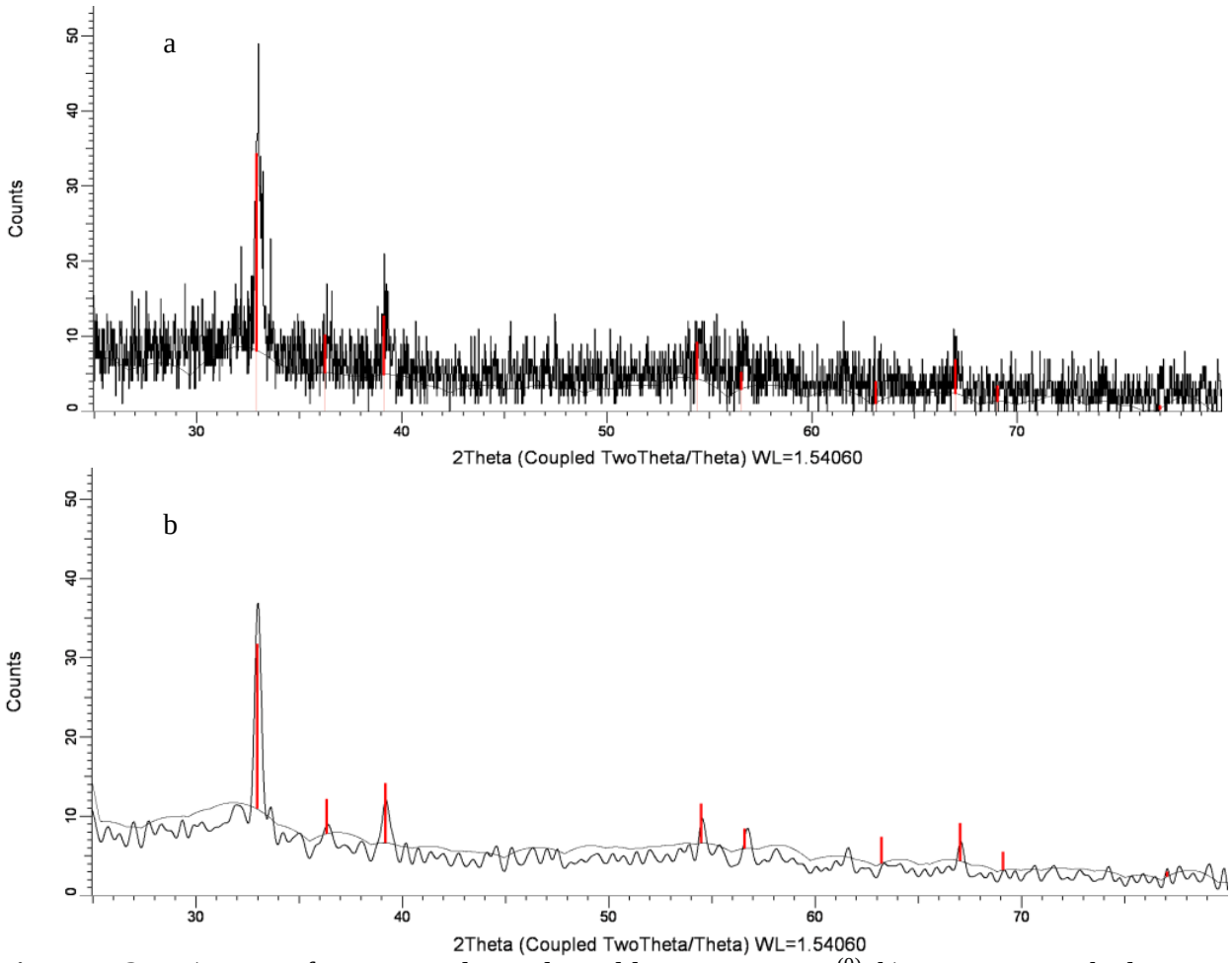

Figure B.2.4: a) XRD of as-prepared sample, red line represent $In^{(0)}$. b) Fourier smoothed XRD of as-prepared sample.

175 °C for 20 minutes. The amount of imine formed is 0.20 mmol, as shown in Figure B.2.5. The reaction can produce $In^{(0)}$ and InN, as shown in Figure B.2.6. TEM images of as-prepared and after-treated sample were shown in Figure B.2.7 and Figure B.2.8, respectively.

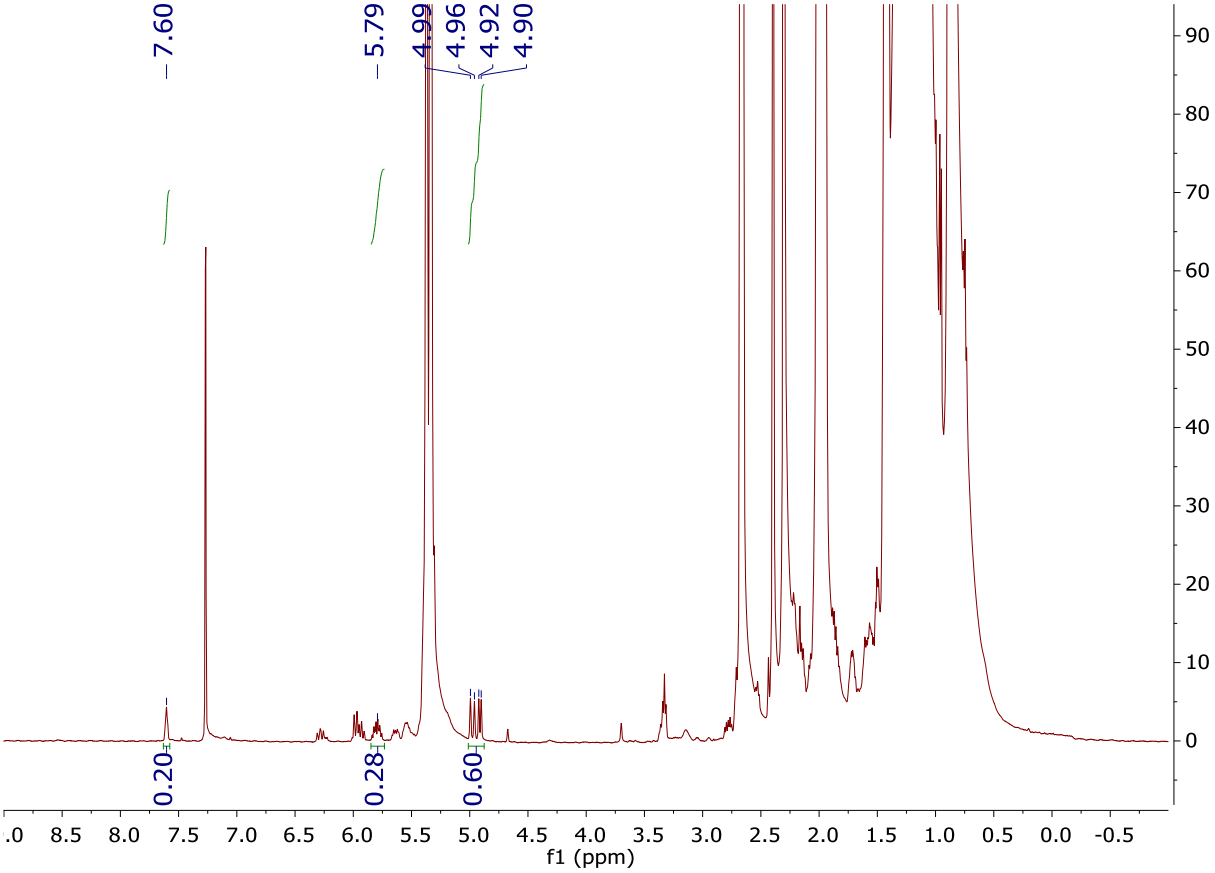

Figure B.2.5: ^{1}H NMR of reaction mixture.

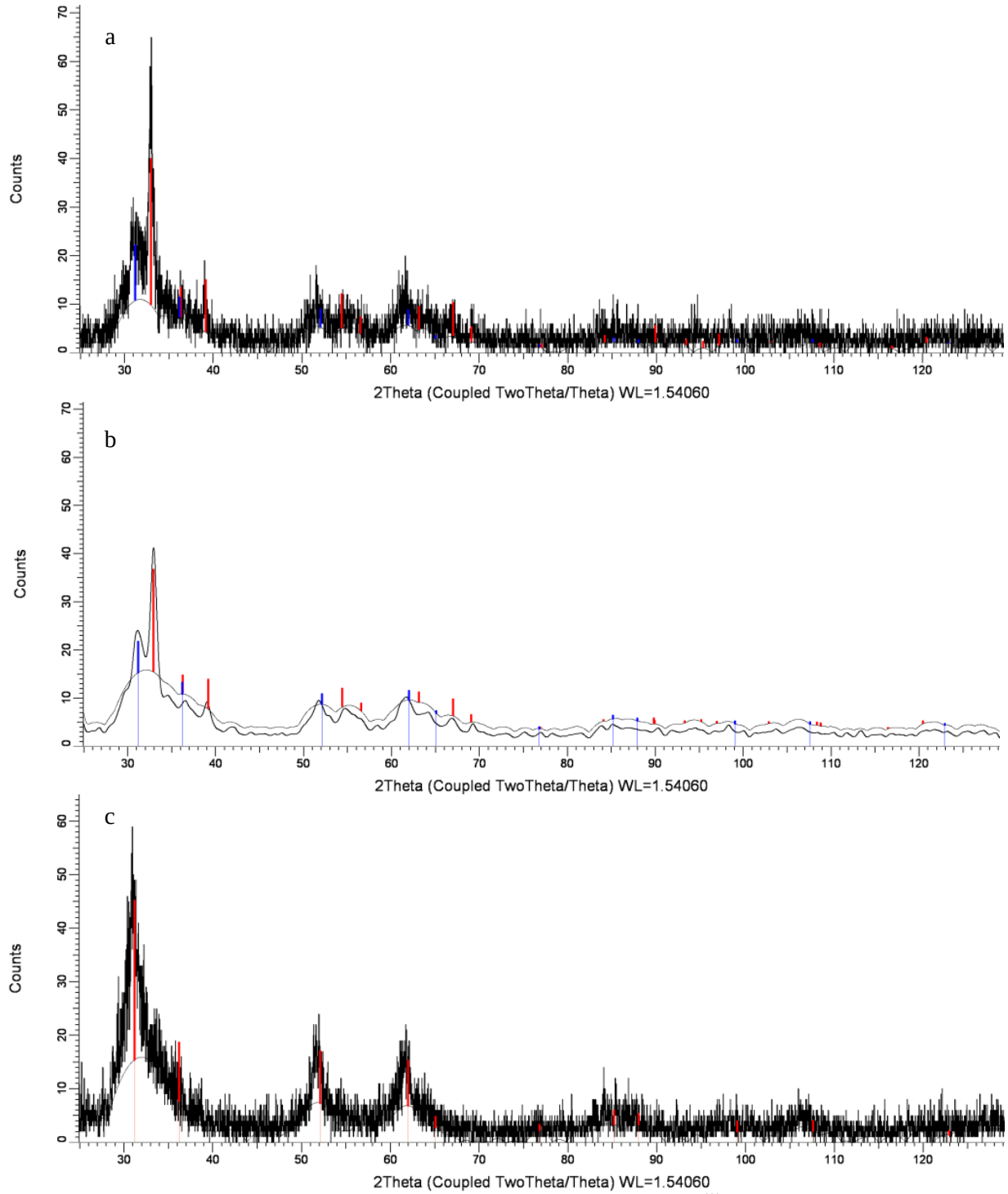

Figure B.2.6: a) XRD of as-prepared sample, red lines represent $In^{(0)}$, blue lines represent InN. b) Fourier smoothed XRD of as-prepared sample, red lines represent $In^{(0)}$, blue lines represent InN. c) XRD of after-treated sample, red lines represent InN. d) Fourier smoothed XRD of as-prepared sample, red lines represent InN.

Figure B.2.6 (cont'd)

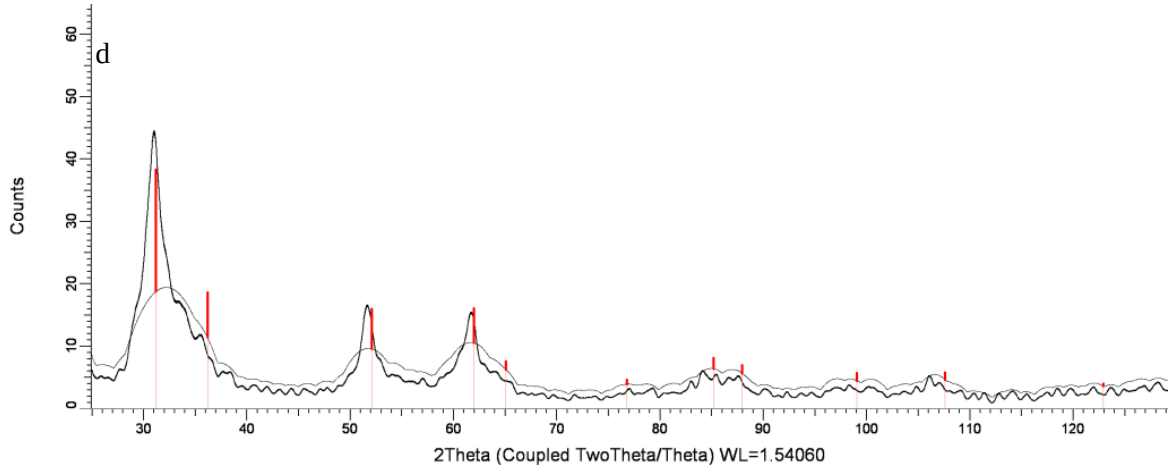

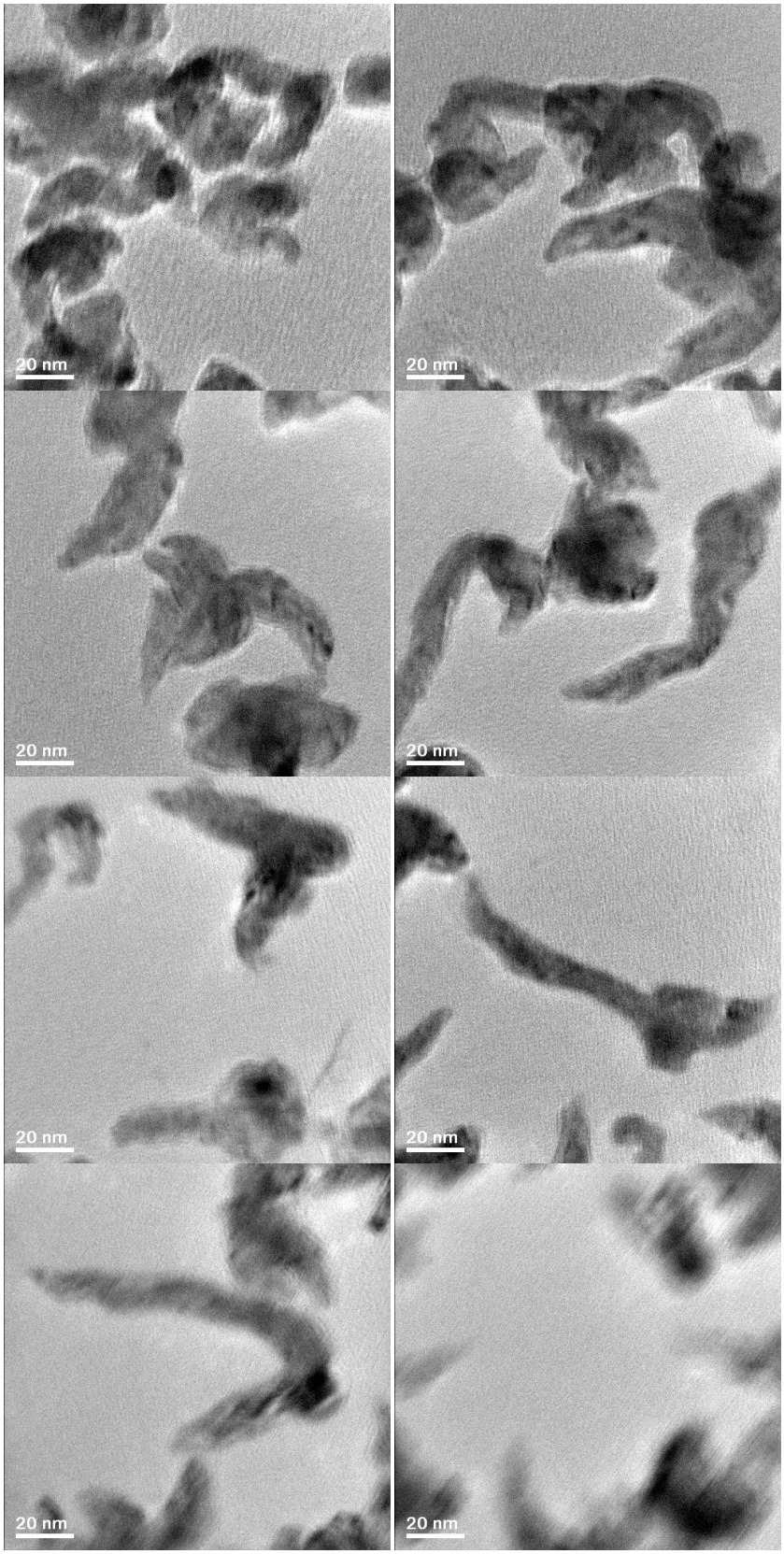

Figure B.2.7: TEM images of as-prepared sample.

Figure B.2.7 (cont'd)

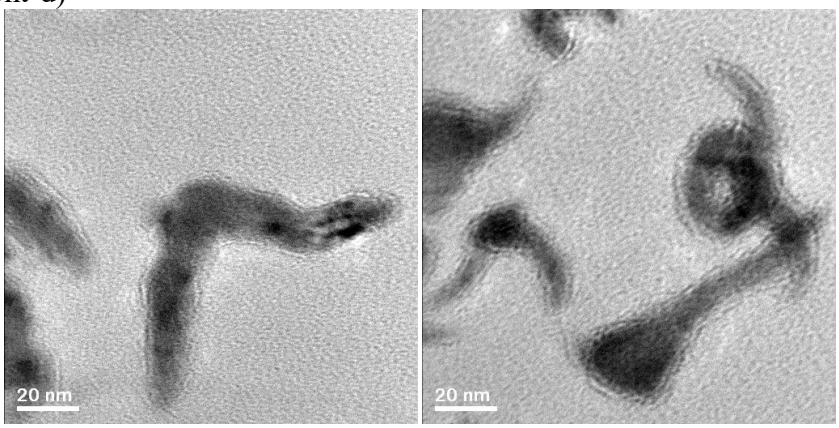

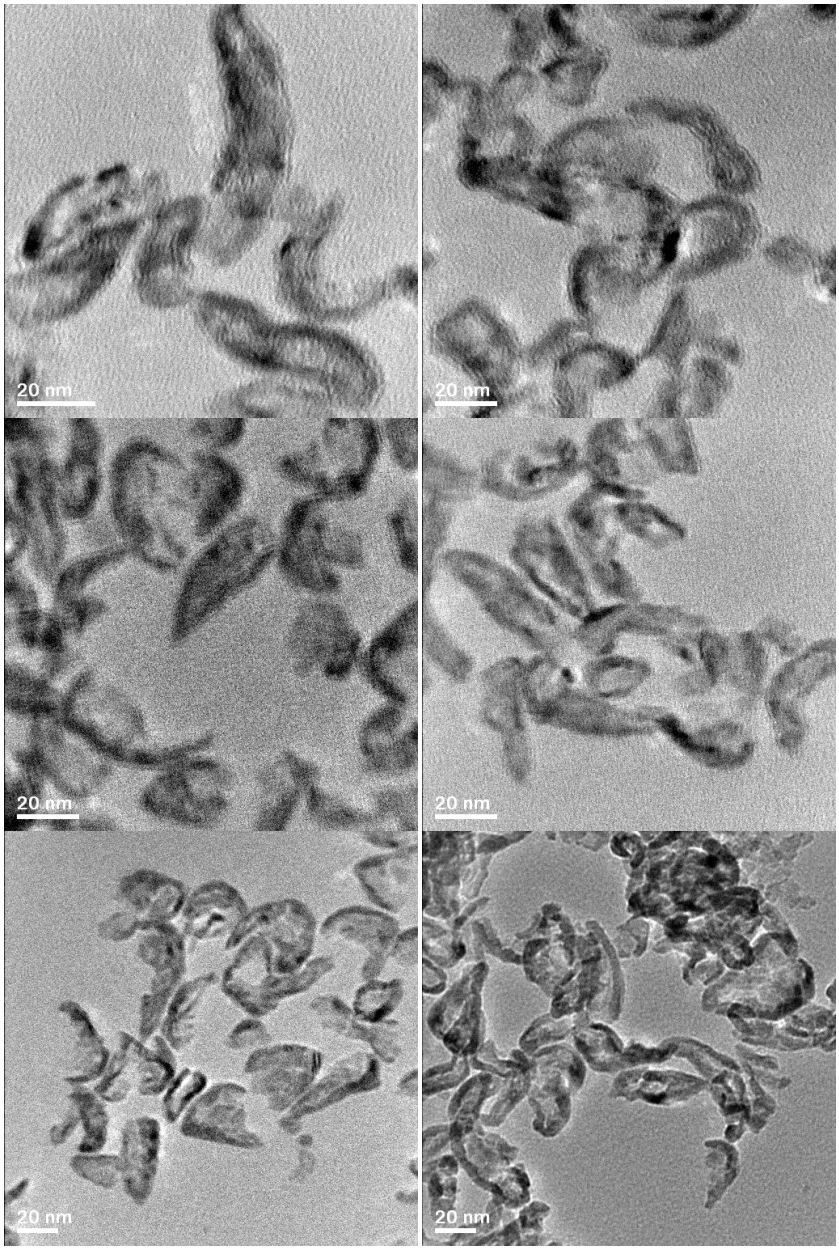

Figure B.2.8: TEM images of acid-treated sample.

Injection Temperature Dependence.

In a three-neck round-bottom flask equipped with a water-cooled-condenser and kept under air-free conditions (N_2 Schlenk line), 180 mg $InBr_3$ (0.5 mmol) are solubilized in 2 ml of oleylamine (6.08 mmol), 96 ul of octadecene (0.3 mmol) and 5 ml of hexadecane. A complete dissolution of the salt is achieved by heating the solution to certain temperature under constant

vigorous stirring. An alkylamide precursor solution is separately prepared under air-free conditions (N_2 glove box) by reacting 0.50 ml of OLA (1.5 mmol) with a mixture of 0.60 ml of a n-BuLi solution (2.5 M hexane solution, 1.5 mmol n-BuLi) and 0.45 ml TMEDA (3 mmol). This alkylamide solution is then injected promptly with a 6 ml syringe into the indium-OLA mixture to initiate the reaction. The reaction is stopped after 30 minutes by removing the heat source and letting the solution cool down to room temperature. A small amount of resulting solution is directly dissolved in deuterated chloroform for NMR measurements.

Results: Injection temperature dependence experiment is conducted at different temperature: (1) 250 ^oC for 30 minutes. (2) 230 ^oC for 30 minutes. (3) 210 ^oC for 30 minutes.

250 ^oC for 30 minutes. Figure B.3.1 clear shows the formation of $In^{(0)}$ and an extremely low intensity (111) InN peak, which indicating almost no InN was formed. And we find 0.69 mmol Imine was produced (Figure B.3.2).

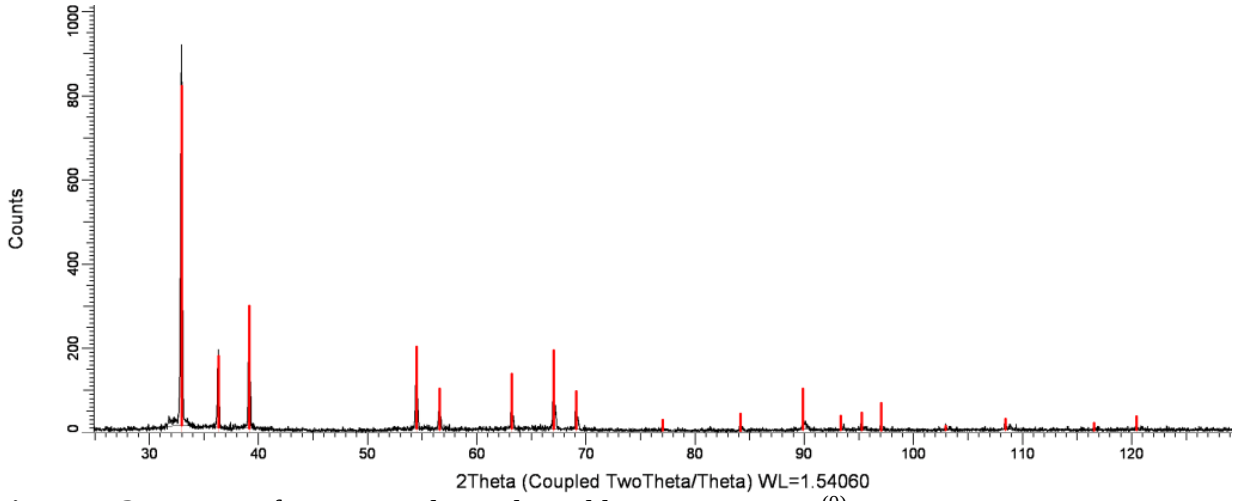

Figure B.3.1: XRD of as-prepared sample, red lines represent $In^{(0)}$.

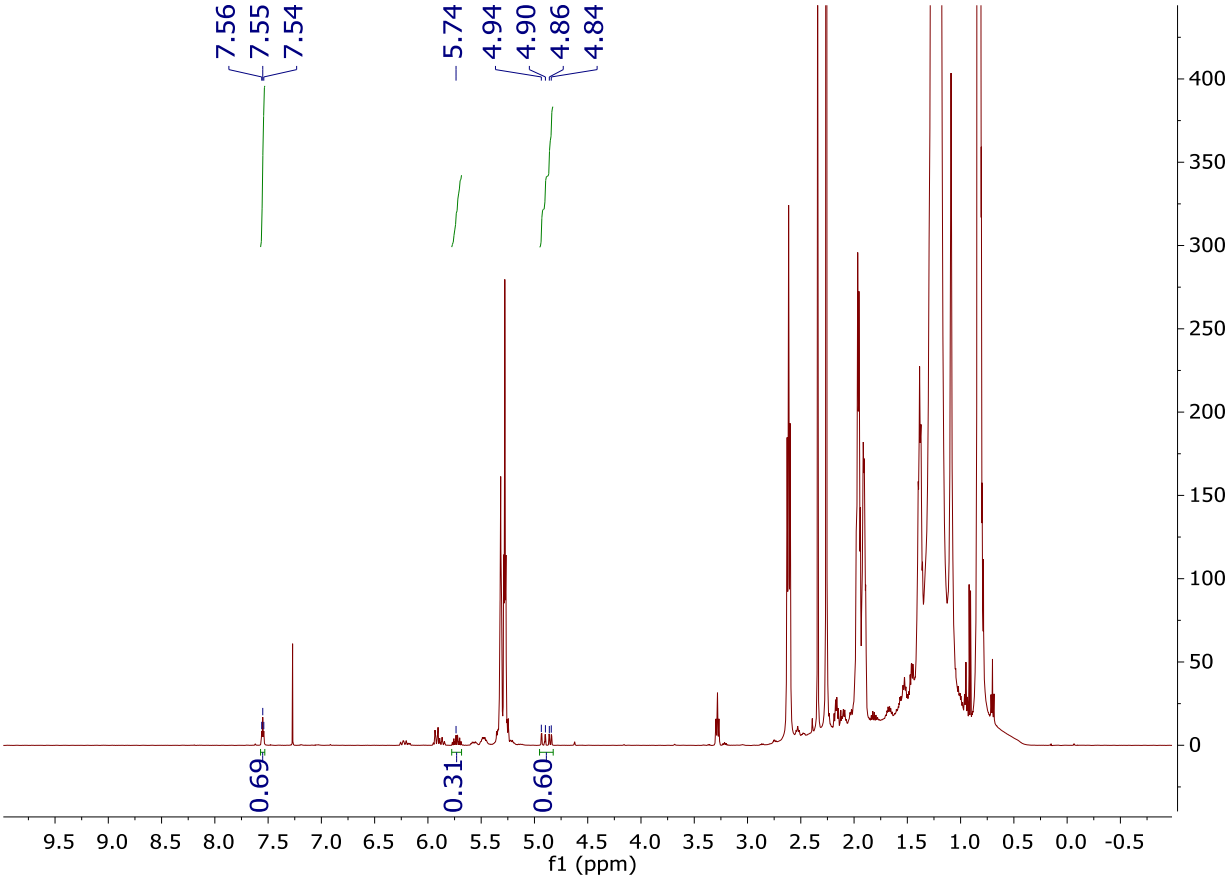

Figure B.3.2: ^{1}H NMR of reaction mixture.

230 ºC for 30 minutes. Though this reaction also produce a negligible amount of InN (Figure B.3.3), compared with the reaction conducted in 250 ºC, more InN was formed. And we do see the amount of Imine formed decrease to 0.6 mmol (Figure B.3.4).

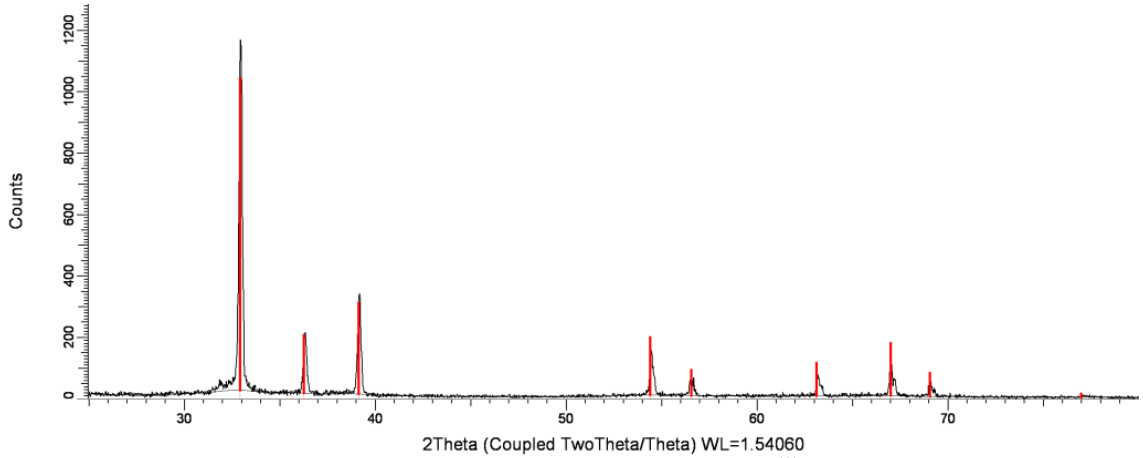

Figure B.3.3: XRD of as-prepared sample, red lines represent $In^{(0)}$.

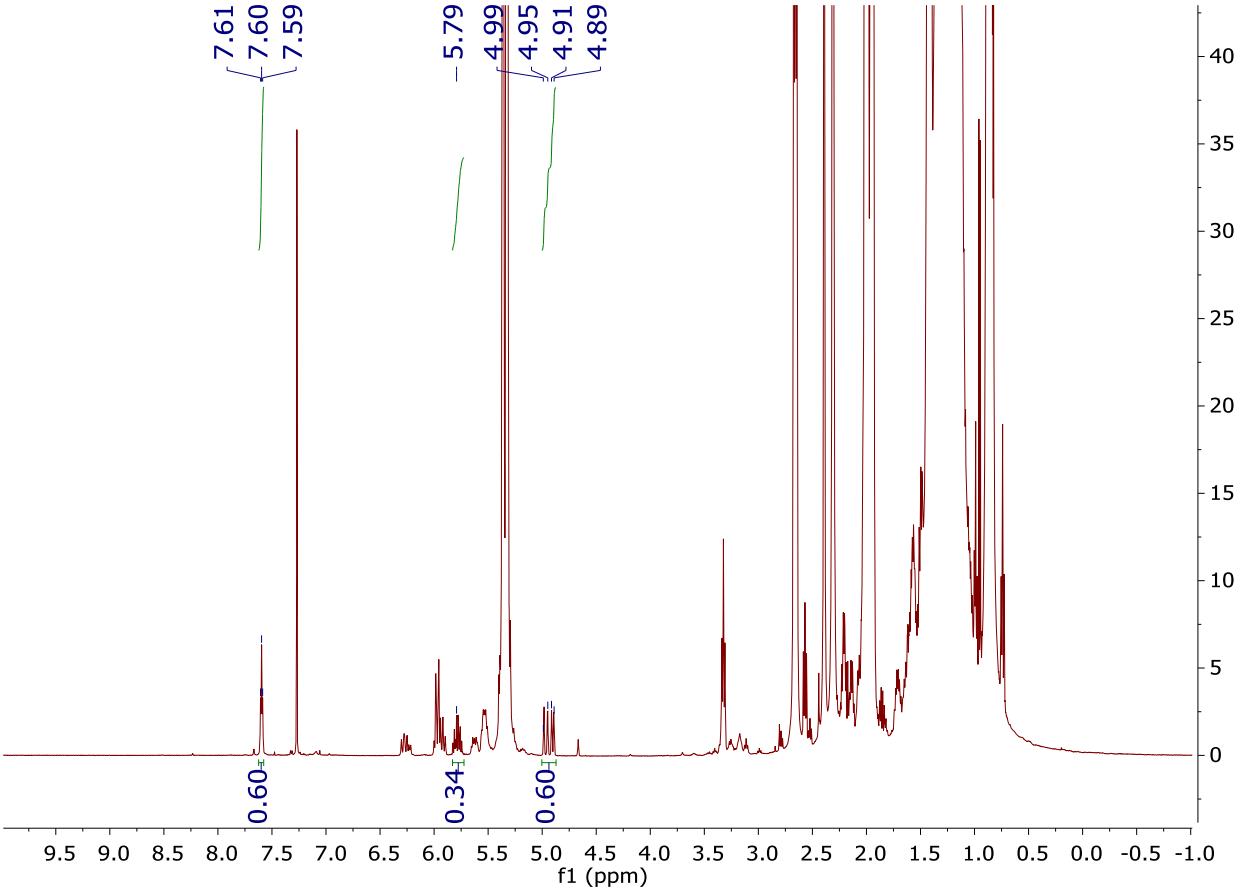

Figure B.3.4: ^{1}H NMR of reaction mixture.

210 °C for 30 minutes. In this reaction, 0.52 mmol Imine was formed (Figure B.3.5).

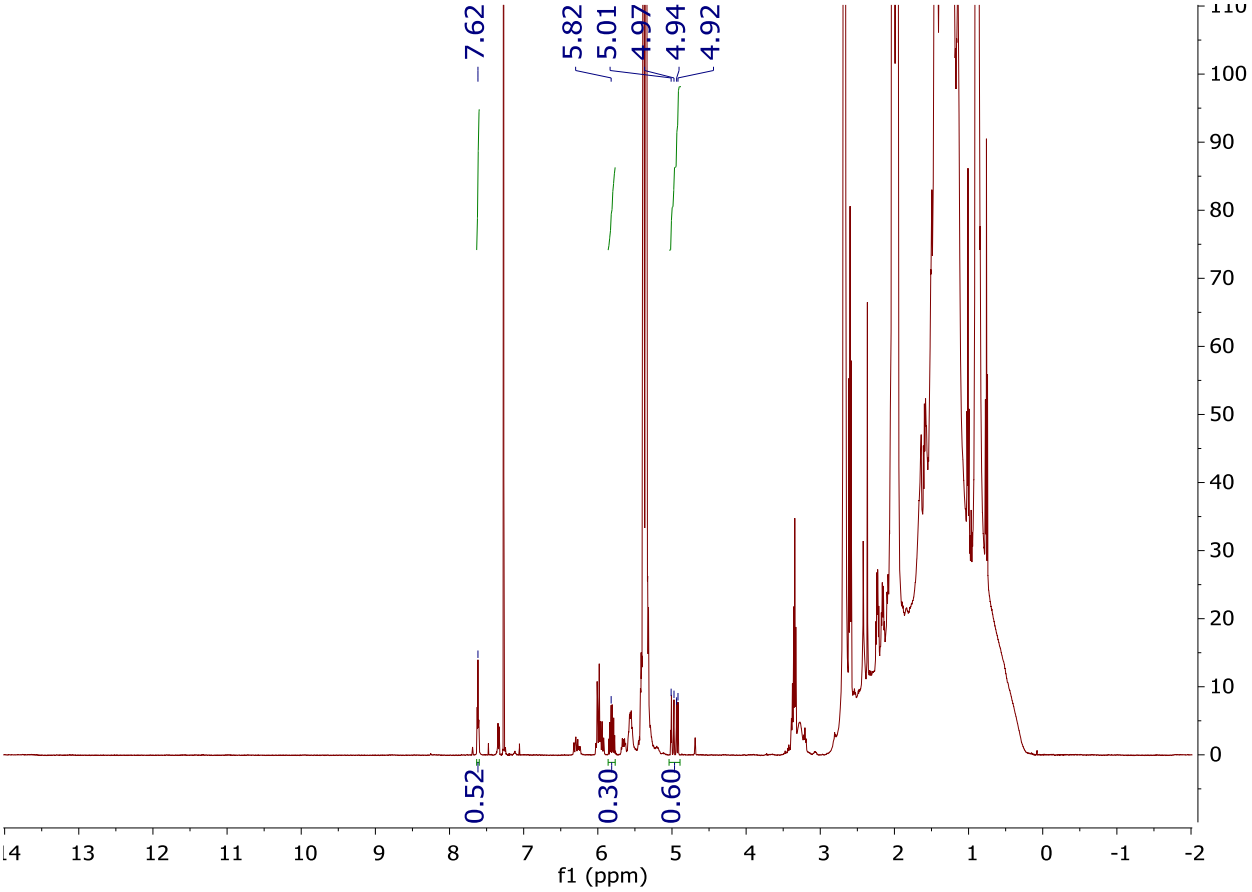

Figure B.3.5: ^{1}H NMR of final liquid.

Investigation of the Decomposition of Indium Nitride.

Reaction C. In a three-neck round-bottom flask equipped with a water-cooled-condenser and kept under air-free conditions (N_2 Schlenk line), 180 mg $InBr_3$ (0.5 mmol) are solubilized in 2 ml of oleylamine (6.08 mmol), 96 ul of octadecene (0.3 mmoml) and 5 ml of hexadecane. A complete dissolution of the salt is achieved by heating the solution to 210 °C under constant vigorous stirring. An alkylamide precursor solution is separately prepared under air-free conditions (N_2 glove box) by reacting 0.50 ml of OLA (1.5 mmol) with a mixture of 0.60 ml of a n-BuLi solution (2.5 M hexane solution, 1.5 mmol n-BuLi) and 0.45 ml TMEDA (3 mmol). This alkylamide solution is then injected promptly with a 6 ml syringe into the indium-OLA mixture

to initiate the reaction. The reaction is heating to 250 ºC after 35 minutes The reaction keep going for another 45 minutes at 250 ºC, then was stoped by removing the heat source and letting the solution cool down to room temperature.

Reaction D. In a three-neck round-bottom flask equipped with a water-cooled-condenser and kept under air-free conditions (N_2 Schlenk line), 180 mg $InBr_3$ (0.5 mmol) are solubilized in 2 ml of oleylamine (6.08 mmol), 96 ul of octadecene (0.3 mmoml) and 5 ml of hexadecane. A complete dissolution of the salt is achieved by heating the solution to 210 ºC under constant vigorous stirring. An alkylamide precursor solution is separately prepared under air-free conditions (N_2 glove box) by reacting 0.50 ml of OLA (1.5 mmol) with a mixture of 0.60 ml of a n-BuLi solution (2.5 M hexane solution, 1.5 mmol n-BuLi) and 0.45 ml TMEDA (3 mmol). This alkylamide solution is then injected promptly with a 6 ml syringe into the indium-OLA mixture to initiate the reaction. The reaction is heating to 250 ºC after 25 minutes. The reaction keep going for another 45 minutes at 250 ºC, then was stoped by removing the heat source and letting the solution cool down to room temperature.

Results. In reaction C, when the temperature is raised to 250 ºC, we do see the reaction mixture change color from black to little grey, indicating the conversion from InN to $In^{(0)}$. As shown in Figure B.4.1, the final product obtained from reaction C is $In^{(0)}$ (it may contain an extremely amount of InN due to a very small InN peak presenting in XRD), and the amount of imine produced in this experiment is only 0.6 mmol (Figure B.4.2). In reaction D, when the reaction run in 210 ºC for 25 minutes, the amount of imine produced is 0.37 mmol (Figure B.4.3). After running in 250 ºC for another 45 minutes, the amount of imine produced is 0.47 mmol (Figure B.4.4). The final product obtained from reaction D is $In^{(0)}$ (it may contain an extremely amount of InN due to a very small InN peak presenting in XRD, as shown in Figure B.4.5).

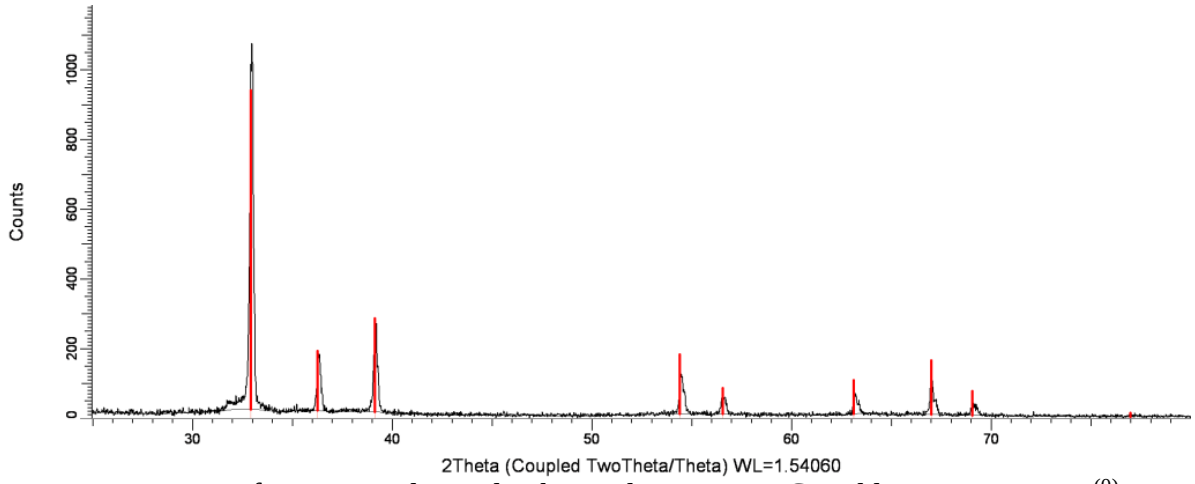

Figure B.4.1: XRD of as-prepared sample obtained in reaction C, red lines represent $In^{(0)}$.

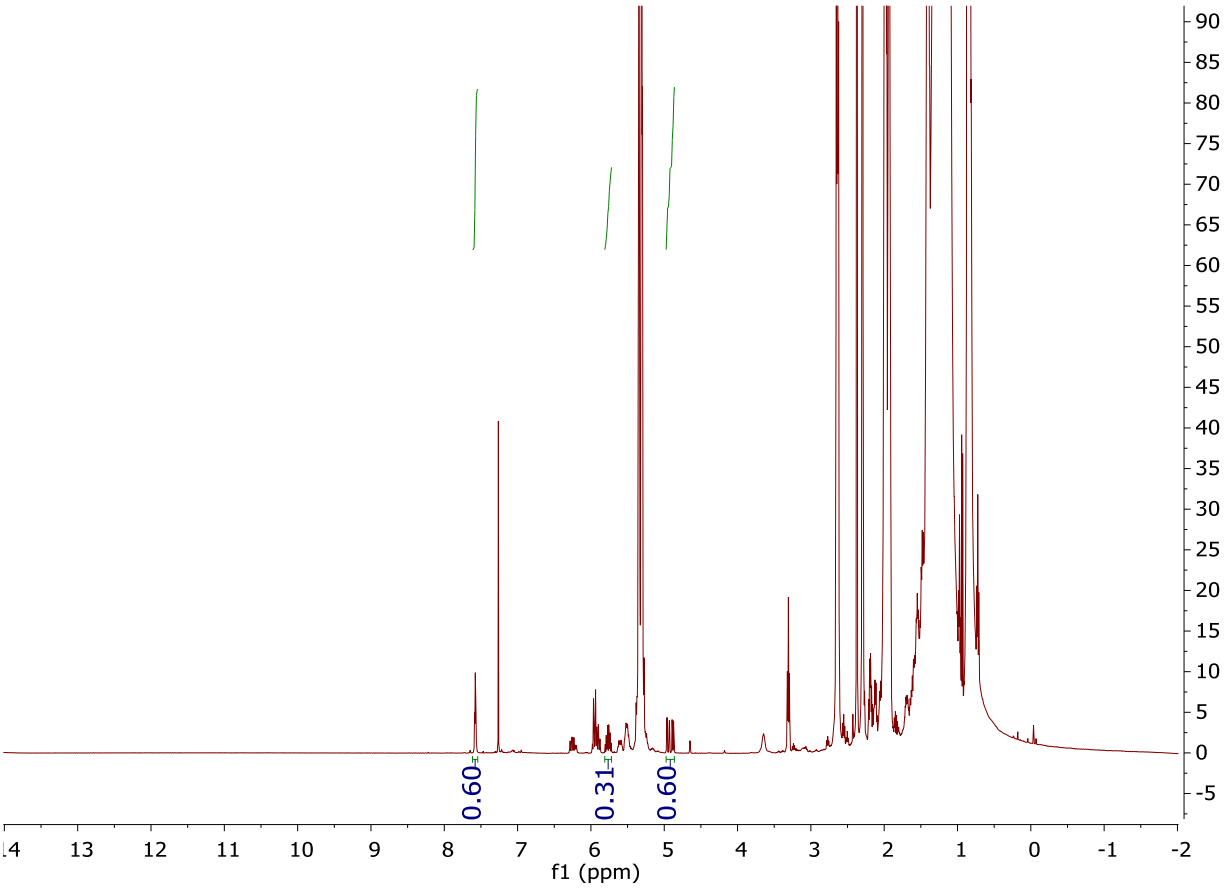

Figure B.4.2: ^{1}H NMR of reaction C mixture.

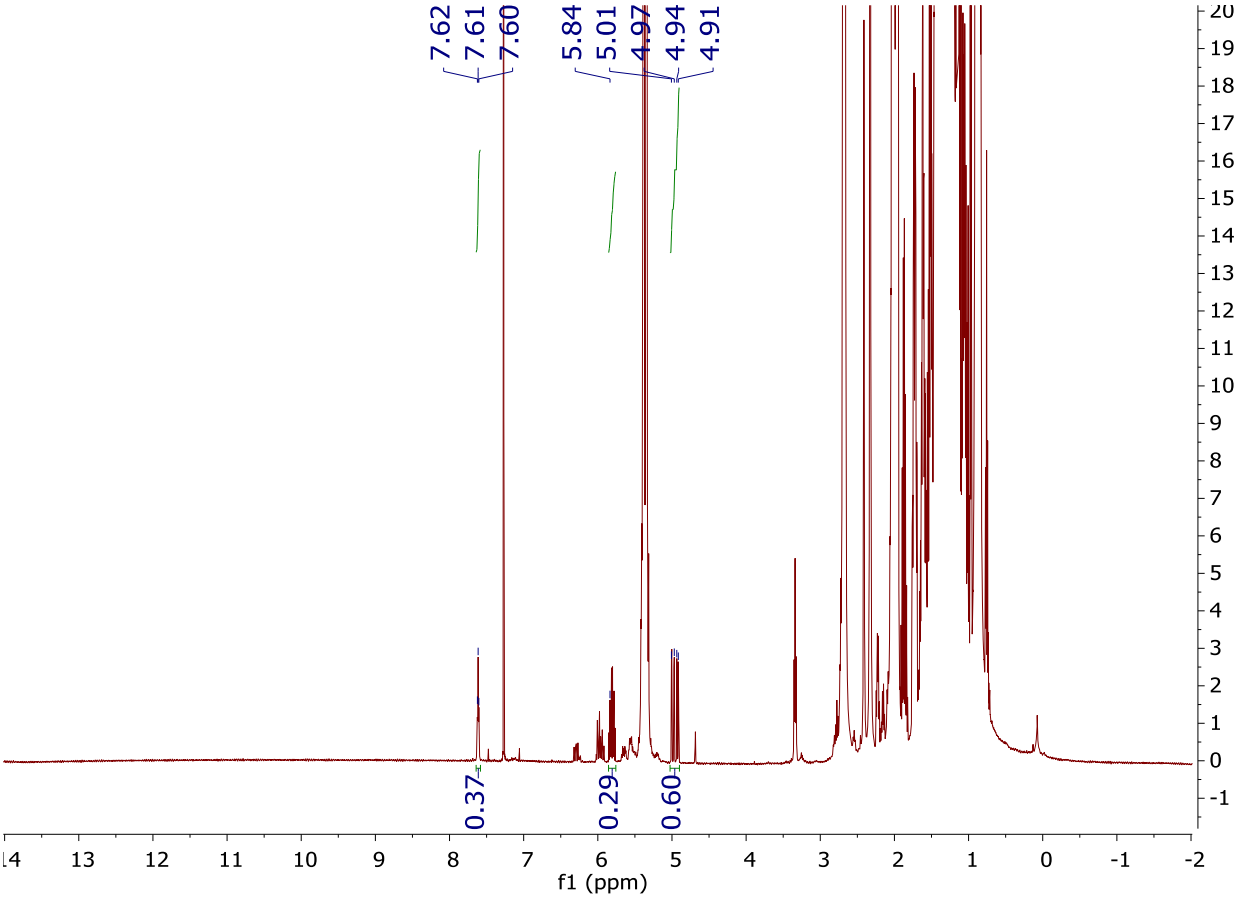

Figure B.4.3: ^{1}H NMR of reaction D mixture at 210 ^{o}C.

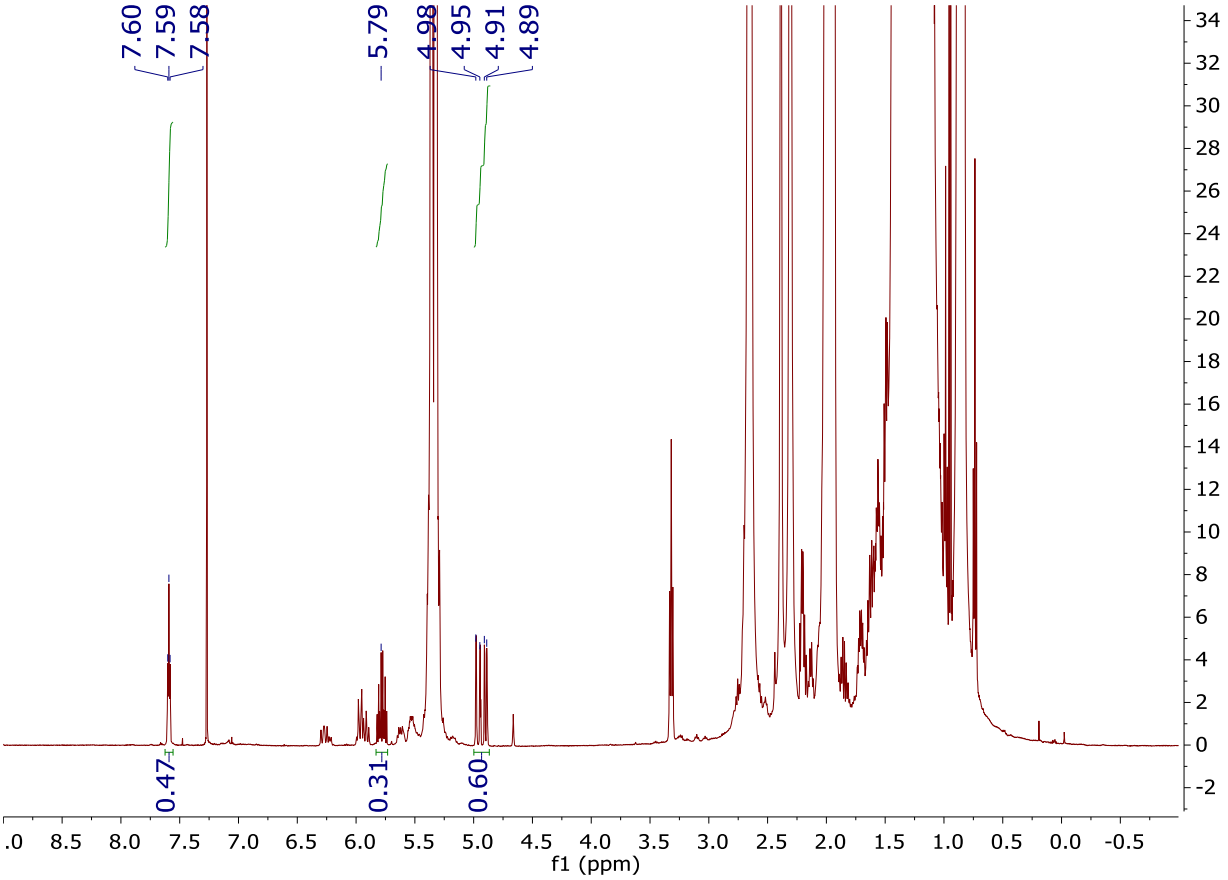

Figure B.4.4: ^{1}H NMR of reaction D mixture at 250 ^{o}C.

Influence of deprotonated-HMDS on conventional reaction.

Experiment A: In a three-neck round-bottom flask equipped with a water-cooled-condenser and kept under air-free conditions (N_2 Schlenk line), 180 mg $InBr_3$ (0.5 mmol) are solubilized in 2 ml of oleylamine (6.08 mmol) and 5 ml of hexadecane. A complete dissolution of the salt is achieved by heating the solution to 210 ^{o}C under constant vigorous stirring. An alkylamide precursor solution is separately prepared under air-free conditions (N_2 glove box) by reacting 0.32 ml of HMDS (1.5 mmol) with a mixture of 0.60 ml of a n-BuLi solution (2.5 M hexane solution, 1.5 mmol n-BuLi) and 0.45 ml TMEDA (3 mmol). This alkylamide solution is then injected promptly with a 6 ml syringe into the indium-OLA mixture to initiate the reaction. Small aliquots (0.6 ml) are taken out at precise times after temperature for TEM measurements.

Results. Figure 5.1 shows the TEM results. Figure 5.2 shows the XRD results.

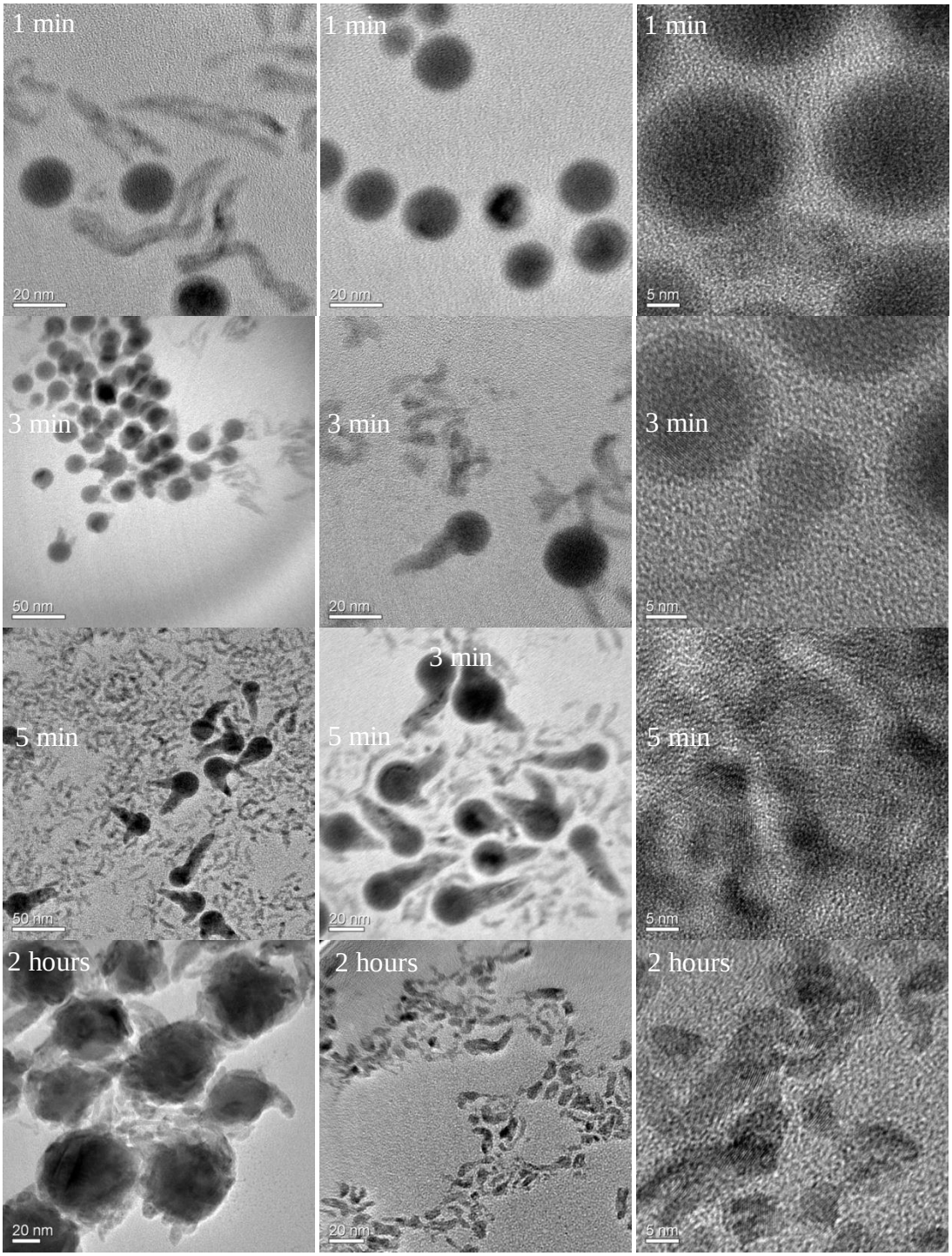

Figure B.5.1: TEM images of reaction aliquots obtained at different reaction time.

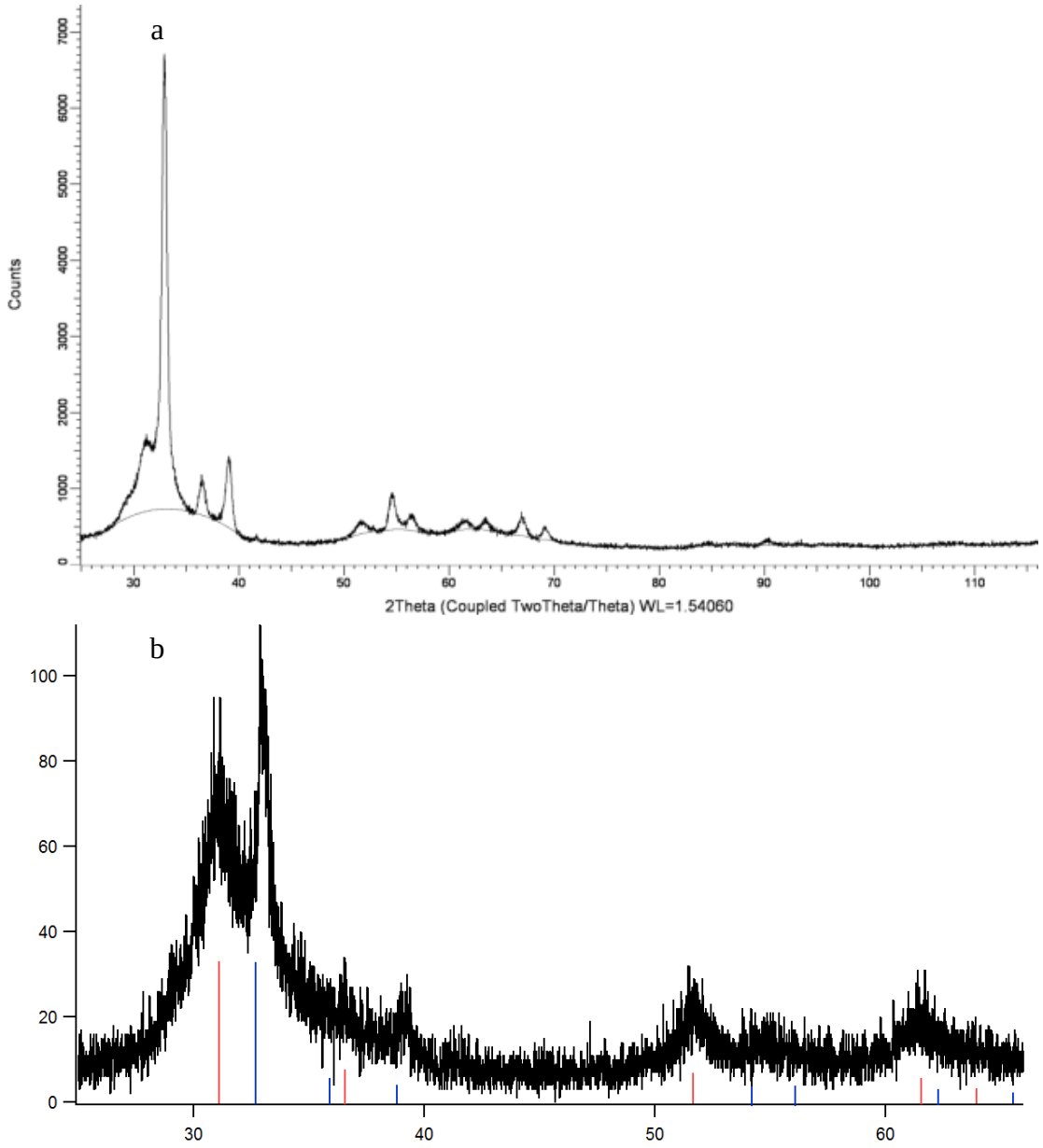

Figure B.5.2: a) XRD of reaction aliquots obtained after 1 minute. b) XRD of reaction aliquots obtained after 10 minute. (red lines represent InN, blue lines represent $In^{(0)}$)

Kinetics Study

Reaction C. In a three-neck round-bottom flask equipped with a water-cooled-condenser and kept under air-free conditions (N_2 Schlenk line), 360 mg $InBr_3$ (1.0 mmol) are solubilized in 10 ml of oleylamine (30.4 mmol), 96 ul of octadecene (0.3 mmol) and 4 ml of hexadecane. A complete dissolution of the salt is achieved by heating the solution to 210 ^oC under constant

vigorous stirring. An alkylamide precursor solution is separately prepared under air-free conditions (N_2 glove box) by reacting 1.0 ml of OLA (3.0 mmol) with a mixture of 1.2 ml of a n-BuLi solution (2.5 M hexane solution, 3.0 mmol n-BuLi) and 0.90 ml TMEDA (6 mmol). This alkylamide solution is then injected promptly with a 6 ml syringe into the indium-OLA mixture to initiate the reaction. Small aliquots (0.5 ml) of reaction mixture are taken out at precise times after injection; these aliquots are immediately injected in 6 ml Hexane at room temperature to stop the reaction. Then evaporate hexane by vacuum and dissolve the residual into deuterated chloroform for NMR measurements.

Reaction D. In a three-neck round-bottom flask equipped with a water-cooled-condenser and kept under air-free conditions (N_2 Schlenk line), 360 mg $InBr_3$ (1.0 mmol) are solubilized in 4 ml of oleylamine (12.16 mmol), 96 ul of octadecene (0.3 mmol) and 10 ml of hexadecane. A complete dissolution of the salt is achieved by heating the solution to 210 ^oC under constant vigorous stirring. An alkylamide precursor solution is separately prepared under air-free conditions (N_2 glove box) by reacting 1.0 ml of OLA (3.0 mmol) with a mixture of 1.2 ml of a n-BuLi solution (2.5 M hexane solution, 3.0 mmol n-BuLi) and 0.90 ml TMEDA (6 mmol). This alkylamide solution is then injected promptly with a 6 ml syringe into the indium-OLA mixture to initiate the reaction. Small aliquots (0.5 ml) of reaction mixture are taken out at precise times after injection; these aliquots are immediately injected in 6 ml Hexane at room temperature to stop the reaction. Then evaporate hexane by vacuum and dissolve the residual into deuterated chloroform for NMR measurements.

Reaction E. In a three-neck round-bottom flask equipped with a water-cooled-condenser and kept under air-free conditions (N_2 Schlenk line), 360 mg $InBr_3$ (1.0 mmol) are solubilized in 1 ml of oleylamine (3.04 mmol), 96 ul of octadecene (0.3 mmol) and 10 ml of hexadecane. A

complete dissolution of the salt is achieved by heating the solution to 210 ^{o}C under constant vigorous stirring. An alkylamide precursor solution is separately prepared under air-free conditions (N_2 glove box) by reacting 1.0 ml of OLA (3.0 mmol) with a mixture of 1.2 ml of a n-BuLi solution (2.5 M hexane solution, 3.0 mmol n-BuLi) and 0.90 ml TMEDA (6 mmol). This alkylamide solution is then injected promptly with a 6 ml syringe into the indium-OLA mixture to initiate the reaction. Small aliquots (0.5 ml) of reaction mixture are taken out at precise times after injection; these aliquots are immediately injected in 6 ml Hexane at room temperature to stop the reaction. Then evaporate hexane by vacuum and dissolve the residual into deuterated chloroform for NMR measurements.

Reaction F. In a three-neck round-bottom flask equipped with a water-cooled-condenser and kept under air-free conditions (N_2 Schlenk line), 360 mg $InBr_3$ (1.0 mmol) are solubilized in 1.608 mg octadecylamine (6.0 mmol), 96 ul of octadecene (0.3 mmol) and 10 ml of hexadecane. A complete dissolution of the salt is achieved by heating the solution to 210 ^{o}C under constant vigorous stirring. An alkylamide precursor solution is separately prepared under air-free conditions (N_2 glove box) by reacting 0.64 ml of HMDS (3.0 mmol) with a mixture of 1.2 ml of a n-BuLi solution (2.5 M hexane solution, 3.0 mmol n-BuLi) and 0.90 ml TMEDA (6 mmol). This alkylamide solution is then injected promptly with a 6 ml syringe into the indium-octadecylamine mixture to initiate the reaction. Small aliquots (0.5 ml) of reaction mixture are taken out at precise times after injection; these aliquots are immediately injected in 6 ml Hexane at room temperature to stop the reaction. Then evaporate hexane by vacuum and dissolve the residual into deuterated chloroform for NMR measurements.

Results. Figure B.6.1 compares the kinetics of reaction C, D and E, in which we used different concentration of oleylamine to solubilize $InBr_3$. Figure B.6.2 shows the comparison of the

kinetics of reaction D and F, in which we used different type of amine to solubilize $InBr_3$. The concentration of imine produced of reaction C, D, E, and F in different time were shown in Figure B.6.3, Figure B.6.4, Figure B.6.5 and Figure B.6.6, respectively.

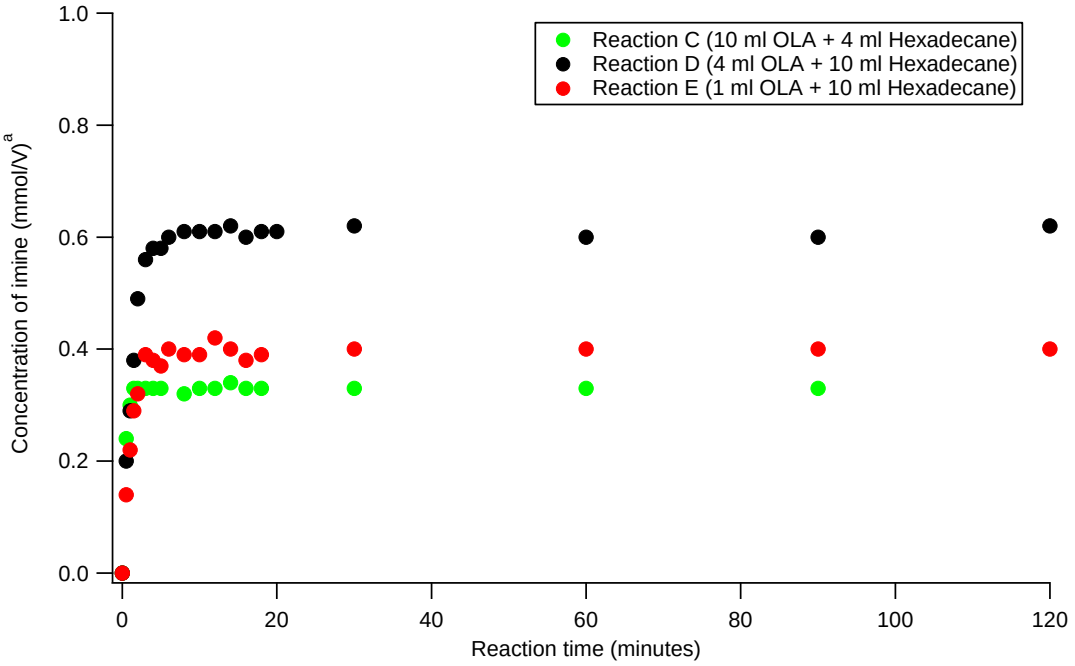

Figure B.6.1: Comparison of the kinetics of reaction C, D and E. [a]Because it is hard to calculate the accurate volume of the reaction mixture at each reaction time, here we use V to represent the accurate volume of the reaction mixture at each reaction time.

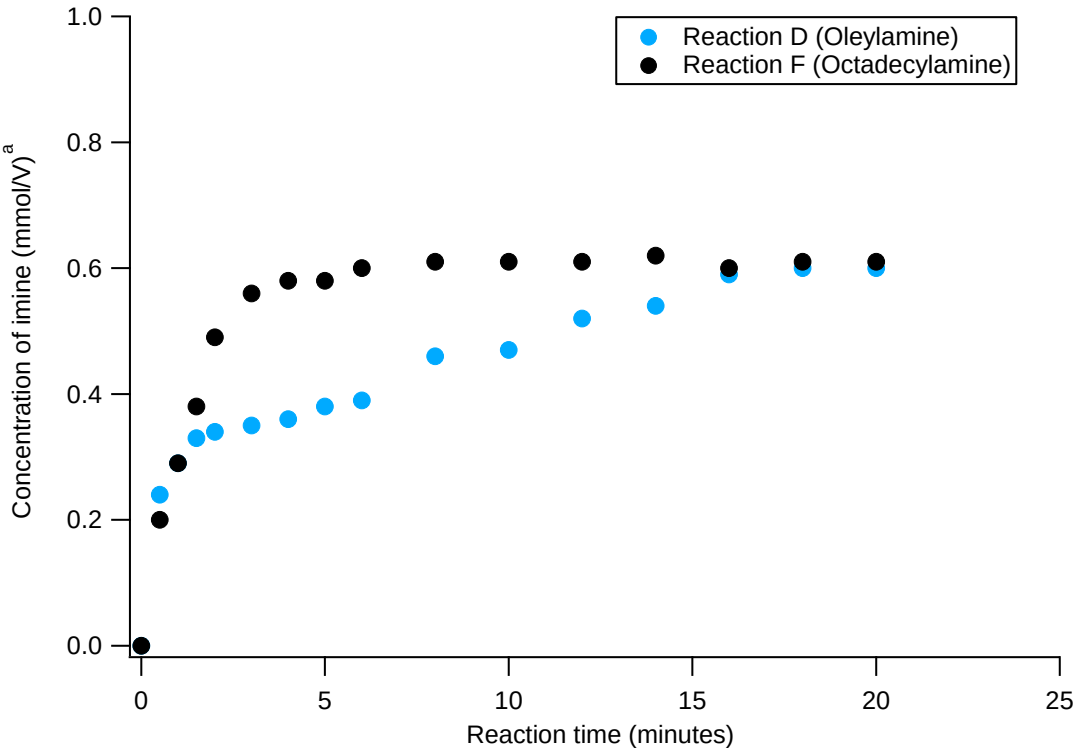

Figure B.6.2: Comparison of the kinetics of reaction D and F. [a]Because it is hard to calculate the accurate volume of the reaction mixture at each reaction time, here we use V to represent the accurate volume of the reaction mixture at each reaction time.

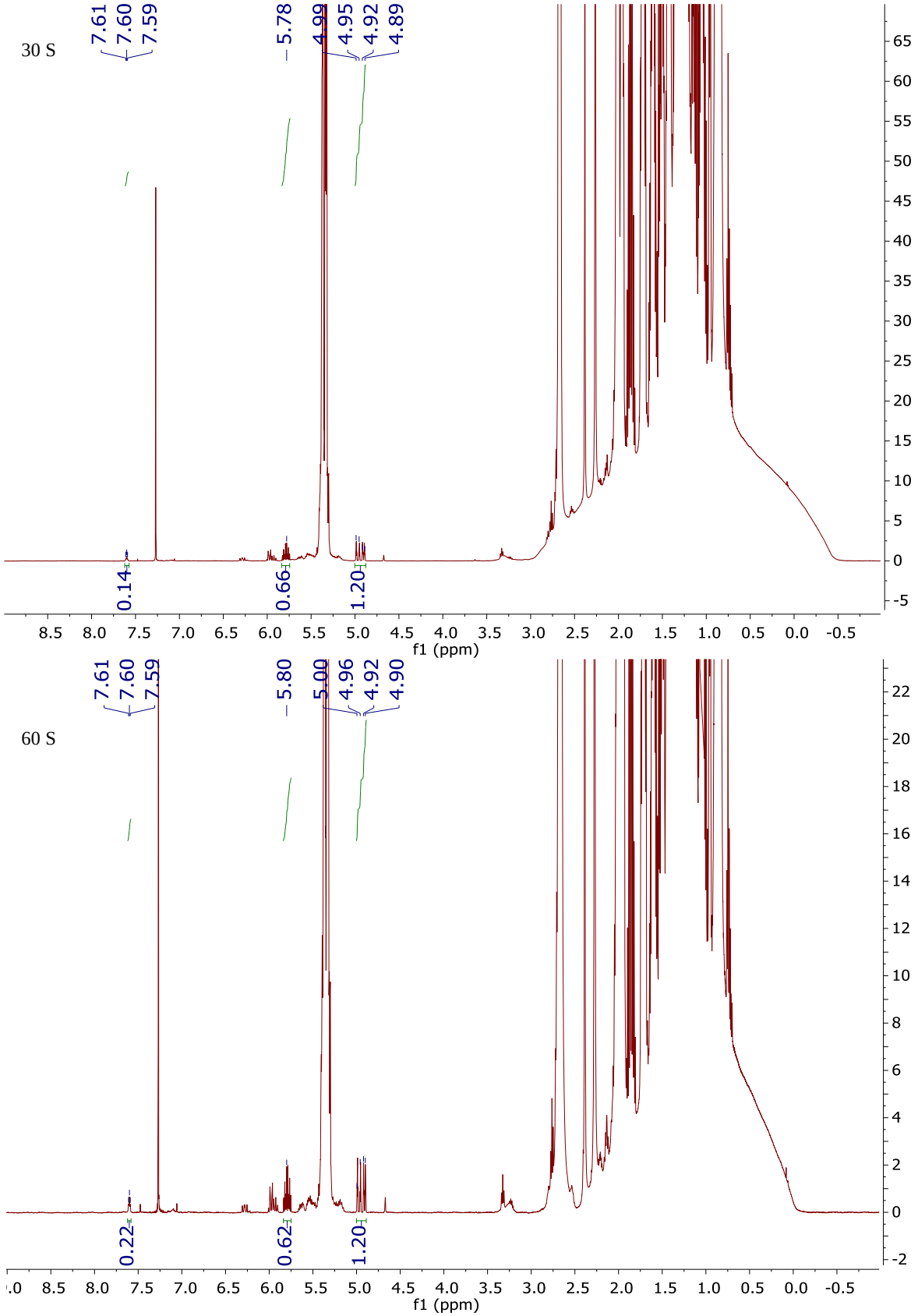

Figure B.6.3: ^{1}H NMR of reaction C mixture in different time.

Figure B.6.3 (cont'd)

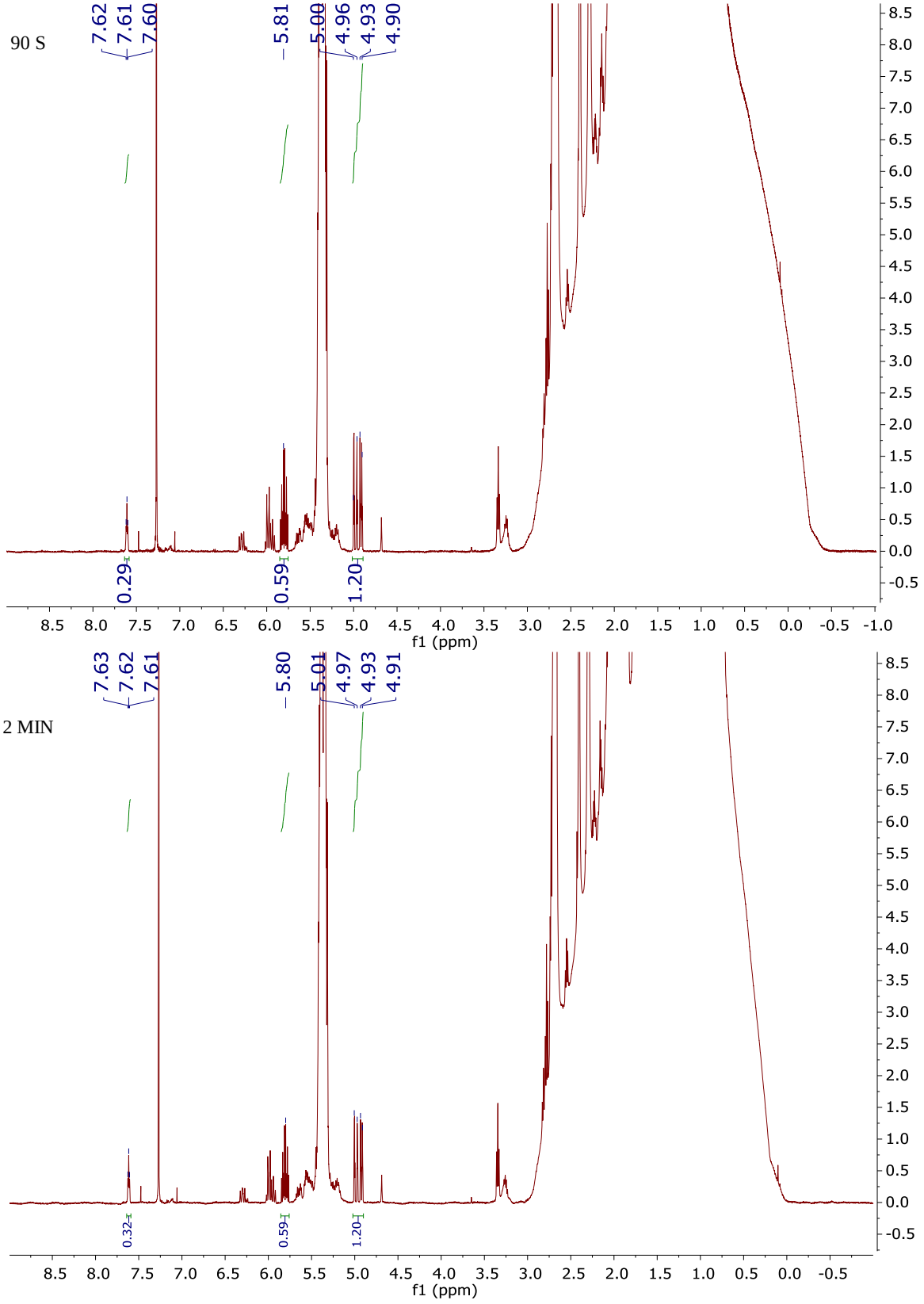

Figure B.6.3 (cont'd)

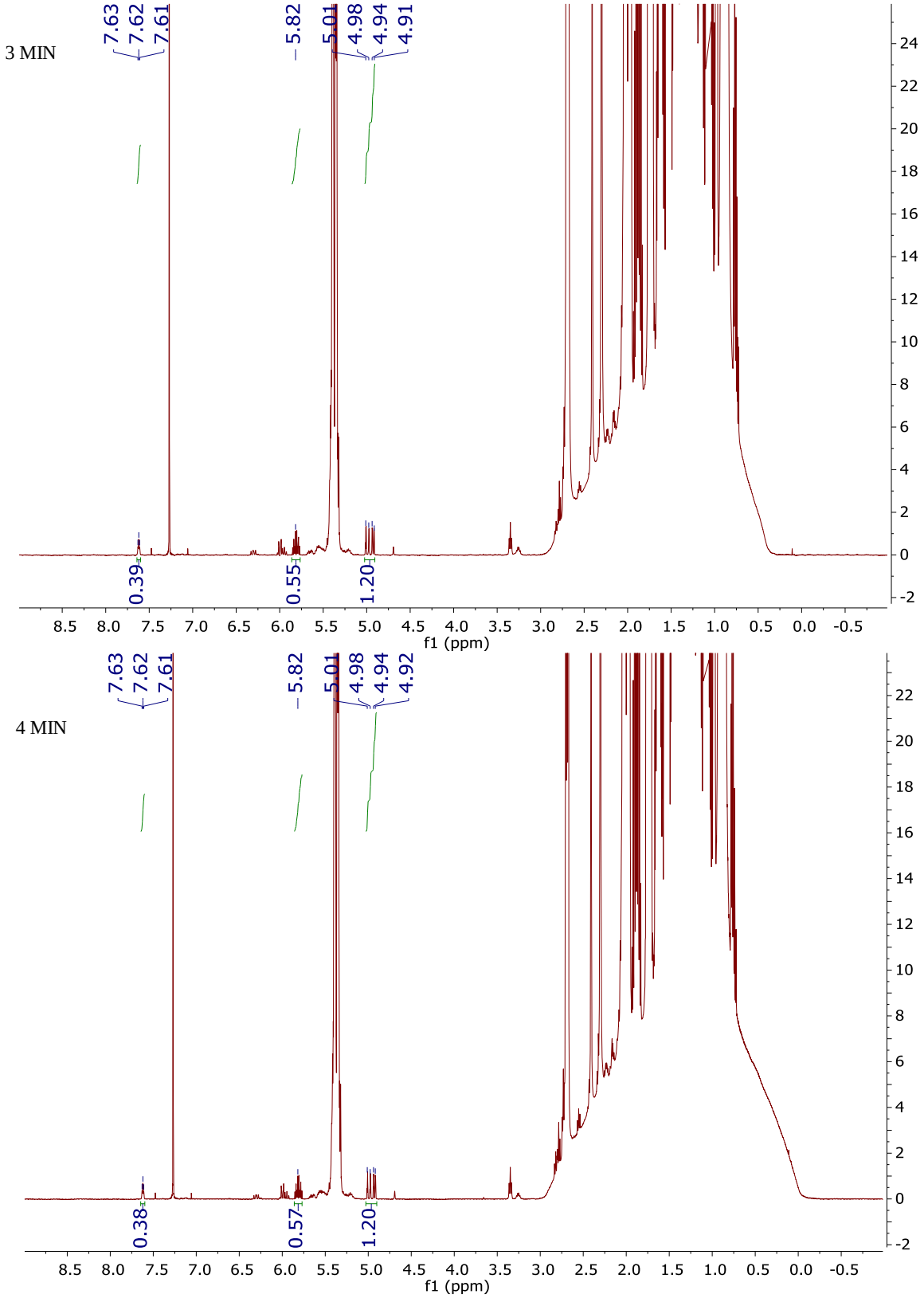

Figure B.6.3 (cont'd)

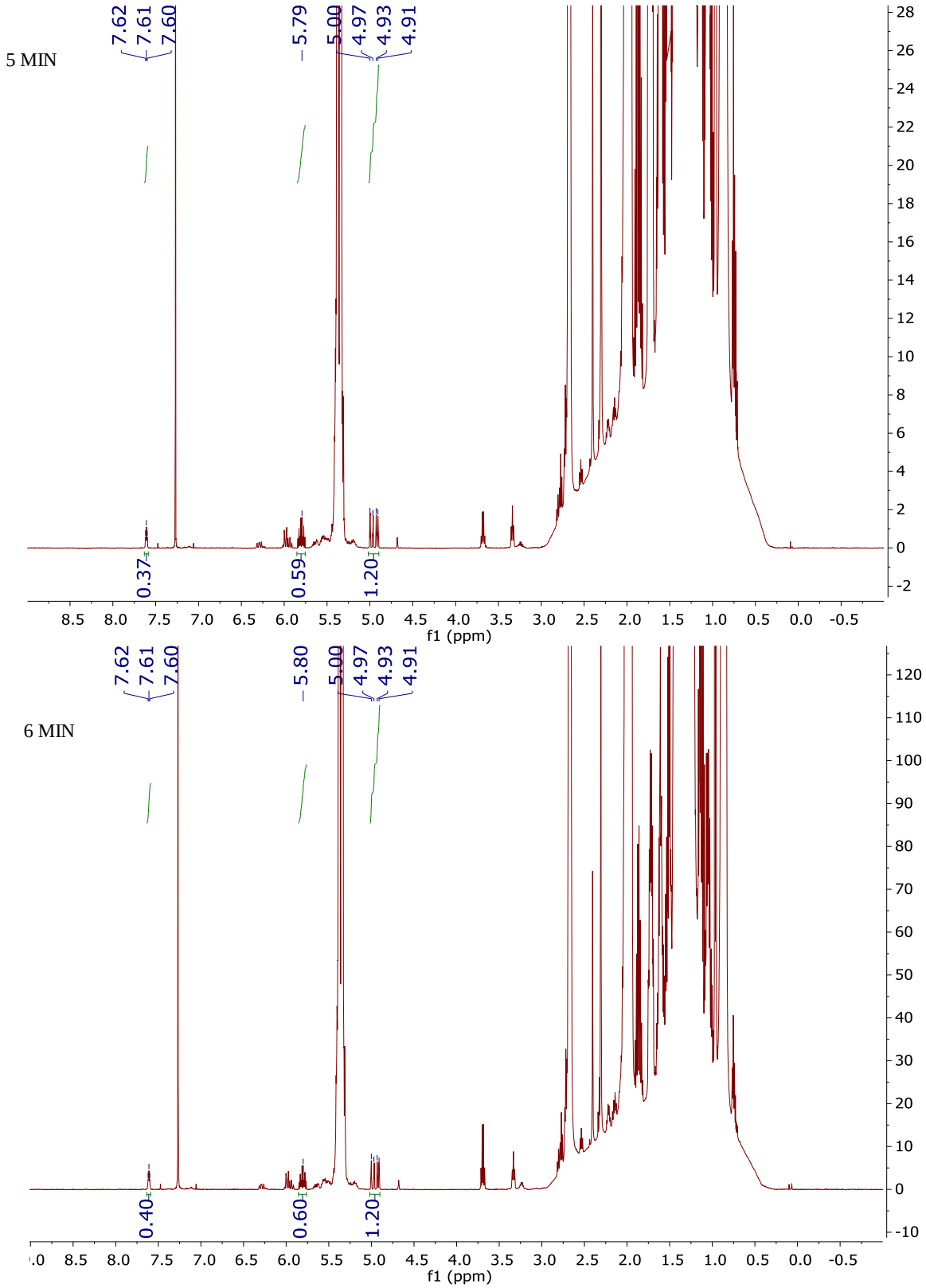

Figure B.6.3 (cont'd)

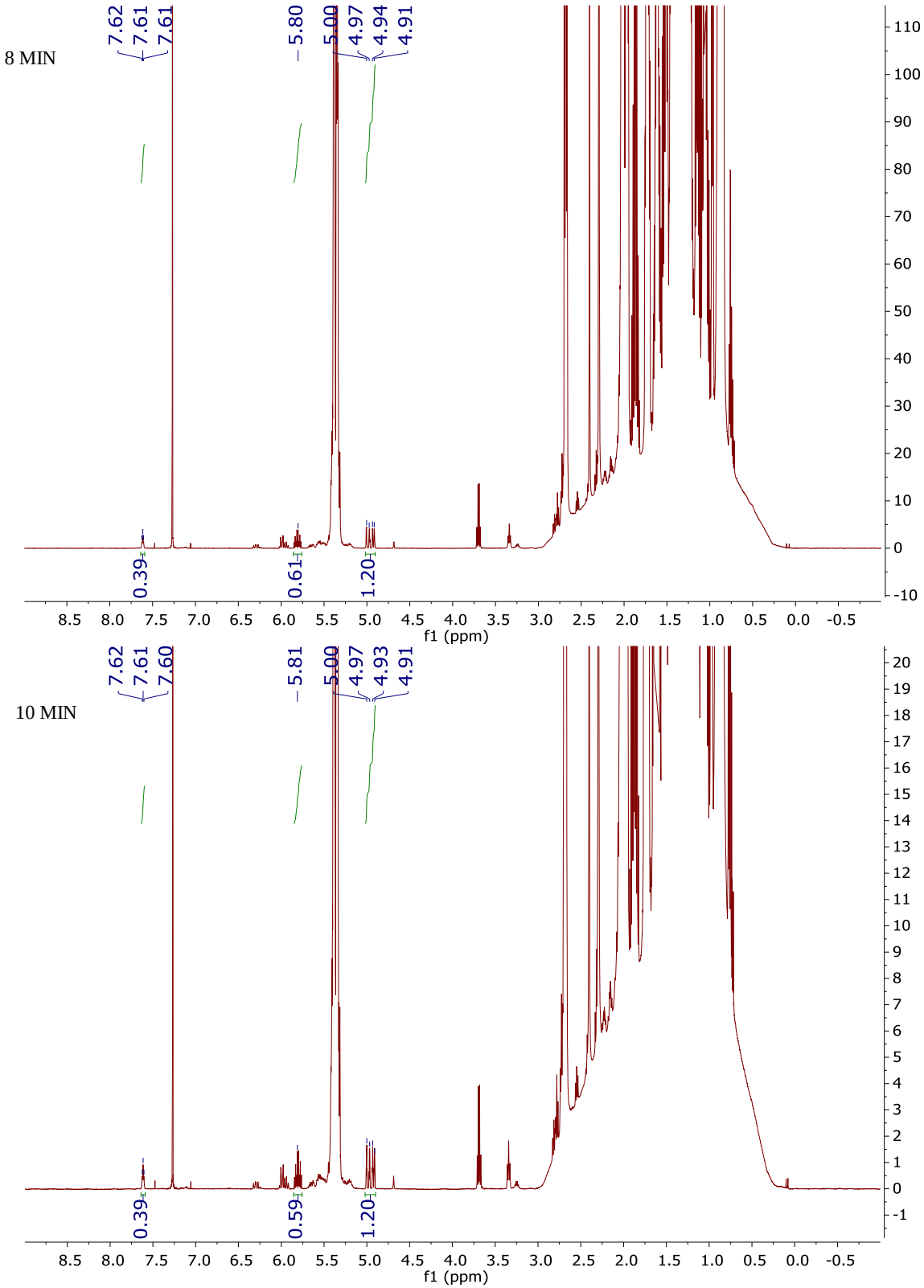

Figure B.6.3 (cont'd)

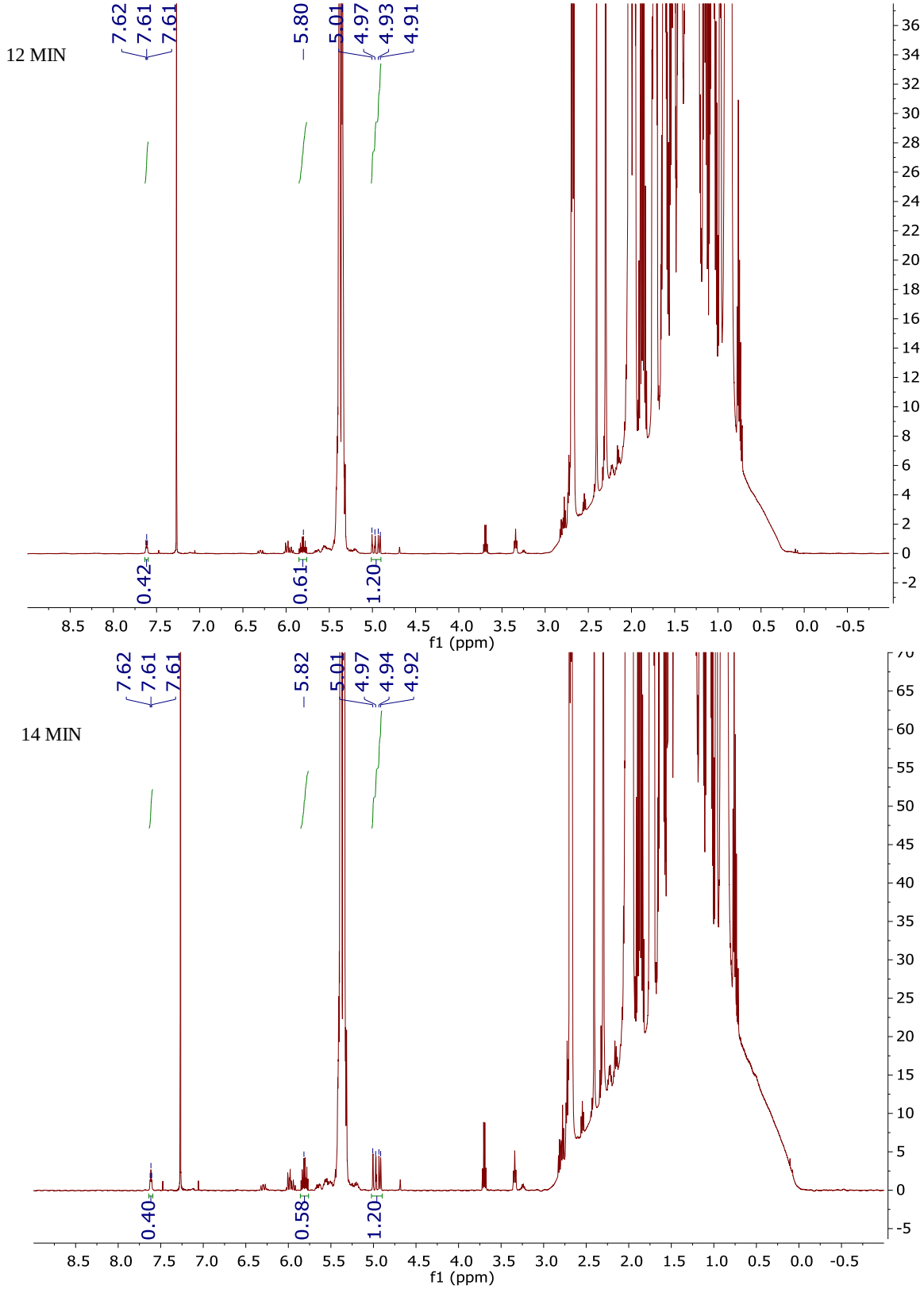

Figure B.6.3 (cont'd)

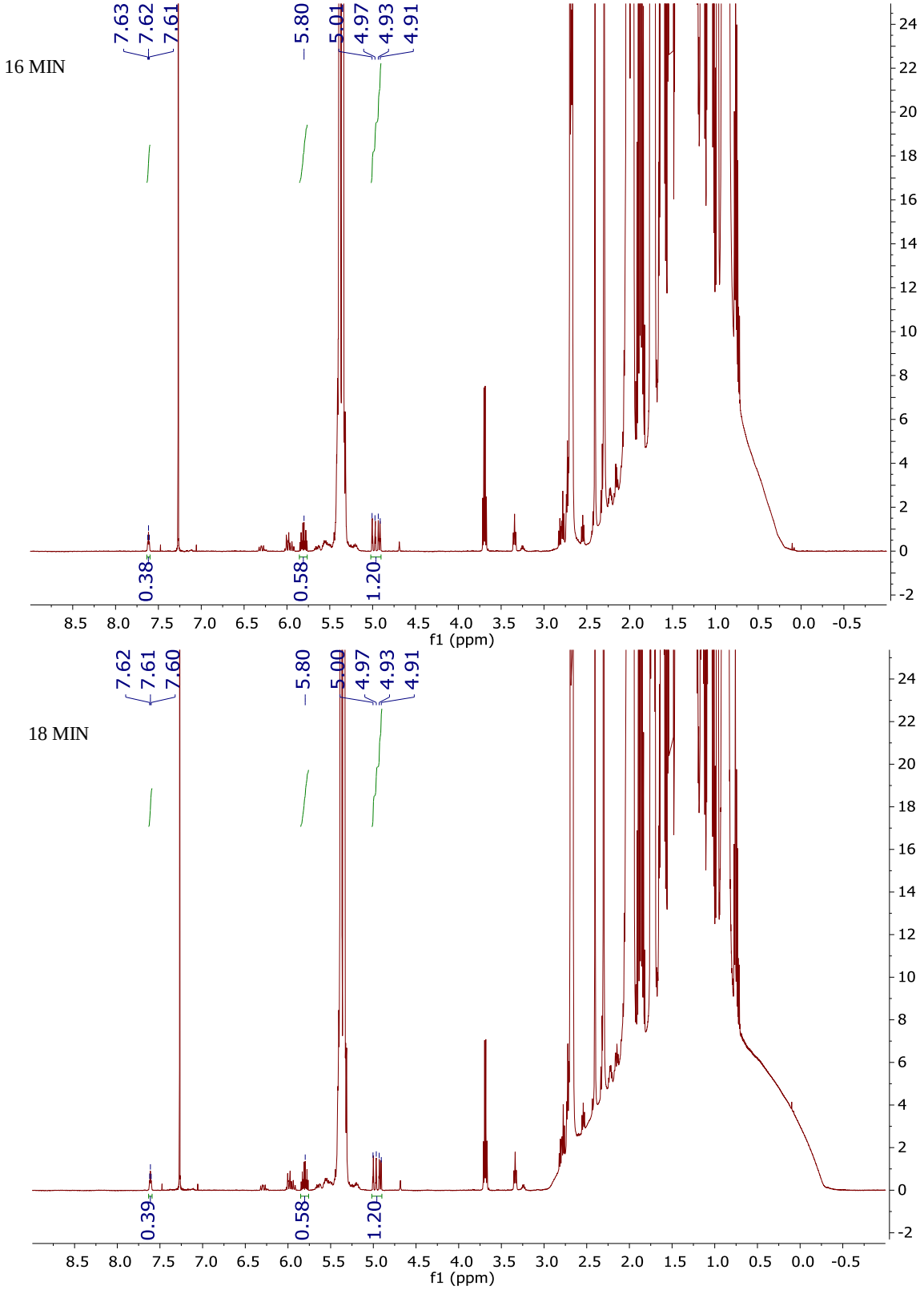

Figure B.6.3 (cont'd)

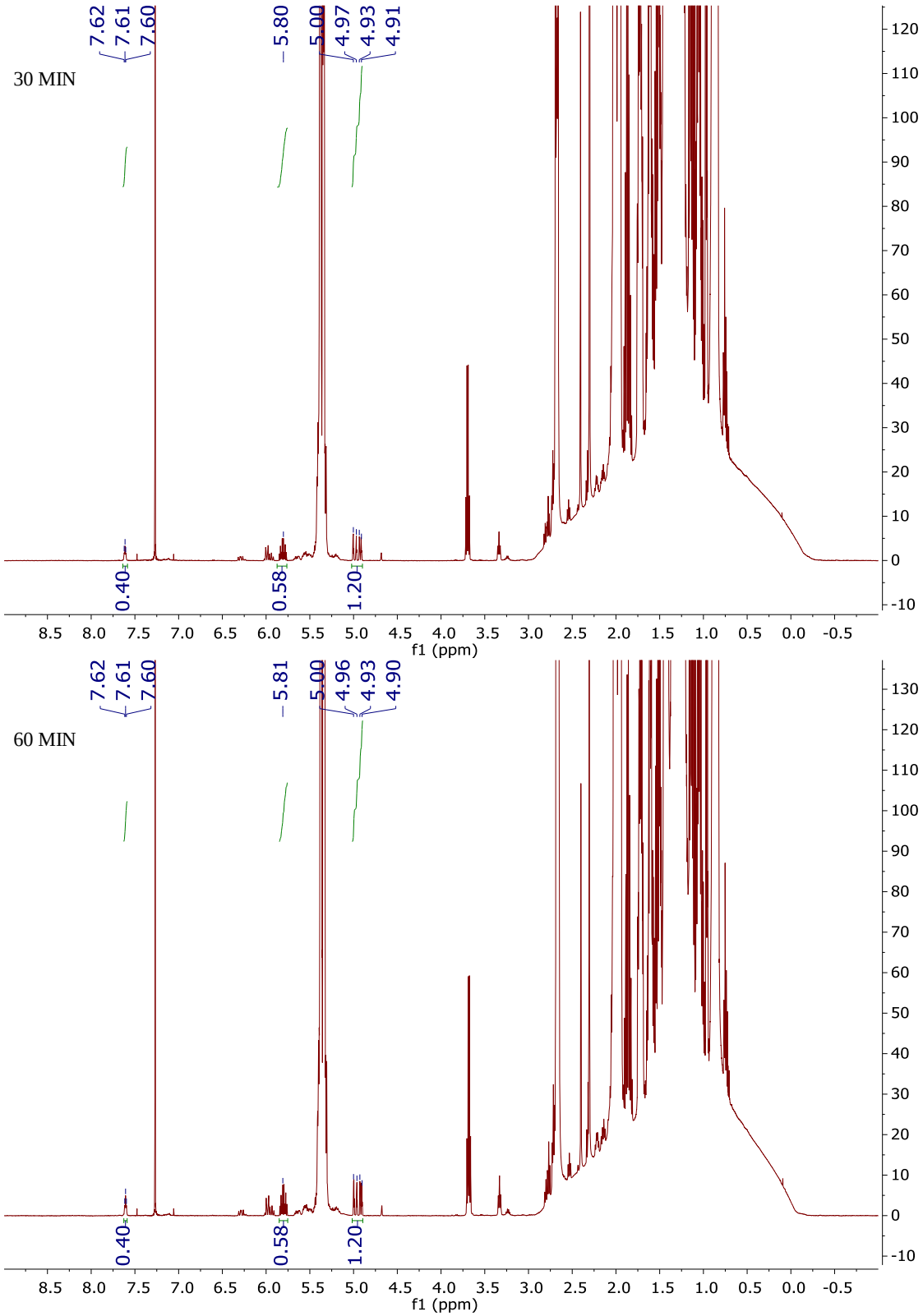

Figure B.6.3 (cont'd)

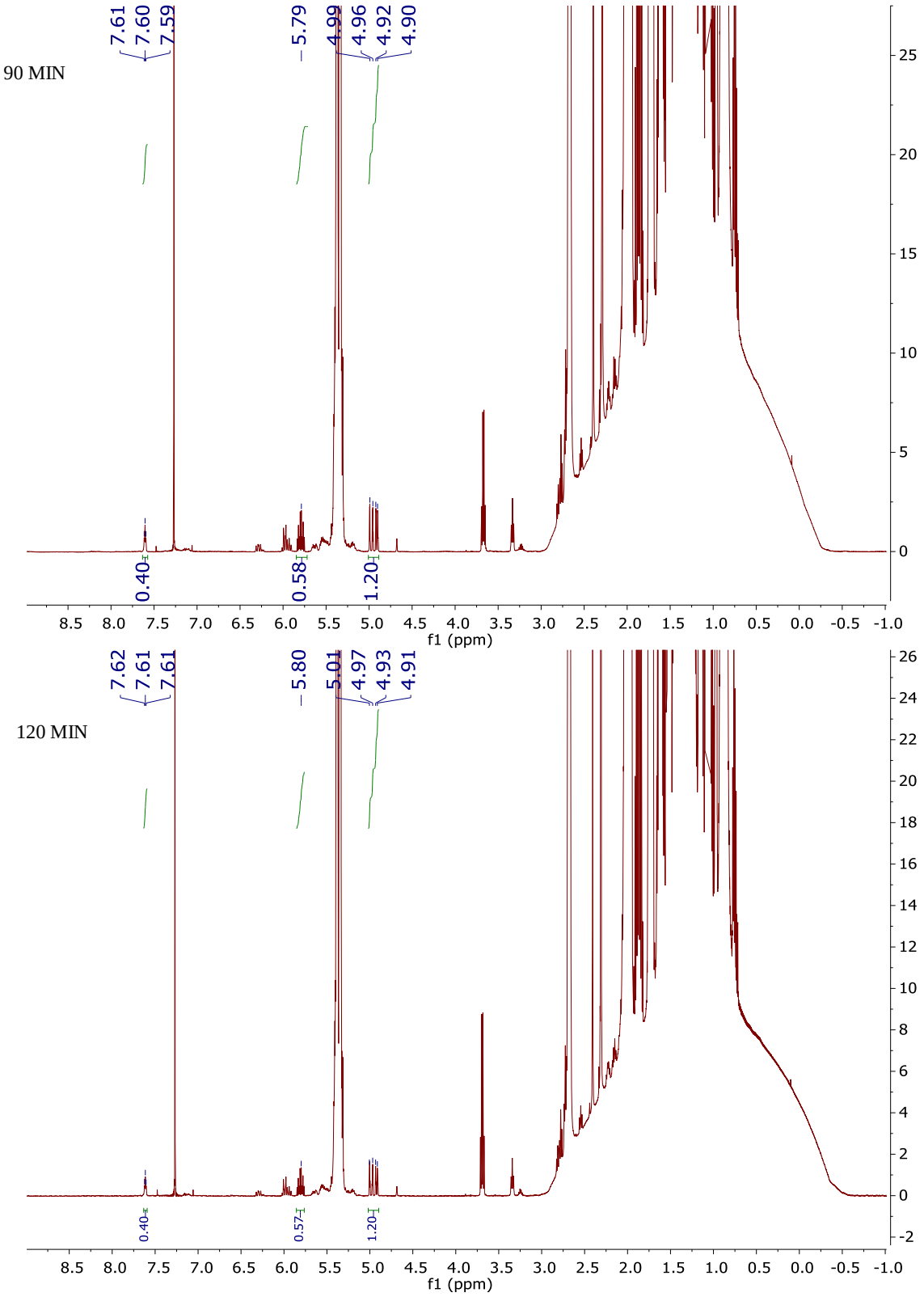

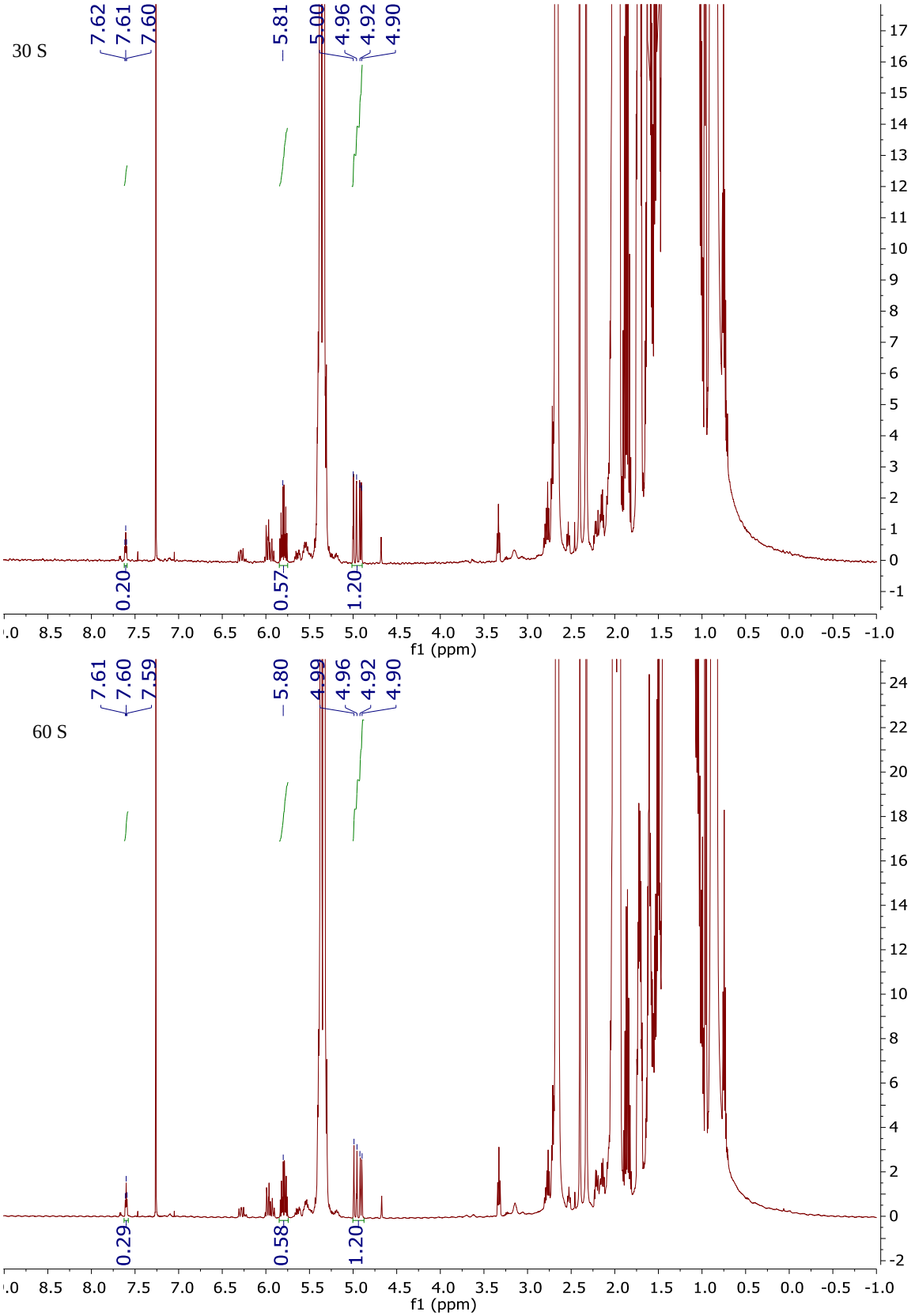

Figure B.6.4: ^{1}H NMR of reaction D mixture in different time.

Figure B.6.4 (cont'd)

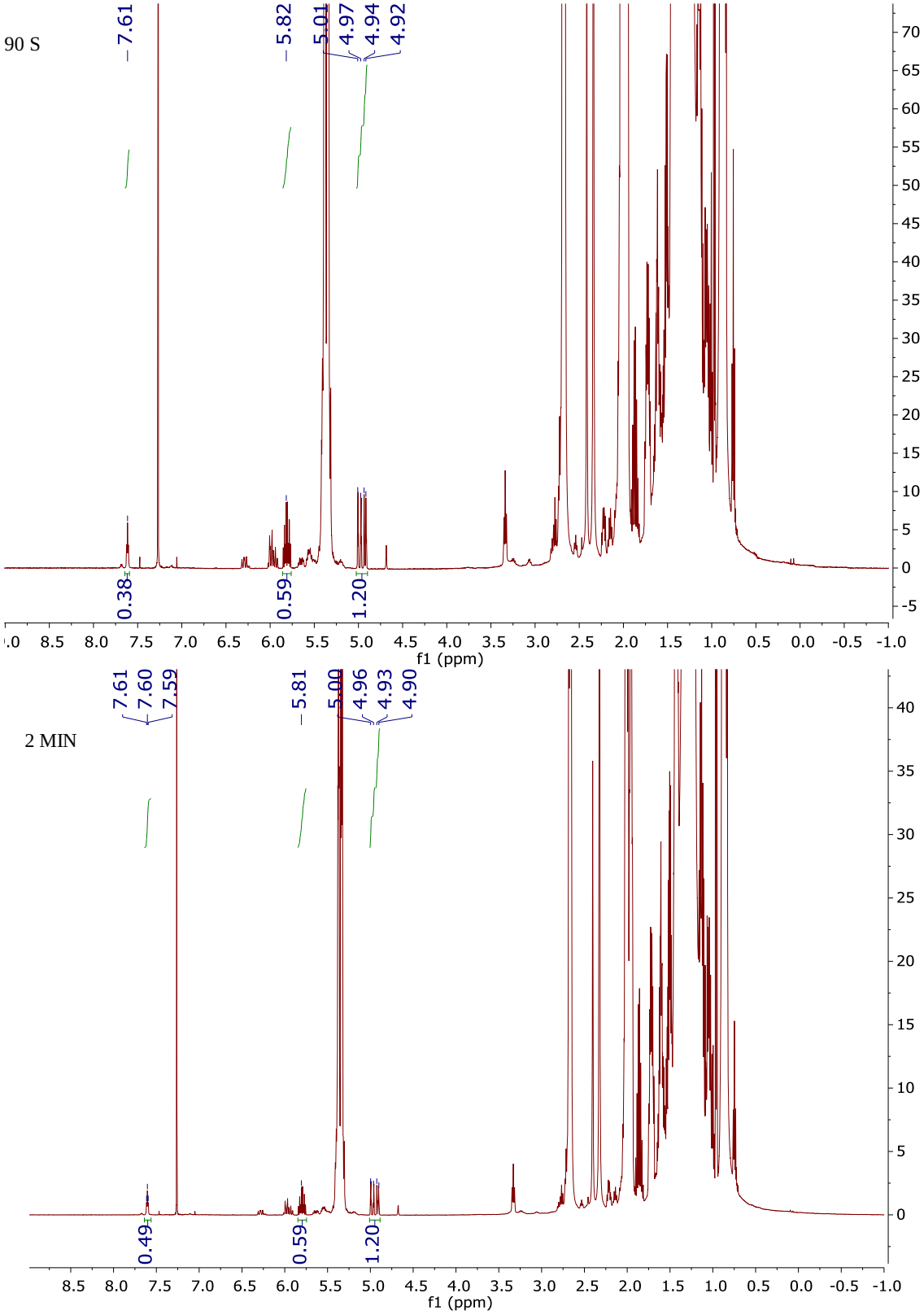

Figure B.6.4 (cont'd)

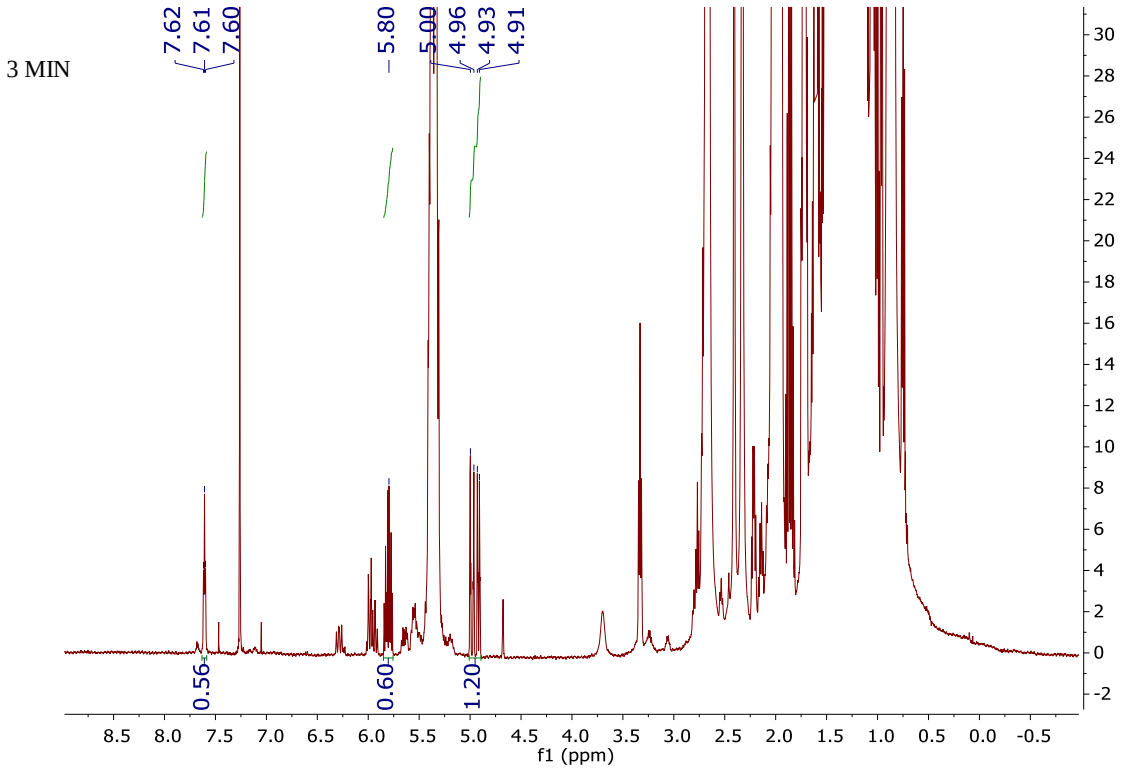

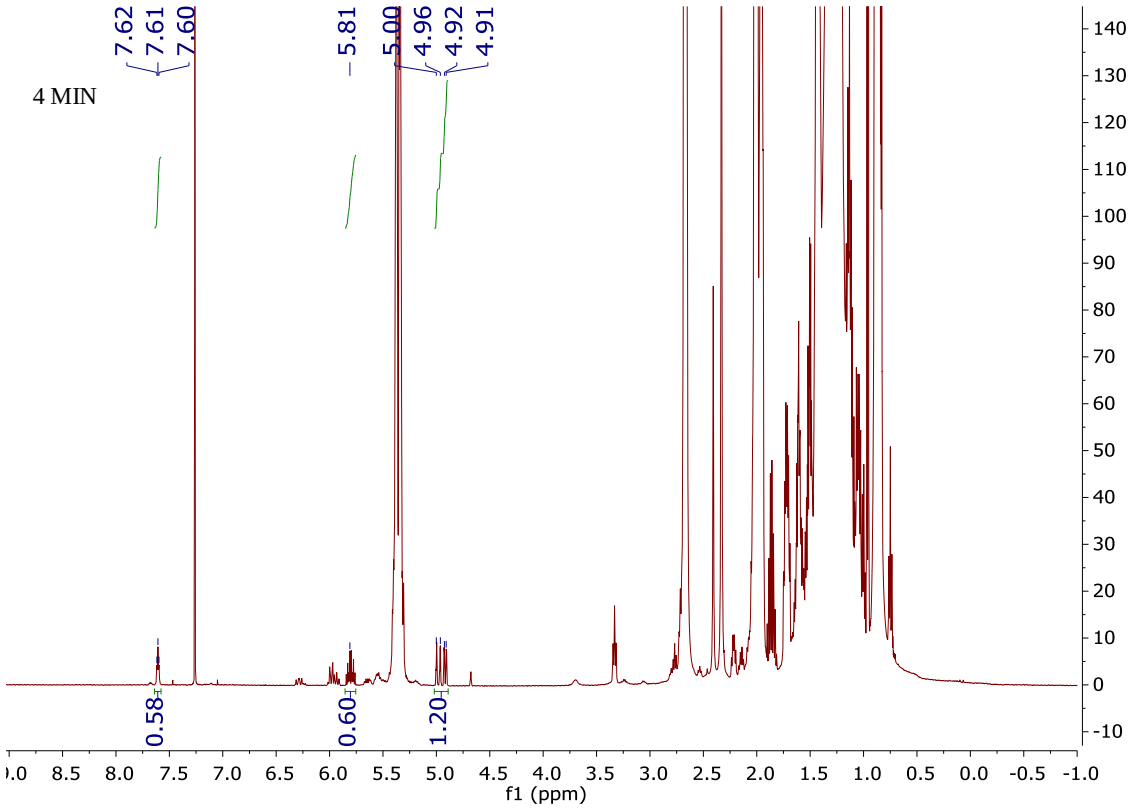

Figure B.6.4 (cont'd)

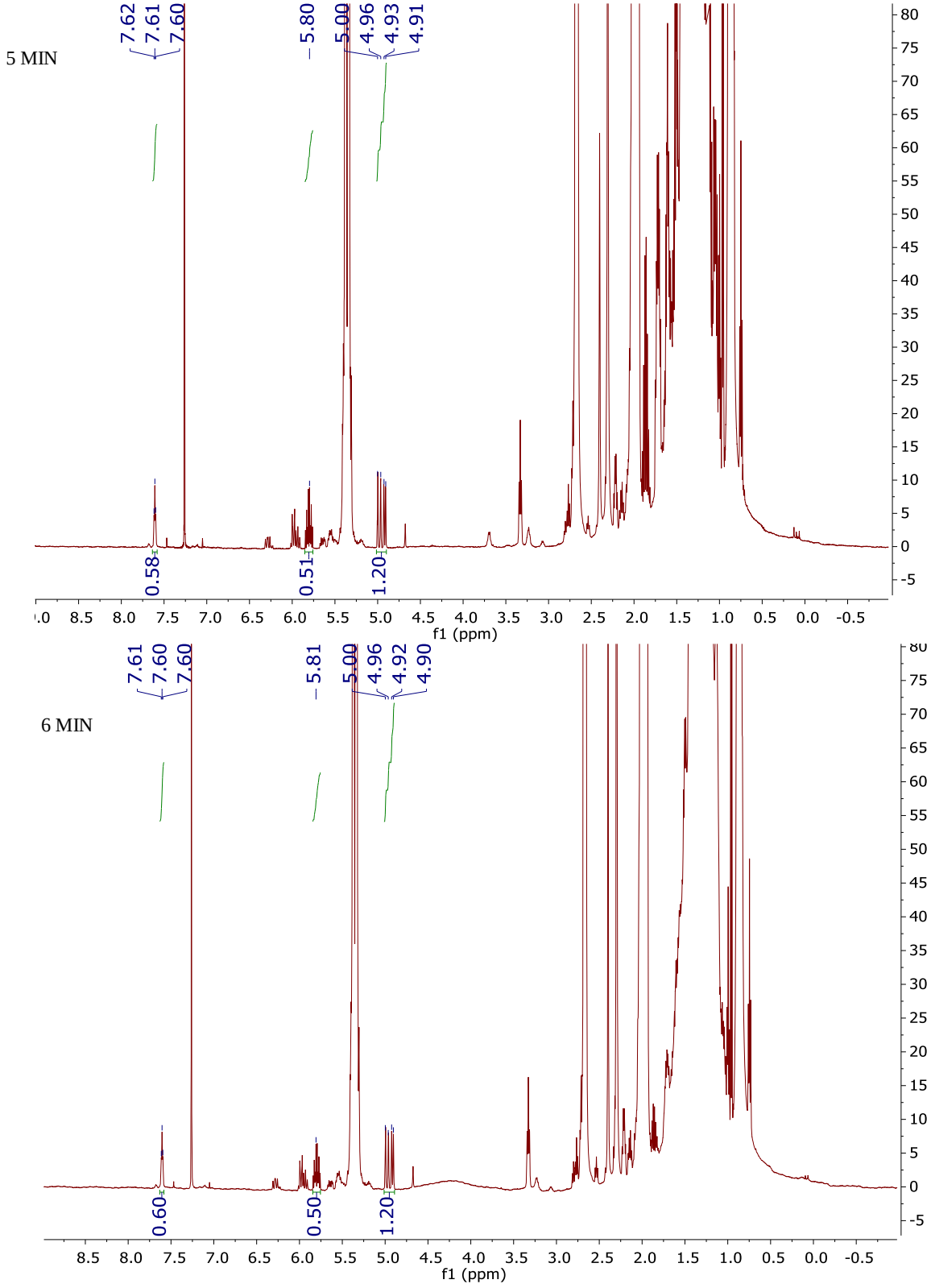

Figure B.6.4 (cont'd)

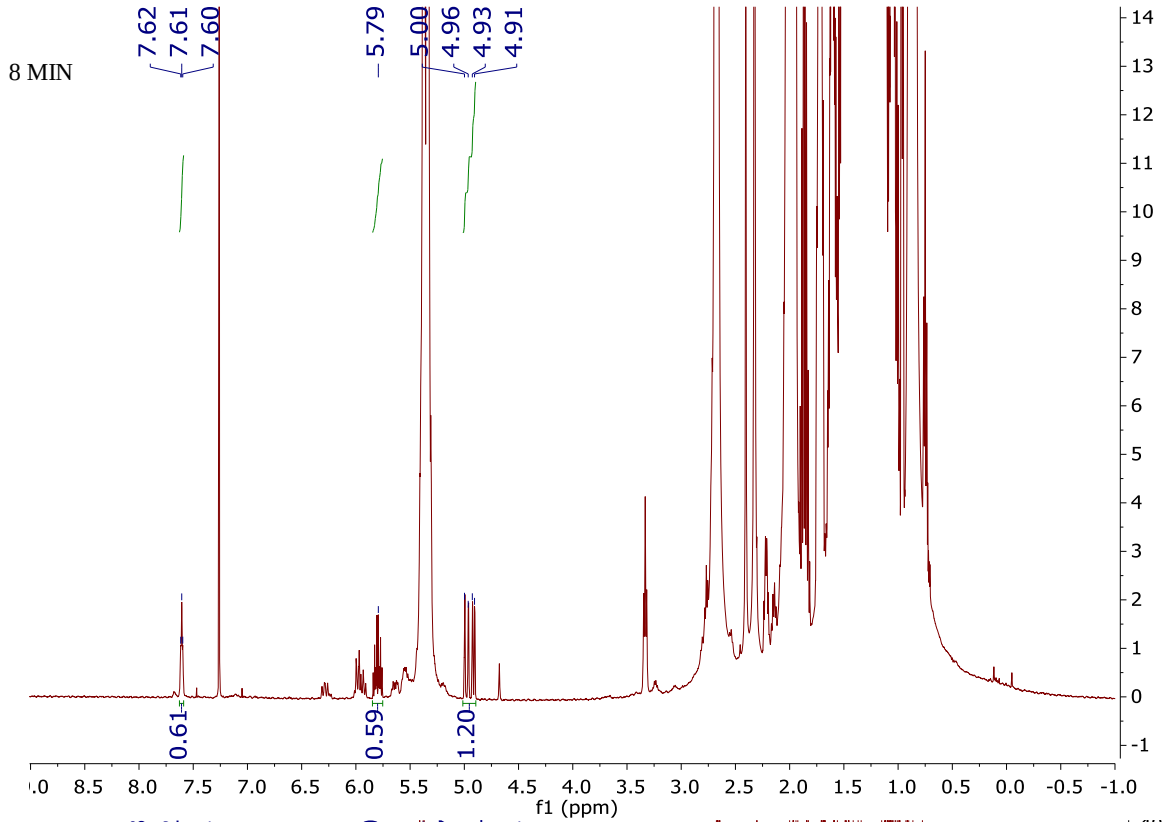

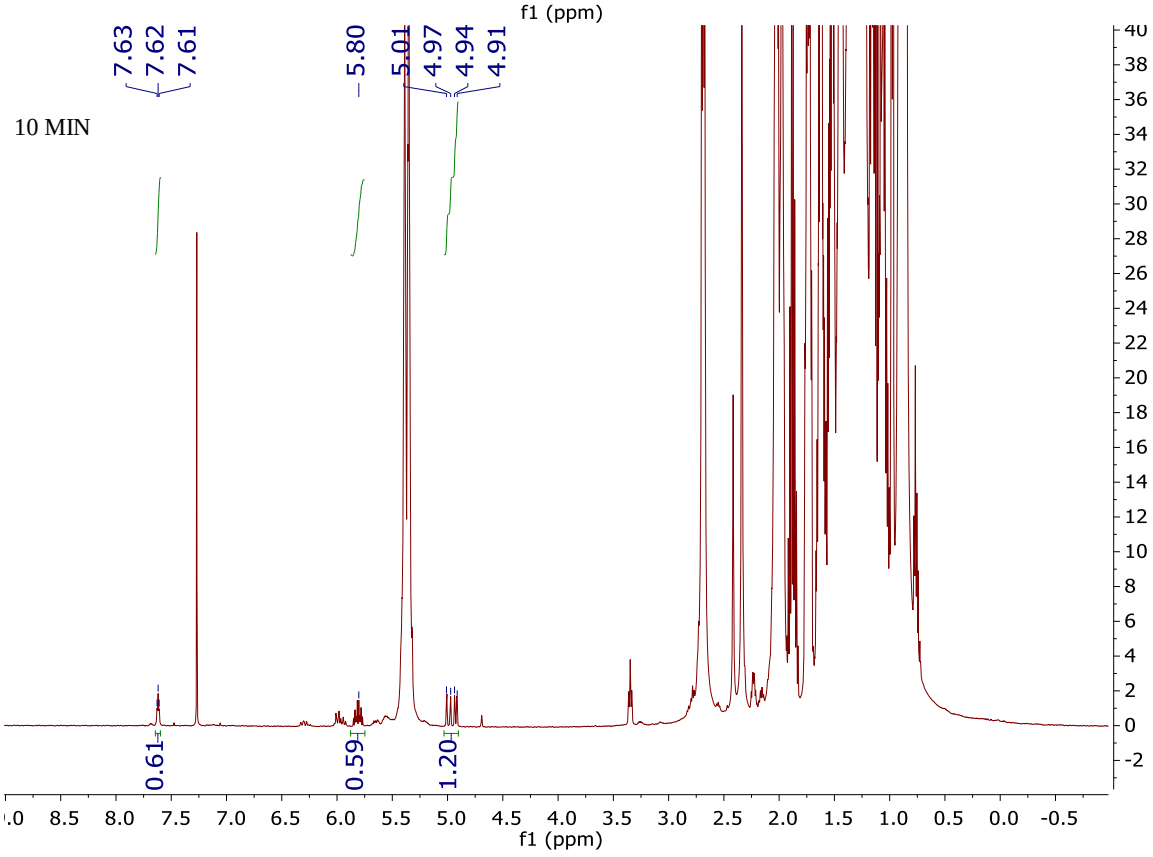

Figure B.6.4 (cont'd)

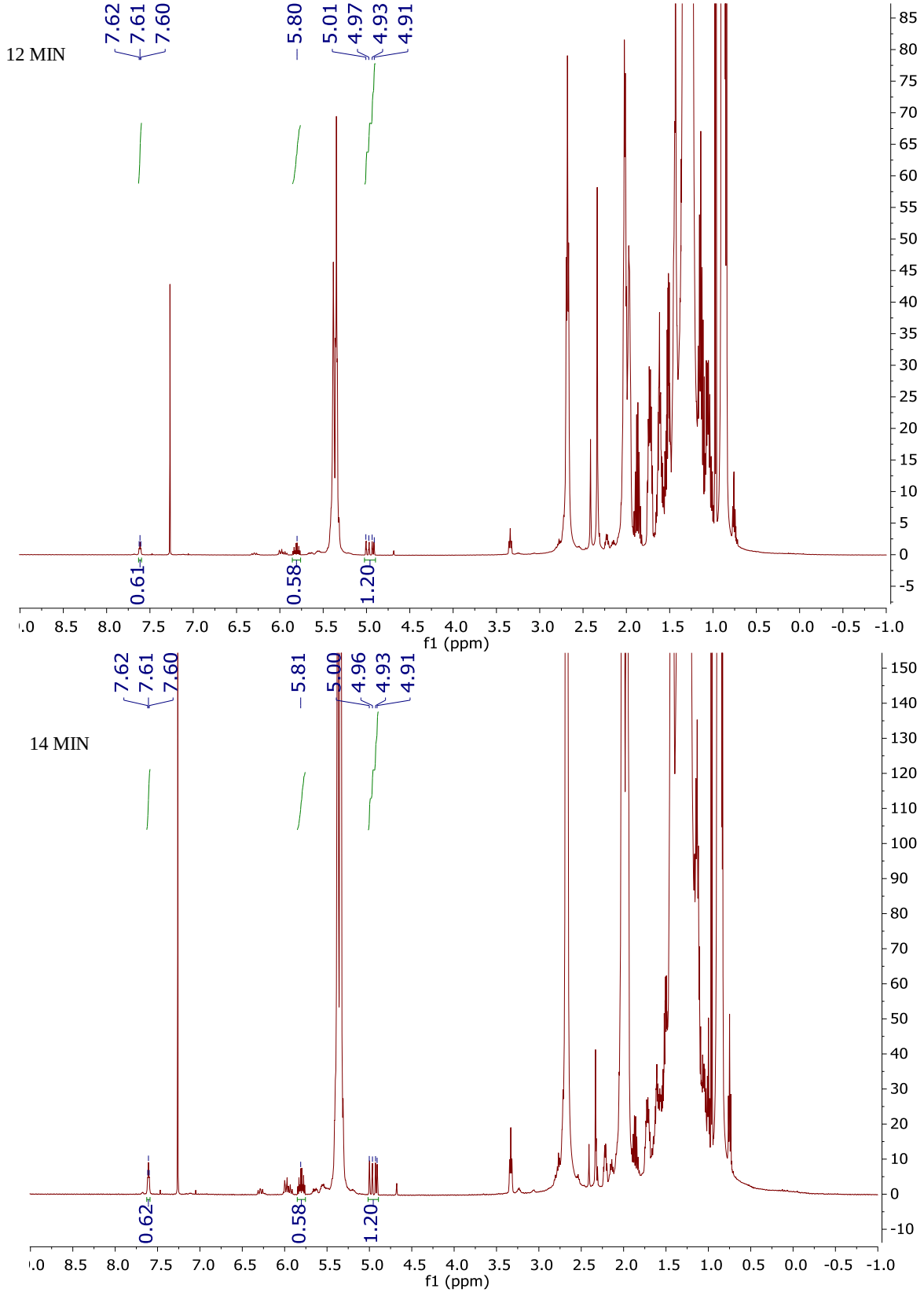

Figure B.6.4 (cont'd)

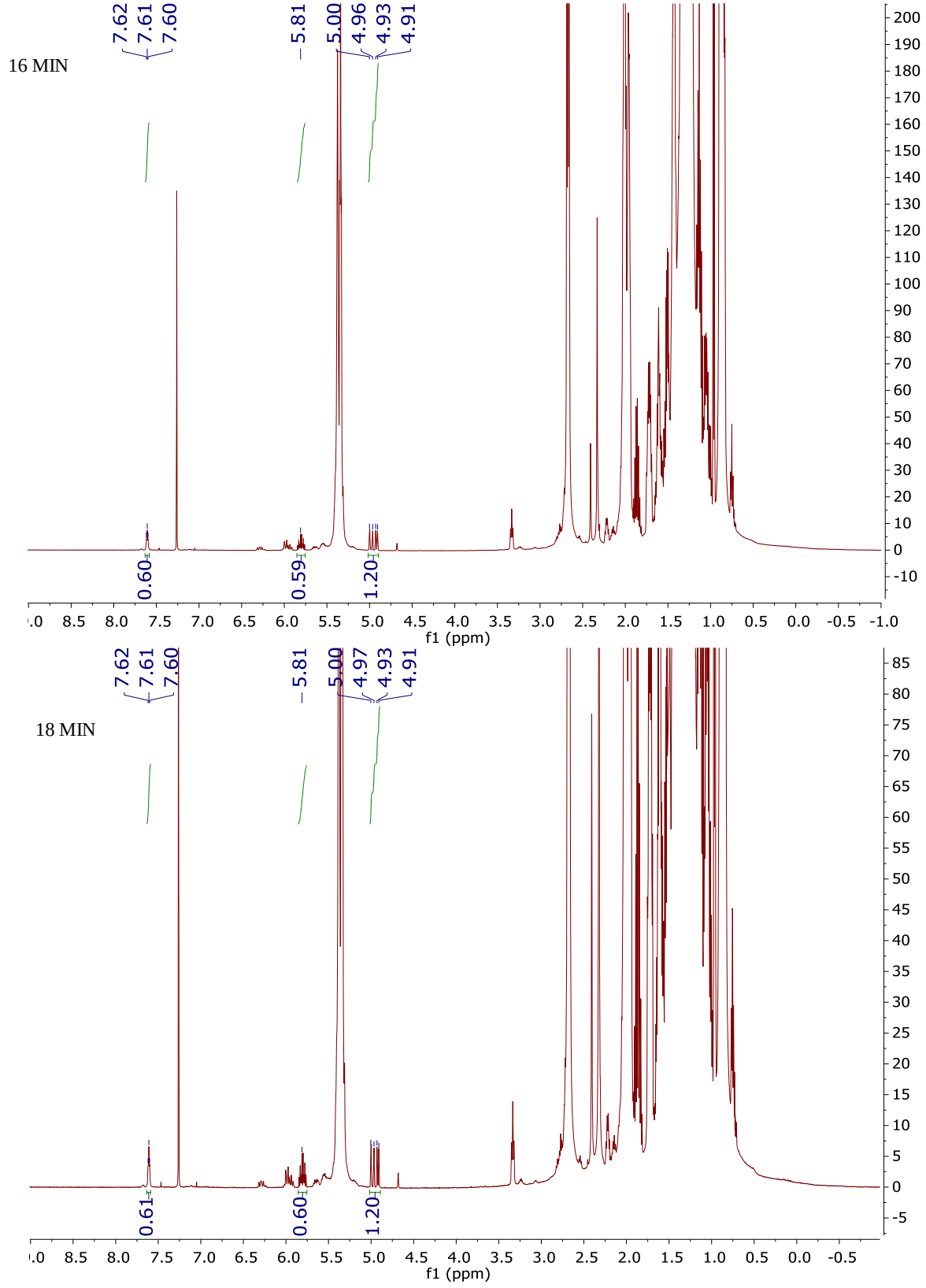

Figure B.6.4 (cont'd)

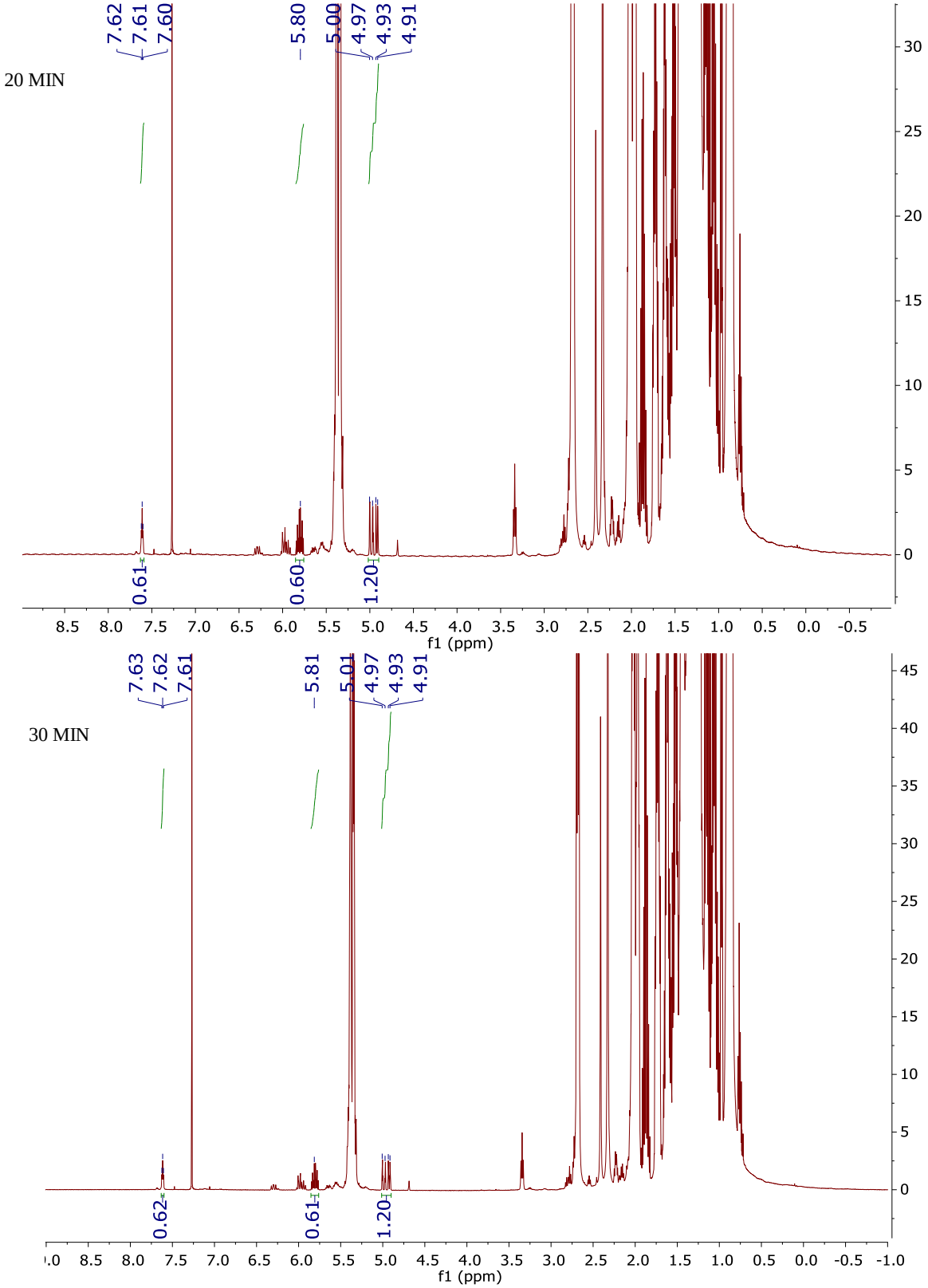

Figure B.6.4 (cont'd)

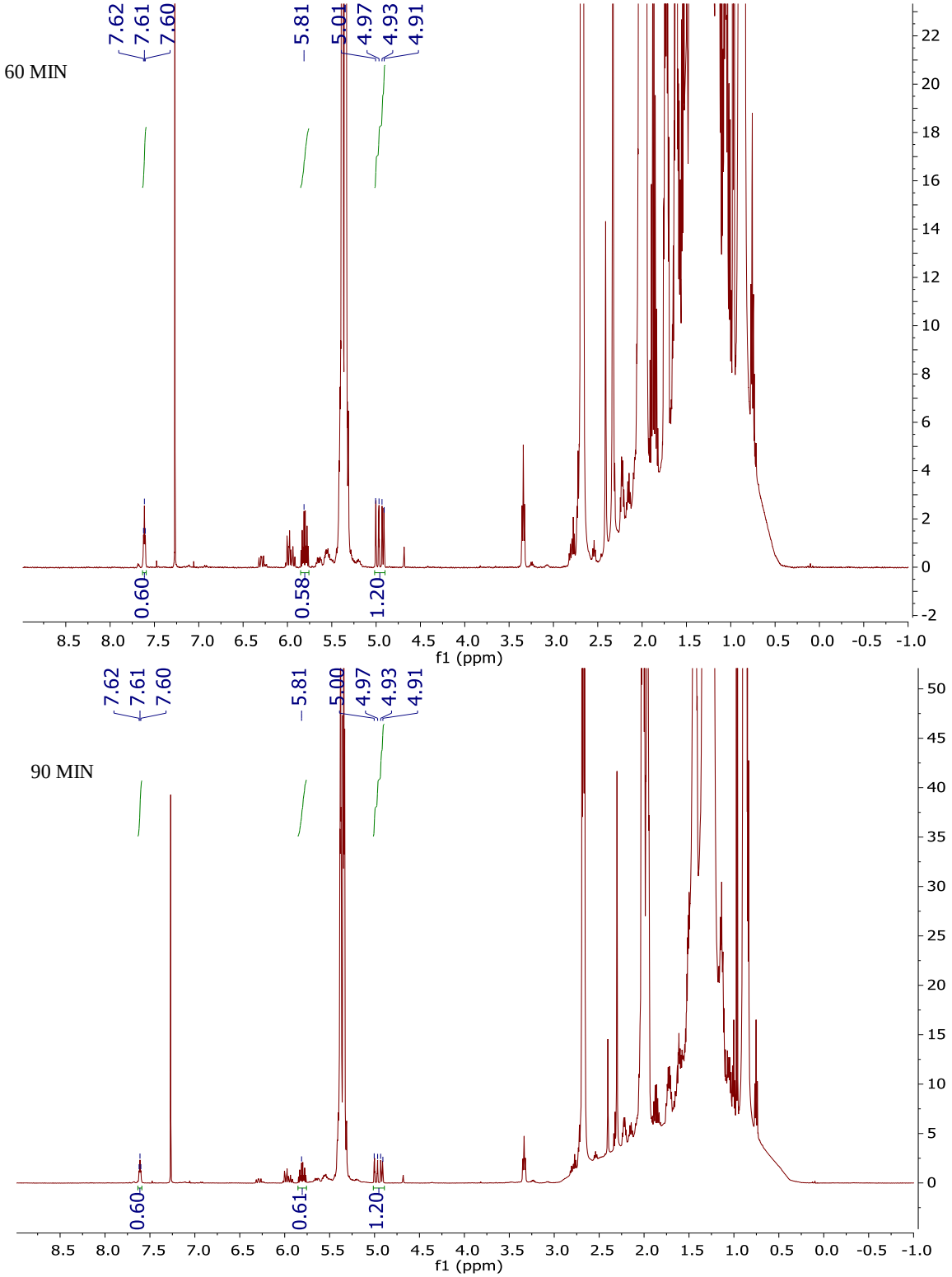

Figure B.6.4 (cont'd)

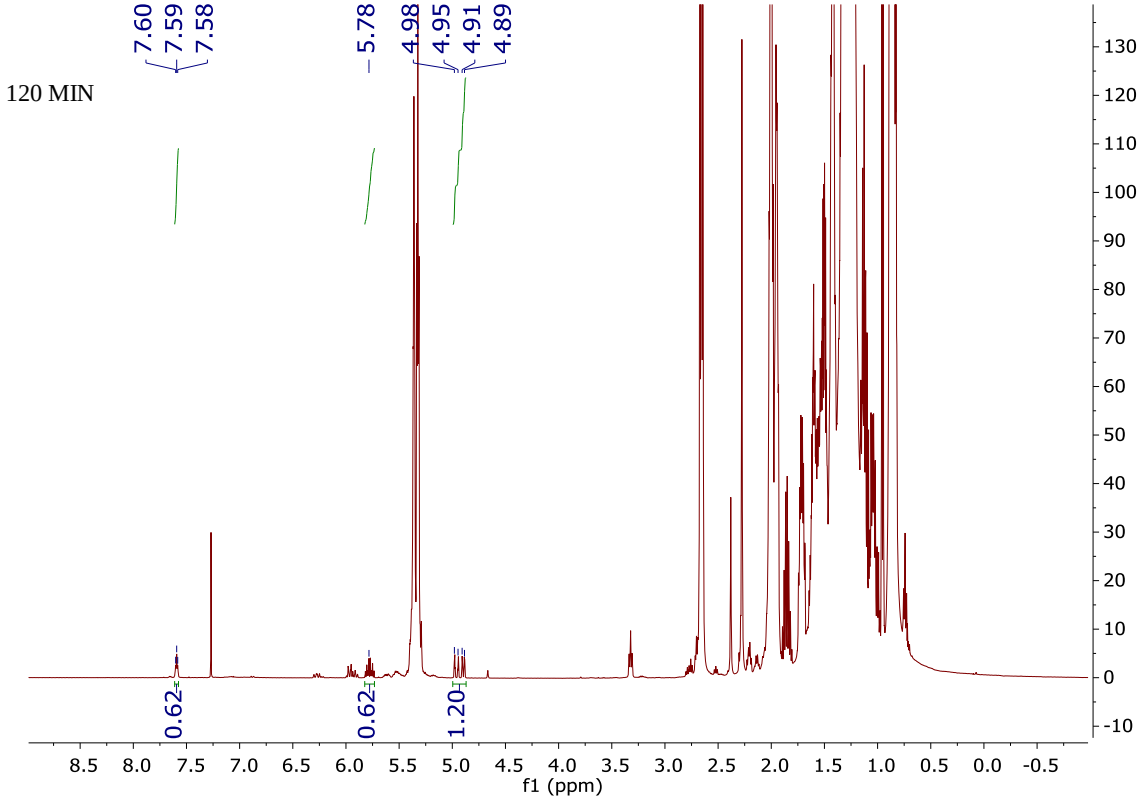

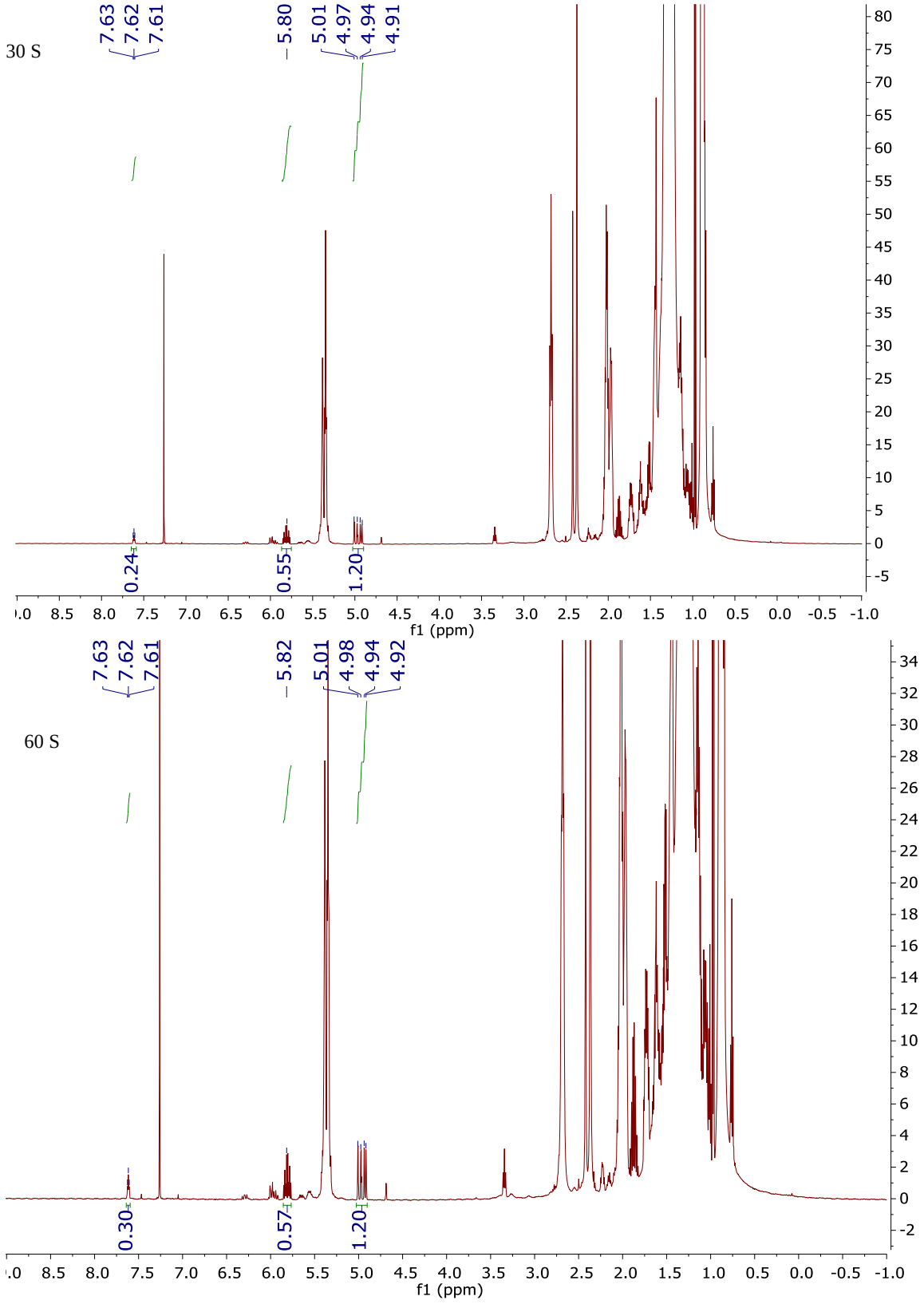

Figure B.6.5: ^{1}H NMR of reaction E mixture in different time.

Figure B.6.5 (cont'd)

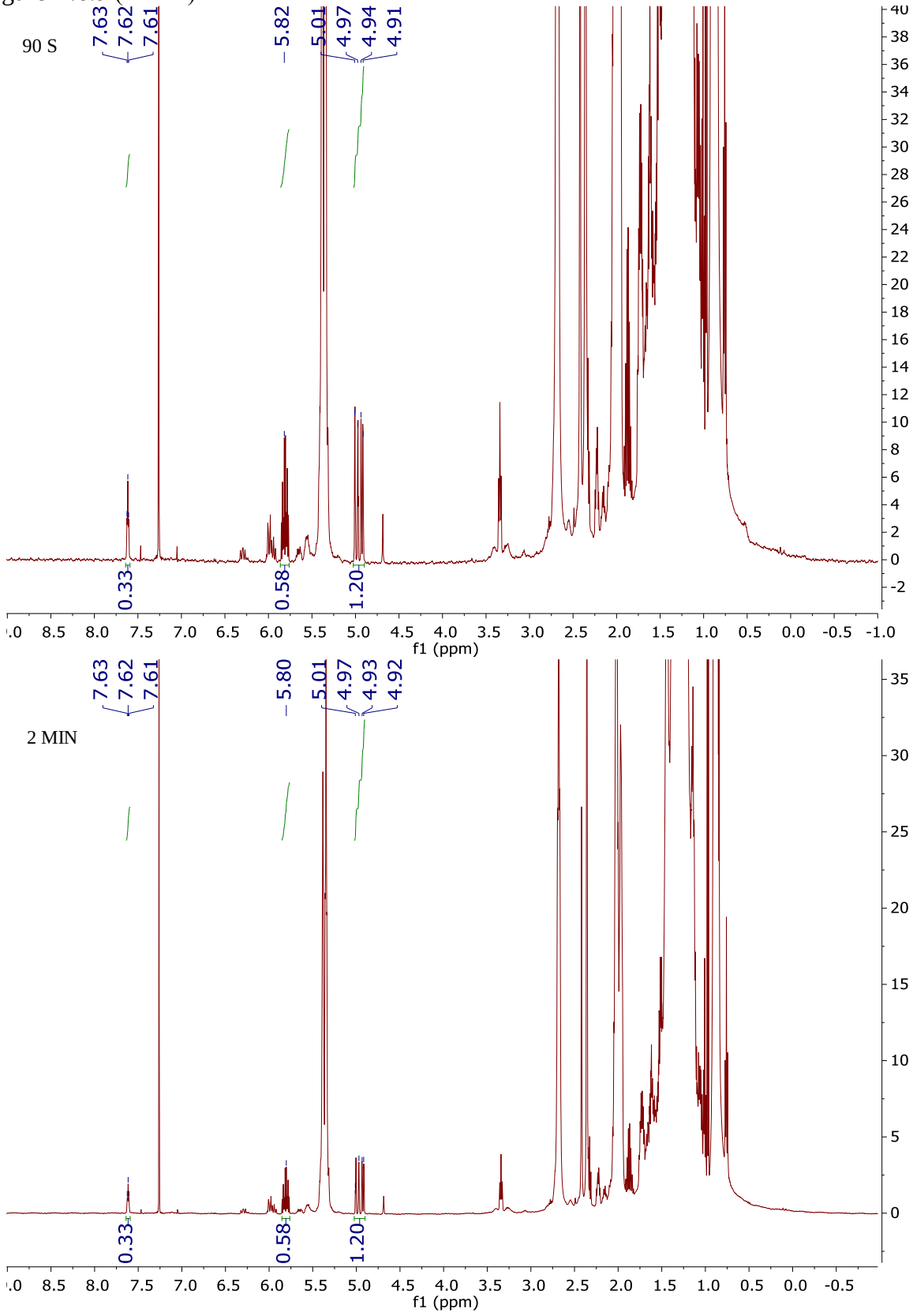

Figure B.6.5 (cont'd)

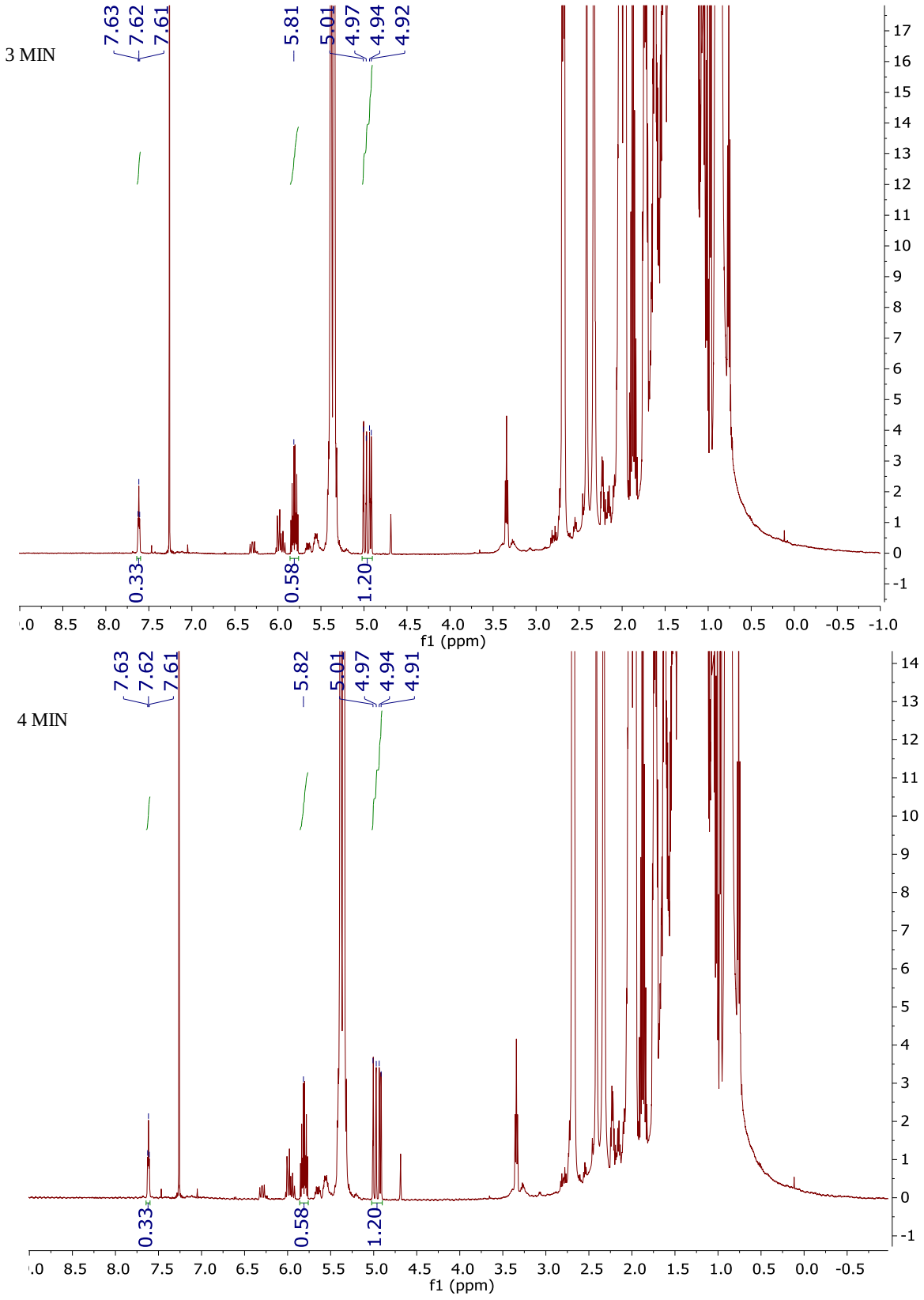

Figure B.6.5 (cont'd)

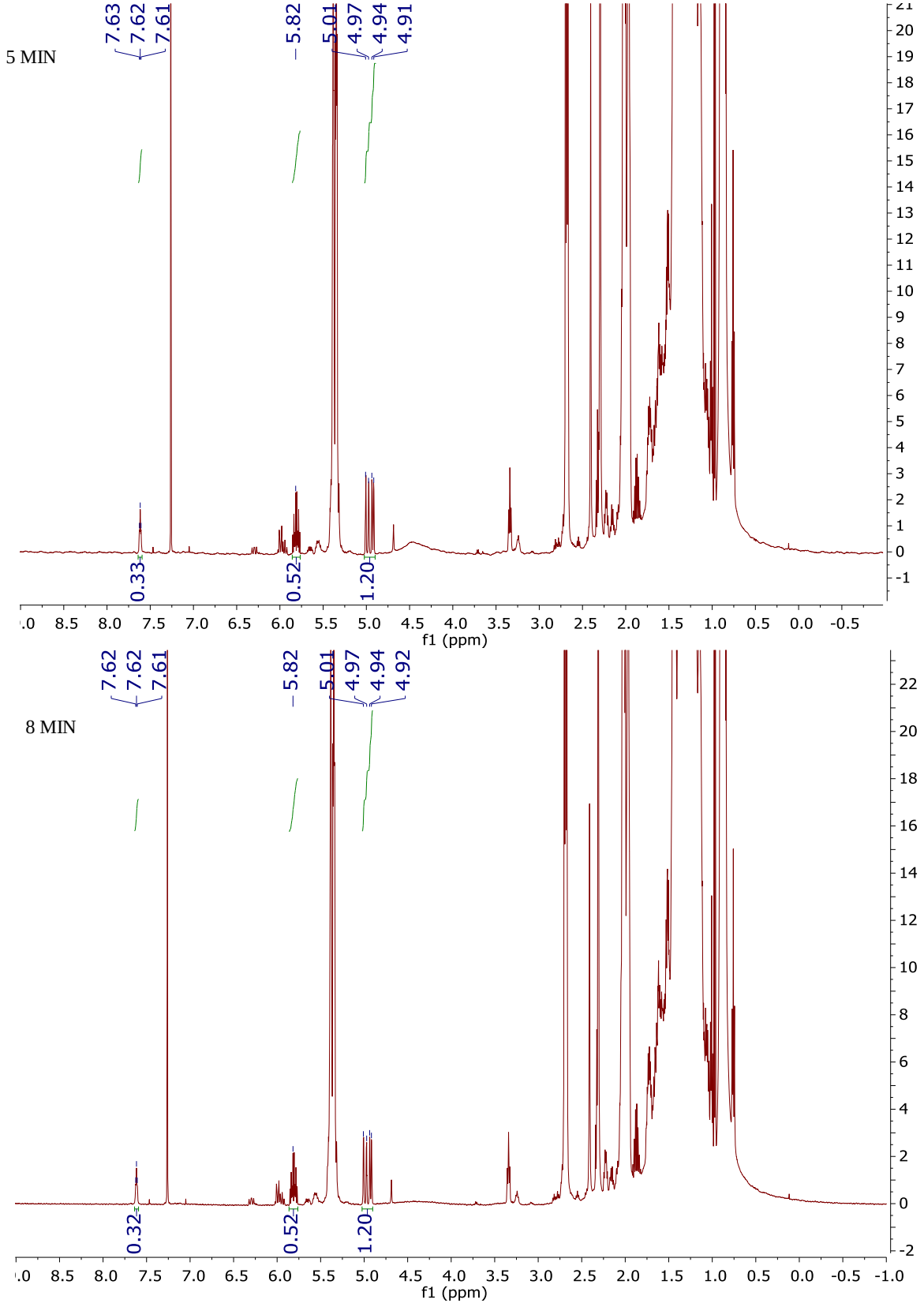

Figure B.6.5 (cont'd)

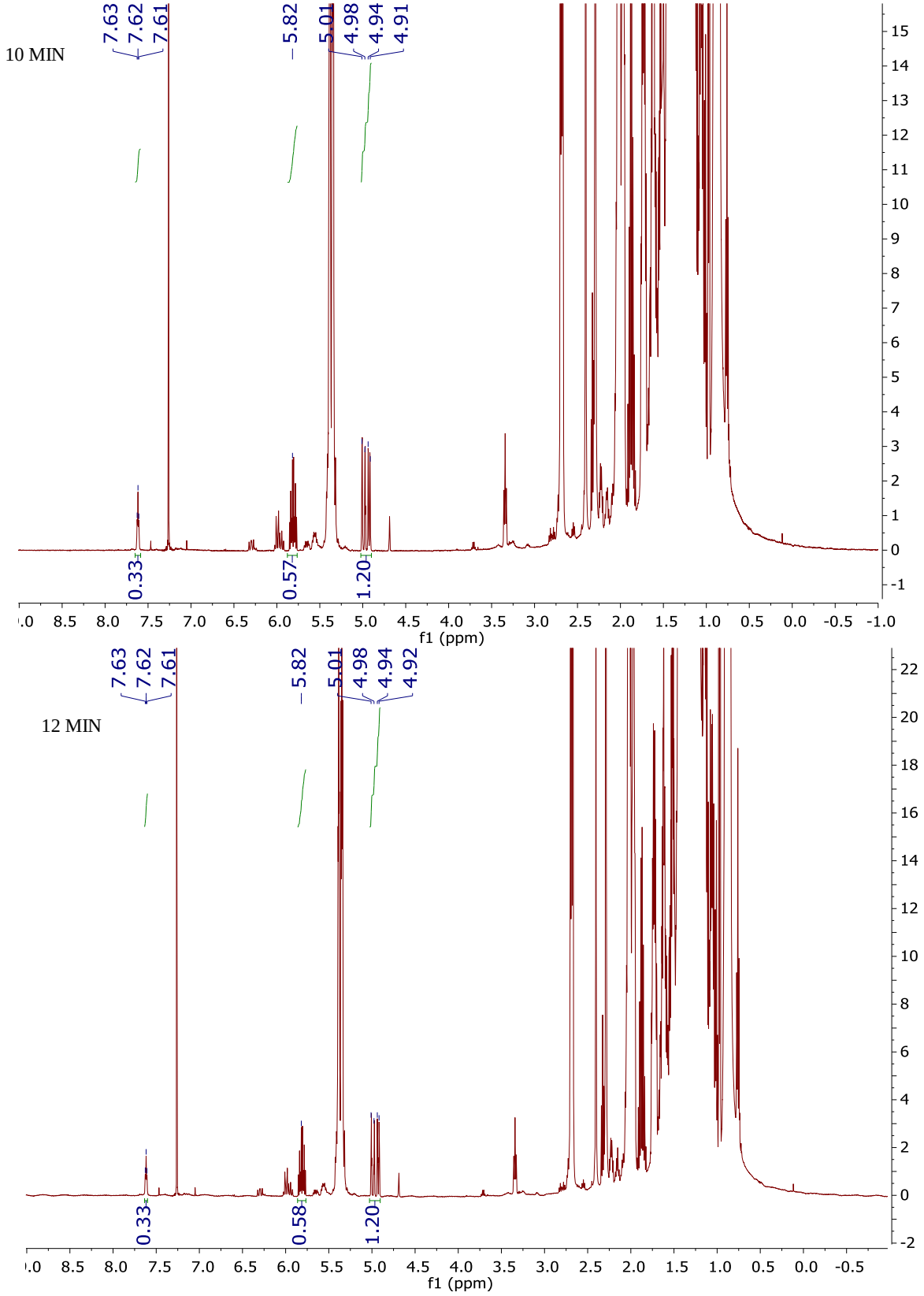

Figure B.6.5 (cont'd)

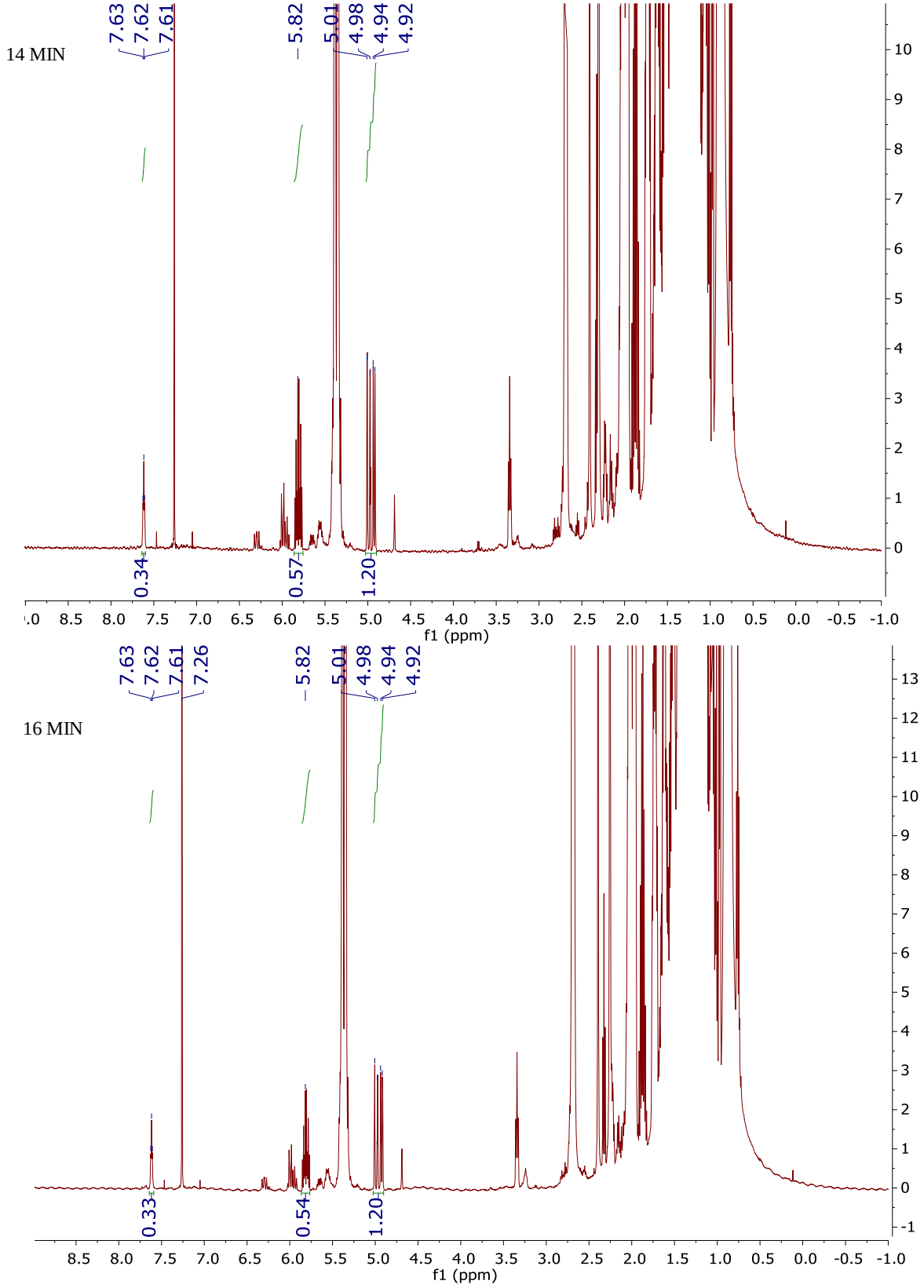

Figure B.6.5 (cont'd)

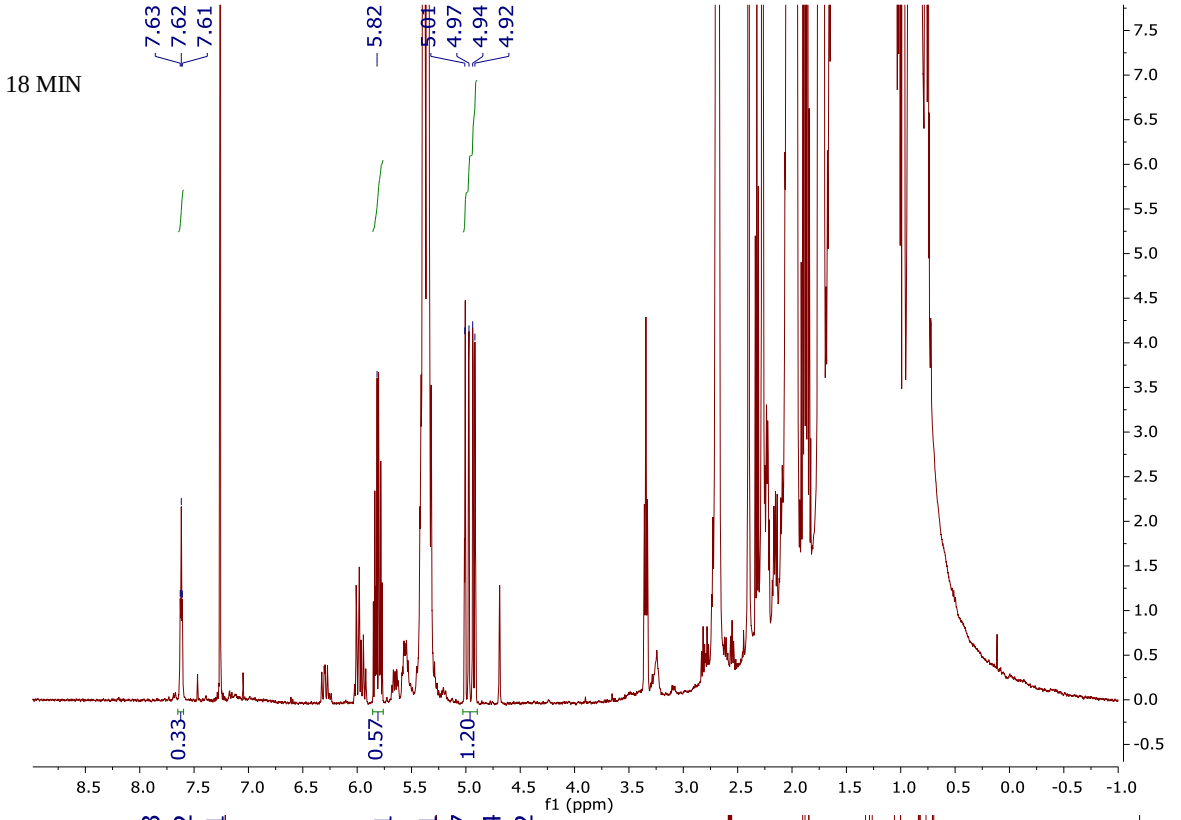

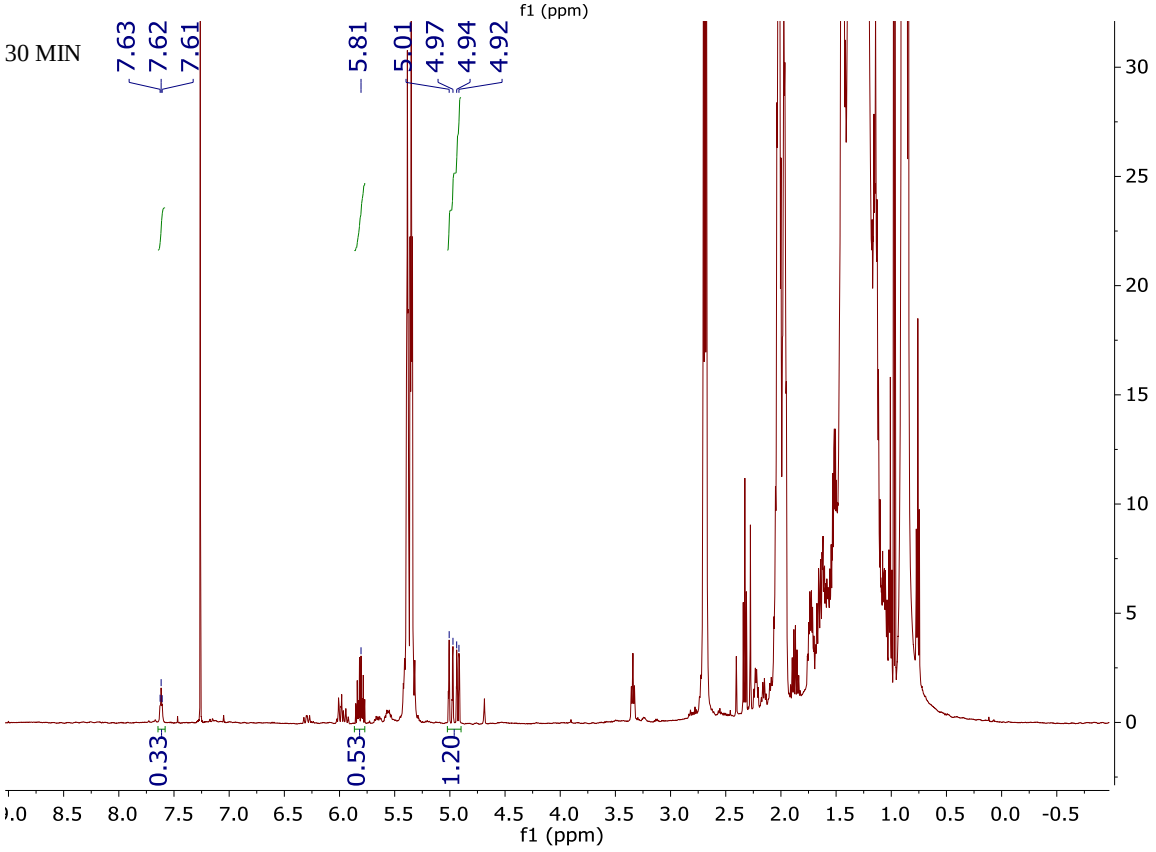

Figure B.6.5 (cont'd)

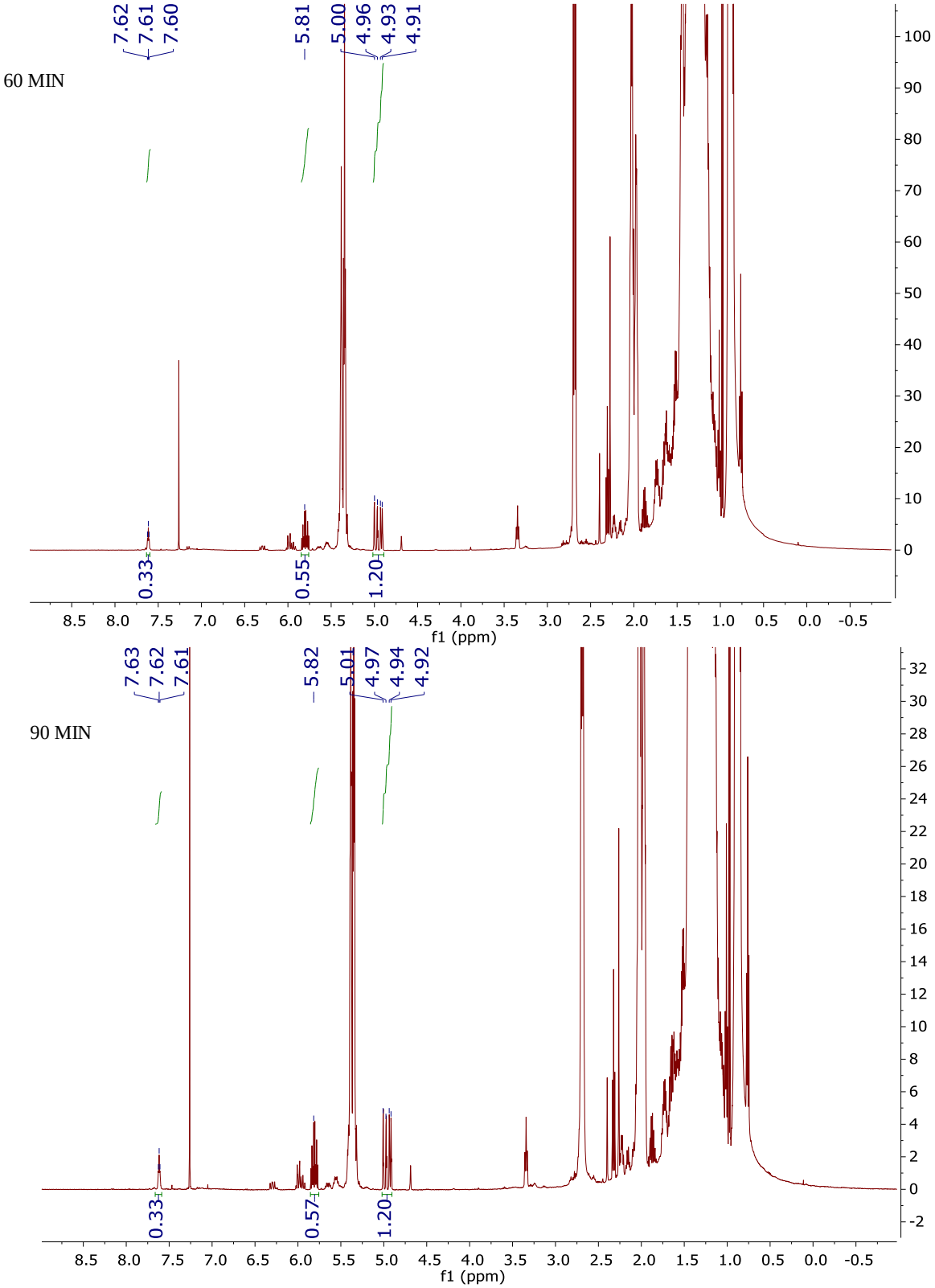

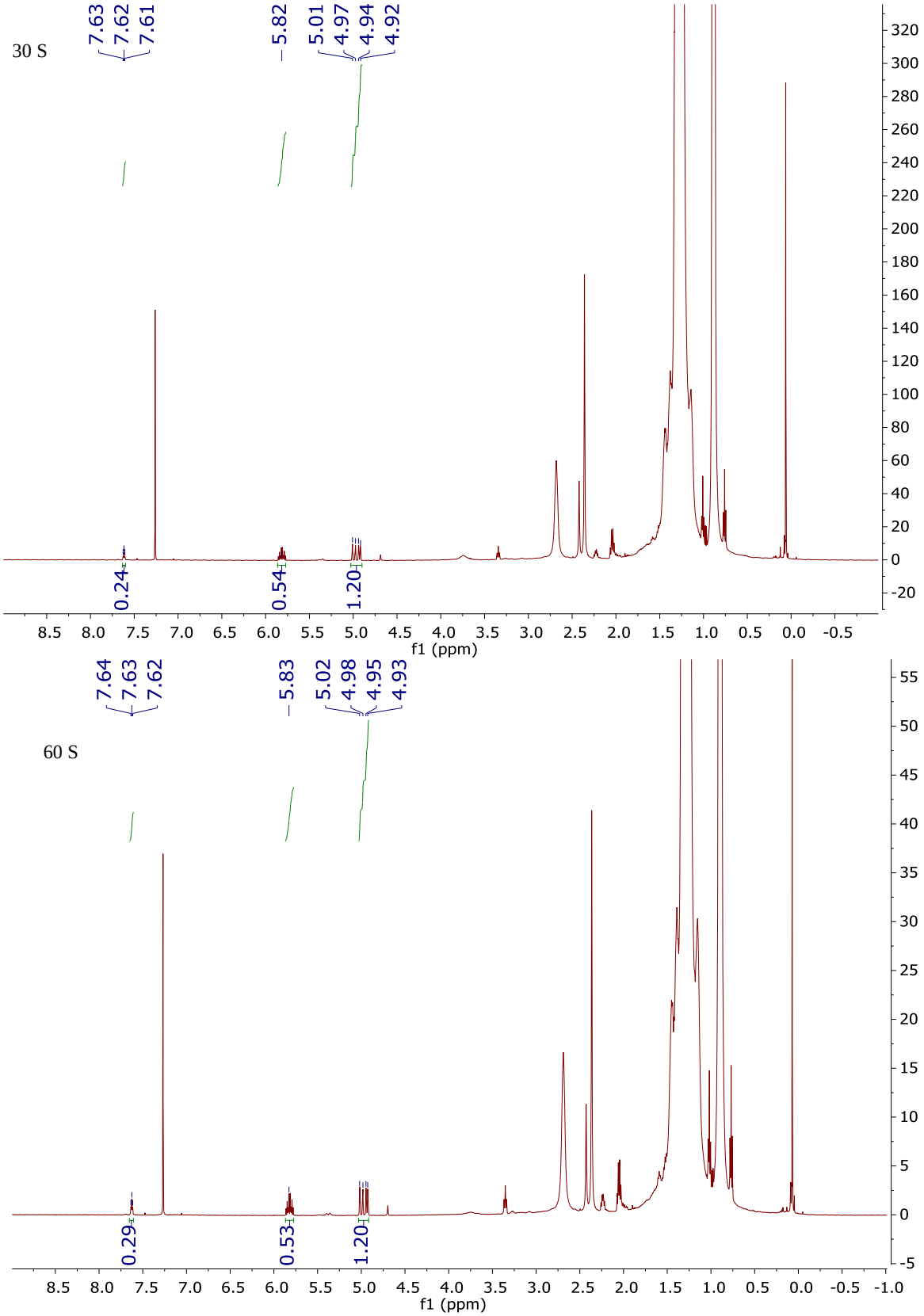

Figure B.6.6: ^{1}H NMR of reaction F mixture in different time.

Figure B.6.6 (cont'd)

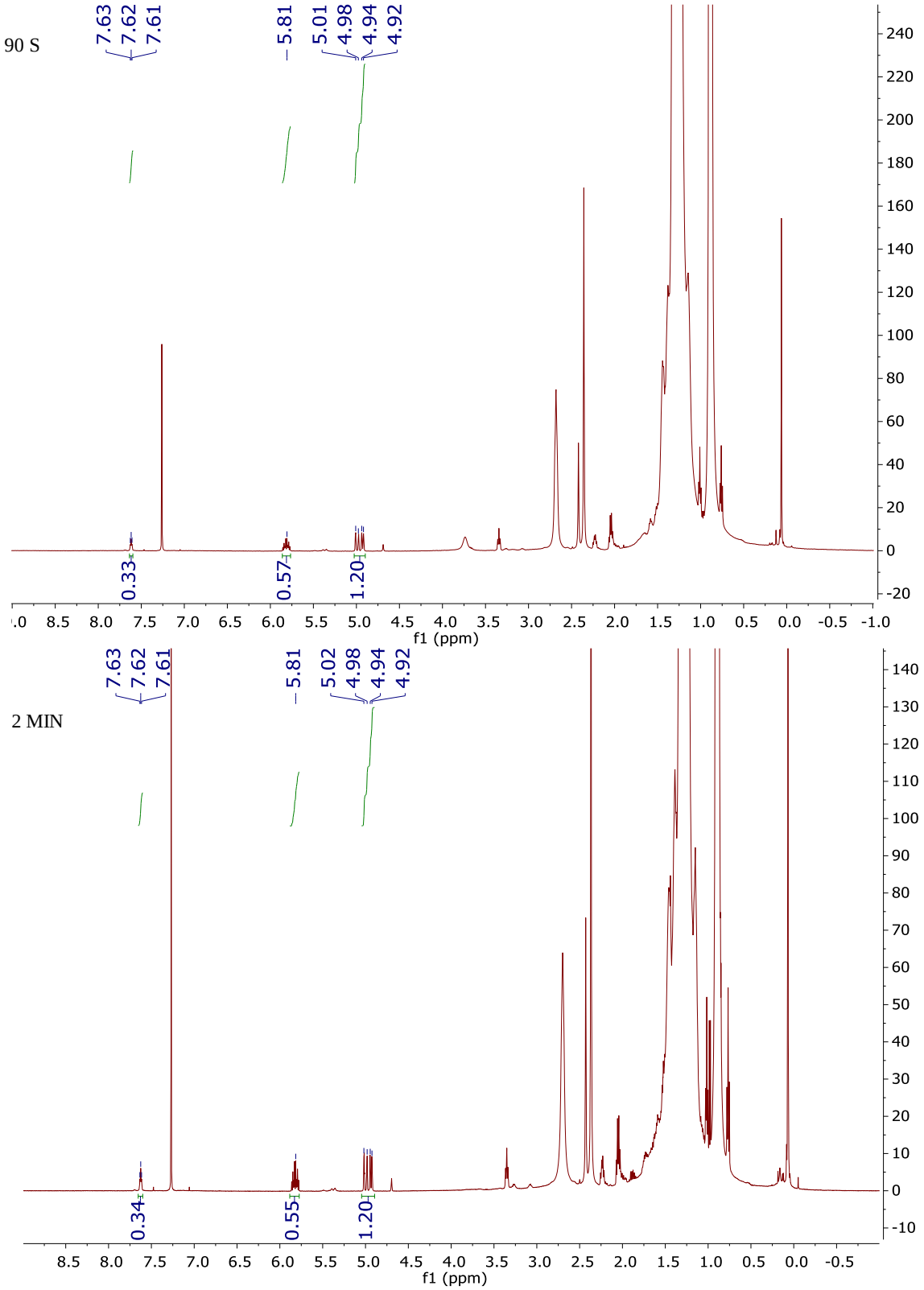

Figure B.6.6 (cont'd)

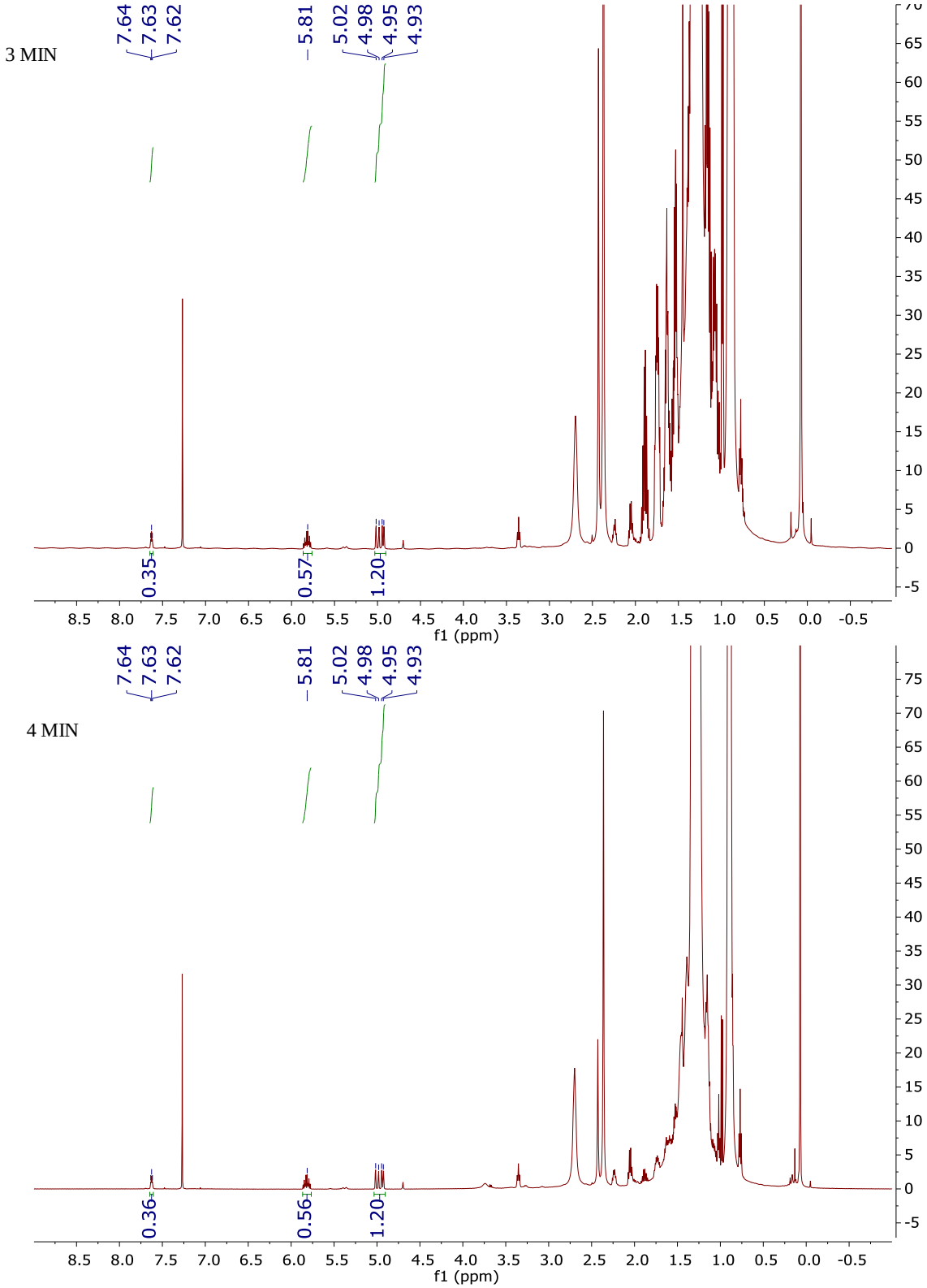

Figure B.6.6 (cont'd)

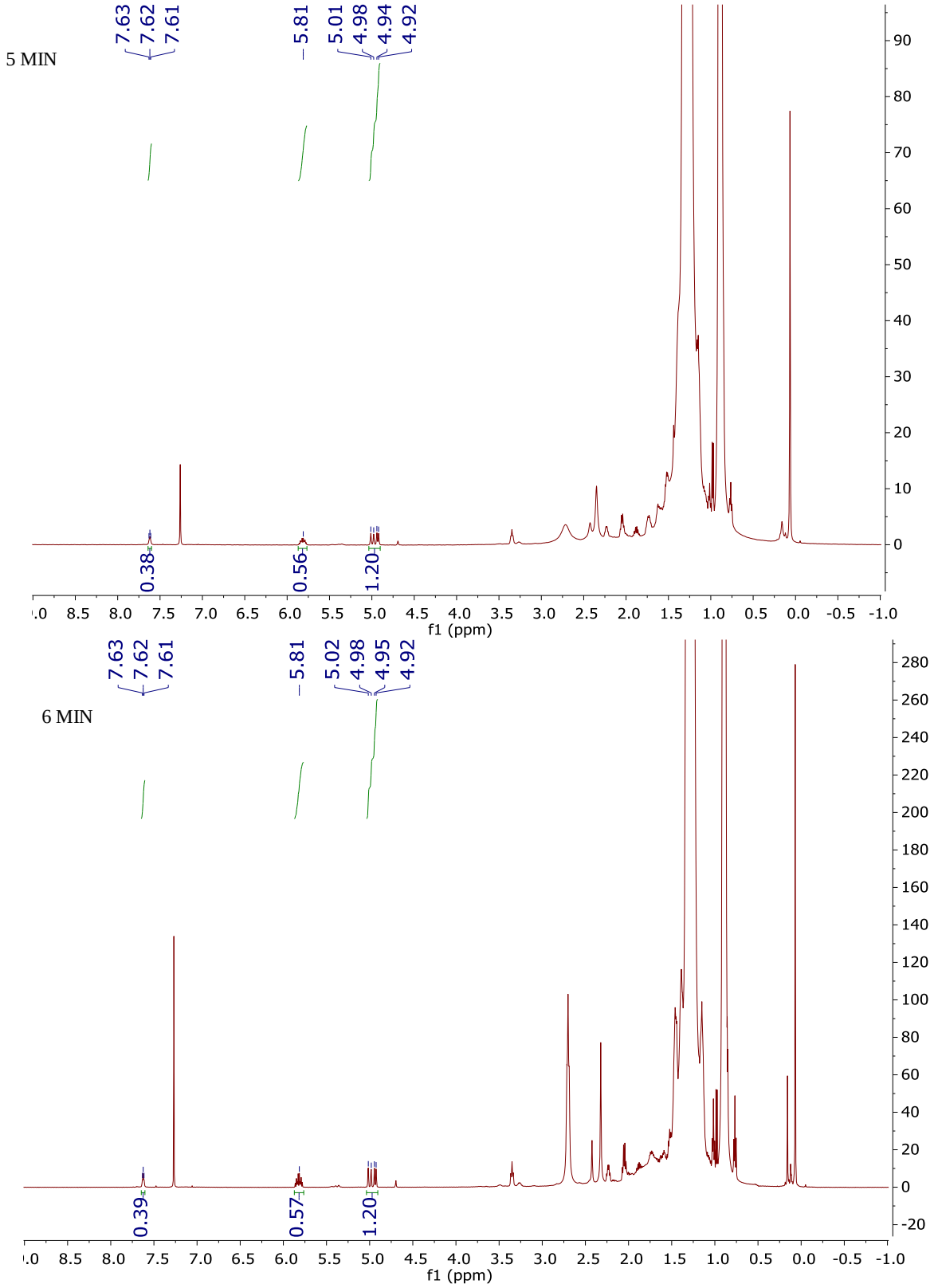

Figure B.6.6 (cont'd)

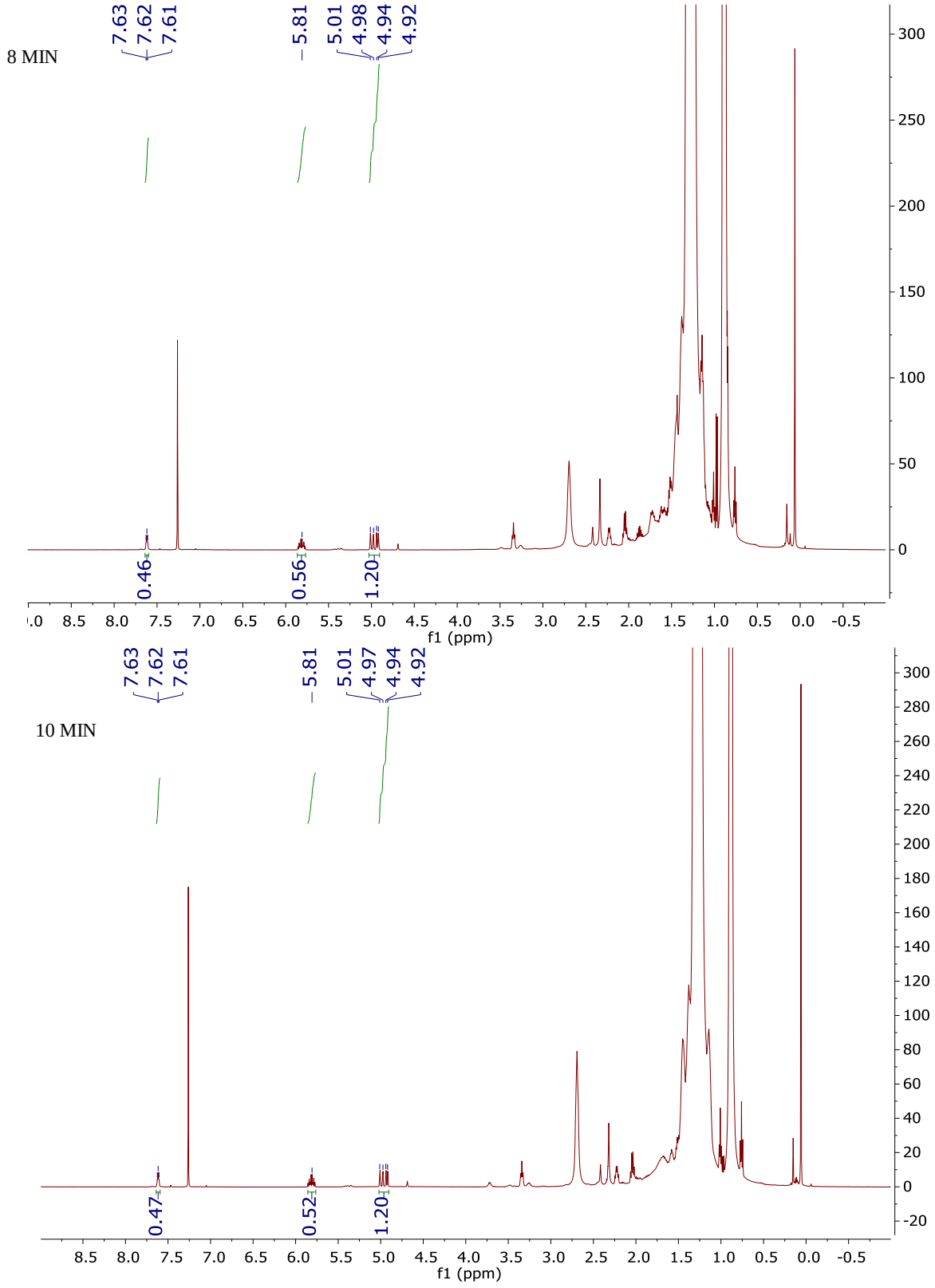

Figure B.6.6 (cont'd)

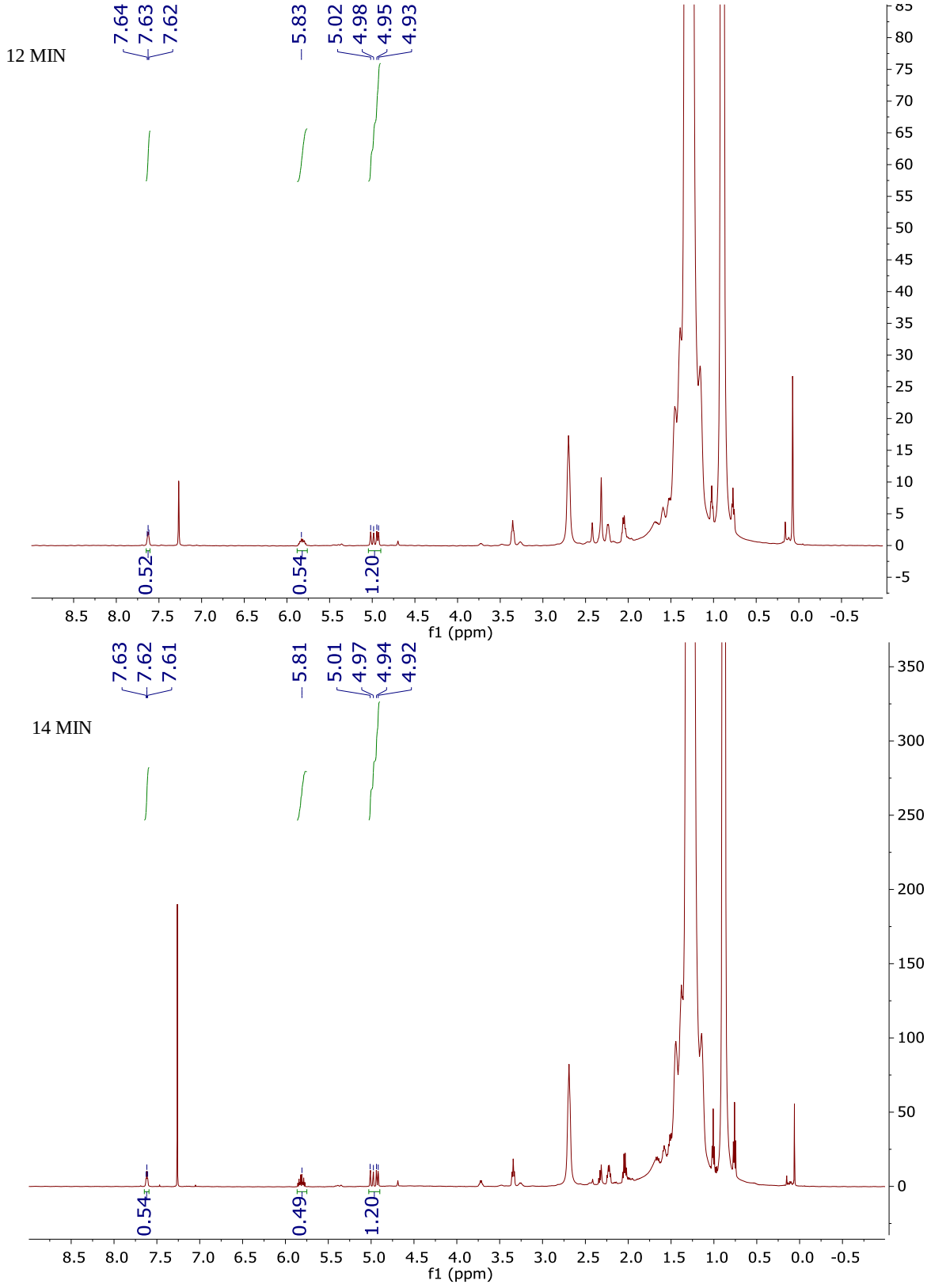

Figure B.6.6 (cont'd)

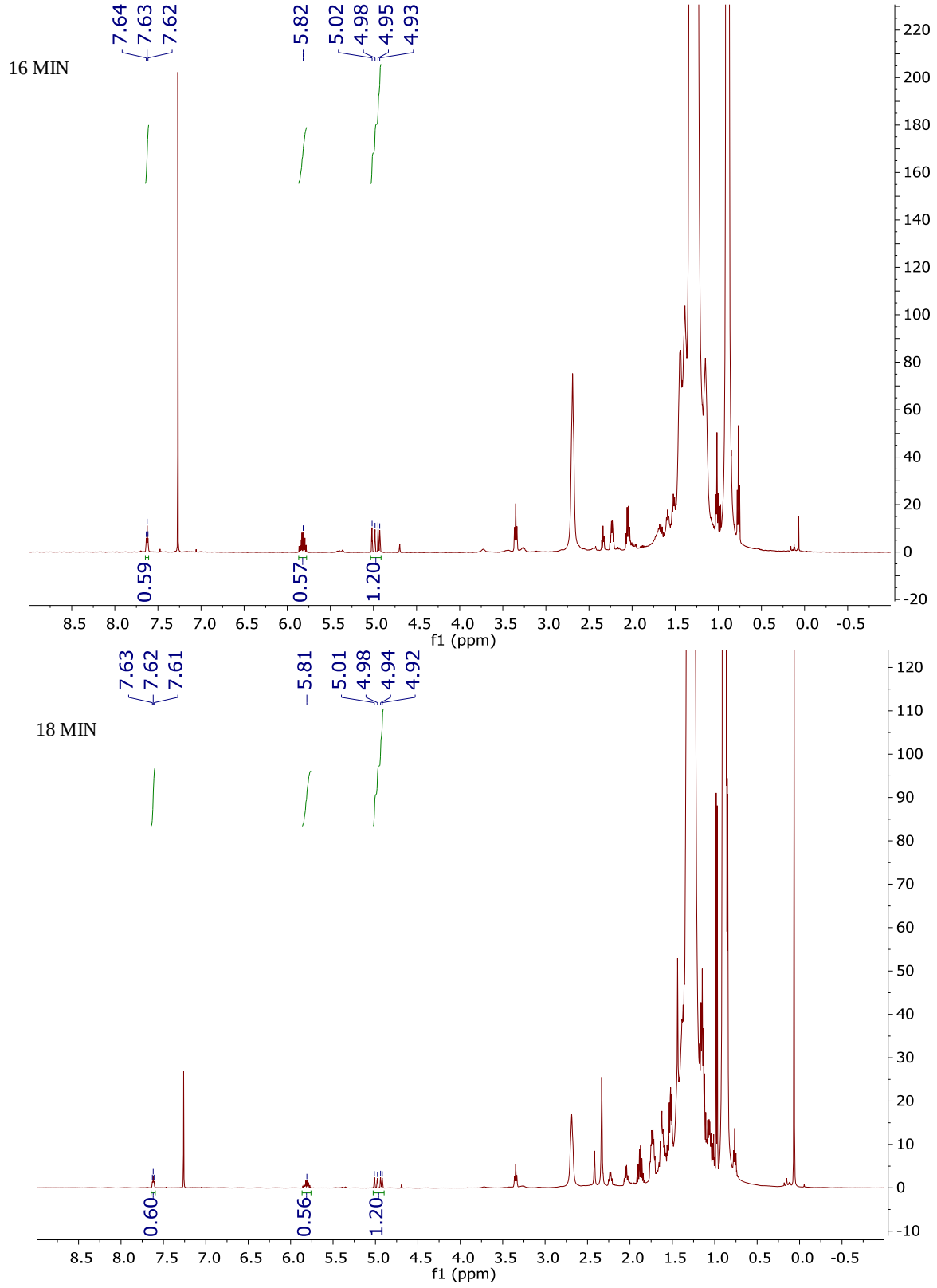

Figure B.6.6 (cont'd)

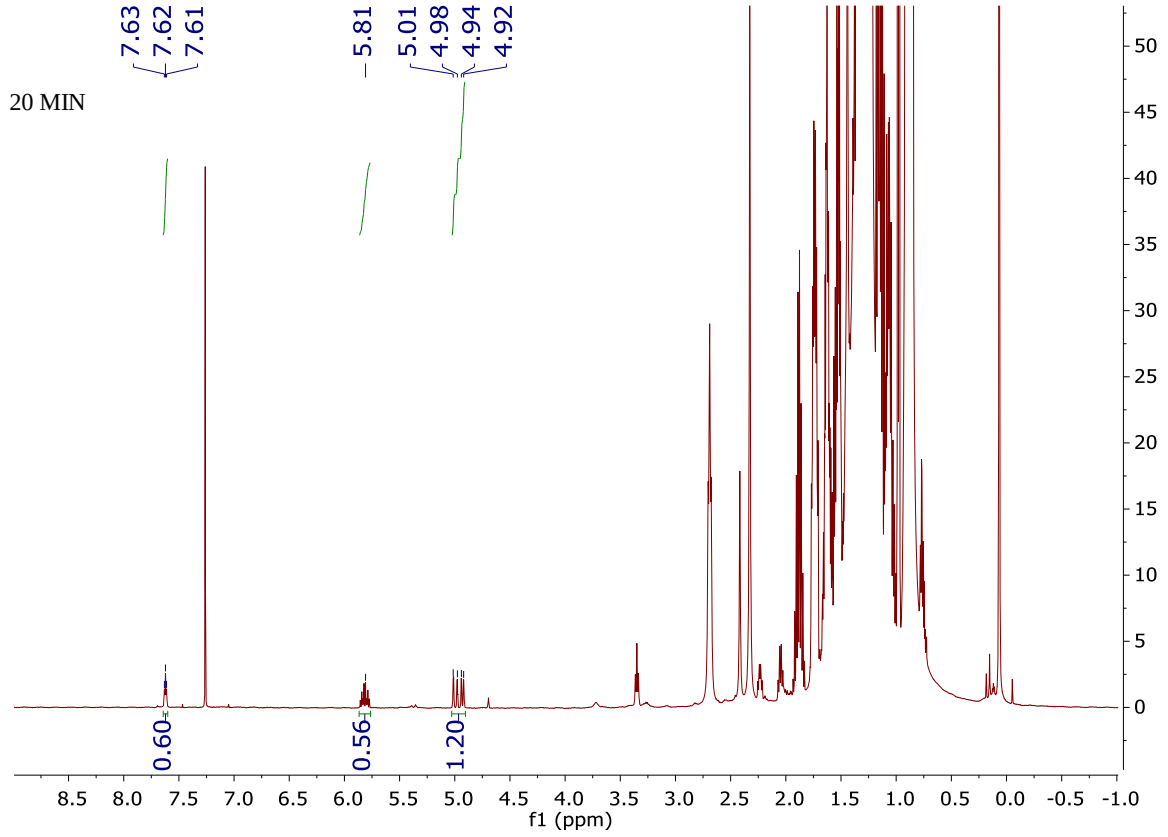

Reaction between oleylamine and oleylamide.

In a three-neck round-bottom flask equipped with a water-cooled-condenser and kept under air-free conditions (N_2 Schlenk line), 96 ul of octadecene, 2.00 ml of OLA (3.0 mmol), 1.20 ml of a n-BuLi solution (2.5 M hexane solution, 1.5 mmol n-BuLi) and 0.90 ml TMEDA (3 mmol) are dissolved in 5 ml of hexadecane. This oleylamine and oleylamide mixture is heated to 210 ^{o}C. After four hours, the reaction mixture is directly dissolved in d-$CHCl_3$ for NMR measurenment.

Results: 0.31 mmol imine was formed (Figure B.7).

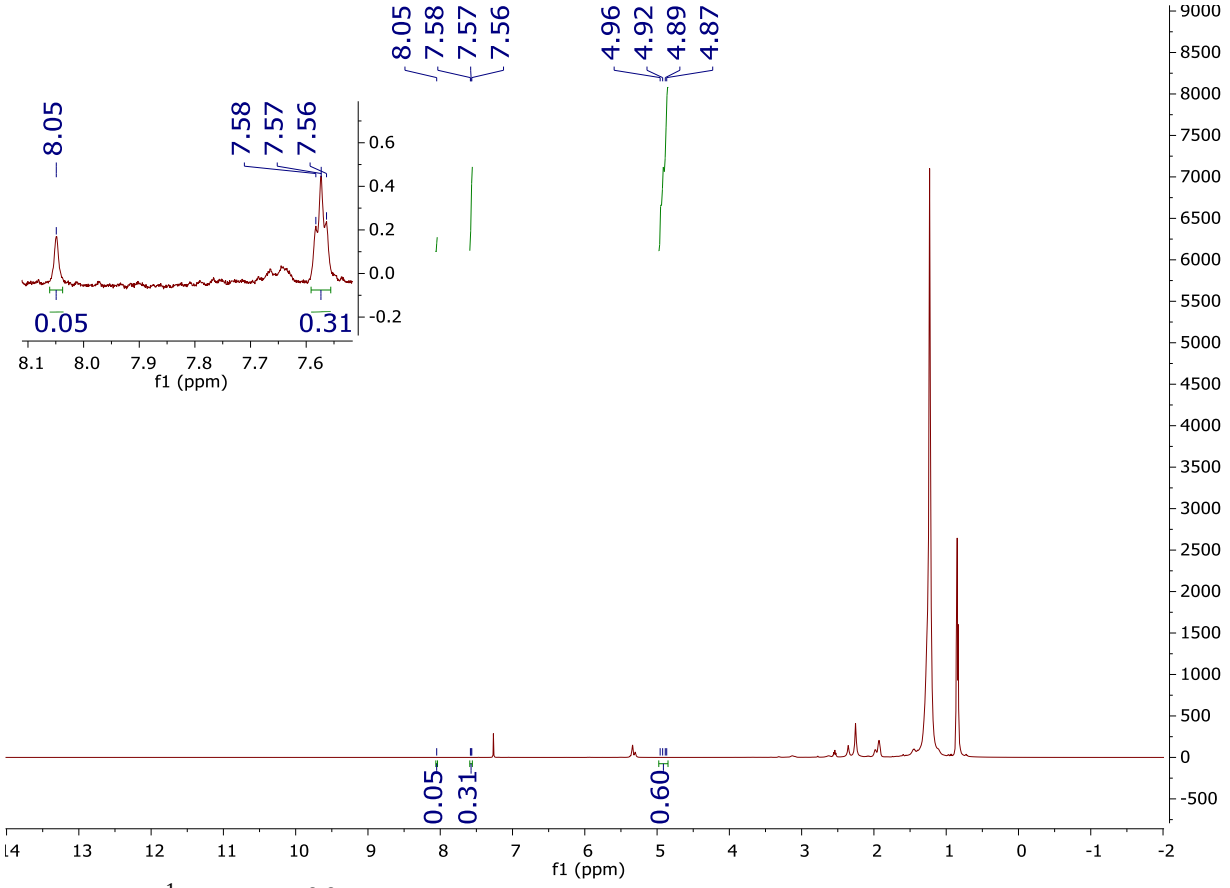

Figure B.7: ^{1}H NMR of final liquid.

LITERATURE CITED

LITERATURE CITED

[1] Trentler, T. J.; Goel, S. C.; Hickman, K. M.; Viano, Ann. M.; Chiang, M. Y.; Beatty, A. M.; Gibbons, P. C.; Buhro, W. E. *J. Am. Chem. Soc*. **1997**, *119*, 2172-2181.

[2] Purdy, A. P. *Inorg. Chem*. **1994**, *33*, 282.

[3] Guillemin, J. C.; Denis, J. M. *Tetrahedron* **1988**, *44*, 4431-4446.

[4] Kadoya, K.; Matsunaga, N.; Nagashima, A. *J. Phys. Chem. Ref. Data*. **1985**, *14*, 947.

[5] Younglove, B. A.; Hanley, H. J. M. *J. Phys. Chem. Ref. Data*. **1986**, *15*, 1323.

[6] Xiao, J. P.; Xie, Y.; Tang, R.; Luo, W. *Inorganic Chemistry* **2003**, *42*, 107.

[7] Hsieh, J. C.; Yun, D. S.; Hu, E,; Belcher A. M. *J. Mater. Chem*. **2010**, *20*, 1435.

[8] Huang, J. M.; Zhang, J. F.; Dong, Y.; Gong, W. *J. Org. Chem*. **2011**, *76*, 3511.

[9] Paquin, L.; Hamelin, L.; Taxier-Boullet, F. *Synthesis*, **2006**, *10*, 1635

[10] Morales, S.; Guijarro, F. G.; Ruano, J. L. G.; Cid, M. B. *J. Am. Chem. Soc*. **2014**, *136*, 1082.

[11] Reeves, J. T.; Visco, M. D.; Marsini, M. A.; Grinberg, N.; Busacca, C. A.; Mattson, A. E.; Senanayake, C. H. *Org. Lett*. **2015**, *17*, 2442.

[12] Mourdikoudis, S.; Liz-Marzan, L. M. *Chem. Mater*. **2013**, *25*, 1465.

[13] McSkimming, A.; Colbran, S. B. *Chem. Soc. Rev*. **2013**, *42*, 5439.

Chapter 4

CONCLUSION AND FUTURE WORK

The main goal of this work was to design a solution-based approach to synthesize high quality colloidal InN nanoparticles, characterize the properties of InN obtained by this new approach and understand the reaction mechanism. In our new approach, commercial $InBr_3$ and oleylamine were employed as indium and nitrogen precursor, respectively. Direct injection alkylamide precursors into indium(III)-amine mixture at relatively low temperature (210 ^oC) under ambient pressure can afford colloidal zinc-blende InN nanorods with an average length of 25.7 ± 3.6 nm and width of 5.9 ± 1.2 nm. Progression of this approach was traced by TEM, showing $In^{(0)}$ nanoparticles form first then catalyze the growth of InN nanorods through a solution-liquid-solid mechanism. Vis-NIR absorption measurements indicated InN prepared by this new approach is degenerately-doped. Characterizations by XRD, Raman and XPS support this method as a convincing advancement toward high quality zinc-blende InN nanoparticles. In addition, we also confirmed NH_3, H_2 and secondary imine ($R\text{-}CH{=}N\text{-}CH_2\text{-}R$, $R{=}CH_3(CH_2)_7CH{=}(CH_2)_8$) are side products of this approach by using NMR and GC. A possible reaction mechanism was also proposed here: (1) An important NH_2^- intermediate was produced as a result of the formation of the secondary imine. (2) NH_2^- intermediate reacted with In^{3+} to form complex which easily decomposed to form $(InN)_n$ cluster. (3) $In^{(0)}$ nanoparticles catalyze these $(InN)_n$ cluster to zinc-blende InN with high crystallinity. Besides, we also discovered a new family of nitrogen precursor for the synthesis of nitrides semiconductor.

For the future work, we will focus on four areas: First, we will keep on investigating the mechanism. Since we already know the side products of our approach, we can quantify the amount of these by products, which may give us some hints to have a deeper understanding on

this mechanism. Second, we will seek methods to tune the size of InN nanorods. Since we can quantify the concentration of this imine at each reaction time by using ^{1}H NMR, the secondary imine is a very good indicator to study the kinetics of our approach. Through the kinetics study, we may know which parameters can affect the kinetics, such as concentration of oleylamine, type of amide and temperature. Hence, size of InN can be tuned by changing the kinetics. Third, we will fully characterize the doping level of these InN nanorods. Fourth, we will build the $In_xGa_{1-x}N$ system and apply it into solar cells.